# ACOUSTIC ACTUATION OF VAPOR-LIQUID INTERFACES IN BOILING AND CONDENSATION PROCESSES

A Dissertation
Presented to
The Academic Faculty

by

Thomas Robert Boziuk

In Partial Fulfillment
Of the Requirements for the Degree
Doctor of Philosophy in Mechanical Engineering

Georgia Institute of Technology
George W. Woodruff School of Mechanical Engineering

December 2017

**ACOUSTIC ACTUATION OF VAPOR-LIQUID INTERFACES**

**IN BOILING AND CONDENSATION PROCESSES**

Approved by:


Professor Ari Glezer, Advisor
School of Mechanical Engineering
*Georgia Institute of Technology*

Professor Marc K. Smith
School of Mechanical Engineering
*Georgia Institute of Technology*

Professor S. Mostafa Ghiaasiaan
School of Mechanical Engineering
*Georgia Institute of Technology*

Professor Roman Grigoriev
School of Physics
*Georgia Institute of Technology*

Professor Michael Schatz
School of Physics
*Georgia Institute of Technology*


Date Approved: July 25th 2017

*Dedicated to anyone curious.*

## ACKNOWLEDGEMENTS

I would like to thank, first and foremost, my family for supporting me not only through these studies but through the many years prior. I would like to thank my wife, Kelly-Ann, for her support, encouragement, patience, and understanding; without this – who knows?

I would like to acknowledge and thank my advisor, Professor Ari Glezer, for guiding me through this work, and acting as a motivational force when necessary. You have taught me to not despair when a stray observation begins to lead down a related rabbit-hole, but instead to push my sleeves up and start digging. Without this, the work in this thesis would be far less interesting, and far less rewarding.

I am also indebted to the other members of my thesis committee; Professor Smith, Professor Ghiaasiaan, Professor Grigoriev, and Professor Schatz, for spending their time and effort helping to guide this work. Their expertise and input is very much appreciated.

I would also like to thank members of Dr. Rogers's acoustics lab, especially Michael Gray and James Martin, for helping with the characterization of the acoustic actuators.

I would like to thank all the FMRL alumni for helping to turn lab into a home-away-from-home, starting all the way back in 2009 when I'd just moved a thousand miles from where I grew up, knowing no one. In no particular order: Abe, Alon, Ash, Bojan, Chris F., Curtis, Dan, George, John C., John K., Mark, Michael, Pablo, Philip, Slava, Sourabh, Taylor, Tom C., Tom L., Travis, Yuehan, and Zicheng… thank you!

Finally, I would like to thank *all* the teachers and students along my path who have always encouraged me, starting back in Sudbury, through Tufts and Georgia Tech. Without encouragement from above as well as support from the sides… I certainly could not have accomplished this on my own.

## TABLE OF CONTENTS

## LIST OF FIGURES

## NOMENCLATURE

| | |
|---|---|
| CHF | Critical Heat Flux, W/cm$^2$ |
| $\Delta T_s$ | Change in Surface Superheat under Actuation |
| $T_s$ | Surface Temperature |
| $T_{sat}$ | Saturation Temperature of Liquid |
| $T_{bulk}$ | Temperature of the Bulk Fluid |
| $T_{subcool}$ | Subcooling ($T_{sat}$ - $T_{bulk}$) |
| $q''$ | Heat Flux |
| $q$ | Heat Transfer Rate |
| $t$ | Time |
| $r$ | Radius |
| $r_{ij}$ | Distance between Bubbles $i,j$ |
| $U$ | Overall Heat Transfer Coefficient |
| $A$ | Area |
| $A^*$ | Normalized Area $A/A_{mean,base}$ |
| $P_A$ | Pressure Amplitude of Acoustic Field |
| $R_i$ | Radius of Bubble $i$ |
| $F$ | Frequency of Surface Wave Disturbances |
| $f$ | Frequency of Acoustic Field |
| $Z$ | Acoustic Impedance $Z = \rho c$ |
| $c$ | Speed of Sound |
| $I$ | Acoustic Intensity |
| $a$ | Acoustic Source Radius |
| $U_a$ | Source Velocity of Acoustic Field |
| $\Delta t$ | Time Step |

$V$ Volume

$V_o$ Initial Volume

$<\tilde{A}_{vap}>$ Vapor Area Fraction $<\tilde{A}_{vap}> = A_{vap}/A_{total}$

$V_t$ Terminal Velocity of Spherical Bubble of Fixed Size

$d_o$ Orifice Diameter

$T_o$ Actuation Period

$T_b$ Bubble Ejection Period

$\dot{m}_i$ Mass Flow Rate of Material $i$

$v_g$ Specific Volume of Gaseous Phase

$h_f$ Specific Enthaly of Liquid Phase

$h_g$ Specific Enthalpy of Gaseous Phase

$h_{fg}$ Specific Enthalpy of Vaporization

$P$ Pressure

$u_g$ Specific Internal Energy of Gaseous Phase

**Greek symbols**

$\theta$ Azimuthal Angle of Acoustic Actuation relative to Heater Plane

$\phi$ Incident Angle of Acoustic Actuator relative to Heater Plane

$\sigma$ Surface Tension

$\kappa$ Polytropic Exponent

$\rho$ Density

$\lambda$ Wavelength of Surface Wave Disturbances

$\lambda_a$ Wavelength of Acoustic Field

$\phi_o$ Relative Phase of Bubble Oscillations

$\omega$ Angular Frequency

$\omega_o$ Natural Frequency

$\delta_i$ Change in Radius of Bubble $i$

$\delta_t$ Thermal Boundary Layer Thickness

$\Psi$ Maximum of Average Vapor Bubble Size

$\gamma$ Ratio of Mass Flow Rate and Observed Mass Flow Rate through an Orifice

$\Gamma$ Ratio of Observed Mass Flow Rate and Mass Flow Rate of Condensing Vapor

## SUMMARY

Two-phase heat transfer involving boiling and condensation in a liquid pool is widely used to accommodate high heat fluxes. However, coupling this attractive approach to system-level heat transfer is hampered by the rate-limiting steps of vaporization (inhibited by the critical heat flux limit on the maximum heat transfer rate) and condensation (limited by the subcooled liquid temperature and heat transport at the liquid-vapor interface). The performance of thermal systems that utilize two-phase heat transfer can be significantly enhanced by independent augmentation of boiling and condensation using nonintrusive, low-power acoustic actuation at the flow boundary that exploits the acoustic properties mismatch at the liquid-vapor interface. The present investigations focus on the fundamental mechanisms of acoustic enhancement of two-phase heat transfer at long and short actuation wavelengths (order 1 m and 1 mm, respectively). It is shown that surface capillary waves induced by long wavelength actuation enhance condensation by forcing mixing at the interfacial thermal boundary, while short-wavelength actuation enhances boiling by affecting vaporization and advection of vapor bubbles to extend the critical heat flux limit, and enhances direct contact condensation by bulk deformations at vapor-liquid interface that inject subcooled liquid into the vapor volume.

# CHAPTER I

## INTRODUCTION

Two-phase heat transfer processes involving boiling and condensation in quiescent and flowing liquids are widely used to accommodate high heat fluxes in numerous applications ranging from cooling and heating of continuous-flow or batch reactors and separation processes in the chemical process industry, to thermoelectric power plants, to thermal management of electronic hardware. However, coupling this attractive approach to system-level heat transfer is hampered by the rate-limiting steps of vapor formation and condensation. Vapor formation is inhibited by the critical heat flux (CHF) limit on the maximum heat transfer rate during vapor bubble formation on the heated surface and transition to film boiling, which leads to large increases in surface temperature. Vapor condensation is normally limited by the temperature of subcooled liquid, convective mixing, and conduction- and diffusion-limited heat transport at the liquid-vapor interface. The performance of thermal systems that utilize two-phase heat transfer can be significantly enhanced by independently (or simultaneously) augmenting the boiling and condensation processes to enable high heat fluxes by using acoustic actuation that is transmitted through the working liquid. This nonintrusive approach which exploits the inherent mismatch in acoustic properties at the liquid-vapor interface of the vapor bubbles is attractive because it is relatively simple and low-power compared to mechanical or fluidic enhancement techniques.

The present investigations focus on the fundamental mechanisms of the acoustic enhancement of two-phase heat transfer and demonstration of independent control and regulation of the vapor bubbles that form on the heated surface (to overcome the critical

heat flux limit), and of direct contact condensation of vapor bubbles that are advected in subcooled liquid. The interfacial coupling of the actuation varies substantially with the actuation wavelength and the present investigations considered two limits. Long actuation wavelength that is much larger than the characteristic scale of the vapor bubbles [O(1 kHz, 1 m)] leads to the formation and amplification of capillary surface waves on the liquid-vapor interface with sufficient amplitude to force mixing of the interfacial thermal boundary layer surrounding vapor bubbles. Short actuation wavelength [O(1 MHz), O(1 mm)] exploits the surface force of the acoustic radiative pressure to effect local interfacial deformations and injection of a subcooled liquid jet and atomized droplets into the vapor volume.

Following the overview in Chapter 1, Chapter 2 of this dissertation includes a summary of relevant prior work related to enhancement of boiling and condensation, Chapter 3 describes the experimental apparatus and techniques, and Chapter 4 describes the essence of the acoustic actuation that was used in the present investigations. The main results of the present investigations are described in Chapter 5-8. The effects and mechanisms of long and short wavelength acoustic actuation on submerged pool boiling are described in Chapter 5 including the development of a passively enhanced boiling surface using open microchannels, the effects of long and short wavelength actuation on a smooth surface including the extension of the CHF, the effects of short wavelength actuation on discrete vapor nucleation sites, and the effects of short wavelength actuation in combination with the microchannel-enhanced boiling surface to significantly increase the CHF. The effects of the actuation on condensation are discussed in Chapters 6-8. Chapter 6 describes the use of long wavelength actuation to enhance the condensation process and includes the effects on the vapor area and volume above a venting orifice atmospheric pressures, a Schlieren-based investigation of the capillary wave enhancement mechanism, and extensions of this enhancement technique at reduced

ambient pressure and above a boiling surface. Chapter 7 describes the use of short wavelength acoustic actuation for acceleration of the condensation process and includes a configuration using actuation pulses triggered to the exiting vapor bubbles as well as a configuration using continuous cross-orifice actuation. Also presented is a lower power dissipation condition which, in conjunction with the pulsed actuation and control volume analysis, allowed for the development of temporal assessments of heat transfer enhancement. Chapter 8 discusses the changes in the flow field of the condensing bubbles in the presence and absence of pulsed actuation using particle image velocimetry. Finally, Chapter 9 summarizes the findings and includes recommendations for future work.

# CHAPTER II

# BACKGROUND

## 2.1. Boiling and its Passive Enhancement

Boiling, in general, and the critical heat flux of boiling surfaces, specifically, have been the subject of intensive investigations since the early 1900's. One of the more significant contributions dates back to 1934 with the development of a boiling curve for pool boiling, and identification of the regimes of nucleate boiling, transition boiling, and film boiling (Nukiyama 1934; translated reprint Nukiyama 1984). The boiling curve included the critical heat flux (CHF), a local peak in total heat transfer prior to the development of film boiling. In many applications, the CHF constitutes the upper limit at which the thermal system can operate as designed.

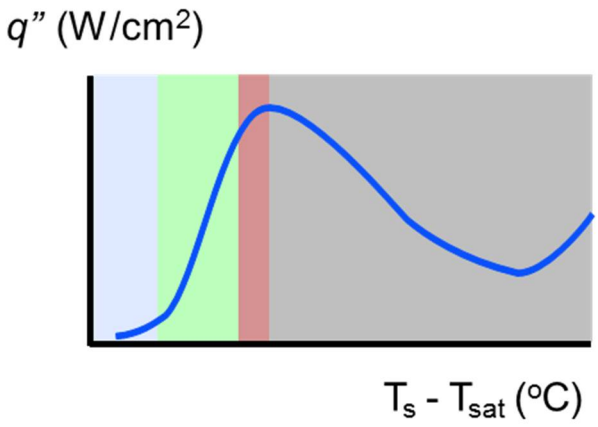


**Figure 2.1.** Rendition of a boiling curve showing stable surface superheat and heat flux: as surface superheat increases (to the right), heat flux through the surface increases slowly prior to the onset of nucleate boiling (blue shading) then supports a wide range of heat fluxes over a narrow range in surface superheat during nucleate boiling (green shading), followed by transition boiling (red shading) that ends at the critical heat flux associated with a local maximum, and film boiling (grey shading).

The boiling process in a quiescent environment is sensitive to a remarkably large number of parameters (or conditions) including surface wettability, porosity, thermal conductivity, thermal diffusivity, and roughness, as well as liquid surface tension, latent heat of vaporization and liquid/vapor specific volume ratio. The presence of a cross flow and complex geometry only add to the relevant parameters. Clearly, the large number of parameters complicate experimental investigations and comparisons between related experiments. Furthermore, often experimental setups must be designed with specific measurement techniques in mind (for example, clear resistive heaters for a boiling surface allows for visualization of the nucleation process, such as Pascual *et al.* 2002), but the use of this technique may preclude the investigation in a particular parameter space (in the above example, the material properties are determined by the desire to use visualization through the heater surface). Despite some limitation (e.g., range of surface wettability or of heat flux, etc.), there are numerous models of the boiling process as discussed in Dhir's 1998 review article. These models provide a useful framework for considering experimental results, even if the variation in experimental setups exceeds the models applicability.

Two boiling-related phenomena that are particularly relevant to the present investigations are the role and effects of nucleation sites (surface defects where vapor bubbles form during nucleate boiling and whose density generally increases with surface superheat; Kocamustafaogullari and Ishii, 1983) and the effects of microlayer evaporation (the thin liquid layer between the boiling surface and a vapor bubble; Cooper and Lloyd, 1969) on the boiling process.

Passive enhancement of pool boiling on submerged heated surfaces through geometric modification of the heated surface with the objectives of creating nucleation sites, facilitating vapor bubble detachment and potentially increasing the CHF, and reduction of the characteristic dimensions of the heated surface have been reported in numerous

earlier investigations. For example, McGillis and Carey (1991) performed a parametric study of a rectangular fin array having characteristic pitch, height, and fin thickness of 1.5, 5.0, and 2.7 mm, respectively and reported an increase in CHF of up to 150 percent. These authors also concluded that the fin thickness was not an important parameter and noted that the fin length should be about 1.4 times larger than the fin spacing. The effects of surface geometry on boiling heat transfer were reviewed in detail by Bergles (1997) who also noted that while surface geometry can have a profound effect on boiling heat transfer processes, understanding the underlying physical mechanisms is necessary for the development of new generations of surface-induced boiling enhancements. Chien and Webb (1998) worked with subsurface 0.35 mm wide channels, and noted that an ample supply of liquid to the evaporating surface was crucial for attaining the highest heat transfer coefficients (2 $W/K/cm^2$) that were afforded by the surface geometry. In a hybrid micro-nano-structure, Launay et al. (2006) used carbon nanotubes grown onto a grooved silicon heat sink to produce improvements at multiple scales. They found that nanotubes improved performance primarily at low heat fluxes (< 15 $W/cm^2$), while micro-scale grooves provided the majority of improvement at higher heat fluxes (up to 130 $W/cm^2$). Investigations of heat transfer in laminated-screen surfaces have shown that layers of copper mesh bonded to the heat transfer surface can increase CHF and the stability of the wall temperature along the boiling curve (Li and Peterson 2007; Sloan *et al.* 2009). More complex surface designs have included nano-scale deposits of copper tubes that increase the wettability of the copper surface as well as the nucleation site density (Li *et al.* 2008). Cooke and Kandlikar (2011) used silicon heat sinks that were fabricated with added notches for nucleation sites and showed significant migration of nucleating bubbles from the bottom to the top surface surfaces of the heat sink channels.

## 2.2 Acoustic Enhancement of Boiling

Boiling on submerged heated surfaces can be significantly enhanced by exploiting the drag force on vapor bubbles from a cross flow of subcooled liquid over the heated surface to effect forced detachment (i.e., flow boiling) . However as shown by Agostini et al. (2007), such heat transfer improvements come at a cost in the power, weight, and size of the cooling hardware. Some of these limitations can be overcome by using cross flow that is induced by submerged synthetic jets that require no external fluid source (Heffington et al., 2003, Tillery et al., 2006).

Body and surface forces that modify the evolution of vapor bubbles on heated surfaces can be applied indirectly by using acoustic actuation over a range of actuation wavelengths. The utility of ultrasonic acoustic fields at frequencies ranging from 20 to 300 kHz for the removal of vapor bubbles from wire heaters has been investigated by a number of authors since the 1950's (e.g., Isakoff, 1956, Wong and Chon, 1969, Park and Bergles, 1988, Iida and Tsutsui, 1992, and Kim et al., 2004). These works demonstrated that ultrasound can lead to the formation of small cavitation bubbles near the surface of the heater that enhance mixing in the bulk liquid and thereby increase natural convection heat transfer near the onset of boiling. However, these provided limited effects on nucleate boiling, because the cavitation bubbles are apparently overwhelmed by the appearance of the natural vapor bubbles during nucleate boiling. Several authors also reported some increases in the CHF (5-10% by Park and Bergles, 1988, 20% by Iida and Tsutsui, 1992, and 60% by Isakoff, 1956). Sitter *et al.* (1998) examined boiling on a wire in the presence of an acoustic field (10.18 kHz) in terrestrial and microgravity experiments and found that the acoustic actuation led to an increase in the heat transfer coefficient on the wire by direct coupling with the natural oscillations of vapor bubbles through the action of the primary Bjerknes force. Hao et al. (2001) investigated numerically the effect of the primary and secondary Bjerknes forces on a vapor bubble near a planar rigid wall and proposed that these acoustic effects could be used to improve

boiling heat transfer from a horizontal surface. Douglas *et al.* (2012) reported the effect of acoustic actuation (0.9-22.5 kHz) on the contact line of pinned air and vapor bubbles, as well as the critical heat flux of boiling over a submerged plain copper surface. In a related investigation of highly subcooled (80$^{o}$K) submerged boiling on wire heaters (characteristic diameters 50-250 μm) mounted in tension Hetrosini et al. (2014) used a 40 kHz acoustic field to induce wire vibrations and enhance the heat transfer. These authors reported that that the induced vibrations decrease with increasing wire diameter, and noted a maximum reduction of 40$^{o}$K in the temperature of the 200 μm wire. More recently, Li et al. (2016) studied the effect of acoustic fields (21 and 45 kHz) on boiling over the surface of smooth and textured (azimuthal and spiral fins) cylindrical tubes and showed that the respective acoustic enhancement increased from 16% to up to 42% in the presence of surface features.

## 2.3 Bubbles and Direct-Contact Condensation

### *Condensing Bubbles and Their Shapes*

Direct contact condensation of single vapor bubbles and of bubble trains in the absence of external actuation has been investigated extensively both theoretically (Sideman and Moalem-Maron focused on theoretical models of bubble trains, 1982) and experimentally (Schmidt injected vapor and focused on the separation process in relation to the separation size of vapor bubbles, 1977; Cho and Lee focused on the heat transfer during the growth phase of steam bubbles, 1991; Terasaka *et al.* focused on the heat transfer during the growth phase for an immiscible vapor material, 1999). Floreschuetz and Chao (1965) developed a widely-used numerical solution for the spherically symmetric collapse of a vapor bubble including liquid inertia-constrained and heat transfer-constrained solutions. The experimental investigations of Celata et al. (1986) focused on the heat transfer coefficient at the planar interface between a co-flowing layers of steam and subcooled water, and reported little to no dependence on the steam superheat or liquid subcooling but rather on the relative flow speed at the interface.

More recently, Kalman and Mori (2002), using experimental data of single condensing vapor bubbles in immiscible liquids, proposed a simple correlation for Nusselt number which depended only on the Peclet number. Kar *et al.* (2007) generated a refined predictive model for heat transfer coefficient during vapor bubble growth using an increased number of effects such as viscous forces and vapor flow rate. Kim and Park (2011) used image processing on vapor bubbles in low-pressure, subcooled boiling flow to develop a heat transfer coefficient correlation. al Issa *et al.* (2014) similarly used image processing to track large numbers of condensing bubbles injected into quiescent flow at atmospheric conditions to develop a correlation of heat transfer coefficient.

A catalogue of fascinating vapor bubble shapes including the formation of a torus during collapse was provided by Kamei and Hirata (1976) after injection of vapor into a subcooled liquid pool. Topological changes of a single bubble from a spheroid to a torus

were observed; at higher mass flow rates, interaction between subsequent bubbles were observed to lead to the second bubble traveling into the liquid region in the center of the prior bubble, where they subsequently collapsed together. Kamei and Hirata (1990) later expanded this work by comparing their vapor bubble shape results with nitrogen bubbles (in the absence of phase change) and reported similar shapes (i.e., entrainment of a second bubble into the lower interface of the preceding bubble, although complete torus formation of a non-condensing single bubble was not observed). Measurements of the flow field of the condensing vapor bubbles using tracer particles showed an overall advection rate of 20-25 cm/s for a bubble and up to 1.5 m/s for the tracer particles traveling through a toroidal collapsing bubble (Kamei and Hirata 1990). In later experiments Eames, in 2010 showed that a topological change in bubble shape as it condenses (i.e., the formation of a torus) results in a vortex ring whose size and propagation speed are related to the corresponding characteristics of the vapor bubble.

Recent numerical studies can also capture more complicated bubble shapes through the advection process and have led to new correlations, having been compared to image processed experimental data (Tian *et al.* 2014) or having used image processed experimental data to guide numerical solutions (Qu *et al.* 2014).

Direct-contact vapor suppression, often used for emergency containment in nuclear power plants, was investigated experimentally by de With *et al.* (2007) who developed a three-dimensional regime map of the chugging, bubbling, and various jetting regimes. The non-bubbling regimes are purposefully avoided in the work in this thesis; however, Dahikar et al. (2010) used particle image velocimetry (PIV) and temperature field measurements by planar laser induced fluorescence (PLIF) to aid a CFD simulations of a condensing steam jet. These experimental techniques may be used on other regimes as well, albeit with greater difficult due to the changing locations of the steam/water interface (unlike in a steady jet).

Finally, a useful review of vapor bubble research, including vapor bubble growth as well as condensation considerations in quiescent flow and the presence of relative motion was compiled by Prosperetti (2016).

### *Injection Geometry*

The flow of both condensing and non-condensing materials through multiple-orifice plates for liquid-gas heat transfer was an area of research primarily for chemical and processing engineering, and can form bubbles similar to those investigated in this thesis.

A useful review that includes bubble-condensation-based heat transfer geometries as well as dispersed droplet direct contact condensation and packed bed directed contact condensation is available in Jacobs 1988.

A similar review specifically aimed at energy recovery is available in Fair 1990. The work related to spray columns, packed columns, and baffle-tray columns is not of interest; however, the sieve-tray column configuration which uses multi-stage, multiple-orifice plates is an example of an applied version of the condensation test cell.

Investigations of plate thickness, hole spacing, and the interaction between multiple levels of orifice plates have been considered. The most important consideration for the work in this thesis is the desire to avoid “weeping,” or backflow of liquid into the vapor reservoir; i.e., to operate in a pure bubbling regime by exceeding a critical velocity through the holes. This is more difficult when the conditions are such that phase change is possible (although weeping can occur even without phase change at low flow rates). Other research on systems consisting of many unorganized bubbles (such as bubble column reactors) are concerned primarily with bubble rise time, fluid velocity, bubble coalescence and other aspects not particularly relevant to the work in this thesis, although the dynamics of bubble interaction could possibly be relevant to future applications of this work.

### *Acoustics and Bubbles*

Acoustic actuation can also be exploited for affecting direct-contact condensation of detached vapor bubbles in stationary and moving subcooled liquids. There is a significant body of work on the interaction between gas bubbles suspended in liquids and acoustic fields, that has been driven to a large extent by the implementation of sonar technologies. These investigations have considered primarily various gases other than vapor of the embedding liquid, and liquid vapor within cavitation bubbles. Although the earlier investigations do not include the effects of heat transfer on vapor formation during phase change, these investigations enable assessment of the potential of harnessing acoustic actuation for inducing surface deformations to enhance condensation heat transfer.

Theoretical investigations of the forces effected by acoustic fields on bubbles date back to 1906, with the description of what would eventually be known as the Bjerknes forces, which affect the time-averaged motion of pulsating bubbles in an acoustic field (Bjerknes, 1906). There have been many subsequent theoretical and experimental advancements throughout the ensuing decades. A comprehensive treatise on interactions of acoustic fields with gas bubbles embedded in liquid was authored by Leighton (Leighton, 1994), and the most relevant investigations of body forces are by Prosperetti (1984, who also noted that surface forces are ultimately responsible for observed time-averaged "body" forces). The most relevant investigations of surface forces are by Bunkin *et al.* (1986, radiation pressure and self-focusing from interface displacement) and Abe *et al.* (2002, standing waves in microgravity conditions). The formation of surface interface waves and their descriptions begin with Faraday (1831) and continue through to Kelvin (1871) and Rayleigh (1883). Eller and Crum (1970) investigated the stability threshold for shape oscillations of oscillating bubbles in a sound field; Trinh *et al.* (1998) further investigated the shape stability for both drops and bubbles; Maksimov

and Leighton (2012) developed an expression to describe the patterns which can form on an oscillating bubble. It is noteworthy that acoustically-driven Faraday waves on the liquid gas interface of a liquid droplet were used by Vukasinovic et al. (2007) to drive the interface to droplet ejection.

In regarding acoustic enhancement of condensation, the role of 50 Hz acoustics in enhancing mass transfer at a bubble interface was considered to be primarily a function of increasing the interface area, with increases in Nusselt number observed when the forcing amplitude exceeded 4.5 times the forcing amplitude necessary for capillary wave formation (Hopfinger and Das, 2009). More recently, the observation of the importance of microbubble emission boiling in highly-subcooled steam condensation processes led to investigations that determined a large jump in condensation rate is observed when subcooling is raised to higher than 35-40 K (Ueno *et al.*, 2011). Interest in this phenomena inspired the use of ultrasonic (20 kHz) acoustic actuation to further enhance the interface disturbances, reducing the necessary subcooling for rapid collapse of steam bubbles (Tang *et al.* 2016) and increasing the Nusselt number for condensation of a steam/air mixture (Tang *et al.* 2015) by up to ~100 percent. Prior work by the same researchers postulated that the small-amplitude surface waves available at 20 kHz did not increase the mixing process in the thermal boundary layer (Tang et al. 2009).

Despite the large amount of prior work, the wide parameter space and inherent difficulty of modeling heavily flow-field dependent multiphase processes result in a lack of satisfactory correlation(s) for many applications and therefore continued interest in the process; this is only further exacerbated when considering the role of acoustics and the additional parameters present. Work which focuses on describing the enhancement mechanism, such as this thesis, is required to accurately model and predict these processes without requiring the enormous caches of experimental data used to develop correlations.

# CHAPTER III

# EXPERIMENTAL SETUP AND TECHNIQUES

Boiling and condensation processes were investigated using a modular test cell that could be configured for vapor formation and advection using either boiling on a surface-embedded heater submerged in a subcooled liquid (water) pool (§3.1), or by direct injection into the subcooled liquid pool from an attachable vapor generator using interchangeable orifices in a partition plate (§3.2). Vapor formation and advection in the subcooled liquid cell was visualized using backlight illumination and vapor high-speed video imaging (12-bit Phantom v12.1 CMOS camera at 10,000 fps). Image processing of condensing vapor bubbles is discussed in §3.3. Some of the thermal characteristics of the boiling and condensation were captured using high-speed Schlieren visualization (§3.4), and the flow fields near the liquid vapor interfaces were captured using high frame rate particle image velocimetry (PIV, §3.5)

## 3.1 The Boiling Test Cell

The boiling process on a submerged calibrated heated surface is investigated in a water test cell shown schematically in Figure 3.1. The heater is comprised of a cartridge heating element that is inserted within a copper cylinder. Time-dependent heat flux and estimates of the heater's surface temperature are acquired using two sets of three collinear vertical thermocouple sensors with sets mounted 8.7 mm apart and offset 5 mm relative to the centerline of the heater, with the top sensor 3 mm below the heater's top surface. Each K-type thermocouples sensor was sheathed in a 250 μm diameter ungrounded stainless steel tube. The temperature measurements were acquired using

LabView software and National Instruments SCXI-1303 module which included cold junction compensation. Comparison of the heater's power dissipation (using its voltage and resistance) with measurements of heat flux through the thermocouple sets showed heat loss to the ambient was less than 10%. The top, 16 mm diameter (10 mm high) segment of the cylindrical heater that forms the boiling surface in contact with the liquid pool is flush-mounted within and sealed to a cylindrical ceramic module that forms the

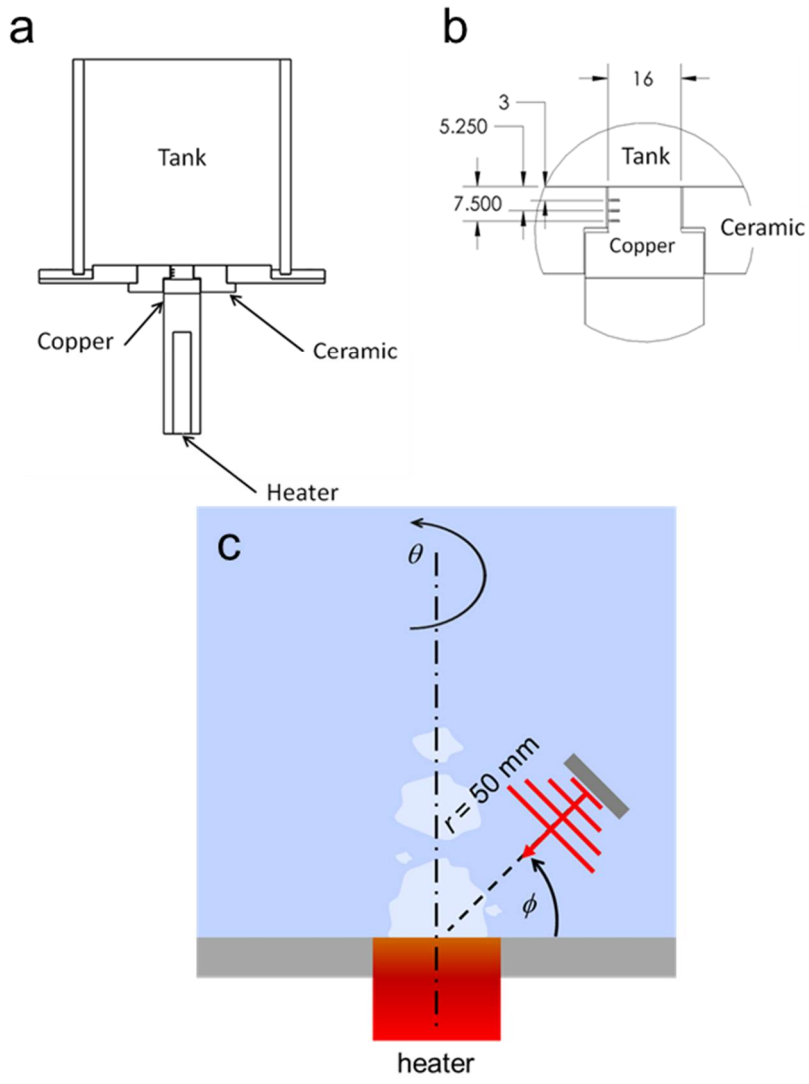


**Figure 3.1.** a) The boiling test cell assembly with a calibrated heater, b) the calibrated heater with integrated thermocouple sensors, and c) the position of the acoustic transducer relative to the heated surface.

center segment of the bottom surface of the test cell. This heater segment is interchangeable for testing the effects of plain and textured boiling surfaces on the nucleation and evolution of vapor bubbles. One of the plain removable surface heater segments is instrumented with three surface-soldered flush-mounted miniature thermocouple sensors (250 μm diameter, stainless steel sheathed) that are equally-spaced azimuthally along a 12 mm diameter circle for direct temporal measurement of the superheat temperatures at the boiling surface (the sensors' time constants are nominally 4-5 msec). In the present investigations, textured surfaces are formed by a square grid of intersecting open-surface machined microchannels with widths varying from 200 to 1000 μm, and depths of up to 1.8 mm that enable liquid flow into nucleation sites at the intersections for enhanced heat transfer.

As noted above, the surface temperature of and the heat flux through the heater is typically estimated using the two sets of three embedded thermocouple sensors along the heater's cylinder using a linear extrapolation based on 1-D heat transfer (the uncertainties of the surface temperature and heat flux are estimated to be ±0.4°C and ±7%, respectively). The estimated temperature was compared directly with the temperature that was measured by the surface soldered thermocouple sensors at 100 W/cm$^2$, and it was shown that the extrapolated surface temperature was 1.7°C or about 0.44% higher than the measured temperature (averaged over the three sensors). In addition, the surface temperature of the heater computed using a numerical simulation of the axisymmetric heat transfer through the entire heater was compared with the simulated extrapolated surface temperature derived from the locations of the thermocouple sensors and one-dimensional heat flux assumption. These simulations predicted that at a heat flux of 100 W/cm$^2$ the extrapolated surface temperature would be about 1.8°C higher than the actual surface temperature, while the heat flux would be underestimated by about three percent. This is in agreement with the observed results of the extrapolated and directly measured

surface superheats. Therefore, it is concluded that measurements of the heat flux and the calculations of the extrapolated surface temperature using the embedded thermocouple sensors are acceptable approximations. Considering the thermal mass of the heater, the characteristic thermal time constant of these measurements is estimated to be between 200 and 1,000 msec (depending on the heat flux).

A secondary immersion heater is used to control and regulate the bulk temperature of the subcooled liquid to within ±1°C. In the present experiments, the nominal bulk temperature is 93°C, yielding 7°C subcooling at atmospheric pressure. It is noted that the variations of the bulk temperatures within the set range (±1°C) can result in somewhat different vapor volumes above the boiling surface as a result of slight differences in the condensation rate (although, as noted further below, these variations did not affect the time-averaged boiling curves). These variations coupled with different settings of the imaging (lenses and frame rate) impede comparisons between data sets from different experiments. This is demonstrated in Figure 3.2 which shows images of the same heater surface operated at 75 W/cm$^2$ with the setpoint temperature bulk fluid at 93°C. These images show that variation in the vapor volume above the surface as a result of the changes in the bulk temperature changes and in camera location. For this reason, video sequences that were used for digital image processing utilized a single scene (less that 2 sec long) that included flow imaging first in the absence of actuation and then immediately followed with imaging in the presence of actuation to ensure that the visualized vapor volumes were not significantly affected by changes in the bulk temperature that occur on a much longer time-scale.

Prior to thermocouple data acquisition, the heater surface was cleaned to yield a smooth and unoxidized surface using a polishing compound (Brasso) and isopropyl alcohol, and was then rinsed with distilled water. The tank was filled with pre-boiled distilled water (pre-boiling significantly reduces but does not eliminate noncondensable

gas). The surface was heated at nominally 50 W/cm$^2$ for at least 10 minutes to help remove any remaining impurities, and initiate nucleation sites on the surface (this explains why there is no sudden reduction in superheat that is caused by the onset of boiling in the boiling curves in Figures 5.1, 2, 4, 9, 17). Following this procedure, the heater power was set to the desired level. Boiling curves are generated using a quasi-steady approach by stepping the power every 2-3 minutes (the initial power steps were 15 W/cm$^2$ and were reduced closer to CHF). A full boiling curve could be produced within 60 minutes (depending on the experimental conditions). Once the transition to film boiling is detected (by a sudden increase in thermocouple temperatures), the power to the heater was turned off. The raw temporal extrapolated heat flux and surface superheat data were subsequently smoothed using a 40-second sliding window. It was verified that the resulting measurements are indistinguishable from the steady heat flux and surface superheat, and therefore represent the steady-state response of the boiling system.

The critical heat flux of a plain, polished surface was measured several times using the same setup. The power at CHF was 110 W with a standard deviation 7.8 W (or 7%).

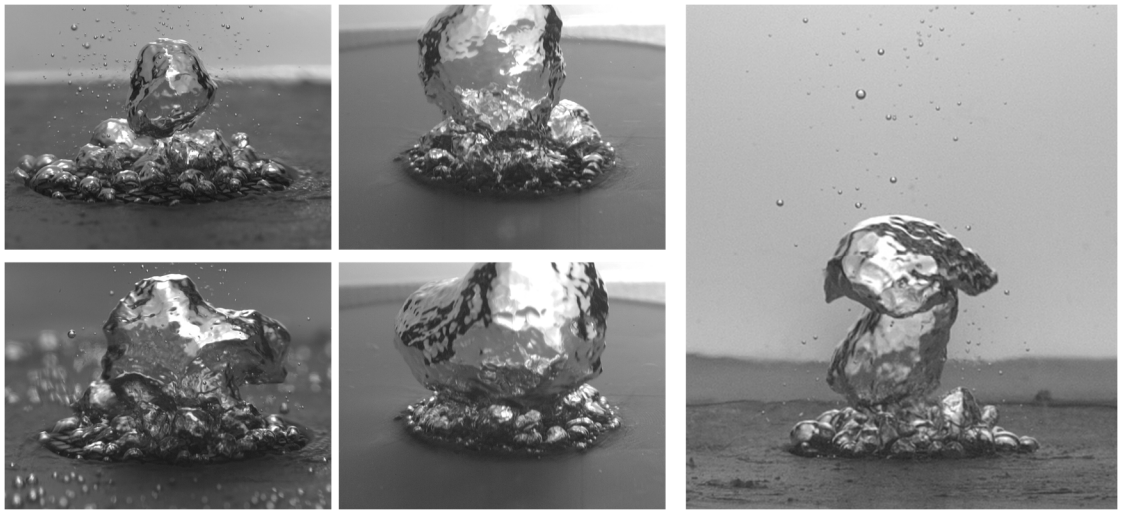

**Figure 3.2.** Comparison of vapor images demonstrating the effects of fluctuation in the set bulk temperature and framing effects. All images show the same textured (microchannel) heater dissipating 75 W/cm$^2$ and the bulk temperature set point of 93$^o$C.

The repeatability of the CHF as measured by the standard deviation is similar to repeatability measures reported by other investigators such as Berenson 1962 (10%), Sun and Lienhard 1970 (20%), and O'Hanley *et al.* 2013 (7.2%). The oxidation of the copper surface, which affects the surface wettability and increases with time after cleaning, is likely the main contributor to variation in the CHF, while slight variations in bulk fluid temperature are of secondary importance.

### 3.2 The Condensation Test Cell

The effects of the acoustic actuation on condensation in the absence of boiling were investigated using direct vapor injection into a main subcooled liquid reservoir from a steam generation cell that is attached from below and separated by a partition with an injection nozzle as shown in Figure 3.3a. In this configuration, both the upper and lower cells are polycarbonate cylinders each having an inner diameter of 10.8 cm. Schematic diagrams showing notional placement of the acoustic actuators for long and short wavelength actuation are shown in Figures 3.3b-d. Steam is generated in the lower reservoir by heating water using a 1.5 kW immersion heater controlled by a variable transformer, and is driven into the subcooled liquid in the top reservoir through a nozzle in the partition plate between the top and bottom reservoirs. The nozzle (internal diameter 9.8 mm) is fitted with an interchangeable orifice plate of exit diameter $d_o$ that along with the vapor heat flux affects the formation scale and detachment frequency of the train of vapor bubble that are advected in the subcooled liquid. The vapor mass flow rate controls backflow of subcooled liquid into the vapor generator (if the vapor flow is too low, "chugging" vapor flow (cf. de With *et al.*, 2007) may occur and is associated with significant liquid backflow into the vapor tank below). Vapor ejection in the present investigations is a simplified model of a number of industrial processes (e.g., distillation processes or condensation in power cycles). The bulk temperature of the liquid in the upper reservoir can be easily controlled using a secondary cooling loop, which was used in the low-ambient pressure investigations, or a secondary heater, which was used in the atmospheric pressure investigations, and it was shown that the bulk temperature was kept within $\pm 1^{o}$C. The operating ambient pressure in the liquid and vapor reservoirs can be reduced to prescribed sub-atmospheric pressure using a vacuum pump to mimic condensation in some industrial processes. For high-quality imaging of condensation through flat surfaces the top tank can be replaced with a cubical glass liquid reservoir (similar to the tank used in the boiling investigations cf. §3.1). Also for investigations of

the effects of the acoustic actuation on gas-liquid interfaces of bubbles in the absence of condensation the vapor injection can be replaced with air injection through the same nozzle.

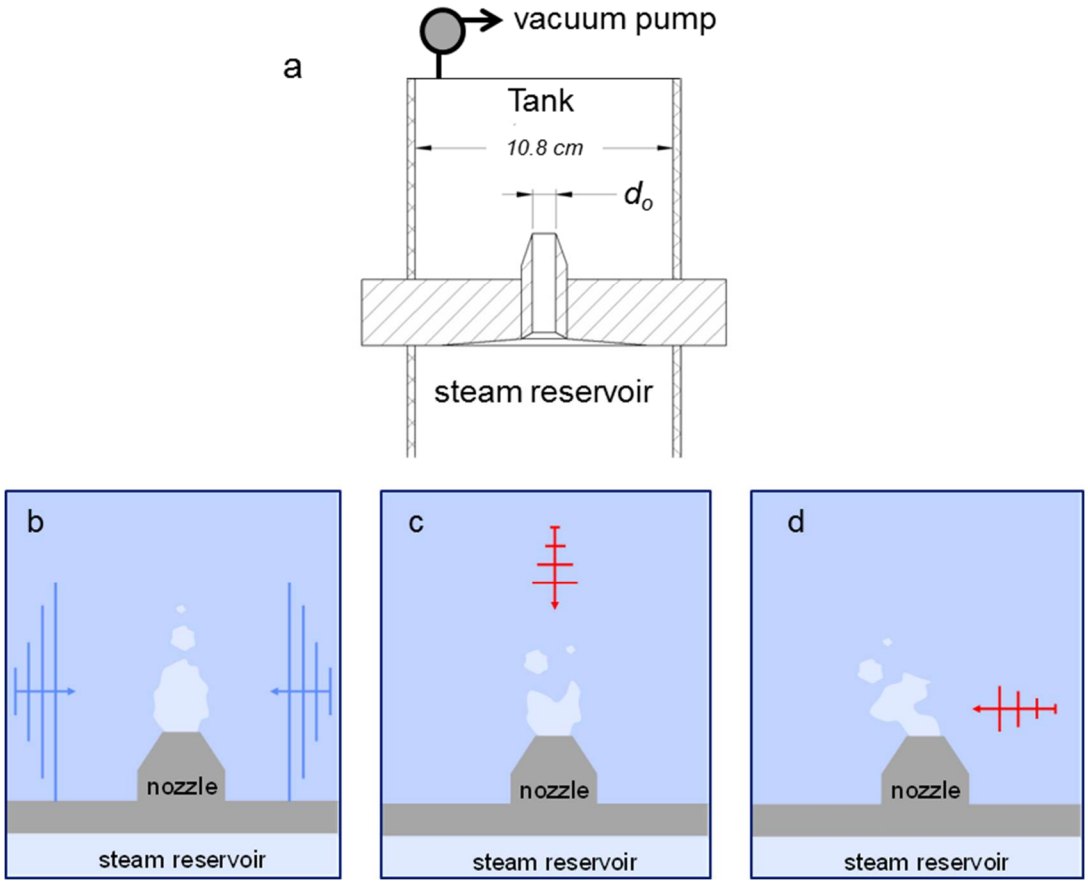


**Figure 3.3.** a) Condensation test cell with adjustable ambient pressure comprising an upper and lower polycarbonate tanks each having an inner diameter of 10.8 cm, the vapor nozzle from the steam reservoir is fitted with an interchangeable orifice plate of exit diameter $d_o$. The subcooled liquid container can be configured for acoustic actuation: a) long-wavelength, c) pulsed short-wavelength, and d) short-wavelength side actuation.

### 3.3 Image Processing of Vapor Volumes

Image processing of high speed video sequences was used to assess the temporal evolution of projected cross sectional area of vapor volume within the field of view. As noted in §3.1, because of the sensitivity of the vapor volume to the instantaneous subcooled temperature of the liquid each high-speed imaging sequence (less than 2 seconds long) comprised successive recordings in the absence and presence of acoustic actuation to ensure that the bulk temperature remained nearly invariant. In investigations of condensation using direct vapor injection into the subcooled liquid, the high-speed imaging could be triggered to the formation of an attached vapor bubble at the exit orifice by using a low power laser beam that was directed normal to the centerline of the orifice at a given elevation above the orifice exit plane and interrupted by the liquid vapor interface (cf. Figures 3.6and 3.7).

The volume of individual bubbles was computed using MATLAB-based processing as demonstrated in Figures 3.4a-e. In this sequence, the objective is to track a bubble that is forming over and attached to the nozzle. An instantaneous raw video image (Figure 3.4a) is preprocessed by cropping extraneous details (e.g., the orifice), and if necessary using Gaussian blurring to reduce the influence of reflections near the edges of bubbles

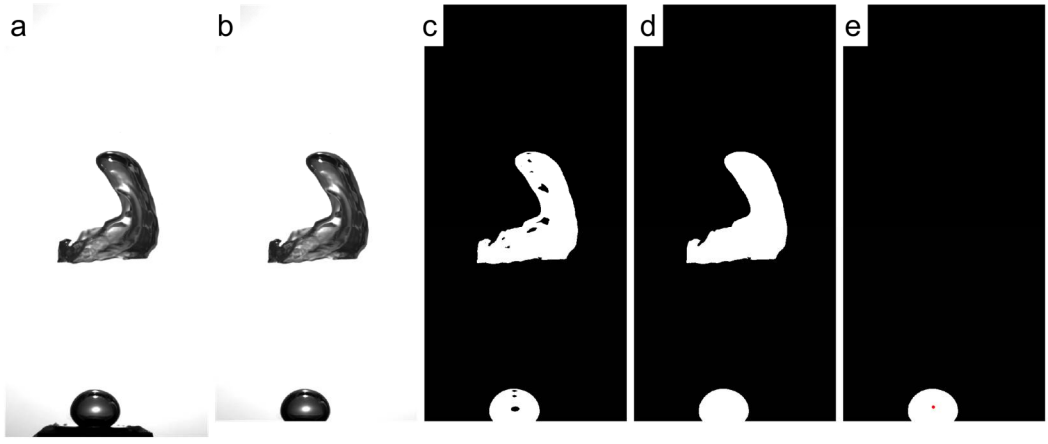


**Figure 3.4.** Image processing of vapor bubbles showing the original image (a), cropped image (b), the application of intensity threshold (c), filling in for light reflections (d), tracked bubble only with centroid marked (e).

(Figure 3.4b), then a grayscale threshold is used to form a binary image (Figure 3.4c), and spurious "holes" resulting from light areas in the center of the bubble are filled (Figure 3.4d). In the example processed image, attention is restricted to the nozzle domain, and therefore the image of the previous advecting bubble is removed (Figure 3.4e). The image of the attached bubble is processed to determine its centroid location, top/bottom interface segments, and the diameter of a circle having an equal projected area $A_{proj}$ from which the equivalent volume $V_{eq}$ is computed [note that the total interface area of a spherical volume is four times the projected and $V_{eq} = 4\pi/3 \cdot (A_{proj}/\pi)^{3/2}$]. These parameters are recorded using a tracking algorithm (in Figure 3.4e the centroid is marked). In the next processed frame the tracked bubble is identified by selecting the centroid of the vapor domain that is closest to the centroid of the vapor domain in the previous image. The present investigations have demonstrated that is tracking algorithm works well in the absence of significant interactions between successive bubbles (e.g., bubbles passing in front of each other). The total projected area of the vapor volume within the field of view is determined using the same algorithm including all vapor areas detected within the field of view (e.g., the area of the white domains in Figure 3.4d).

The typical resolution of the images that are used to compute the vapor area and volume is 25 μm/pixel. Therefore, for a given vapor bubble having a diameter of 1 cm, the threshold error is about 0.5% of the diameter, or about 1.65% of the volume. A secondary error is related to the image quality namely, determination of edges of the vapor-liquid interfaces that are temporarily blurred or distorted by light reflections that typically last < 5% of the bubble's life cycle (sequences in which such reflections lasted more than 5% of a bubble's life cycle were discarded). An investigation using simultaneous imaging of a condensing vapor bubble from a front and side view determined that the aspect ratio was nearly 1 during the life-cycle of the majority of the formed bubbles (i.e., axisymmetry maintained except for the brief toroidal breakup), and

did not significantly affect the calculated volumes. Clearly, the largest source of error is the use of equivalent circular area and volume to approximate irregular vapor areas and volumes. Figure 3.5 compares images of a collapsing toroidal vapor bubble with an overlayed torus geometry (a) and the projected area including equivalent spherical projected area (b). For bubbles of this type, which have significant interior volume of liquid the computed spherical volume is nearly 1.5 times larger than the volume of the ellipsoid-based torus, and the computed spherical surface area is 15% less than the toroidal surface area. Therefore, the equivalent volume may be thought of as the best estimate of the bubble's volume including the liquid within the interior of a bubble, rather than the true vapor volume.

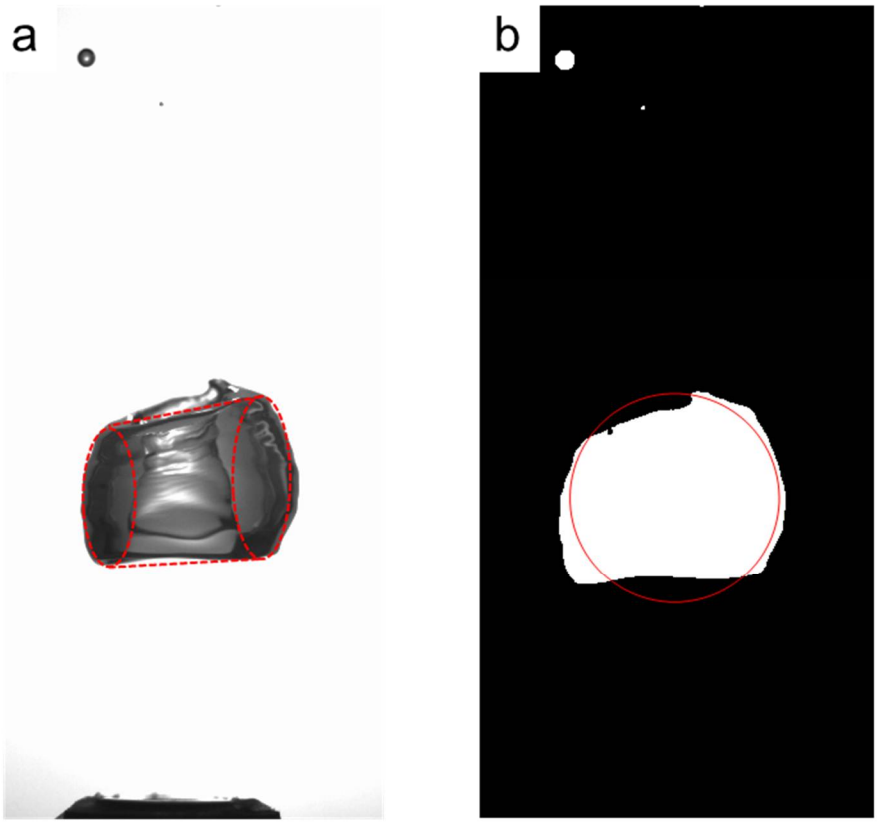


**Figure 3.5.** Image of a collapsing toroidal vapor bubble: a) raw image with overlayed torus approximation; b) projected area with spherical equivalent projected area.

A comparison of the ejected vapor volume to the volume of residual bubbles that are present following the bulk condensation yields a reasonable estimate of noncondensable gas content in the ejected bubbles. The ratio of the total residual volume to the volume of an ejected bubble immediately following its detachment from the orifice was $2.8 \times 10^{-4}$ implying a noncondensable gas content of under 0.03%. This may be considered an upper bound on the noncondensable gas content since the vapor bubble is condensing during its growth process and so its volume at detachment is lower than the actual ejected vapor volume. Furthermore, the vapor reservoir is often held at saturated boiling conditions for extended periods of time (no less than 30 minutes prior to a given experiment) long enough for any noncondensable gases within the vapor to have been vented into the upper tank. This means that the subcooled liquid in the upper tank has noncondensable gas in solution that enters the vapor bubbles during their growth phase and is the dominant cause of the noncondensable bubbles which remain after condensation. Similar transfer of noncondesable gase occurs during the submerged boiling process in the upper tank.

In the present investigations the vapor mass flow rate at atmospheric pressure was set at two primary operating conditions ("baseline" for minimal interactions between successive bubbles and "reduced" with virtually no interactions between successive bubbles) of the vapor reservoir and subcooling of the liquid reservoir $P_{vapor}$ = 225 W, $d_o$ = 5.3 mm, and $T_{subcool}$ = 25°C, and $P_{vapor}$ = 20 W, $d_o$ = 2.3 mm, and $T_{subcool}$ = 8°C.

### 3.4 Schlieren Imaging

Schlieren imaging was used for high-speed (at 10,000 fps) visualization of the thermal effects associated with the formation, evolution, detachment, advection, and ultimate full condensation of the vapor bubbles ejected into the subcooled liquid bath. A schematic diagram of the conventional Schlieren system (e.g., Settles, 2001) is shown in Figure 3.6. The light source is a Nikon fiber optic microscope lamp, powered by a 150 W metal halide bulb that is focused on a 0.4 mm pinhole using a microscope lens ($f$ = 80 mm) to minimize nonuniformities and form an approximately spherical point source. A nearly-uniform parallel beam is formed by an achromatic lens (76.2 mm diameter, $f$ = 500 mm) and passes through the liquid tank where it is distorted by thermally- and acoustically-induced spatial and temporal changes in index of refraction. The light beam is focused by a second achromatic lens (76.2 mm diameter, $f$ = 500 mm) on a double knife-edge on the opposite side of the tank to image the gradients in index of refraction onto the high-speed camera. In the present investigation, the vapor interfaces were also directly illuminated from the side or the front using a white light source for some definition of the inner volume and liquid-vapor interface of the vapor bubbles with some reduction in contrast of the Schlieren image.

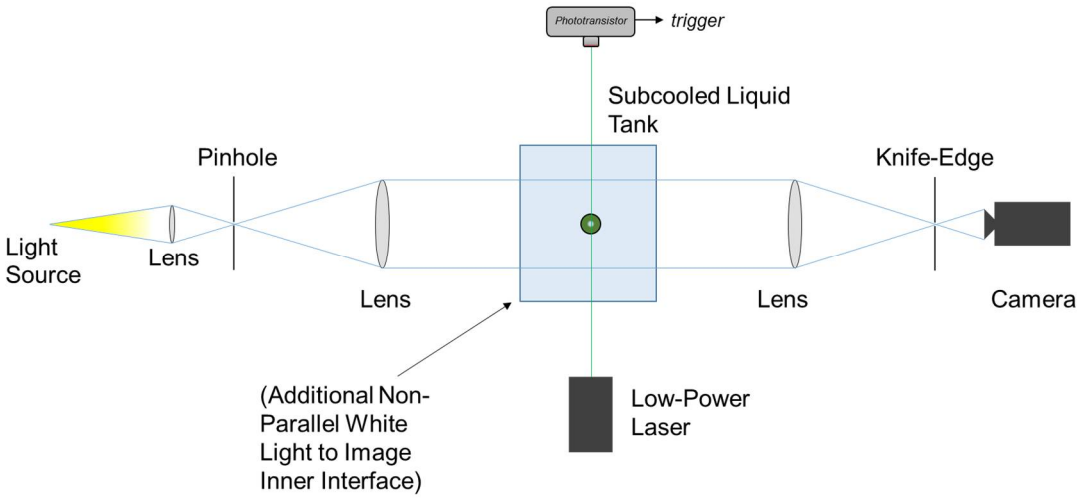


**Figure 3.6.** The Schlieren system showing the optical components, imaging CMOS camera, the additional white light sources and the low power laser for image triggering.

### 3.5 Particle Image Velocimetry

High-speed measurements of the two velocity components in a plane that intersects the centerline of the vapor orifice were acquired using the optical system shown in top and side views in Figures 3.7 and 3.8, respectively. The laser sheet is generated using a Photonic Nd:YLF Laser (527 nm, up to 10 kHz and 25 mJ/pulse). The sheet was formed using a tandem arrangement (50 mm apart) of a cylindrical lens ($f$ = 22.2 mm) and spherical lens ($f$ = 250 mm) that was focused to less than 1 mm within the tank. The liquid tank was seeded with 2 μm $sg$ = 1.05 fluorescent polystyrene particles (Fisher Scientific Fluoro-Max) with peak absorption/emittance wavelengths of 542 and 612 nm, respectively. The camera is the same high-speed 12-bit Phantom v12.1 CMOS camera that was used for visualization in the present investigations. The optical axis of the camera was normal to the centerline of the orifice and to the window of the tank. The camera used a bandpass optical filter (600 – 2750 nm) to remove the laser light thereby visualizing the light emitted by the fluorescence and significantly reducing reflections from the bubbles and the tank. The PIV field of view was calibrated using images of a ruler suspended in water within the plane of the laser sheet above the orifice. The optical

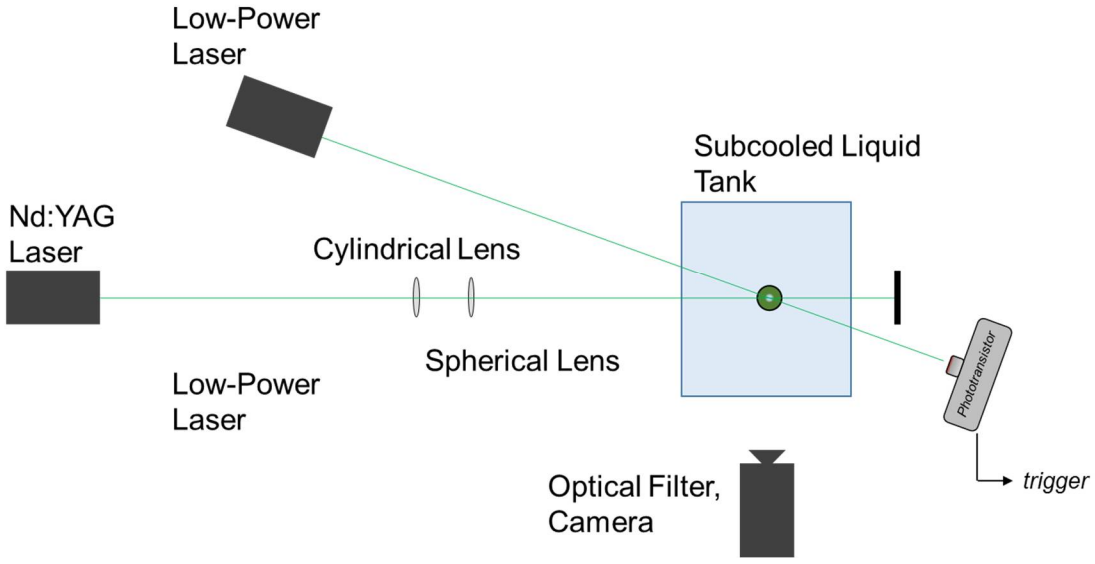


**Figure 3.7.** PIV acquisition setup, top view. Nd:YAG Laser provides laser sheet captured by CMOS camera.

system also included a low-power triggering red laser (Figure 3.7) that was used to detect the liquid vapor interface of a vapor bubble while it is attached to the orifice and provide a clear phase reference for the temporal PIV data (the laser beam was normal to the centerline of the orifice and at an angle of 20$^o$ relative to the laser sheet).

Sets of 800 successive PIV images were acquired at 10,000 fps. This approach enabled post processing of the velocity data using incremental time steps $\Delta t$ between image pairs in integer multiples the frame rate period (100 μsec). While for vapor bubbles $\Delta t$ = 100 μsec was appropriate, longer increments were needed for the slower-moving air bubbles ($\Delta t$ = 300 μsec). Clearly, this approach also enables overlap between image pairs. The PIV data acquisition and processing was run using a LaVision system and DaVis 8.3.1 software.

Processing of the velocity field surrounding a (vapor or air) bubble utilized extensive image pre-processing to enhance image quality and generate an image mask to distinguish between the seeded liquid and the vapor thereby avoiding spurious vectors at the interface or in the interior of the bubble. The pre-processing began by generating a smooth version of each image (using a moving average of 3 x 3 pixel array) and

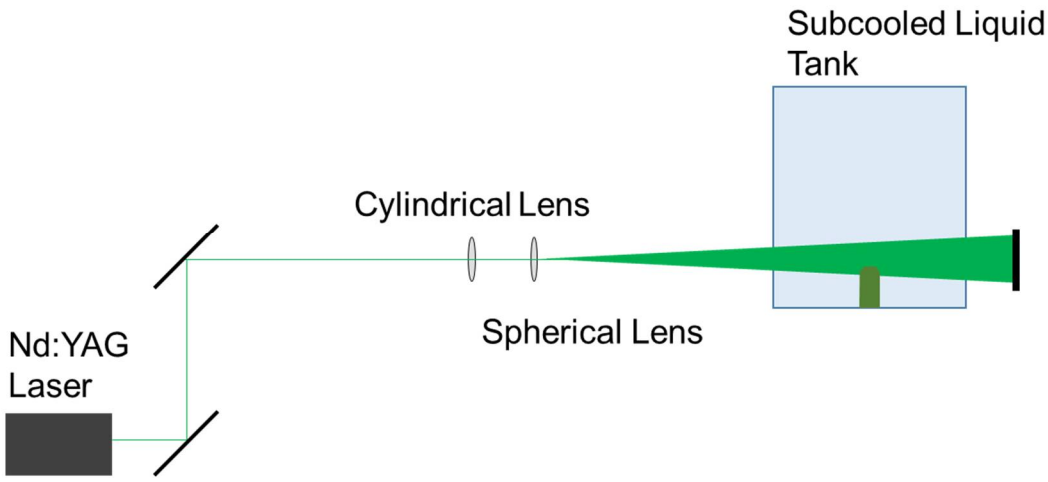


**Figure 3.8.** PIV acquisition setup, front view. Triggering laser not shown for clarity.

subtracting the smoothed background from the raw image to reduce coherent reflections while maintaining the imaged particles. Subsequently, the moving spatial RMS of a 10 x10 pixel window is calculated, with the resulting values smoothed and any pixel in the smoothed, spatially-computed RMS of the image having intensity above a given threshold is masked. This procedure removes the bright edges of the bubbles and the orifice. A similar procedure uses a smaller 5x5 pixel window to mask pixels in the raw image with average local intensity levels that are below a given value (value is set such that particle-laden regions remain, with values changing between optical setups) to remove the domains in which there are no particles (essentially, the unseeded vapor or air within the bubbles).

Velocity vectors in the field of view of the preprocessed images are computed using standard DaVis cross-correlation techniques (multi-pass interrogation windows: 2 passes at 96x96 pixels, 50% overlap, and 3 passes at 48x48 pixels, 75% overlap with a circular Gaussian weighting function). A valid vector is generated if the *Q*-ratio (ratio of the magnitudes of primary and secondary correlation peaks) was greater than three. Vectors are iteratively removed during the multiple passes if their magnitudes are higher than 10 times the standard deviation of the velocity magnitudes of their neighbors within 11 x 11 vector domain. Contiguous domains containing fewer than 100 vectors are removed. Finally, a universal outlier detection (Westerweel and Scarano, 2005; Nogueira *et al.*, 1997) is used to aid vector removal within the central liquid stem of the torus (if their residual exceeds a threshold value relative to their neighborhood of 11x11 vectors).

Each realization of vapor bubble formation and advection through complete condensation is unique in the sense that even for nearly-identical thermal generation conditions, the trajectories followed by successive bubbles and their condensation time-history within a given experiment are inherently somewhat different. For this reason, conventional phase averaging of “similar” realizations in order to yield the temporal

evolution of a "representative" bubble is not viable. Therefore, in the present experiment multiple realizations of similar bubbles are generated from the raw data records by exploiting the high temporal resolution of the PIV vector maps (acquired at 10,000 fps) compared to the characteristic time scales of the advection and condensation. To this end, temporal averaging of the velocity distributions within time windows over multiple images are computed. These averages in the present data were computed over five consecutive velocity fields (i.e., over 0.5 msec) during which the growth or position of the bubble does not vary significantly. Another attribute of this approach is that some spatial locations that are missing velocity vectors in the raw images can be filled with the temporal average at that location. Also, within the temporal set of five images, vectors having magnitudes that were larger than one standard deviation above or below the magnitude of the temporally-mean vector at a given spatial position were excluded from the mean to remove spurious vectors that might have survived earlier processing. This procedure also generated a mask that blanks velocity vectors to the right of the bubble's interface where the light sheet is distorted through the vapor volume within the condensing bubble. As part of this procedure, the characteristic scale of the bubble along the centerline of the interface is determined by considering the blanked vectors along the centerline. The spatio-temporal variation of this scale could be directly compared to scales derived from processing of the bubble images.

An estimate of the accuracy of the current PIV measurements was assessed by acquiring a series of images in the quiescent tank and calculating the RMS fluctuations of the velocity magnitude. The spatial-averaged RMS fluctuations was 0.0053 m/sec. This corresponds to an error of 0.44% in a typical peak velocity (1.2 m/sec) associated with the bubble advection, but clearly represents a limit on resolution of the induced velocity at larger radial distances from the bubble's center during its passage at a given elevation. For example, the induced peak vertical velocity at a distance of $2d_o$ from the centerline

when the bubble passes at an elevation of $4d_o$ from the orifice is 0.13 m/sec, and the corresponding error is 4.1%. The corresponding errors in vorticity are 0.1% and 3.1%. The uncertainty due to thermal effects on observed particle position in close proximity to the vapor and condensed (hot) liquid wake was assessed using a stationary grid on a glass slide positioned such that the bubble collapsed around the markings. The thermal effect on visualized marking position was deemed negligible and is therefore it is assumed that thermal distortion has negligible effects on data processing in the present experiments.

Figure 3.9 shows a sample raw image, masked image, a vector field for a condensing vapor bubble, and a post-processed vector field. Note the presence of spurious vectors within the central liquid stem of the bubble prior to post-processing; the optical distortion of both the inner and outer interfaces between the laser sheet and the camera make these unreliable data, despite the masking functions interpreting the area as containing illuminated particles. These regions (to the right side of the bubbles' interfaces) are masked in MATLAB post-processing, as can be seen in the post-processed vector field.

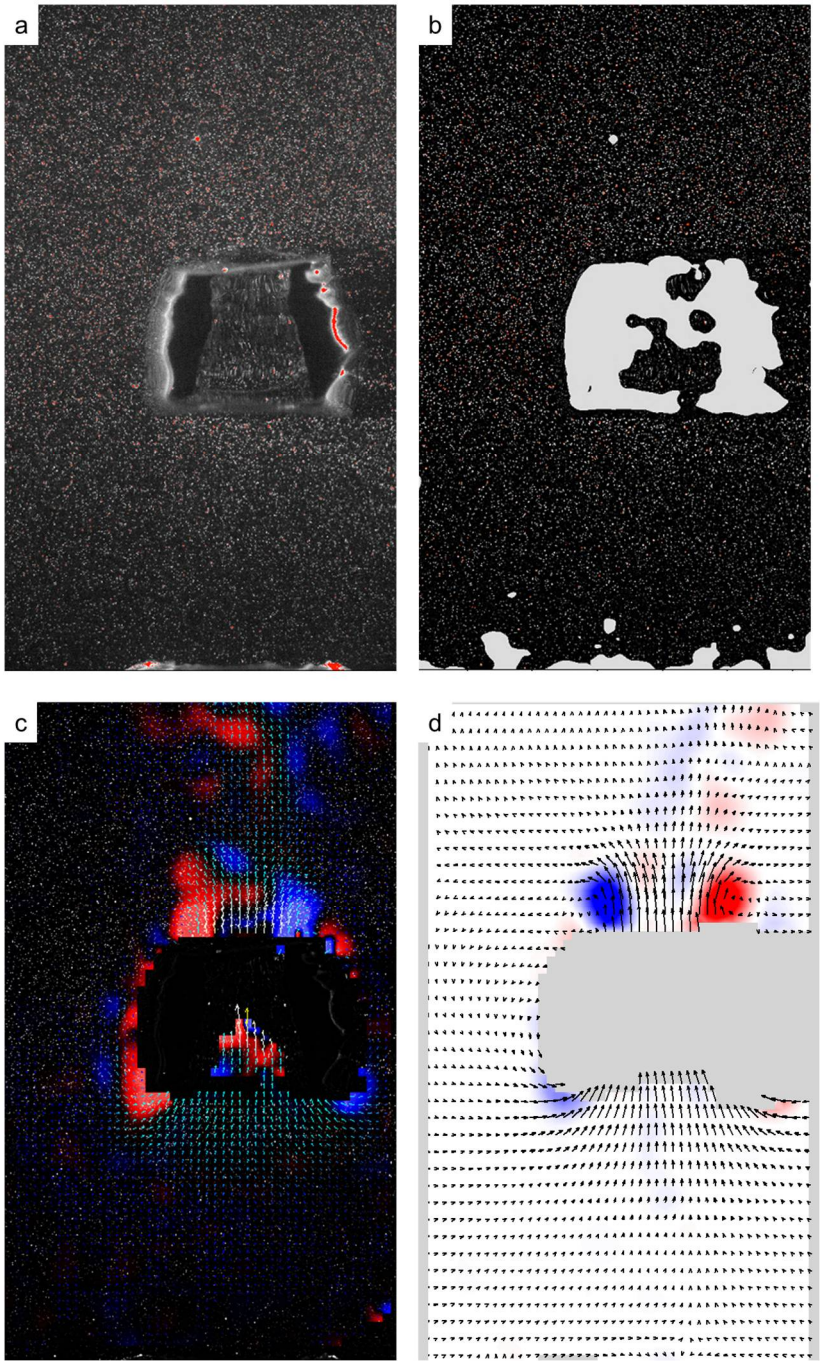


**Figure 3.9.** Sample raw image (a), masked image (b), vector field (c), and post-processed vector field (d) for condensing vapor bubble. Raw image is present in background of original vector field for spatial comparison. Post-processing includes temporal average over 0.5 msec and an additional mask.

# CHAPTER IV

# ACOUSTIC ACTUATION

The present investigations focus on interfacial coupling of acoustic actuation to the liquid vapor interface in two-phase heat transfer. The coupling of the actuation varies substantially with actuation wavelength and the present investigations consider two limits. Long actuation wavelength that is much larger than the characteristic scale of the vapor bubbles [O(1 kHz, 1 m)] leads to the formation and amplification of capillary surface waves on the liquid vapor interface with sufficient amplitude to force mixing of the interfacial thermal boundary layer surrounding vapor bubbles. Short actuation wavelength [O(1 MHz), O(1 mm)] exploits the surface force of the acoustic radiative pressure to effect local interfacial deformations and injection of a subcooled liquid jet and atomized droplets into the vapor volume.

## 4.1 Long-Wavelength Acoustic Actuation

Gas or vapor bubbles in a liquid bath can be modeled approximately as a damped oscillator (second order system) and when subjected to long wavelength [O(1 kHz, 1 m)] acoustic field can undergo nominally time-periodic oscillations at the acoustic frequency with amplitude that increases as the driving and resonance frequencies become closer. The natural frequency of a spherical bubble undergoing reasonably small changes in volume and including surface tension effects is given by:

$$\omega_o{}^2 = \frac{1}{\rho R_o{}^2}\left(3\kappa P_o + \frac{2\sigma}{R_o}(3\kappa - 1)\right) \qquad 4.1$$

(Leighton, 1994) where $\sigma$, $\kappa$, $P_o$, $R_o$, $\rho$ are the surface tension, polytropic exponent (which is 1 if the process is isothermal or is defined by the ratio of specific heats $c_p/c_v$ of

the gas if the process is adiabatic), local static pressure, bubble equilibrium radius, and liquid density, respectively.

Gas bubbles in a long wavelength acoustic field (i.e., much larger than the characteristic length scale of the bubble) are subjected to the primary Bjerknes body force that is colinear with the acoustic pressure gradient, and whose sense is determined by the bubble's proximity to the nearest node of the acoustic field and the ratio of the driving and resonance frequencies. The primary Bjerknes force, is given by

$$F_{B1} = \frac{2\pi^2 {R_o}^3 {P_A}^2}{3P_o\lambda_a\kappa\left(1-\frac{\omega^2}{{\omega_o}^2}\right)}\sin\left(\frac{4\pi z}{\lambda_a}\right) \qquad 4.2$$

(Eller, 1968) where $P_A$ is the amplitude of the acoustic field, $\lambda_a$ is the wavelength of the acoustic field, and $z$ is the distance between the bubble and the nearest node (point of zero pressure fluctuations). While the bubble's position within the acoustic field given by $\sin\left(\frac{4\pi z}{\lambda_a}\right)$ affects the magnitude of $F_{B1}$, $\frac{\omega^2}{{\omega_o}^2}$ affects both its magnitude and sense relative to the nearest node. Therefore, when the acoustic actuation is higher than the resonance frequency the bubble is forced towards nodes, and when the actuation frequency is lower than the resonance frequency the bubble is forced towards antinodes (points of maximum pressure fluctuations). Near the singularity ($\omega^2 = {\omega_o}^2$) the equation for $F_{B1}$ may be modified (Lee and Wang, 1993).

Long wavelength actuation ($\lambda$ = 1.5 m, §3.1-2) in the present experiments is effected by a disc transducer (nominally 32.64 mm diameter) with the acoustic pressure field in the tank having uniform phase and its amplitude determined primarily by spherical spreading from the acoustic source [in the present experiments acoustic attenuation by absorption in water ($10^{-3}$ dB/km at 1 kHz) are negligible]. In essence the acoustic field is similar to a standing wave with the actuator as an anti-node and the "far-field" free surface acting as a node (pressure release condition). Therefore, for a given actuation frequency ($\omega^2$), the primary Bjerknes force attracts small diameter bubbles ($D$ < 5.5 mm,

$\omega^2 < {\omega_o}^2$) towards the actuator, while larger bubbles ($D$ < 5.5 mm, $\omega^2 > {\omega_o}^2$) are driven away from the actuator.

The secondary Bjerknes force effects attraction or repulsion between adjacent gas bubbles in a sound field:

$$F_{B2} = \frac{-2\pi\rho\omega^2\delta_1{R_1}^2\delta_2{R_2}^2}{{r_{12}}^2}\cos\phi_o \tag{4.3}$$

(Crum, 1975) where $\delta_i R_i$ are the changes in the radii of bubbles 1 and 2, $r_{12}$ is the distance between the bubbles, and $\phi_o$ is the relative phase of oscillation between bubbles (positive and negative for in and out of phase, respectively). Bubbles of equal size oscillate in phase, and $F_{B2}$ is attractive. Bubble pairs that are driven below and above their resonance frequencies oscillate out of phase and $F_{B2}$ is repulsive.

Bubble oscillations under long-wavelength actuation lead to the formation of interfacial Faraday or capillary waves (Faraday, 1831) that contribute significantly to vapor condensation (cf. Chapter 6). A simple dispersion relation was developed by Kelvin (1871) relating the frequency and wavelength of the waves on a planar surface:

$$\lambda^3 = \frac{2\pi\sigma}{\rho F^2} \tag{4.4}$$

where $\lambda$ and $F$ are the wavelength and frequency of the surface waves.

Rayleigh (1883) showed empirically that the driving acoustic frequency $f$ is twice as large as the surface oscillation frequency $F$, i.e., $F = f/2$ yielding the primary capillary wavelength

$$\lambda^3 = \frac{8\pi\sigma}{\rho f^2} \tag{4.5}$$

The critical acceleration amplitude necessary for surface disturbance formation on a planar surface was investigated via stability analysis, and was determined to increase with increasing driving frequency:

$$a_c = 8\left(\frac{\rho}{\sigma}\right)^{1/3}\nu{\omega_f}^{5/3} \tag{4.6}$$

where $\omega_f$ is the driving angular frequency, and $\nu$ is the kinematic viscosity (Kumar and Tuckerman 1994; Hopfinger and Das 2009).

The relationship between the dispersion relation in Equations 4.4-6 and the oscillations of a spherical bubble is not simple, and is the subject of ongoing research. It is well established (e.g., Maksimov and Leighton, 2012) that the minimum pressure required to excite surface waves on a bubble exists when the driving acoustic frequency is equal to the natural frequency of the bubble ($\omega = \omega_b$) and the bubble is undergoing spherical expansion and contraction (cf. Eq. 4.1). However, the mode shapes and the ensuing pattern of surface disturbances are complicated by the interaction of multiple excited subharmonics that can even lead to self-focusing of the surface disturbances, preferentially creating surface waves around the perimeter of bubbles (Maksimov et al., 2008).

### *Characterization of the Long-Wavelength Acoustic Actuator*

Long-wavelength acoustic actuation is effected at 1 kHz and generated using a 32.6 mm diameter piezoelectric transducer disc (Thunder, Face International) operating in flexural mode that is submerged in the subcooled liquid tank. The stainless steel disc surface is in direct contact with the subcooled liquid, and the housing (constructed using stereolithography, SLA) is designed so that the back surface is placed in an air cavity that is sealed to the liquid but vented to the ambient air at the surface of the water tank by a small diameter flexible tube. An exploded cutaway view of the housing in Figure 4.1 shows the three SLA elements (front housing ring, retaining ring, and rear housing) and an actuator disc model. The variation of the induced acoustic pressure along the centerline of a single submerged actuator was measured by traversing a calibrated hydrophone (Brüel & Kjær, type 8103). Figure 4.3 shows the variation of the peak to peak amplitude of the induced acoustic pressure $P_{act}$ as measured by the submerged hydrophone with the distance $r_{act}$ from the 1 kHz transducer and the fitted curve indicates

that that the pressure of the spherically spreading acoustic beam decays nominally as $(r_{act})^{-1}$ of a fitted curve. The induced acoustic pressure near the surface of the transducer in the boiling experiments (Chapter 5) is measured using two transducers that are mounted within the subcooled liquid tank (cf. Figure 3.1) at an elevation of 35 mm above the heater, symmetrically opposite about the centerline of the heater such that the center of each transducer is located 50 mm away from the central point of the heater surface and the centerline of each transducer is inclined at $60^o$ relative to the centerline of the heater and intersects the central point of the heater surface. The amplitude of the driving signal of the piezoelectric transducers was varied over a range that included the level that was

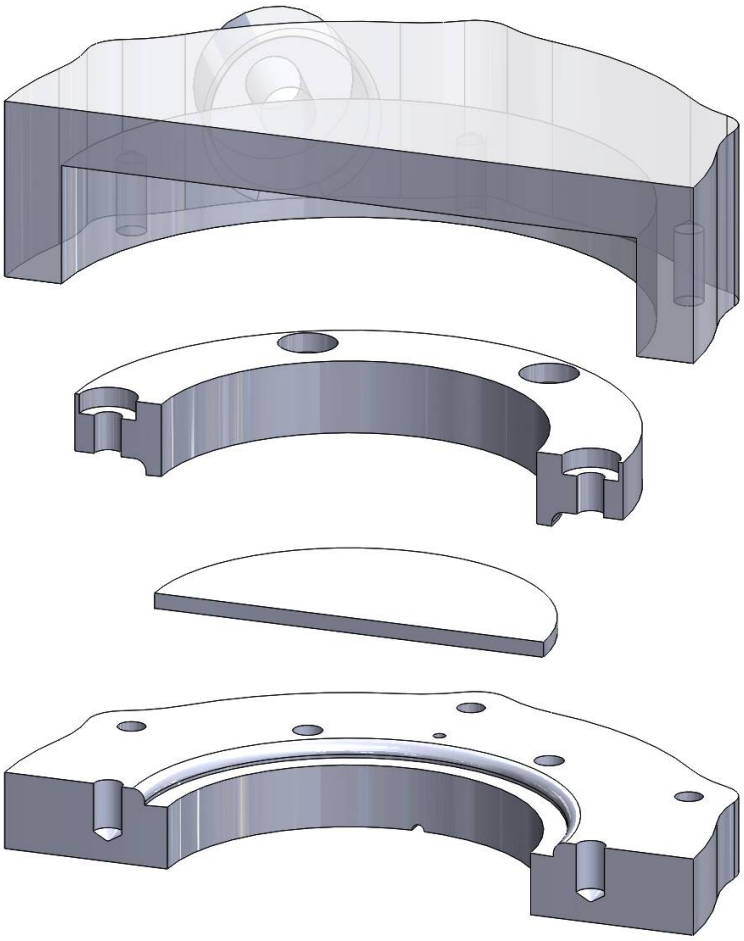

**Figure 4.1.** Long wavelength actuator housing showing (from bottom to top) the front housing ring, disk, retaining ring, and the rear air cavity housing.

later used for determination of the effects of the actuation on the boiling curves (Chapter 5). Figure 4.2 shows the variation of the peak to peak amplitude of the induced acoustic pressure $P_{act}$ as measured by the submerged hydrophone with the corresponding peak-to-peak amplitude $V_{act}$ of the driving sinusoidal waveform (1 kHz) to the amplifier. During the boiling experiments the induced pressure $P_{act}$ was nominally 5 ± 0.5 kPa.

In the condensation test cell (cf. Figure 3.3), the symmetrically-opposing transducers were mounted within the subcooled liquid tank at an elevation of 10 mm above the exit plane of the vapor orifice, such that the center of each transducer is located 30 mm away from the centerline of the vapor orifice and its centerline is normal to the orifice centerline. The actuators were typically operated at actuation levels that yielded $P_{act}$ = 5 kPa at the exit plane of the vapor orifice. Since the hydrophone could not be used when

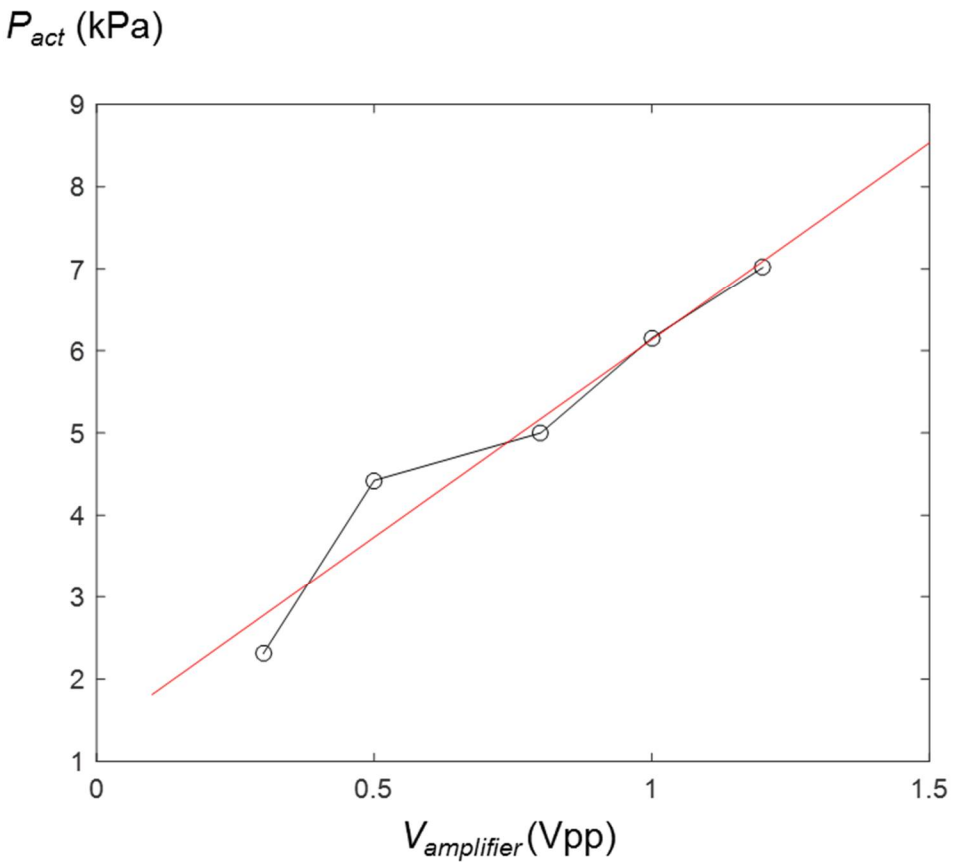


**Figure 4.2.** Variation of average peak-to-peak pressure with the actuator's drive amplitude including a least squares linear fit.

the condensation test cell was operated at subatmospheric pressure of 15 kPa, a laser vibrometer was used to measure the actuator disc displacement and confirmed that there was no change in actuator displacement and it was therefore assumed that the induced pressure field was also unchanged.

***Effects of the Long-Wavelength Acoustic Actuation on Air Bubbles***

The effect of the 1 kHz acoustic field on rising air bubbles was investigated in the same tank that was used for the condensation experiments (§3.2) using a 5.3 mm diameter injection orifice. To simplify the characterization of the acoustic actuation the volume of air in the lower chamber was adjusted such that the injection rate was below the level that leads to complicated interfacial dynamics of the formed bubbles (i.e. torus

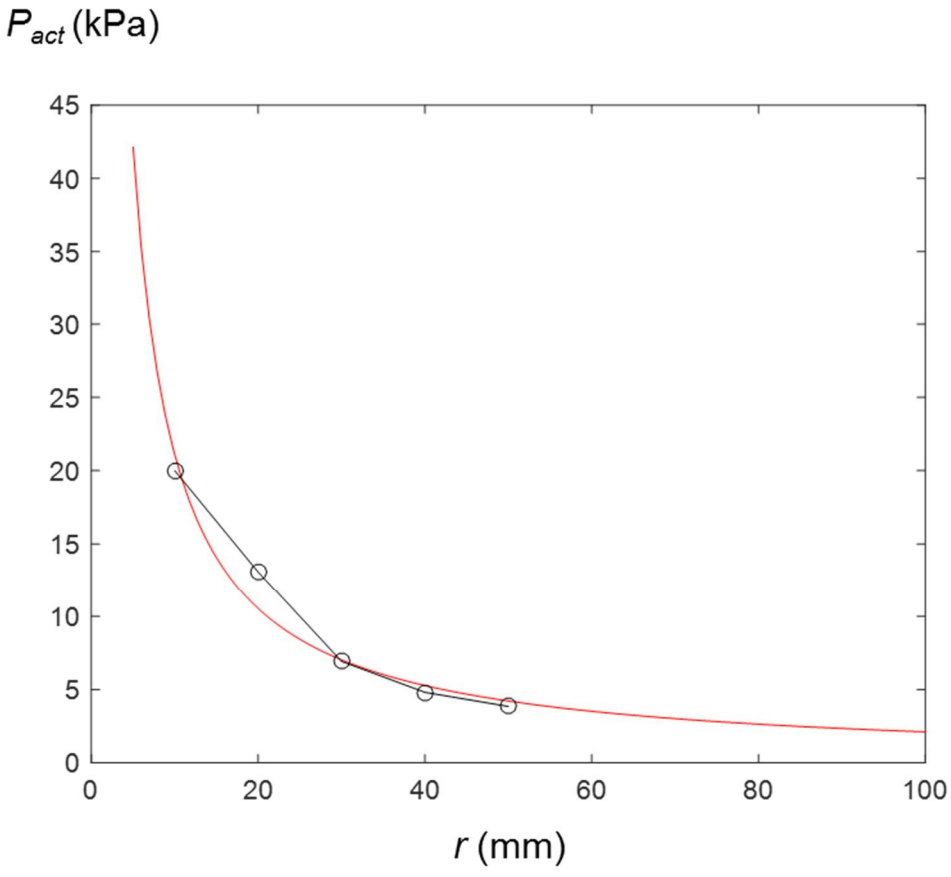


**Figure 4.3.** Variation of induced average peak-to-peak pressure at the surface of the heater distance along the actuator's centerline including a least squares $(r)^{-1}$ fit.

formation, bubble-cap breakup, etc., cf. §3.2). Figure 4.4 shows a sequence of high-speed video images (captured 60 msec apart) during the injection and subsequent detachment and advection of air bubbles in the absence of acoustic actuation (a-g), and in the presence of 1 kHz acoustic actuation at $P_{act}$ = 5 kPa (h-n) and 8 kPa (o-u), such that there are 60 actuation cycles between successive frames. In the absence of actuation the bubble's shape oscillates after pinch-off due to surface tension effects after the initial necking process (figure 4.4e-g, lower bubble). The shape does not change from a spheroid in this configuration.

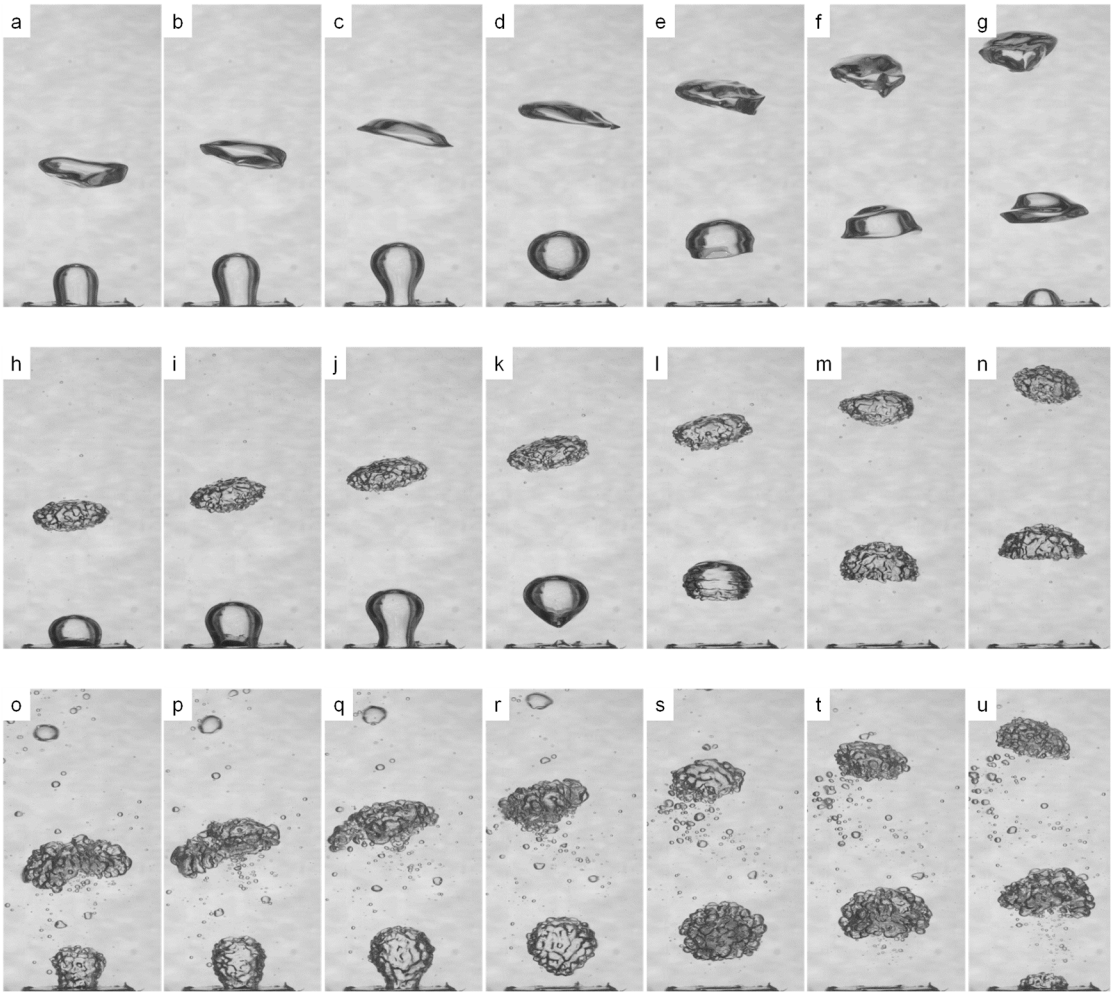


**Figure 4.4.** Air bubbles rising from the injection orifice orifice in the absence (a-g) and presence of long wavelength acoustic field. Acoustic field is 5 kPa peak-to-peak (h-n) and 8 kPa peak-to-peak (o-u). $\Delta t$ between frames = 10 msec.

In the presence of actuation at $P_{act}$ = 5 kPa (Figures 4.4h-n), the formation and detachment of the air bubble (Figures 4.4 h-k) is not significantly different from the corresponding images in the absence of actuation (Figures 4.4a-c). However, following the detachment, surface waves appear on the bubble's surface (Figure 4.3m and n), and are clearly apparent on the surface of the earlier bubble. These surfaces waves have a wavelength 1.15 mm from Equation 4.5, with the relatively long length of the capillary waves advantageous as it allows for a high amplitude oscillation on the bubble's surface. This would suggest that in the presence of acoustic actuation at this level, the condensation may be preferentially enhanced after the bubble is detached. Also, comparison of the trajectory of the detached air bubble in the absence and presence of actuation indicates that the presence of actuation does not appear to alter the advection rate by adding surface "roughness". In the presence of actuation at $P_{act}$ = 8 kPa (Figures 4.4o-u), the induced surface waves appear during the formation of the bubble (Figures 4.4 o-q), and their amplitude appears to increase following detachment (Figure 4.4t). The presence of the stronger actuation leads to the ejection of small-scale bubbles near the larger rising bubble that are clearly visible in Figures 4.4o-u (fewer, smaller secondary bubbles are also visible in in the presence of actuation at $P_{act}$ = 5 kPa). These small air bubbles are ejected into the embedding liquid in a fashion that is similar to droplet ejection from a larger vibrating droplet reported by Vukasinovic *et al.* (2007). Clearly, the same mechanism can also lead to ejection of liquid droplets into the volume of the air bubble. It is apparent that these ejections could significantly enhance condensation. It is also noted that there is little or no effect of the Bjerknes forces on the paths of the rising air bubbles, indicating that buoyancy is much larger than the Bjerknes forces and so attraction to the preceding or following bubbles is negligible.

The effects of the actuation on the propagation of the air bubble at $P_{act}$ = 5 kPa is assessed using the image processing analysis that is described in detail in §3.3 to track the

centroid of individual bubbles and estimate their volumes;. As indicated by the images in Figures 4.4, the actuation effects little change in the rise time of the individual bubbles at this actuation level, bubble ejection is limited (cf. Figure 4.4h-n). The variation with time of the elevation of the bubble's centroid $h$ (normalized by the orifice diameter of 5.3 mm) in the absence and presence of actuation is shown in Figure 4.5 (time is normalized by the actuation period $T_o$). These data exhibit a slight increase (~10%) in vertical speed from 0.17 m/sec to 0.19 m/sec in the absence and presence of actuation, respectively. It appears that this change is caused by a small increase in size of the air bubbles in the presence of actuation that is ostensibly caused by a slight change in the detachment

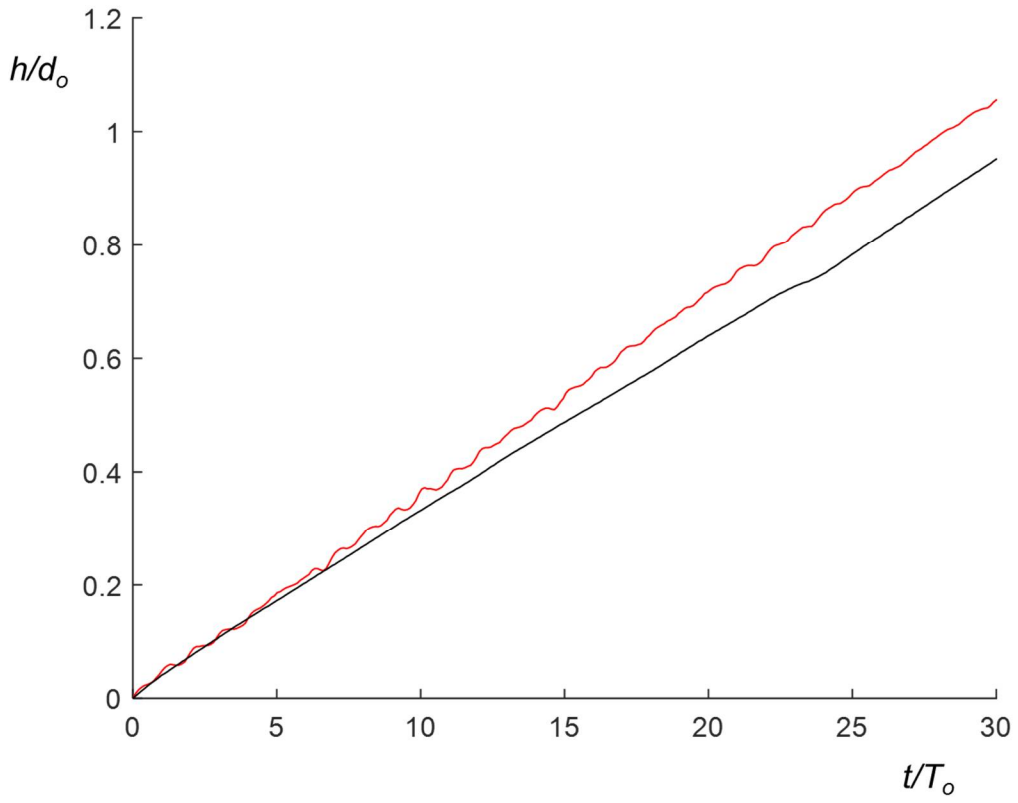


**Figure 4.5.** The variation of the elevation air bubbles centroid in the ***absence*** and ***presence*** of actuation. $P_{act}$ = 5 kPa

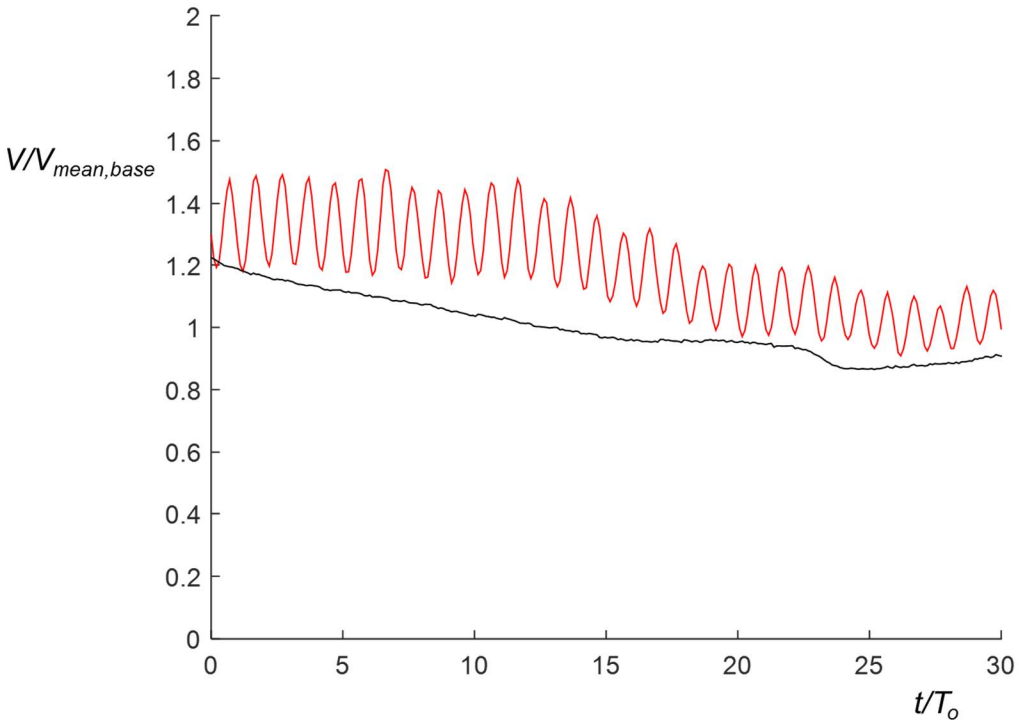


**Figure 4.6.** Time traces of the volume of an individual air bubble in the ***absence*** and ***presence*** of actuation. The volume is normalized by the mean volume of the baseline air bubble. $P_{act}$ = 5 kPa

process from the orifice, and perhaps by the primary Bjerknes force that is acting in the same direction as the buoyancy.

Time traces of the bubble's volume in the absence and presence of actuation are shown In Figure 4.6 (the volume is normalized by the initial volume of the bubble in the absence of actuation). The volume of the base bubble is essentially time-invariant, and the variation in Figure 4.6 reflects the fidelity of the image processing algorithm associated with determination of the spherical volume equivalent (cf. §3.3) as the bubble become distorted (e.g., Figure 4.4c, top bubble; disk-shaped). The volume of the bubble in the presence of actuation exhibits similar trend although it is offset by about 20% indicating an increase in volume due to the presence of actuation during the detachment process. The time trace also shows volume oscillations that are induced by the actuation

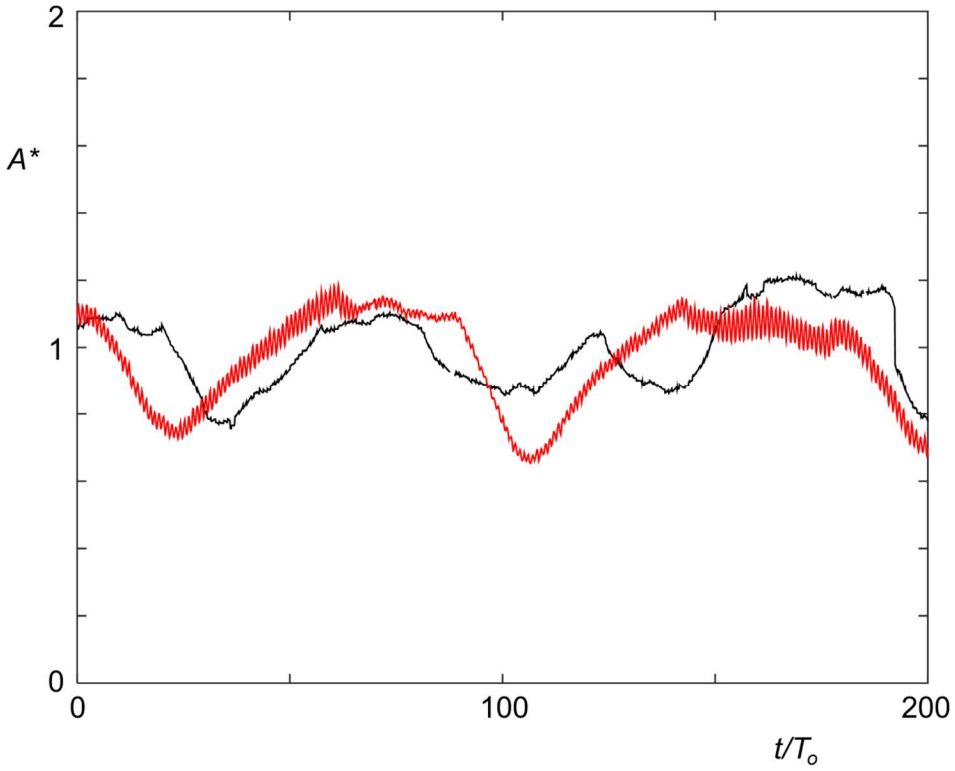


**Figure 4.7.** Time traces of the total projected area in the ***absence*** and ***presence*** of acoustic actuation. The projected area is normalized by the time-averaged vapor area in the absence of actuation. $P_{act}$ = 5 kPa

with a peak-to-peak amplitude of about 20% of a local time-average. The time series of total projected gas area normalized by the time-averaged projected area in the absence of acoustic actuation, $A^*$ (plotted in Figure 4.7) in the absence and presence of actuation show that there is no significant increase of total gas area observed in the system, indicating the changes in detachment process which led to larger air bubbles under acoustic actuation did not affect the overall gas flow rate through the orifice. Despite the difficulties associated with the volume approximation, the time average of the total area $A^*$ occupied by air bubbles (i.e., including multiple bubbles) during acoustic actuation is within 1% of the value without acoustic actuation.

### 4.2 Short-Wavelength Acoustic Actuation

When the actuation wavelength is much shorter than the characteristic scale of the vapor volume the bubble natural resonance and the related body forces (Bjerknes force) and capillary waves on the liquid vapor interfaces are of secondary importance or negligible. The primary acoustic effect is a surface force that is effected by the radiation pressure of the acoustic beam due to a local mismatch in acoustic impedance at the vapor-liquid interface. This mismatch can lead to significant distortion of the interface, and induce motion of the bubbles away from the actuator.

For typical boiling and condensation applications,

$Z_{water} = \rho_{water} \cdot c_{water} = 963 \cdot 1549 = 1.49 \text{x} 10^6$ kg/(m$^2$s),

and

$Z_{steam} = \rho_{steam} \cdot c_{steam} = 0.596 \cdot 472 = 281$ kg/(m$^2$s).

The intensity reflection coefficient (assuming a simple planar surface) is then given by

$$R = \frac{(Z_{steam} - Z_{water})^2}{(Z_{steam} + Z_{water})^2} \tag{4.7}$$

(Kinssler et al., 2000). For these conditions, $R = 0.9992$, or essentially unity. Then from the following relationship of intensity:

$$I = \frac{P_A{}^2}{2\rho c} \tag{4.8}$$

(Cheeke, 2002) where $P_A$ is the amplitude of the acoustic pressure, and $c$ is the speed of sound, and assuming $R \approx 1$, the radiative pressure of the reflecting beam is defined by

$$P_r = \frac{2I}{c} = \frac{P_A{}^2}{\rho c^2} \tag{4.9}$$

This force is referred to by Torr (1984) as the radiation pressure that can lead to deformation of liquid/vapor interfaces, especially at high frequencies which can easily attain high pressure level.

As shown by Bunkin et al. (1986), if the liquid/gas interface is larger than the cross-sectional scale of the ultrasonic beam, the interaction leads to a spear-like protrusion of

the liquid into the gas. As the interface deforms, the beam is focused due to internal reflections within the spear which further increases the acoustic intensity at the interface. The front of the liquid spear consists of a "drop-chain," or several globules of water, having a diameter of the wavelength of the acoustic field in the medium (Simon et al., 2015). In addition to the spear-like deformation, this high intensity ultrasound can eject droplets into the vapor bubble by the formation of capillary waves which can pinch off to become micron-scale droplets that match the capillary wavelength (Barreras et al., 2002, and Simon et al., 2015). Several correction factors have been applied to Equation 4.5 to determine the capillary droplet size (e.g., Lang (1962) used a correction factor of 0.34 from 10 kHz to 800 kHz while Tomita (2014) used 0.63 at 1 MHz). As shown by Tomita (2014) larger droplets [O(100 μm)] can be produced by the formation and subsequent collapse of cavitation bubbles that occur preferentially within the center of liquid globules due to reflection of the acoustic beam by the curved surface.

In the present investigations, short wavelength acoustic actuation is effected as an acoustic beam at 1.7 MHz, which in water has a wavelength of about 0.9 mm (natural frequency of 1.7 MHz corresponds to bubble diameter of about 2 μm). The acoustic beam is produced by a 20 mm diameter, 1.7 MHz ultrasonic piezoelectric transducer that is driven by an external amplifier. The piezoelectric disk has an active diameter of 12 mm, set by the diameter of a rear electrode. The actuator assembly is shown schematically in Figure 4.8. Electrical contacts are provided by a spring mounted in the center of the housing assembly and the retaining ring. The transducer is mounted in the tank above the heated surface using an articulated support such that the acoustic beam can be directed at the heated surface over a range of angles as shown schematically in Figure 3.1. The acoustic pressure along and normal to the centerline of the transducer was measured using a calibrated submerged hydrophone (CTS-Valpey Pinducer type VP-1063) at several driving voltages and distances, yielding maximum peak-to-peak pressure

fluctuations of 6.82× $10^3$ kPa at a distance of 50 mm (6% uncertainty). This centerline pressure corresponds to an acoustic intensity of 3.8 x $10^6$ W/$m^2$ (Equation 4.7). This also corresponds to an average radiation pressure of 5.1 kPa (Equation 4.8). The corresponding maximum radiation pressure based on the maximum acoustic intensity (i.e, not time-averaged over an actuation cycle) is 10.2 kPa. Additional measurements were used to characterize the spreading of the beam and its attenuation.

The variation of the normalized pressure amplitude $P^*_{act}$ (normalized by the maximum experimental pressure amplitude measurement in the plotted data) with distance $r$ from

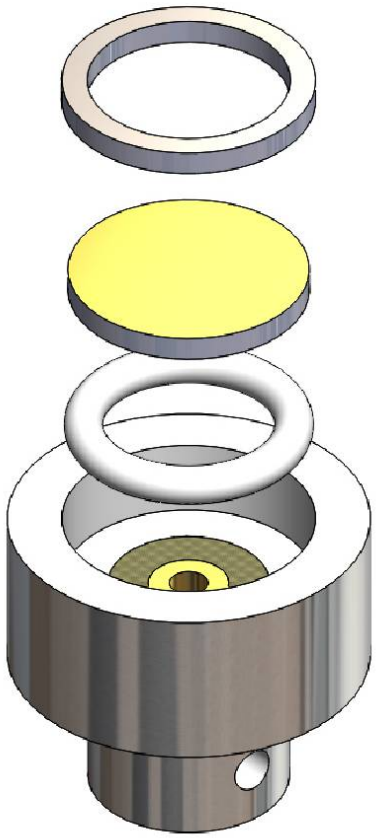

**Figure 4.8.** Short wavelength actuator. From top to bottom: Retaining ring, actuator disc, o-ring, and housing. Electrical contacts (not shown) are provided by a spring on back side of the transducer disc (not shown) and the retaining ring.

the actuator is plotted in Figure 4.9 for a driving voltage of 12 VDC along with for a fitted curve for $r^{-1}$. Although the distance of 50 mm is lower than the typical distance at which spherically-spreading beam would yield a good fit (generally for $r > \pi a^2/\lambda_a$, in water at 93ºC corresponds to $r > 125$ mm), the "ideal" theoretical plane circular piston's pressure amplitude differs by only 30% from the spherically-spreading far-field beam at 50 millimeters. The far-field solution (Kinssler et al., 2000)

$$P_{cl,ff} = \frac{a^2 \pi c U_a \rho}{\lambda_a r} \tag{4.10}$$

where $a$ is the source radius, $U_a$ is the source velocity, $\lambda_a$ is the wavelength and $r$ is the distance along the centerline, and the exact solution (Kinssler et al., 2000)

$$P_{cl} = 2\rho c U_a \left| \sin\left[ \frac{2\pi}{\lambda_a r} \left( \sqrt{1 + \left(\frac{a}{r}\right)^2} - 1 \right) \right] \right| \tag{4.11}$$

are also included for reference in Figure 4.9. Pressure nodes are expected in the near-field due to the phase difference between different sections of the actuator and the node locations. However, these nodes occur with 20 mm of the actuator, and therefore are unimportant in the present work. Figure 4.9 confirms that drops in pressure amplitude with increasing $r$ are primarily due to spherically spreading (i.e., $r^{-1}$ dependence) and not due to significant absorption by the water. At 1.7 MHz the sound absorption coefficient is ~$5 \times 10^2$ dB/km, and in the present set up this corresponds only to a 0.025 dB drop. Acoustic streaming can be induced when the acoustic field propagates (and is absorbed) in an undisturbed medium over a long distance and time (Krasil'nikov 1963). Acoustic streaming due to the absorption in quiescent liquid using the present actuators was observed to reach up to 0.12 m/sec under continuous actuation, which is significantly lower than the speed of the liquid-gas interfaces and lower than the terminal velocity of typical vapor bubbles in the present investigations (cf. the PIV measurements in Chapter 8). Furthermore, acoustic streaming over the surface of a hot (but not boiling) surface using the experimental setup of §3.1 did not result in any observable changes in surface

superheat. The variation of the normalized pressure $P^*_{act}$ (normalized by the maximum experimental pressure amplitude measurement in the plotted data) measured at 200 mm with amplifier driving voltage (Figure 4.10) is nearly linear up to 22 V, and saturates above 25 V.

Normalized pressure distributions $P^*_{act}$ (normalized by the maximum experimental pressure amplitude measurement in the plotted data) across the actuator's centerline at $r$ = 50, 100, and 200 mm are shown in Figure 4.11. At $r$ = 50 mm, $P^*_{act}$ decreases by 45% and 84% at offset radius $\tilde{r}/r_d$ ±0.5 and ±1 away from the centerline respectively (where $r_d$ = actuator disk active radius). The acoustic beam widens as the distance from

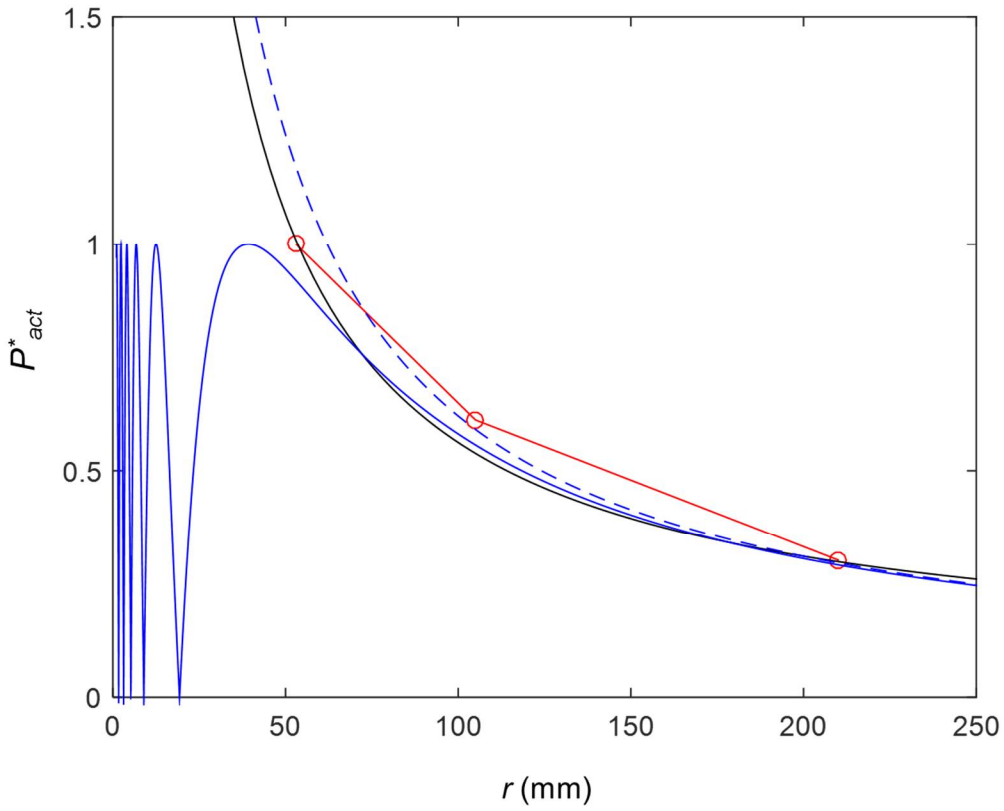


**Figure 4.9.** Variation of the normalized pressure with distance along axis of short wavelength actuator as function of distance: **1/*r* fit**; spherically-spreading far-field (***blue, dash***) and exact planar circular piston solution (***blue, solid***).

the actuator is increased, making the pressure falloff at a given distance offset from the centerline significantly higher at 50 mm.

The acoustic intensity necessary for the atomization of droplets when the acoustic beam is aimed a planar water-air interface is $1 – 2 \times 10^6$ W/m$^2$ (Tomita, 2014), and is demonstrated in Figure 4.12 using a high-speed video (2.5 msec apart) following the step-function onset of actuation from a transducer that is placed 25 mm below the free surface such that its axis is normal to the surface. The images capture the formation of the spear-like protrusion of water into the air, as well as the formation of droplets having multiple length scales. After the onset, the initially planar surface (Figure 4.12a) deforms as the acoustic beam reflects off the surface, forming a disturbance which grows to a

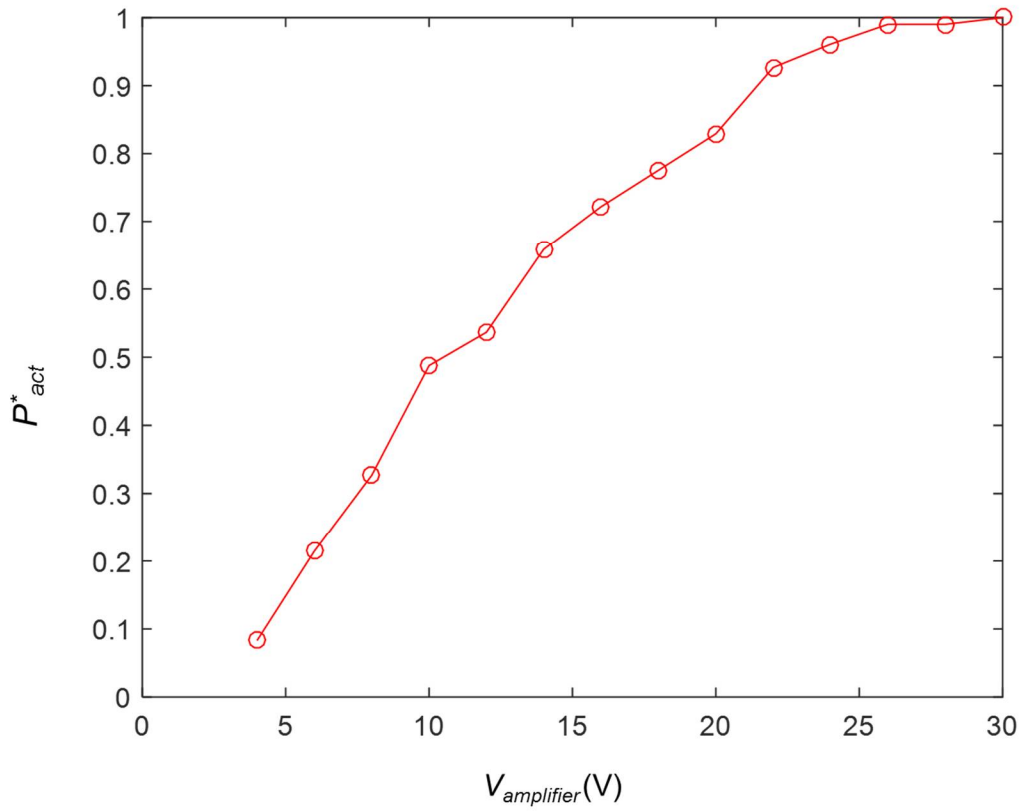


**Figure 4.10.** Normalized pressure along axis of short wavelength actuator as function of voltage at 200 mm distance.

conical shape (Figure 4.12e), allowing self-focusing of the reflected acoustic beam within this cone. Figure 4.12g shows mist of ejected, micron-scale droplets from capillary pinch-off. Larger droplets are ejected in subsequent frames (Figure 4.i onwards) as cavitation occurs. The droplet formation occurs preferentially in the narrow regions of the liquid stem (Figure 4.12k-p, where the large globular top section does not show significant ejection, even before its separation from the rest of the liquid stem). Note that as such, by the end of the sequence (Figure 4.12.q-t) the droplet formation continues only near the high end of the liquid spear, while the conical section of liquid near the planar interface (lower third of the liquid stem) does not reach the necessary pressure amplitudes

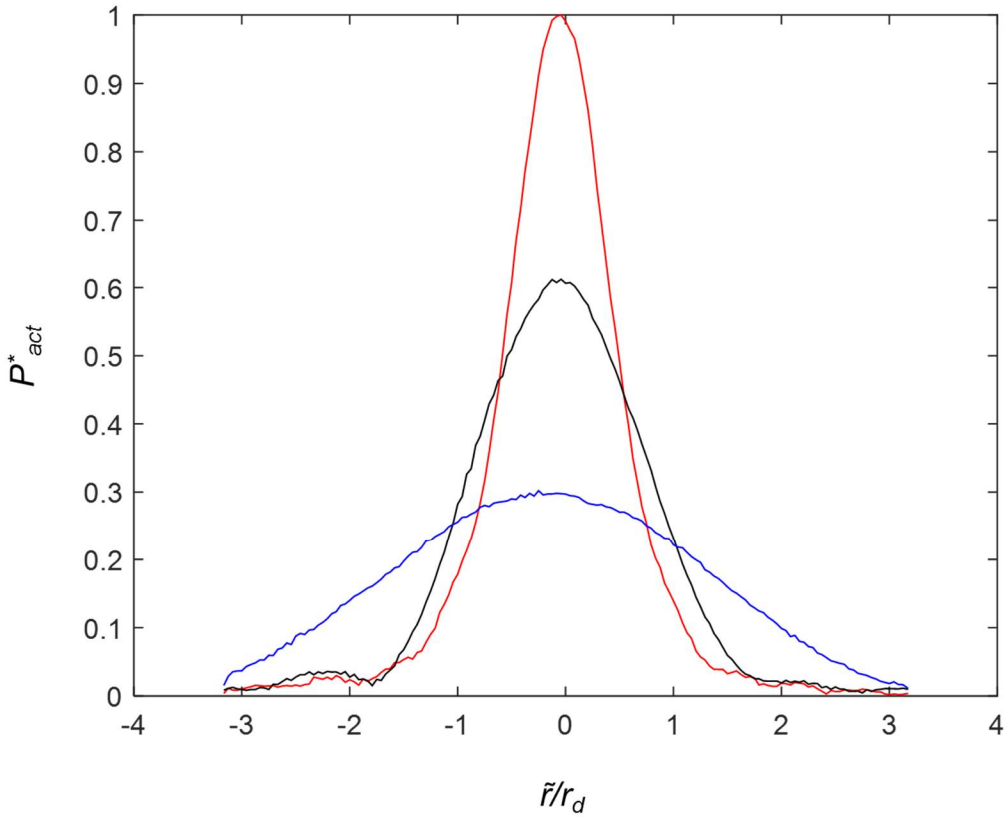


**Figure 4.11** Radial variation of the normalized acoustic pressure at three axial positions ($r$ = **50**, **100**, and **200** mm).

for ejection. The spear-like protrusion reaches a final height (not shown) due to gravity, even as actuation continues.

Note that droplets are first visible in Figure 4.12g after 15 msec from the onset of the step-function actuation; in other configurations where the force of gravity does not oppose the development of the liquid spear necessary for self-focusing (i.e., when the spear forms downwards into a vapor bubble without opposition from gravity), droplet ejection was observed to occur within 5 msec.

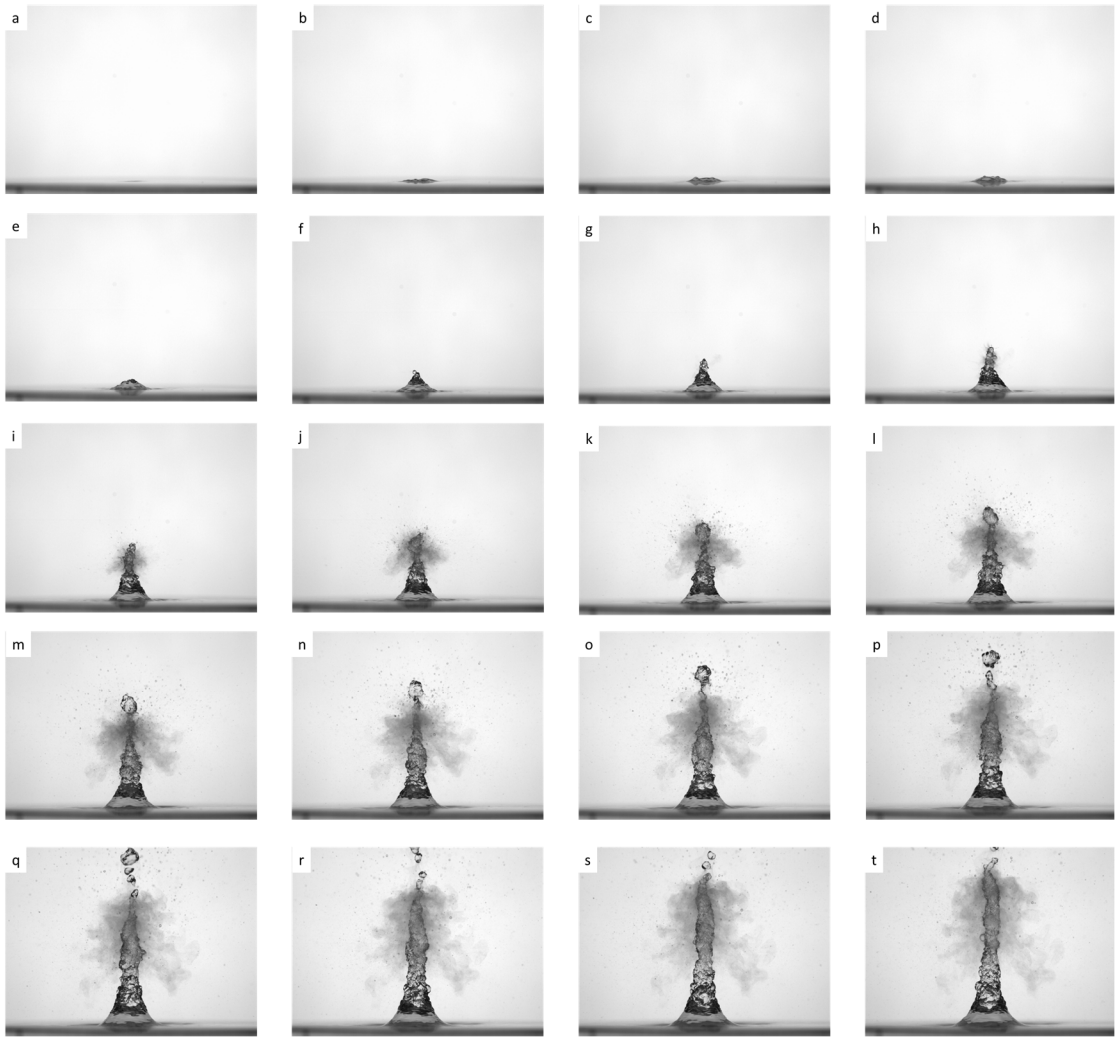


**Figure 4.12** High-speed video images (2.5 msec apart) following the onset of an ultrasonic beam aimed at a planar water-air surface from a submerged transducer (25 mm below the surface).

A magnified view of the droplet ejection acquired at higher frame rate (20,000 fps) is shown in a sequence of images (0.5 msec apart) in Figure 4.13a-x. The timing of the first image corresponds to Figure 4.12f. The sequence shows the early formation of several liquid globules (Figures 4.13a-g) whose diameter is essentially equal to the wavelength of the 1.7 MHz acoustic actuation, which are characteristic to this radiation-pressure induced process (Simon *et al.* 2015). Simon et al., as well as other investigators (Tomita 2014) observed cavitation in the center of the globules due to spherical focusing of the acoustic field. Also visible in Figures 4.13p-x are droplets of sizes ranging from 300 μm diameter down to O(1 μm). Even at this high frame rate and larger magnification, the formation of the smallest droplets is only resolvable as mist.

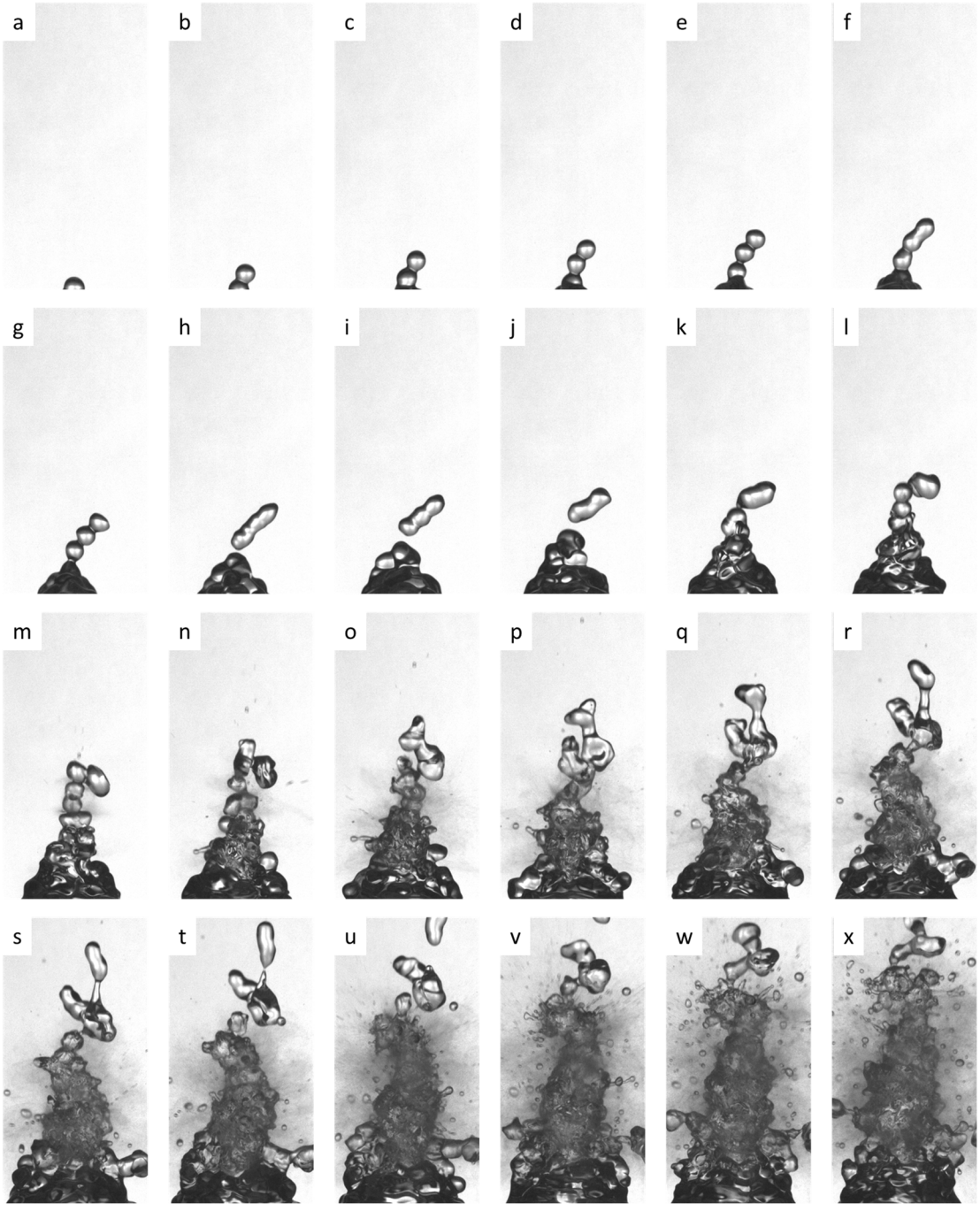


**Figure 4.13** Magnified views of droplet ejection from the spear tip caused by short-wavelength acoustic actuation, captured 0.5 msec apart.

# CHAPTER V

# ACOUSTICALLY-ENHANCED POOL BOILING

The onset and evolution of vapor formation on smooth and textured heated (copper) surfaces submerged in a subcooled liquid pool is altered using acoustic actuation to enhance the boiling heat transfer. The effects of the actuation on discrete vapor bubbles that are formed over the surface are investigated at two disparate characteristic scales using wavelengths (and frequencies) that are three orders of magnitude apart: long- [m-scale, O(1 kHz)] and short- [mm-scale [O(1 MHz)] wavelength. The characterization of boiling heat transfer over smooth and textured surfaces in the absence of actuation is described in Section 5.1. The effects of meter- [O(1 kHz)] and mm-scale [O(1 MHz)] actuation on a smooth surface are described in Sections 5.2 and 5.3, respectively. The effects of the ultrasonic actuation at discrete boiling nucleation sites measured using surface-embedded thermocouple sensors are analyzed in Section 5.4. Boiling over a textured (open microchannels) surface in the absence and presence of ultrasonic actuation is described in Section 5.5.

## 5.1 Boiling Characterization over Smooth and Textured Surfaces

The boiling process over smooth and textured surfaces (open microchannels and dimples) was characterized using boiling curves showing the variation of the heater's power with surface overheat temperature during a series of quasi-steady increments in heater power (or heat flux) until the onset of the critical heat flux (CHF) was reached (i.e., when nucleate boiling completely transitions to film boiling). Figure 5.1 shows the boiling curves for the smooth surface and in the presence of three grids of intersecting surface microchannels having width/pitch/depth 0.2 /0.8 /0.5 mm, 0.4 /1.2 /1 mm, and

1 /2.2 /1.8 mm, as well as a grid of dimples (1 mm deep) having equal diameter and spacing (600 μm). For theses heater configurations, the respective wetted surface areas are 200, 570, 600, 520, and 825 $mm^2$. The CHF of the smooth heater (the surface was polished to yield isolated vapor bubbles with contact angles of nearly $90^o$) was 110 $W/cm^2$ at a surface superheat of 17 $^oC$. Since the formation of the vapor bubbles at the nucleation sites on a surface and their ultimate advection into the liquid pool are accompanied by radial entrainment of subcooled ambient liquid, the CHF is reached when the transport of the subcooled fluid to the surface is disrupted by the rapid formation of bubbles as the heat flux from the surface is increased, leading to transition to film boiling. The purpose of the textured surfaces in the present investigations is to passively transport subcooled liquid to the nucleation sites in order to sustain the evaporation and prevent local dry-outs at the surface that usher transition to film boiling and CHF. This is accomplished using a square grid of intersecting, open-surface microchannels (manufactured using wire-EDM) that provide a regular array of nucleation sites at the grid intersections while transporting subcooled liquid to these sites by exploiting the momentary low local pressure induced by the rising vapor bubbles. Furthermore, spreading of local surface dry out is reduced by isolating vapor production at the surface to distinct locations within the microchannels. As noted above, a grid of hemispherical dimples was used to anchor vapor bubbles and is included for comparison. The heat flux was computed using the projected area of the surface (2 $cm^2$ for all surfaces) and the surface temperature was extrapolated to the bottom of the channels which corresponds to the hottest wetted surface, using the temperatures measured by thermocouple sensors embedded in the heater (cf., §3.1). The heat transfer curve was measured for each heater geometry up to the CHF as shown in Figure 5.1a. These data show that 0.4 mm channels yield the highest CHF (up to 350 $W/cm^2$) at the lowest surface superheat. It is noteworthy that the dimpled surface, which has nucleation sites

but no organized transport of subcooled fluid, has a higher surface superheat compared to the base (plain) surface ostensibly because vapor fills the cavities with limited replenishing of fluid resulting in an insulation of some surface fraction and therefore raising the mean surface superheat for a given heat flux. The "optimal" 400 μm channel represents a balance between the flow rate of subcooled liquid through the channel required to maintain nucleate boiling (which increases with increasing channel width) and preheating of the liquid as it moves through the channels which aids in the evaporation (which decreases with increasing channel width). This is shown as the peak CHF when using 400 μm channels in Figure 5.1b, where no microchannels ($w/D = 0$) and infinitely wide microchannels ($w/D \rightarrow \infty$) are both equivalent to the smooth, featureless heater. The average increase in CHF due to the presence of open microchannels (140%) is similar to the increases in CHF (up to 150%) reported by McGillis and Carey (1991), with the maximum increase of 218% by 400 μm-wide channels an improvement compared to their findings.

While for most applications, the relevant surface area is the projected area, it is instructive to normalize the boiling curves by wetted area rather than projected area. Although the wetted areas of the featured surfaces were designed to be reasonably similar, they were not exactly equal due to the desire to keep channel pitch such that the edges of the heater surface consisted primarily of pillars (rather than channels) to provide the greatest possible surface area for the sealing adhesive around the perimeter. If the boiling curves in Figure 5.1a are scaled by the wetted contact area (Figure 5.1c), the heat flux of the textured surfaces decreases significantly. The dimpled surface's poor performance, noted previously, is further highlighted by this normalization, as its increased surface superheat is now also accompanied by a significantly reduced CHF. Interestingly, the three surfaces with microchannels collapse onto a single curve before

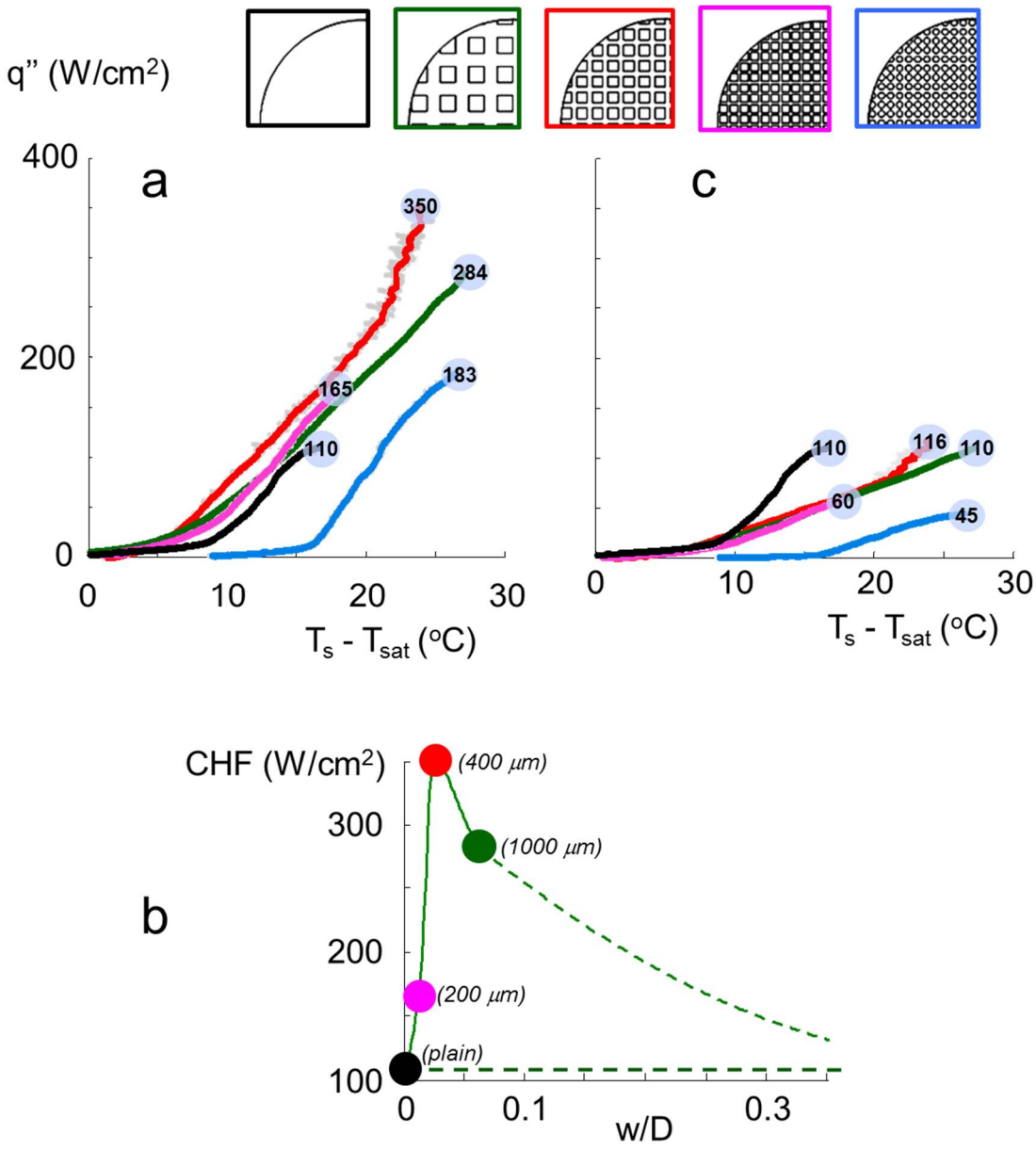


**Figure 5.1.** (a) Boiling curves for the smooth and several textured heat transfer surfaces shown in insets above: ***smooth***, *microchannels*: ***0.2, 0.4***, and ***1 mm wide,*** and *dimpled* ***0.6 mm diameter***. The CHF for each boiling curve is noted at its upper end. The gray data points represent the magnitude of the instantaneous deviation in both q'' and $T_s$-$T_{sat}$ relative to the smoothed data. (b) Variation of critical heat flux with channel width for several textured heat transfer surfaces. (c) As in Figure 5.1a with heat flux normalized by wetted areas: *plain* ***200 mm²***; *microchannels*: ***200 μm (570 mm²)***, ***400 μm***, (***600 mm²***), and ***1000 μm (520mm²***), and *dimpled* ***600 μm (825mm²***).

the CHF is reached, indicating that under this normalization flow and heat flux are similar regardless of the characteristic width of the microchannels. In fact, the 400 μm wide channels exhibit improved performance relative to the other surfaces only for $T_s$-$T_{sat}$ > 22 $^oC$. Interestingly, the 400 and 1000 μm wide channels reach CHF at nominally same heat flux as the smooth surface, indicating that this limit is imposed by the physical properties (wettability, small-scale texture) of the boiling surface and of the working liquid rather than the geometry and area of the wetted surface or the induced flow field. Furthermore, it should be noted that prior to CHF, the microchannel surfaces have a higher surface superheat than the smooth surface. This is not surprising, since the temperature gradients within the copper features prevent nucleation of vapor on the top surfaces and along most of the vertical surfaces of the heater pillars. Therefore, the total wetted area where surface temperatures are high enough to sustain boiling is reduced by the presence of microchannels, and the boiling occurs primarily at the bottoms of the channels which form about 50% of the projected area. Consider that if the surface area used to determine heat flux were limited to actual boiling sites, this area would be reduced when microchannels are used and therefore the heat flux calculated would not be only slightly higher (as seen when using projected area definition for heat flux in Figure 5.1a), but significantly higher due to the reduction in boiling area. Since the exact area over which boiling occurs cannot be determined accurately (and probably increases with heat flux), this normalization would be both imprecise and impractical, although considering it conceptually highlights that the flow that is induced by the presence of the microchannels significantly increases the efficiency of vaporization on a per-active-boiling-area basis.

## 5.2 Boiling Enhancement using Long Wavelength Acoustic Actuation

The use of long-wavelength actuation for enhancement of the boiling process was previously explored by Douglas (2007), and subsequently by Douglas et al. (2012). The boiling curves for the smooth heater in the absence and presence of acoustic actuation where actuation having a kHz characteristic frequency is produced using the actuators described in §4.2. Compared to Douglas 2007, the present investigations had significantly better agreement with the findings of earlier works (e.g., Isakoff 1956; McGillis and Carey 1991; Zuber 1959) on the measured and expected CHF on a smooth copper surface. Note that the application of a subcooled temperature correction to the boiling curves of Douglas (2007) resulted in an unrealistically high base CHF (over 300 W/cm$^2$). The boiling curves acquired using the present setup were obtained at a single bulk temperature (93$^o$C), and are reported without using the correction factor. However,

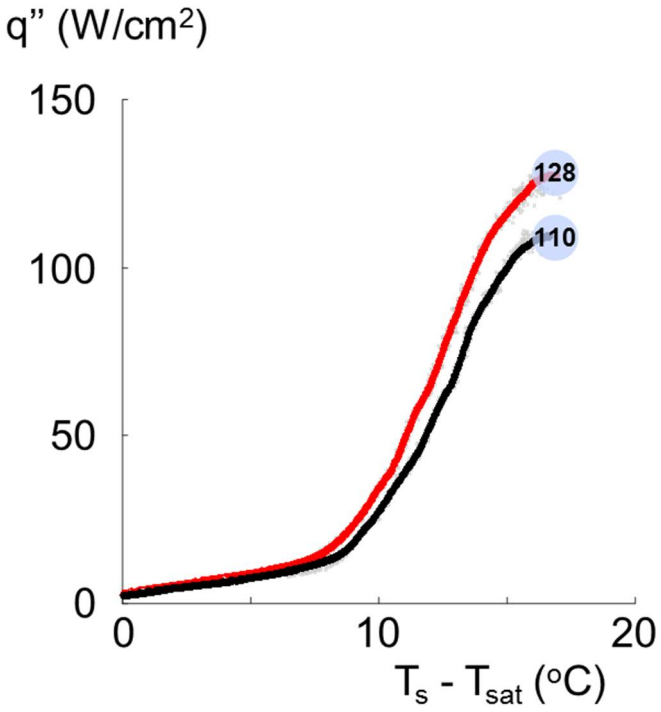


**Figure 5.2.** As in Figure 5.1. Boiling curves for the plain (baseline) surface in the ***absence*** and ***presence*** of long wavelength acoustic actuation. Grey instantaneous data plotted to denote magnitude of instantaneous deviation relative to the smoothed data.

it is noteworthy that compared to Douglas 2007, the present data exhibit a smaller percentage increase in the CHF in the presence of acoustic actuation. As shown in Figure 5.2, the kHz actuation increases the CHF from 110 to 128 W/cm$^2$, with a decrease of about 1 $^o$C in surface superheat through the majority of the boiling curve. Figure 5.3a-j show images from high-speed videos of vapor formation along the heat transfer curve of the base surface (Figure 5.1) in the absence (left column, a-e) and presence (right, f-j) of 1 kHz acoustic actuation. Especially at low heat fluxes (Figure 5.3f) the actuation leads to clumping of vapor bubbles, and lower vapor mass above the surface. The reduction in vapor mass continues at higher heat fluxes, although the amount of vapor *on the surface* does not appear to be significantly reduced at heat fluxes higher than 60 W/cm$^2$, despite the reduction in vapor mass above the surface. This explains the limited increase in CHF, despite the large difference in the appearance of vapor conditions, and indicates that the enhancement mechanism is primarily the result of vapor condensation rather than vapor formation. The effects of long wavelength acoustic actuation on condensation are investigated in §6.1.

The effects of the long wavelength actuation on the boiling process over textured surfaces (e.g., the microchannel surfaces in §5.1) were minimal at lower heat fluxes (< 100 W/cm$^2$) and negligible at higher heat fluxes, ostensibly owing to the mismatch between the characteristic length scales of the actuation and the surface channels. This mismatch prevents effective transmission of the acoustic pressure fluctuations into the channels, as well as any coupling to vapor bubbles within the channels.

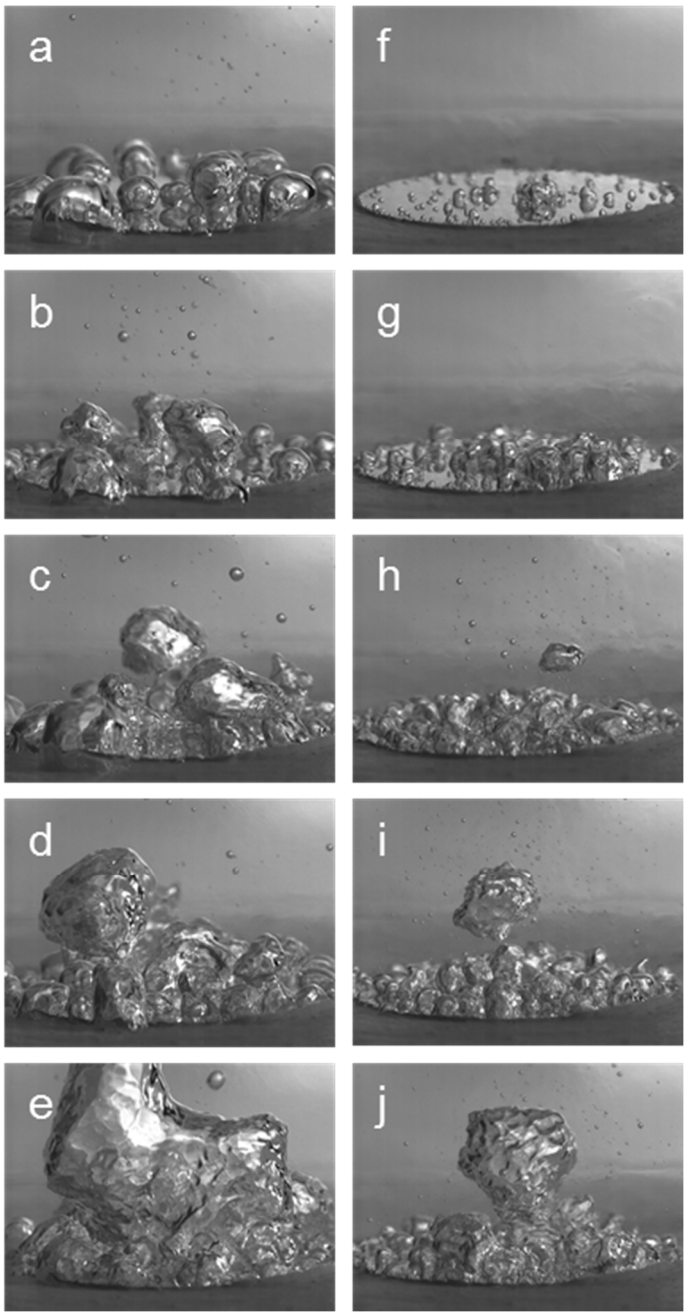


**Figure 5.3.** Images from high-speed videos of vapor formation along the heat transfer curves of the plain surface (Figure 5.4) at 20 (a, f), 40 (b, g), 60 (c, h), 80 (d, i), and 100 (e, j) W/cm$^2$ in the ***absence (left column, a-e)*** and ***presence (right column, f-j) of long wavelength acoustic actuation***.

### 5.3 Boiling Enhancement on a Plain Surface using Short Wavelength Actuation

The effects of ultrasonic (1.7 MHz) acoustic actuation on the evolution of vapor bubble clusters that form over a plain heated surface are investigated over a range of heat fluxes up to the critical heat flux. To assess the effects of the actuation, it is first applied at an incidence angle (of the centerline of the acoustic beam relative to the surface) of 45$^o$ (the effects of the incidence angle of the acoustic beam relative to the boiling surface are discussed in connection with Figure 5.8 below). The boiling curves in the absence and presence of actuation are shown in Figure 5.4. These data show that the presence of actuation significantly increases the surface superheat by up to 7 $^o$C, and, perhaps more significantly, increases the CHF from 110 to 183 W/cm$^2$, an improvement of 65%.

The evolutions of vapor bubbles on the plain surface in the absence and presence of ultrasonic actuation are shown using high-speed video images (10,000 fps) in Figures 5.5a-e and 5.5f-j, respectively. These data are acquired at five levels of power dissipation

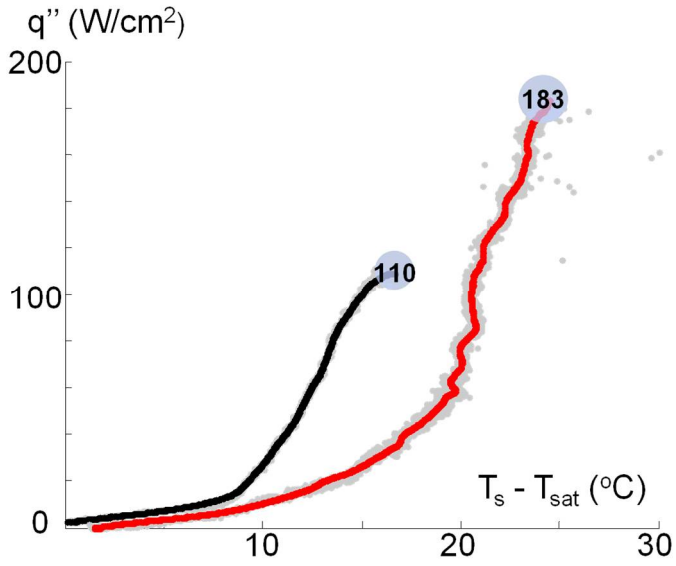


**Figure 5.4.** As in Figure 5.1. Boiling curves for a plain heated surface in the ***absence*** and ***presence*** of short wavelength acoustic actuation.

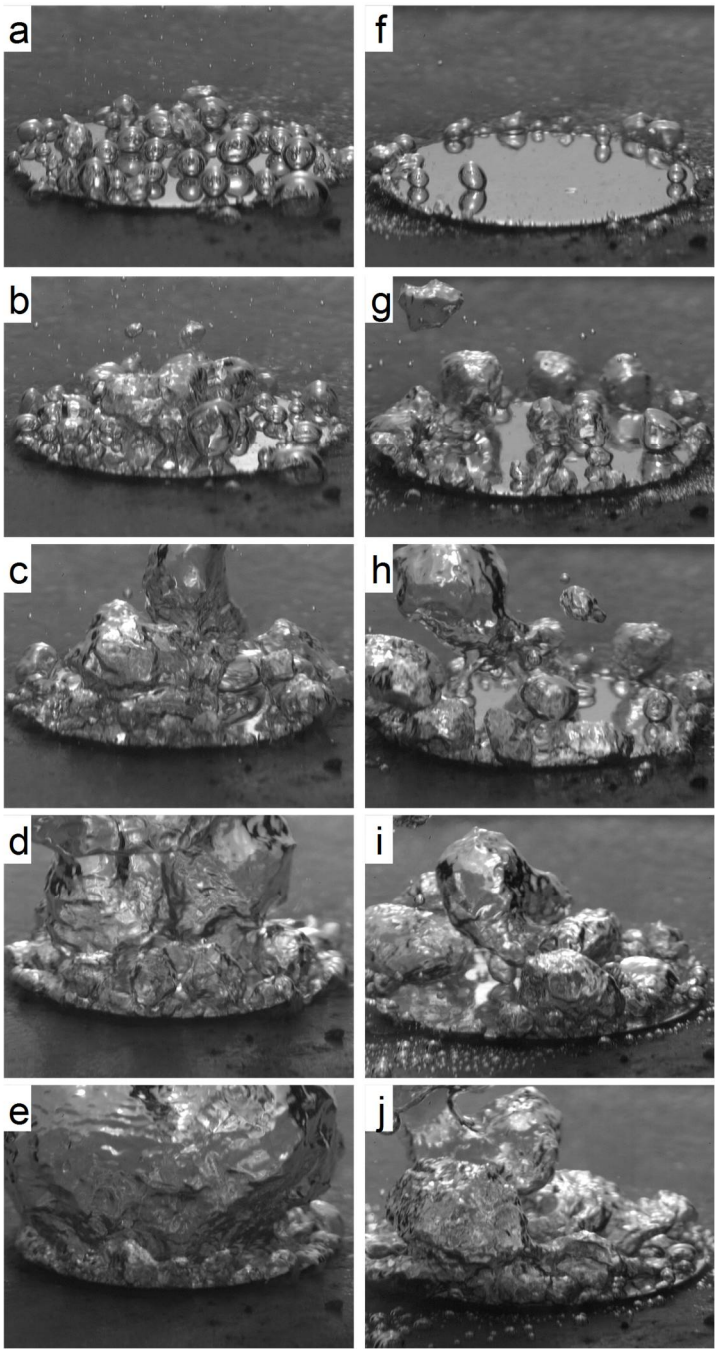


**Figure 5.5.** Images from high-speed videos of vapor formation along the heat transfer curves of the plain surface (Figure 5.6) at 25 (a, f), 50 (b, g), 75 (c, h), 100 (d, i), and 110 (e, j) W/cm$^2$ in the ***absence (left column, a-e)*** and ***presence (right column, f-j) of short wavelength acoustic actuation***.

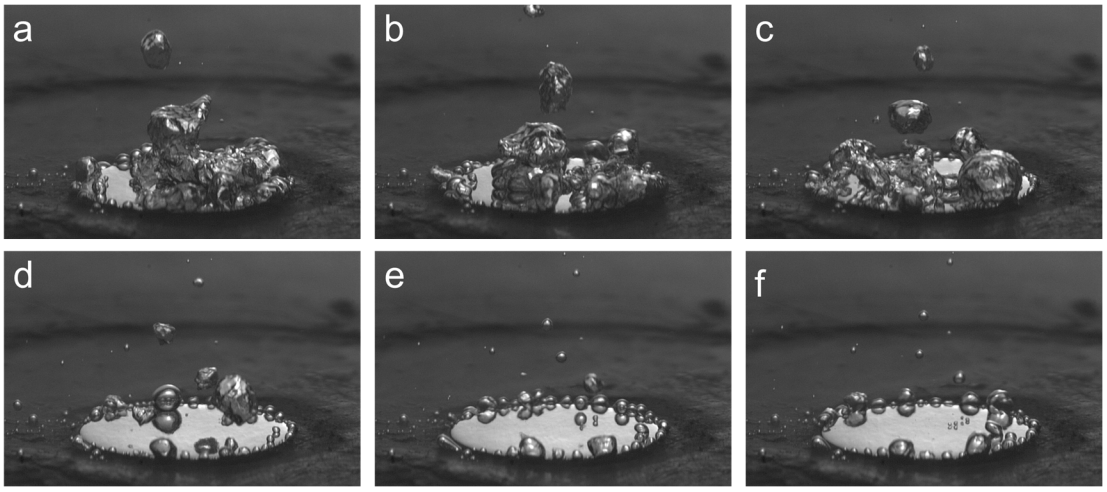


**Figure 5.6.** Onset of short wavelength (1.7 MHz) acoustic actuation on the plain heated surface at 50 W/cm$^2$. The onset occurs between frame a and b, and successive frames are 10 msec apart.

(between 25 and 110 W/cm$^2$). At low power levels (25–75 W/cm$^2$), the actuation results in lower vapor volume on the surface of the heater indicating an increase in the forced detachment of small-scale bubbles that form at various nucleation sites. Furthermore, these data indicate that the evaporation over the surface is diminished and is restricted to fewer ("preferred") nucleation sites such as those along the edge of the heater (Figure 5.5f. The effects of the onset of actuation on the boiling process are shown in a sequence of high-speed images (10 msec apart) in Figure 5.6 that are acquired at a low (50 W/cm$^2$) heat flux for improved visibility of the boiling at the heater's surface. These images indicate that the effects of the actuation become fully established within about 50 msec, which is faster than the characteristic response of the heater surface (about 500 msec, cf. Section 3.1). The effected changes to the boiling process remains the same when using delayed actuation onset, with most vapor nucleating at preferred sites such as those at the edge of the heater with the thermocouples measuring a corresponding rise in surface superheat.Although the differences in vapor mass above the heater surface between the unactuated and actuated flows at higher power levels appears to be somewhat significant in Figure 5.5, larger-scale images in Figure 5.7 clearly indicate that ultrasonic actuation

significantly alters the structure of the vapor column above the heater surface. Time sequences of images of vapor formation at moderate heat flux levels (100 W/cm$^2$) in the absence and presence of actuation are shown in Figures 5.7a-f and 5.7g-l, respectively. In order to show details of the effects of the acoustic actuation, the respective durations of the sequences are 200 and 100 msec (the images in each sequence are equally-spaced in time). In the absence of actuation (Figures 5.7a-f), large vapor masses form time-periodically over the heated surface, detach and are advected into the liquid pool as subcooled ambient liquid is entrained towards the heater's surface. (c.f. Figure 5.5e). It should be noted that the detachment of the vapor may sometimes, especially when the subcooling is low, be followed by the formation of vapor columns (Figure 5.7c) or other complicated structures formed by interaction between vapor masses as the second vapor mass rapidly grows in the hot wake of the previous bubble. The growth of large vapor structures, which occur over a relative long time period (50-100 msec) can temporarily interfere with the flow of liquid to the boiling surface, and are typically a precursor to CHF at these subcooled temperatures.

In the presence of actuation (Figure 5.7g-l) the formation cycle is considerably shorter, i.e., bubbles are formed and detached at a higher rate and the volume of each detached vapor mass is considerably smaller. These images also show that as a result of the actuation the detached bubbles apparently condense rapidly within 1-1.5 heater diameters above the heated surface and only few small vapor bubbles continue to rise in the liquid pool. In addition, the process is much steadier and lacks the long growth phase of large vapor structures which can interfere with the flow of liquid to the heater, which contributes to the higher CHF. The condensation process induced by the short wavelength actuation is discussed further in Chapter 7.

As noted in connection with Figure 5.4, the actuation leads to an increase in surface superheat and ultimately to an increase in the CHF limit. The mechanisms for these

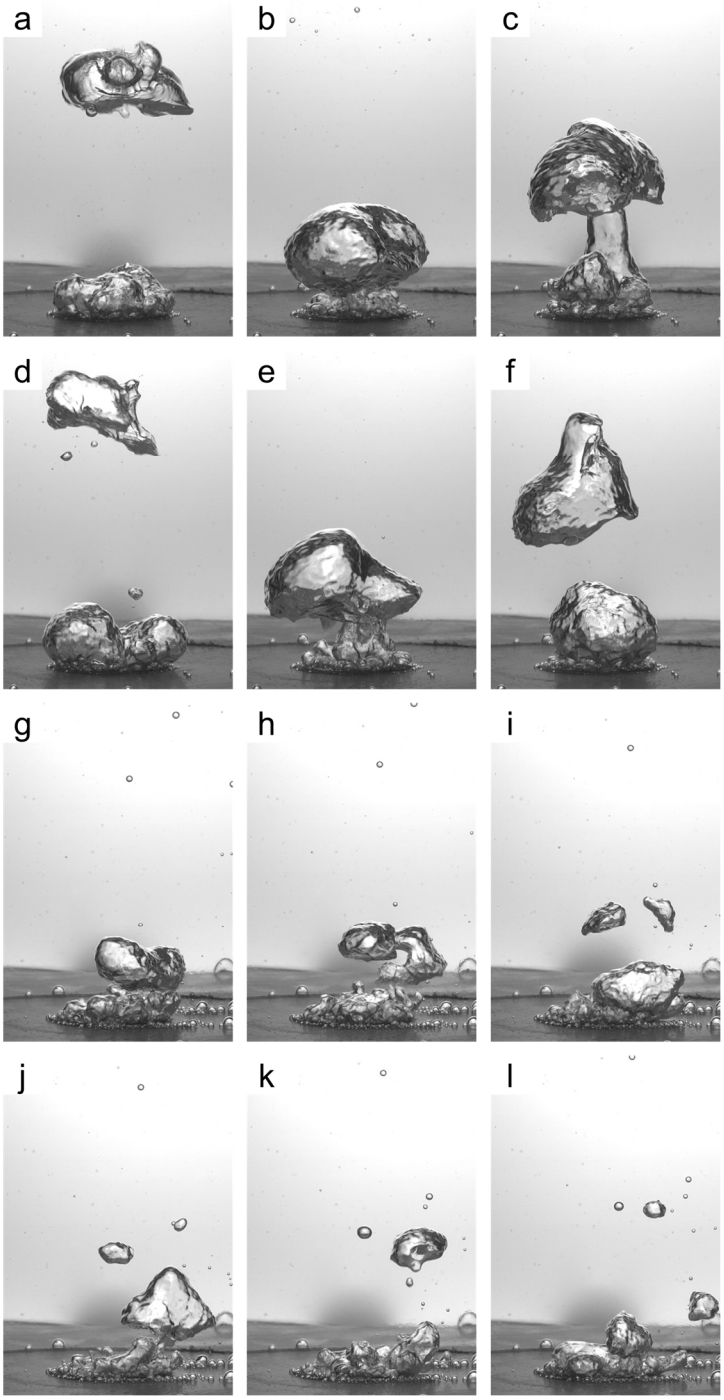


**Figure 5.7.** Vapor column formation over the heated surface at 100 W/cm$^2$ in the ***absence (a-f)*** and ***presence (g-l) of acoustic actuation*** where the total duration of each sequence is 200 and 100 msec, respectively in order to show details of the effects of the acoustic actuation (the images in each sequence are equally-spaced in time).

increases can be surmised from the images in Figure 5.5. Based on Figures 5.5f-j it is conjectured that the acoustic pressure induced on the surface of the heater leads to the removal of small [O(10 μm)] vapor bubbles from their nucleation sites before they can grow significantly. Furthermore, the increase in local time-averaged pressure induced by the acoustic beam can suppress evaporation at multiple nucleation sites. Both of these effects decrease the local rate of vapor formation and because the heat flux that would support evaporation is driven into the adjacent liquid there is an increase in the surface temperature as is evident in Figure 5.4. The magnitude of the increase in surface superheat may be partially related to the magnitude of the radiation pressure of the ultrasound actuation. As noted in §4.2, the magnitude of the pressure along the centerline of short wavelength (MHz) acoustic beam 50 mm from the transducer is nominally $6.82 \cdot 10^3$ kPa, which corresponds to an acoustic intensity of $3.8 \cdot 10^6$ W/m$^2$ and average and maximum reflected (at the surface) pressures of 5.1 kPa and 10.2 kPa that lead to corresponding local increases in the saturation pressure, and therefore saturation temperature by ~1.3 $^o$C and 2.7 $^o$C, respectively. This increase in the local saturation pressure and temperature may account for some, but not all of the observed increase in surface superheat. Other contributors to the increase in surface superheat may be the interaction between the acoustic field and the surface microlayer that is responsible for vaporization (e.g., Cooper and Lloyd 1969), and interaction between the acoustic field and static pressure within nucleation sites that can lead to higher increases in the local static pressure and therefore the local saturation pressure and temperature.

The dependence of the actuation effectiveness on the incidence and azimuthal angles of the acoustic beam relative to the boiling surface were measured using an articulated actuator traverse (cf. §3.1 for coordinate system). The effectiveness of the ultrasonic actuation is assessed using the measured surface superheat $\Delta T_s$ when the heater power is fixed at 100 W/cm$^2$ and the radial distance of the center of the actuator's surface from the

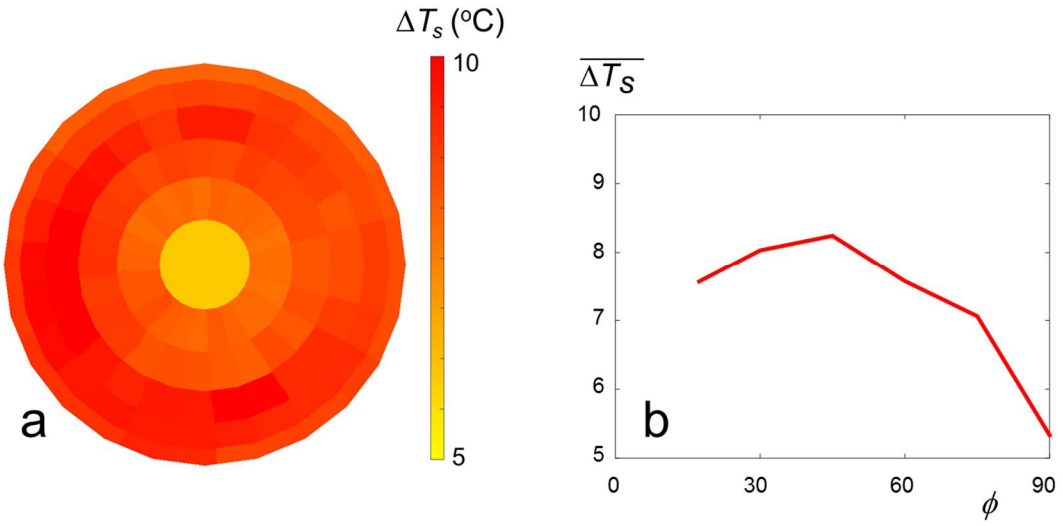


**Figure 5.8.** a) Contour map of surface superheat $\Delta T_s$ for 25 equally spaced azimuthal, and 6 incidence acoustic beam angles (17°, 30°, 45°, 60°, 75°, 90°), and b) Variation of the azimuthally-averaged $\Delta T_s$ with incidence angle.

center of the heater is 50 mm (cf. Figure 3.1). The surface superheat is assessed by extrapolation using the embedded thermocouple sensors (cf. Section 3.1), and the variation of $\Delta T_s$ is depicted using a polar color raster plot for 25 equally spaced azimuthal angles $\theta$ (around the perimeter) and 6 incidence angles $\phi$ (varying radially) as shown in Figure 5.8a. For each azimuthal (and incidence) position, the superheat data were measured by monitoring the heater temperature for 40 sec in the absence of actuation, turning the actuation on ,waiting for 20 sec, and then monitoring the heater temperature for an additional 40 seconds before the actuator was traversed to its next position. The measurement of the base condition in the absence of actuation for each angular mutation enabled mitigation of slight drift in the heater's operation over the several hour-long experiment. Averages of three full azimuthal traverses were used to generate the (discretized) azimuthal variation for a given incidence angle. Each time the actuator was removed to change the incidence angle, the water tank was drained, the boiling surface cleaned, and fresh water used for the next incidence angle data set. The data in figure 5.8a show that the variations in surface superheat are nearly invariant with the azimuthal

position of the transducer. For transducer incidence angles $17^o < \phi < 75^o$, the azimuthally-averaged $\Delta T_s$ varies between 7 and 8.25°C (Figure 5.8b). For $\phi > 75^o$ there is a reduction in the effect of the actuation, and at $\phi = 90^o$ the azimuthally-averaged $\Delta T_s$ is 5.4° C.

Because the acoustic actuation can be applied "on demand" in practical applications with little or no hysteresis effects on the effected enhancement in heat transfer, it is possible to "tailor" the variation of the boiling curve by regulating the dissipated power and the surface superheat. An example is illustrated in Figure 5.9. Three boiling curves are shown: the base curve (in the absence of acoustic actuation) as well as the acoustically-enhanced boiling curve for which actuation is activated before the surface is heated. While the latter curve leads to higher CHF (183 vs. 110 W/cm$^2$), a given heat flux below the CHF limit occurs at higher surface superheat in the presence of acoustic

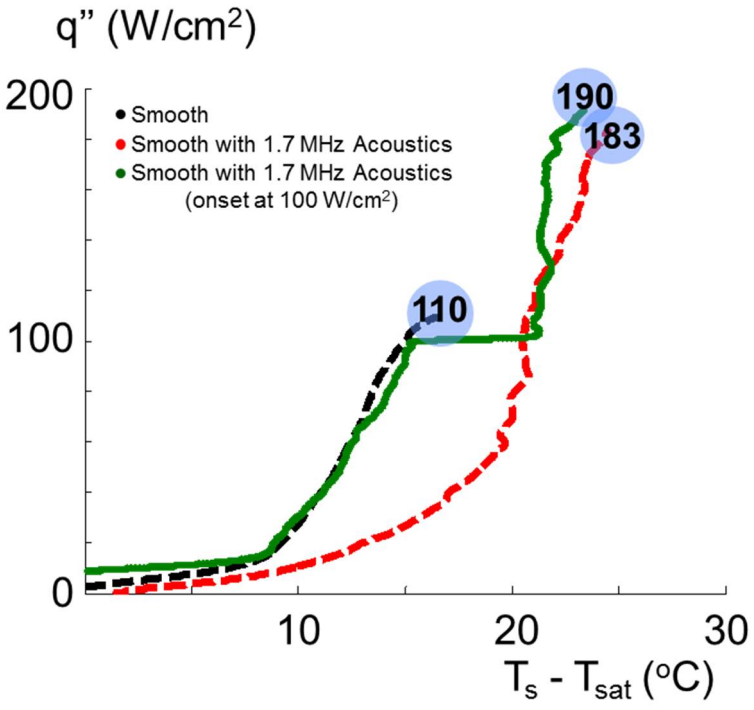


**Figure 5.9.** Boiling curves for the plain heater in the ***absence*** and ***presence*** of ultrasound actuation, along with the boiling curve using ***delayed actuation onset***.

actuation (corresponding to lower heat transfer coefficients). However, when the onset of the acoustic actuation is withheld until the heater reaches 100 W/cm$^2$ along the base boiling curve (and below the base CHF), the heat transfer transitions to the acoustically enhanced curve, and can reach the higher acoustically actuated CHF limit, as shown in the third green curve in Figure 5.9. Therefore, the acoustic enhancement can be staged to retain the lower surface superheat of the base boiling curve at lower heat fluxes, but enable the acoustically-enhanced higher CHF. The transition upon actuation onset is nearly instantaneous (within less than 1 sec) and is visible as the horizontal section in the green boiling curve.

Based on the electric power dissipated by the actuator (12.7 W), the extension of the critical heat flux from 110 W/cm$^2$ to 183 W/cm$^2$ on a smooth 2 cm$^2$ boiling surface represents a coefficient of performance ($\Delta q$ / $P_{act}$) of 11.5.

### 5.4 Effects of Short Wavelength Actuation at Discrete Boiling Nucleation Sites

While short wavelength actuation results in significant suppression of vaporization on the heater's surface, the actuation onset is accompanied by a momentary increase in vapor mass above the surface, and during quasi-steady operation there are occasional, brief bursts of intense vaporization characterized by formation and advection of large vapor masses. Since these effects cannot be directly measured using the thermocouple sensors embedded below the surface, they are measured using an azimuthal array of three miniature (250 μm diameter) thermocouple sensors (defined as TC-1, -2, and -3) about the centerline of the heater (cf. §3.1). These have the advantage of forming discrete nucleation sites directly at the thermocouple location, where vapor formation preferentially occurs and may be readily visualized. The acoustic transducer is mounted at an incidence angle of $\phi = 60^{o}$ and a distance of 50 mm from the surface, and the centerline of the acoustic beam coincides with the circle defined by the three thermocouple sensors. The acoustic beam is consecutively moved to six azimuthal positions around this circle (Figure 5.10): positions 1, 3, and 5 coincide with the thermocouple sensors and positions 2, 4, and 6 are equally spaced between the sensors so that the effect of the actuation is measured when the beam is directed at the sensor and diametrically opposed to it. In the present experiments, the acoustic actuation is turned on for a continuous period of 60 seconds, and time traces of the temperatures measured by each thermocouple sensor are sampled starting 40 seconds prior to actuation onset until 20 seconds after the end of the actuation (120 sec total). The surface boiling at each of the six actuator positions is imaged high-speed video (2,000 fps). The thermocouple data, actuation onset, and high-speed video sequences are locked in time relative to one another through a triggering signal.

Figures 5.10a-f show time traces of instantaneous temperature measured by each of the three thermocouple sensors before, during, and following actuation (at 100 W/cm$^2$) at each of the six azimuthal positions of the acoustic beam. Each figure includes traces of

each of the three sensors. The traces in the left column (Figures 5.10a-c at positions 1, 3, and 5, respectively) correspond to incidence at one of the thermocouple sensors, while the right column (Figures 5.10d-f at positions 4, 6, and 2, respectively) correspond to incidence between two sensors; in all cases, the boiling over the entire surface is affected by the presence of actuation, with variations dependent on the incidence of the acoustic beam's centerline. The time traces in Figure 5.10 clearly exhibit the transitory changes in the surface superheat that are induced by the actuation. As shown in Figures 5.10a-c, the measured increase in the local surface superheat during actuation is nominally lower at the sensors that coincides with the centerline of the acoustic beam (1–2 $^{o}$C) compared to each of the adjacent sensors (3–4 $^{o}$C). However, the magnitude of the temperatures measured by each of the sensors when the actuator's centerline is placed between the sensors is nearly uniform (Figures 5.13d-f). The data in Figure 5.10 show that that the nominal magnitude of the step changes in surface superheat (3–4 $^{o}$C) is *lower* than the corresponding change assessed based on the global measurements (7–8 $^{o}$C) in Figure 5.10. This is attributed to the fact that embedding the thermocouple sensors in the heater surface forms clear (or "preferred") nucleation sites where vapor formation on small scales is not completely extinguished in the presence of actuation. The data in Figures 5.10a-c indicate that this additional vapor formation effectively cools the surface and decreases the local temperature rise (by about 4 $^{o}$C). Such vapor formation is also present in the high-speed video images in Figure 5.5 that are taken in the absence of the surface-embedded sensors. In these images, nearly complete vapor suppression occurs on the smooth segments of the heater, but a few remaining "preferred" nucleation sites at the edge of the heater still continue to produce vapor bubbles.

Another important feature of the temperature traces on the boiling surface in Figure 5.10 is the clear difference between the magnitude of the fluctuations in the absence and

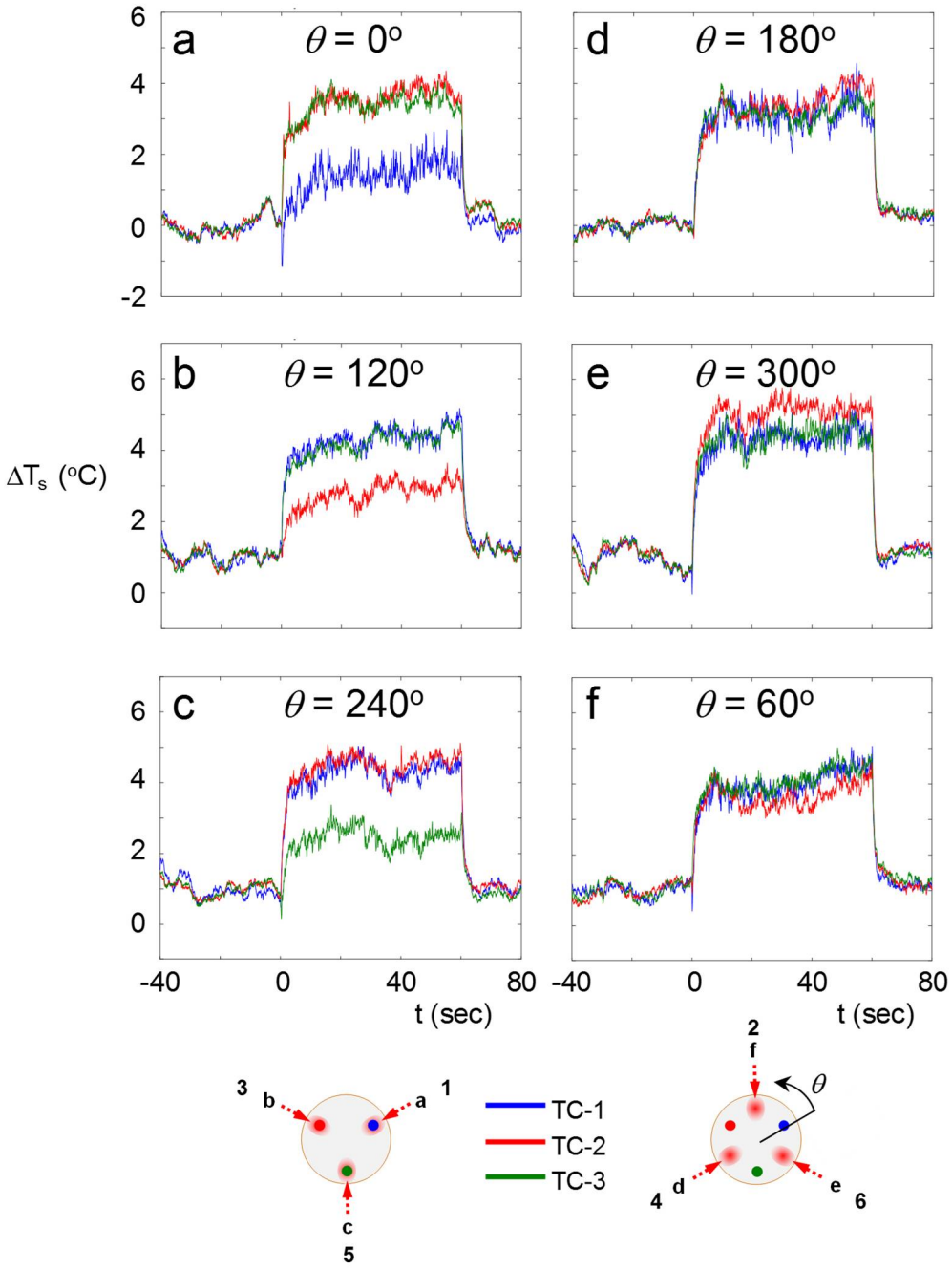


**Figure 5.10.** Time traces of surface superheat $\Delta T_s$ measured by the three surface thermocouple sensors TC-**1**, **2**, and **3** during onset and termination of actuation for six azimuthal position of the acoustic beam on the heater surface. The positions of the acoustic beam are shown schematically by a red spot on the right. At each set of three odd- and even-number equally-spaced azimuthal positions, the acoustic beam is incident upon or between TC-**1**, **2**, and **3**, respectively.

presence of the acoustic actuation. These traces clearly show that the amplitude of the fluctuation increases significantly as a result of the actuation. This is illustrated in Figure 5.11 that shows traces at position 5 using an expanded time scale. It is noteworthy that when the incident acoustic beam is directed at a specific sensor during the onset of actuation, the local temperature experiences a momentary drop of nearly 1 $^{o}$C below the saturation temperature indicating that the interaction of the acoustic wave with the natural nucleation caused by the presence of the sensor promotes enhanced vapor formation that results in a local decrease in the temperature. However, as the interaction of the acoustic beam with the boiling process continues, the temperature traces show similar sporadic fluctuations that are indicative of interactions with vapor formation at the other sensors. These vapor formations appear to occur at varying frequency averaging approximately 1-3 Hz, and are discussed further in Figure 5.12.

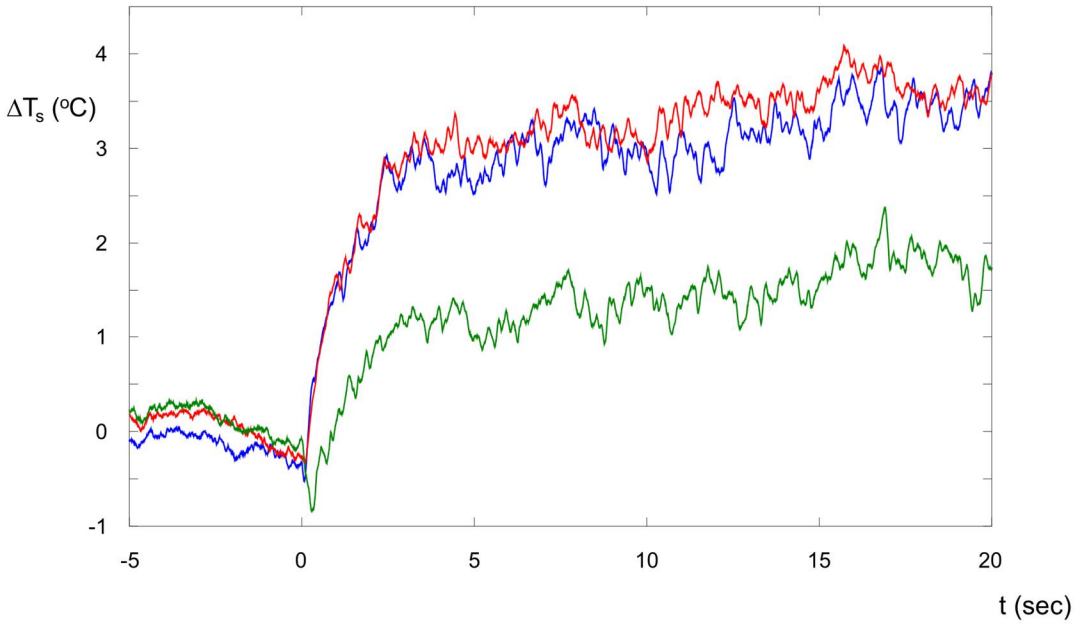


**Figure 5.11.** Time trace of surface superheat $\Delta T_s$ measured by thermocouple sensors TC-**1**, **2**, and **3** during the onset of actuation when the centerline of the acoustic beam is incident on TC- **3** at $\phi = 60^{o}$. The effects on TC-**1** and **2** are symmetric.

As noted in Figures 5.10a-c, the temperature trace measured by the thermocouple sensors when the acoustic beam is directed at each of them shows a brief local minimum at the onset of the actuation, and the ensuing quasi-steady temperature is lower than the corresponding temperatures measured by the adjacent sensors. The lower temperatures result from interactions between the acoustic beam and the boiling process at the sensor, and is evident from a sequence of high-speed video images captured when the beam is directed at one of the sensors (TC-3). Figures 5.12a-f (50 msec apart) follow the onset of the actuation, and unlike the sequence in Figure 5.6, there is a clear brief increase in vapor mass in Figure 5.12b compared to the unactuated boiling (Figure 5.12a) that is accompanied by the transitory minimum in the temperature traces of Figures 5.10c. This vapor mass grows and is ultimately advected away from the surface in Figure 5.12e. Following the advection of the initial vapor mass, the boiling reaches the quasi-steady state as shown in Figure 5.12g and Figure 5.6f. A second sequence of images (25 msec apart) in Figures 5.12g-l show the transitory formation of a secondary vapor mass over sensor TC-3. Video imaging shows that this secondary evaporation recurs regularly over the sensor and appears to be triggered by periodic changes in the local pressure owing to the interaction near the centerline of the acoustic beam. Therefore, the nominally time-averaged temperature over the sensor (cf. Figures 5.10a-c) is lower than the temperatures measured by the adjacent sensors. While the left and right sensors (marked by blue and red dots in Figure 5.12) also act as vapor nucleation sites the local acoustic intensity is sufficiently lower to prevent the time-periodic of a larger vapor mass. Another noteworthy feature of the secondary vapor mass in Figures 5.12i-k is the formation of subcooled liquid protrusion from above (at the top surface of the vapor mass, initially forming between Figure 5.12h-i). This protrusion is induced by the acoustic actuation and leads to accelerated condensation as discussed in more detail in §6.2.

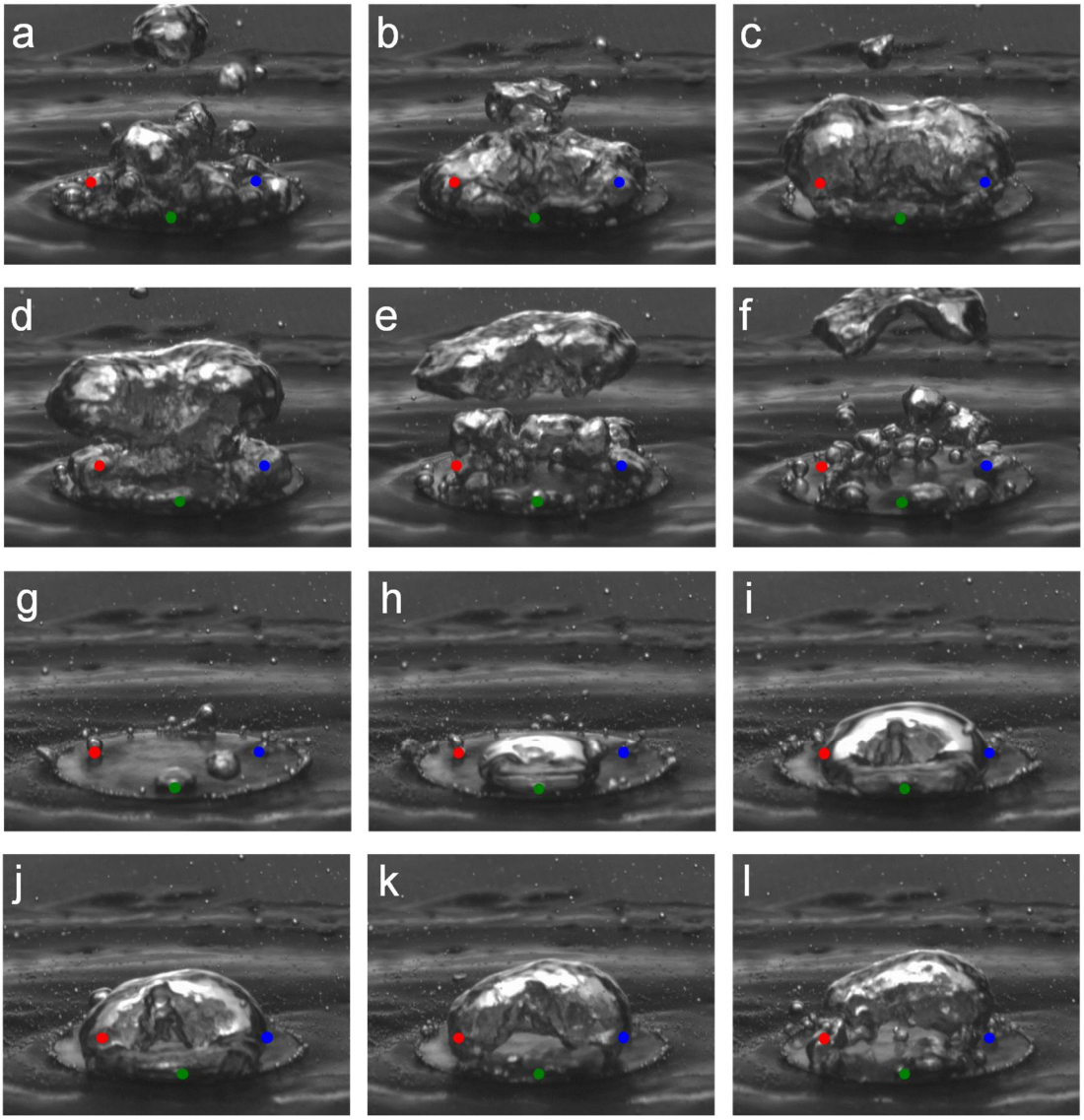


**Figure 5.12.** Vapor formation during the onset of acoustic actuation when the acoustic beam is directed ($\phi = 60^{o}$) at the thermocouple sensor TC-3 (TC-1, -2, and -3 are marked by blue, red, and green dots, respectively). Images a-f (50 msec apart) show the formation of a "starting" vapor mass, and images g-l are (25 msec apart) show transitory formation of vapor mass over TC-3 after the boiling reaches a quasi-steady state in the presence of the acoustic actuation.

The spectral content of the temperature fluctuations corresponding to the six positions of Figures 5.10 are shown in power spectra of each surface sensor (TC-1, -2, and -3) in presence and absence of actuation (Figure 5.13a-f). These power spectra are generated from segments of time traces before and during actuation and are each averaged over 120 realizations (the bandwidth is limited to 15 Hz by the senor response). As expected, the temperature spectra of the three sensors in the absence of actuation are nearly identical (black lines). The increased temperature fluctuations observed in the time traces in Figure 5.10 in the presence of actuation result in increased power in the spectral components of the spectra in Figure 5.13 that are especially pronounced when the acoustic beam is directed at a specific sensor (Figures 5.13a-c). As discussed above, this increase appears to be associated with periodic formation of vapor at the nucleation sites formed by the sensors. Although the spectral content of the temperature traces increases significantly in the presence of the actuation (and more so when the acoustic beam is directed at a specific sensor), these spectra do not exhibit a clear spectral peak that is associated with the time-periodic formation of the vapor mass in Figure 5.12. It is noted that the sensors spectra also exhibit higher power when the acoustic beam is aimed azimuthally between the sensors (Figure 5.13d-f). Specifically, when the beam is radially across from a given sensor, its spectral contents is somewhat higher than the other sensors ostensibly owing to the modulation by the formation of the secondary vapor mass.

The spatial dependence of surface superheat on the acoustic beam incidence discussed in connection with Figure 5.10 is compared with the effects of the actuation when the direction of the acoustic beam is aligned with its direction at the same six azimuthal positions ($\phi = 60^o$ and the transducer is 50 mm away from the surface) and its centerline intersects the center of the heater. For this comparison, the sensors' time-dependent temperature measured by each sensor at a given beam attitude in Figure 5.10 is

represented by the time-averaged superheat $\Delta T$ determined by the difference between the time-averaged temperatures in the absence and presence of actuations. This calculation is repeated for each of the six beam attitudes, and the normalized time-averaged superheat temperatures are plotted in Figures 5.14a and b in terms of the sensors' positions *relative to the centerline of the acoustic beam*, i.e., left (L), center (C), and right (R) (marked by L, C, and R, respectively) as viewed from the acoustic transducer (the time-averaged superheat $\Delta T$ at each sensor is normalized by the averaged superheats $\overline{\Delta T}$ of the two adjacent sensors). The color of the markers of sensor position correspond to TC-1 (blue), 2 (red), and 3 (green). As noted above, the directions of the acoustic beams are aligned with the directions in Figure 5.10, and the data in Figure 5.14a correspond to incidence

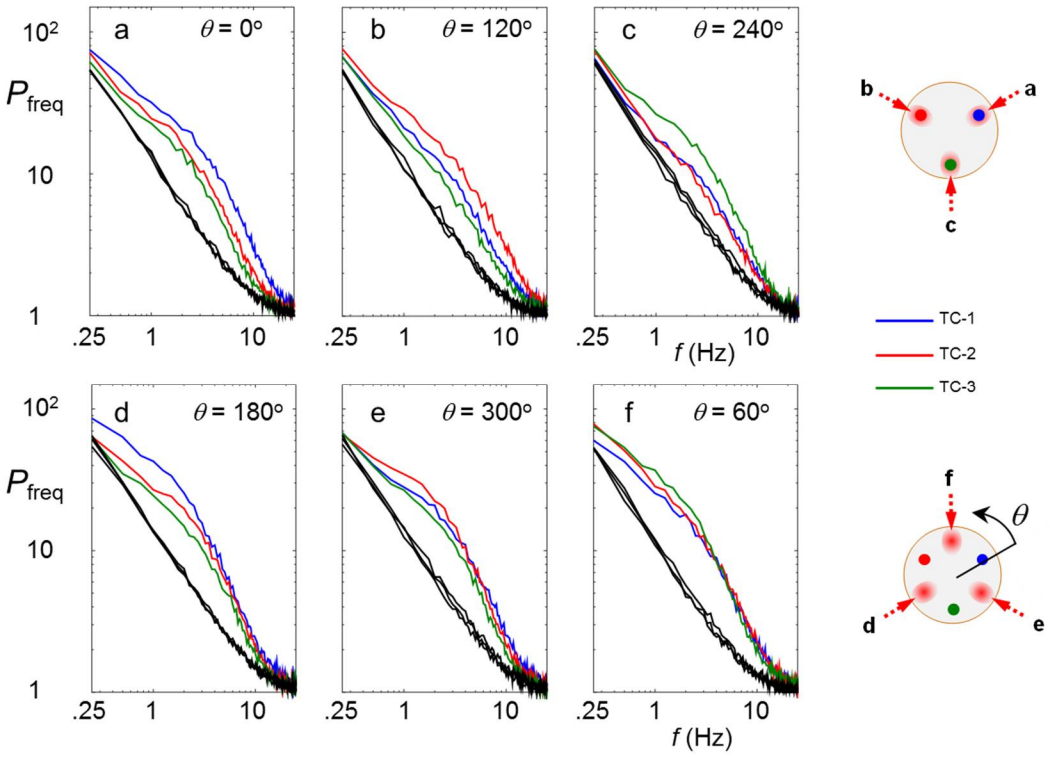


**Figure 5.13.** Power spectra of surface superheat $\Delta T_s$ measured by the surface thermocouple sensors TC-**1**, **2**, and **3** during the absence and presence of actuation (at six azimuthal positions of the acoustic beam on the heater surface, marked schematically by the red circular spot in each inset). Spectra in the absence of acoustic actuation for each thermocouple sensor are shown in black.

along the circle that includes the sensors, while in Figure 5.14b the centerline of the acoustic beam coincides with the center of the heater. Therefore, each of Figures 5.14a and b contains two data sets: in the first data set (connecting lines in red), the azimuthal positions of the actuator are $\theta = 0^o$, $120^o$, and $240^o$ (also the azimuthal positions of the sensors), and in the second data set (connecting lines in black) the azimuthal positions of the actuator incidence are $\theta = 60^o$, $180^o$, and $300^o$ (i.e., between sensors).

As discussed in connection with Figure 5.10, when the centerline of the acoustic beam is pointed directly at one of the sensors (Figure 5.14a, red lines), the increase in surface superheat is smaller, and therefore the normalized superheat at the center sensor (as viewed from the acoustic transducer) has a minimum compared to the L and R sensors. When the centerline of the acoustic beam is aimed between thermocouples (Figure 5.14a,

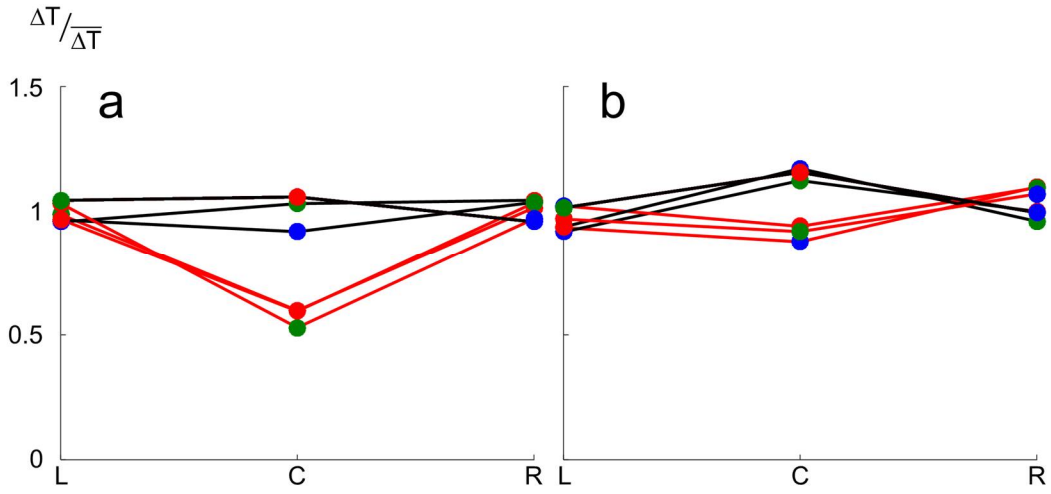


**Figure 5.14.** Distributions of normalized increase in surface temperature $\Delta T/\overline{\Delta T}$ at the left (L) center (C) and right (R) sensors relative to the centerline of the acoustic beam as viewed from the acoustic transducer, where the specific sensors (as in Figure 5.12) are marked TC-**1**, **2**, and **3**: a) The acoustic beam centerline incident along the circle that includes the sensors, and b) The acoustic beam centerline coincides with the center of the heater. Each of Figures 5.16a and b contains two data sets: in the first data set (connecting red lines), the azimuthal positions of the actuator are $\theta = 0^o$, $120^o$, and $240^o$ (also the azimuthal positions of the sensors), and in the second data set (connecting black lines) the azimuthal positions of the actuator are $\theta = 60^o$, $180^o$, and $300^o$ (i.e., between sensors).

black lines), the distribution of normalized superheat is almost flat. When the acoustic beam is aimed at the center of the heater (Figure 5.14b), the spatial dependence of surface superheat changes. For positions that are azimuthally aligned with a sensor on the near side of the heater (Figure 5.14b, red lines), the reduction in normalized surface superheat in Figure 5.14a is weaker, i.e., the average increase in surface superheat at the C sensor is nearly 90% of the L and R sensors as opposed to 55% when the acoustic beam is incident on each of the sensors. When the azimuthal position of the beam is between sensors (Figure 5.14b, black lines), there is a small average increase in effect, to 115% of the normalized superheat at the C sensors relative to the R and L sensors. In this configuration, the distance between the sensors and the incidence of the centerline of the acoustic beam does not change with the beam's azimuthal position, and therefore, these cases illustrate the difference between sensors that are ahead or behind the point of incidence. While the former C sensors measure a slightly lower increase (90%) in surface superheat than the R and L sensors (due to the induced flow caused by the motion of vapor masses affected by the acoustic radiation pressure entraining subcooled liquid to that thermocouple), the former C sensors measure slightly higher increase (115%) in surface superheat than the R and L sensors. (due to the induced flow of warmer liquid across the surface of the heater towards the C sensors). These data show that the effects of direct incidence on a nucleation site (Figure 5.14a, red lines) on spatial variation of surface superheat are more pronounced, but the induced flow caused by the motion of vapor across the heater by radiation pressure is also capable of creating spatial temperature variations on the surface when carefully measured (Figure 5.14b), leading to different $\Delta T_s$ between thermocouples ahead of or behind the point of incidence.

The interaction of the acoustic beam with the vapor at the nucleation sites formed by the thermocouple sensors is investigated when the centerline of the acoustic beam is coincident with the centerline of the heater in a nominally axisymmetric configuration.

Because of the nominal axisymmetric actuation, it is anticipated that the interaction with the sporadic formation of vapor at the sensor sites is stronger because of potential synchronization between the nucleation sites. Figure 5.15 shows the temperature time traces measured simultaneously by the three sensors during the onset of the actuation (using two expanded time scales compared to Figure 5.11). These traces show that the temperature fluctuations are nearly synchronized and corresponding peaks are marked (as i, ii, iii, and iv in Figure 5.15b). These traces are compared with high-speed video images (25 msec apart) in Figure 5.16 that are acquired simultaneously to explore the dynamics of vapor formation (the sensor positions are marked on the images). The video sequence shows multiple vaporization bursts which correspond to simultaneous local minima in the surface superheat in Figure 5.15a measured by the three sensors. The onset of actuation leads to a momentary decrease in the measured superheat marked by "i" in Figure 5.15a and is about 250 msec long (the decrease is nearly 1 $^{o}$C at TC-1). The corresponding video images (Figure 5.16a-d) show large vapor formation that is emanating from the central, smooth section of the heater and appears to be driven by amalgamation of the vapor that forms at the three sensors. During the transition of the heater from its initial temperature to the steady-state higher temperature, several other large vapor formations can be observed, along with temporary reductions in surface superheat. The video image sequence in Figure 5.16e-h corresponds to the reduction in superheat marked in Figure 5.15a by "ii," with the initial image showing the reduced vapor on the surface prior to the transient vapor production. After this temporary dip, the temperature continues to rise, followed by a third vaporization event marked in Figure 5.15a by "iii," corresponding to the images of Figure 5.16i-l. Note that in Figure 5.16i, the initial state now has more vapor around the edges of the heater than Figure 5.16e, as the vapor production is increasing as the surface superheat continues to rise; the

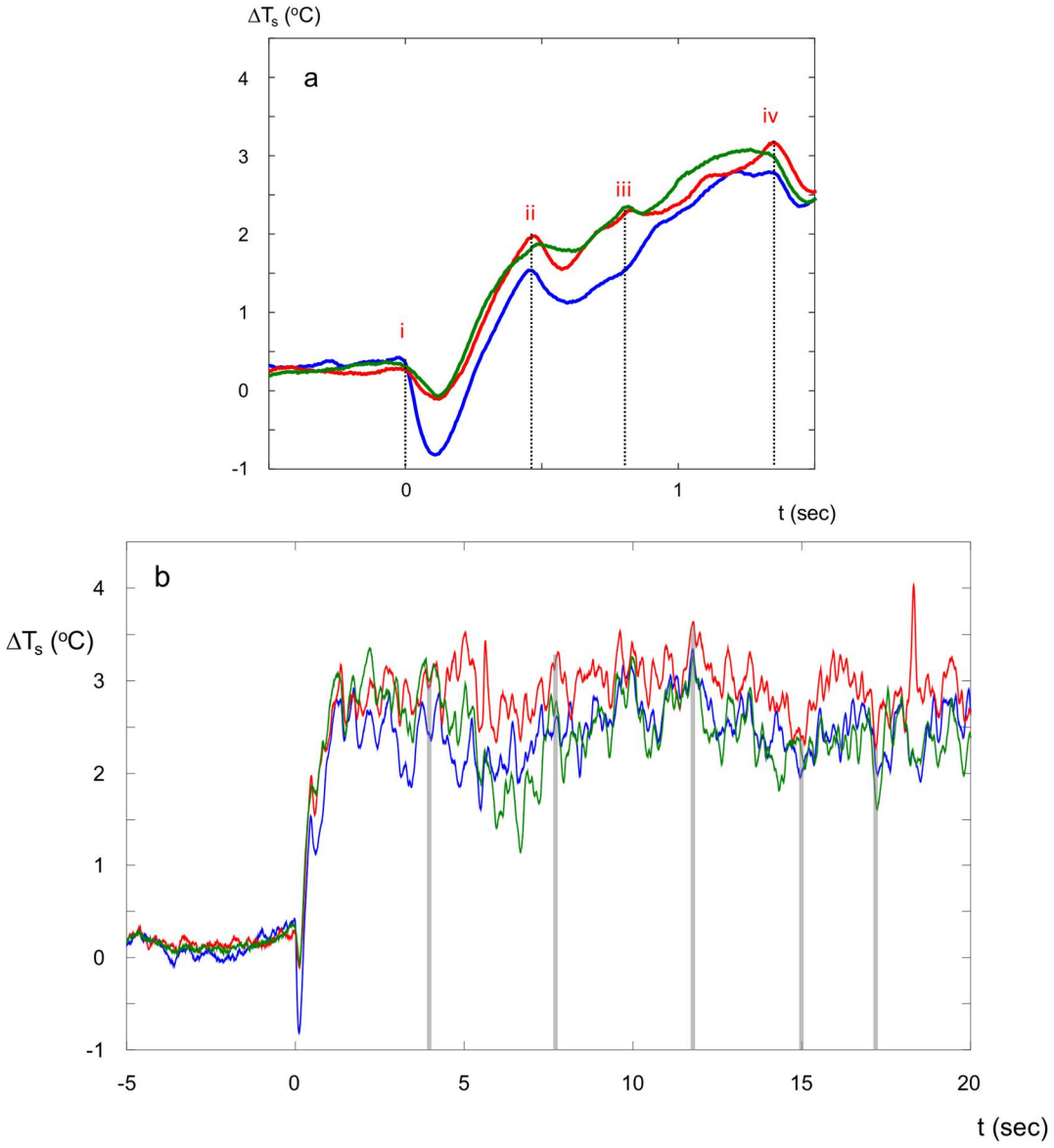


**Figure 5.15.** Top: Time trace of surface superheat $\Delta T_s$ measured by thermocouple sensors TC-**1**, **2**, and **3** during the onset of actuation when the centerline of the acoustic beam is incident at the center of the heater at $\phi = 90^o$ (directly normal to the surface). Corresponding local temperature maxima are marked. Bottom: Equivalent time trace over 25 seconds showing increase in temperature fluctuations. Points of high correlation between all three thermocouples are marked.

transitory vapor production imaged in Figure 5.16k appears biased towards the left side of the heater, and the transitory response of the thermocouples shows the red and green temperatures respond while the blue thermocouple (to the back right side of the heater, obscured by the vapor in front of it) barely sees a reduction in superheat. The final transient vapor production marked by "iv" in Figure 5.15a corresponds to the images in Figure 5.16m-p, with Figure 5.16m showing more vaporization than 5.16i or 5.16e, as the vapor production has further recovered in response to the further increase in surface superheat (although vapor production remains below the unactuated condition of the heater shown in Figure 5.16a). The vaporization event "iv," which creates the large vapor mass in Figure 5.16o, corresponds to a temporary drop in surface superheat of over 0.5 $^{o}$C and affects all three thermocouples and likely the entirety of the heater surface. These

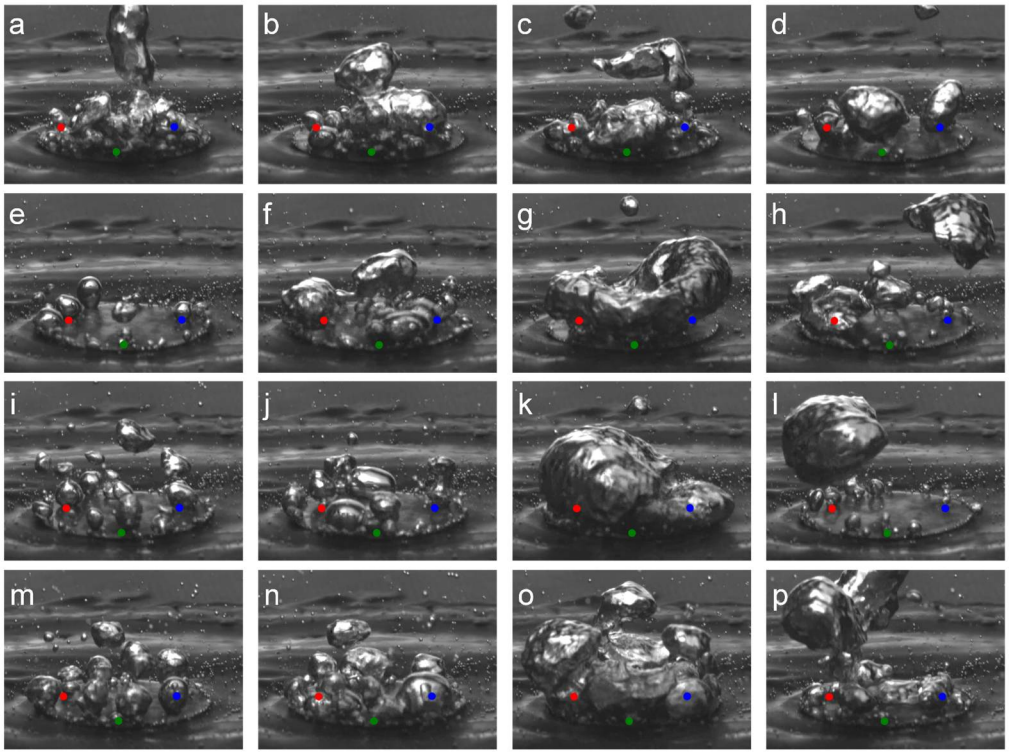


**Figure 5.16.** Sequences of vapor formation images (time increment is 25 msec) during the onset of acoustic actuation (the acoustic beam is incident at the center of the heater, $\phi = 90^{o}$) that are synchronized with the markers on the time traces in Figure 5.18: "i" a-d, "ii" e-h, iii i-l, and iv m-p. The sensors are marked by dots (TC-**1**, **2**, and **3)**.

transient vaporization events continue after the new steady-state temperature is reached, with increased fluctuations in the temperature traces over a longer period (Figure 5.15b) corresponding to future transient vaporization events. Many of the fluctuations occur at only one or two thermocouples; however, other vaporization events (as well as vapor production deficits) clearly affect the entirety of the heater surface. Several local peak temperatures and minimum temperatures correlated across all three thermocouples are marked by grey lines in Figure 5.15b, which also shows the significant increase in temperature fluctuations after actuation onset compared to prior to actuation.

The tendency of preferred nucleation sites to remain cooler in the presence of acoustic actuation is also present when the actuation is applied to textured boiling surfaces as discussed in §5.5.

## 5.5 The Effects of Ultrasonic Actuation on a Textured Surface

The effect of ultrasonic actuation on boiling in the presence of surface textured with microchannels (400 μm, cf. Figure 5.1) is shown using boiling curves in Figure 5.17 (similar to the boiling curves in Figure 5.4) that also include for reference the corresponding curves for the smooth surface. These data show that while the presence of open microchannels results in a significant reduction in surface superheat, acoustic actuation having a characteristic wavelength that is slightly larger than the channel width (0.9 mm, determined by the actuator design prior to choosing channel width) can effectively reduce the surface superheat even further. This reduction implies a significant increase in bubble formation and detachment rates that are accompanied by entrainment of sub-cooled fluid through the channels. It is noteworthy that this reduction in surface superheat in the presence of actuation is opposite to the effect of actuation on the plain surface which leads to an increase in surface superheat. Furthermore, the actuation leads

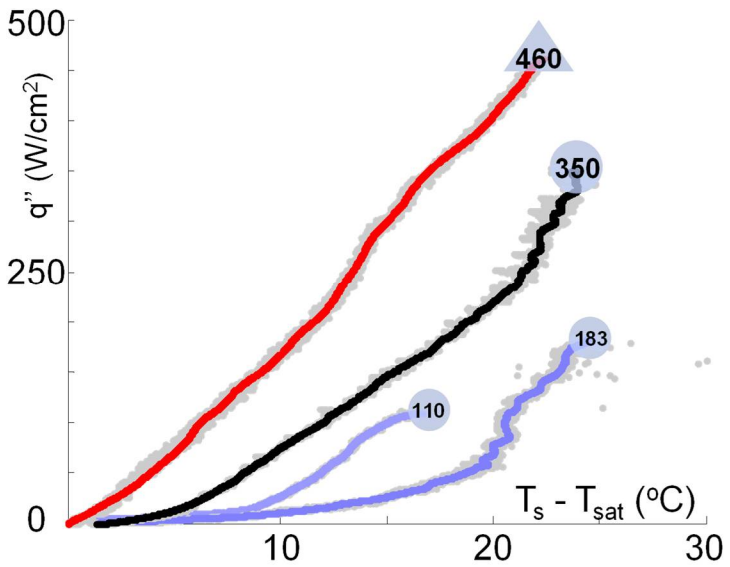


**Figure 5.17.** As in Figure 5.4, boiling curves with 400 μm channels in the ***absence*** and ***presence*** of actuation. The corresponding curves for the plain surface in the *absence* and *presence* of actuation are also shown for reference (higher CHF is attained with actuation).

to a significant increase (exceeding 30%) in the CHF of the textured surface. The instantaneous data, plotted in grey behind each of four boiling curves in Figure 5.17, demonstrate the changes in instantaneous fluctuations due to acoustic enhancement and microchannel enhancements. The smooth surface shows the lowest amount of fluctuations, with increased fluctuations shown when adding acoustic actuation (this effect was heavily investigated in §5.4). The microchannel surface, shown in black in Figure 5.17, has significantly more fluctuations than the smooth surface, especially at high heat fluxes (> 250 W/cm$^2$). When acoustic actuation is used in conjunction with the microchannel surface, the instantaneous fluctuations remain relatively invariant along the boiling curve: the instantaneous fluctuations *increase* at low power levels (as marked by the instantaneous (grey) data behind the curves in the presence (red) and absence (black) of acoustic actuation ed for the microchannel at 100 W/cm$^2$), similar to the the smooth surface, the instantaneous temperature fluctuations *decrease* at higher heat fluxes in the presence of acoustic actuation. It is conjectured that the microchannel surface undergoes intermittent dryout at high heat fluxes prior to reaching CHF; as acoustic actuation interrupts this process (reducing the fluctuations in instantaneous surface superheat at high power levels), it helps increase the CHF.

The variation of surface superheat with heat flux in the presence of acoustic actuation is shown in Figure 5.18 for the textured and plain surfaces. As noted above, the microchannel grid enables regular formation and detachment of the vapor bubbles along the vertical intersection edges of the microchannels and concurrent entrainment of subcooled liquid along the microchannels towards these intersections. This flow reduces the drag on the rising vapor bubbles and simultaneously increases the heat flux capacity of the surface. Since the nucleation sites are at the bottom of the microchannels, the suppression in the rate of evaporation by the actuation is muted and along with the entrainment of subcooled liquid towards the microchannels by the vapor forced across the

surface by the acoustic actuation (cf. Figure 5.14b and the discussion of entrained cool fluid to nucleation sites by the motion of vapor away from the actuation), contribute to the significant *reduction* in surface superheat of the textured surface compared to the *increase* in surface superheat on the plain surface. This effect indicates that perhaps the effects of the acoustic actuation on the boiling in the presence of surface texture is secondary and the actuation primarily affects the condensation (cf. Chapter 7) and liquid flow patterns near the boiling surface, indirectly increasing boiling efficiency. The exact effect of acoustic actuation on the nucleation sites within the channels remains undetermined, as they are not capturable by high-speed photography, but the implication from the boiling curve and the reduction in surface superheat is that vaporization efficiency has been increased. Unlike the heat transfer from the smooth surface in the presence of acoustic actuation, the surface superheat always decreases in the presence of acoustic actuation for a given heat flux; equivalently, the heat transfer coefficient always increases. Therefore, there would be no advantage to delayed actuation onset as was demonstrated with the smooth surface (cf. Figure 5.9) for the microchannel surface.

The boiling process over the textured surface is captured using high-speed video images in Figure 5.19 at several power levels (100, 150, 200, 250, and 300 W/cm$^2$) in the absence (5.19a-e) and presence (5.19f-j) of acoustic actuation. Similar to the effect of the

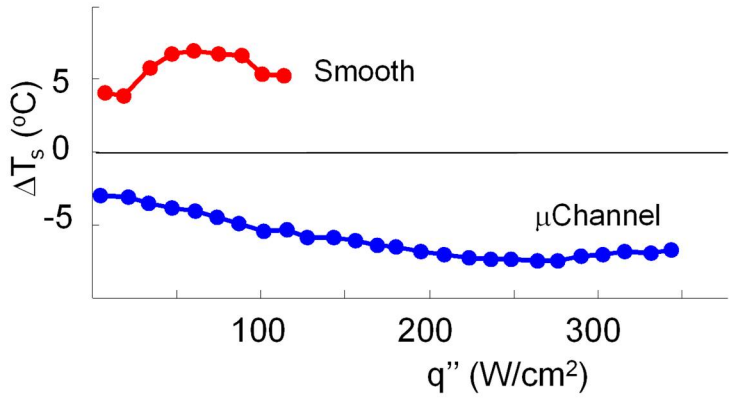


**Figure 5.18.** The change in surface superheat versus surface heat flux for the baseline surface and the surface with 400 μm microchannels.

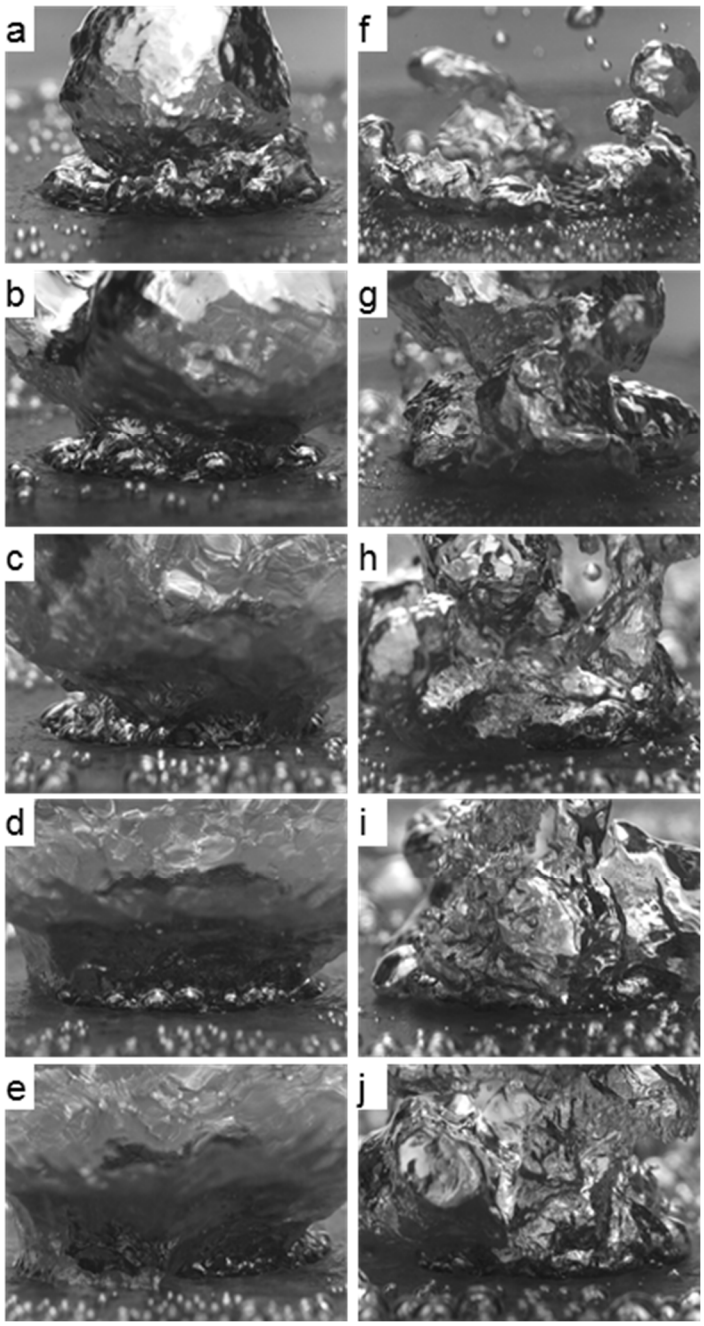


**Figure 5.19.** Images from high-speed videos of vapor formation along the heat transfer curves of the microchannel surface (Figure 5.19) at 100 (a, f), 150 (b, g), 200 (c, h), 250 (d, i), and 300 (e, j) W/cm$^2$ in the ***absence (left column, a-e)*** and ***presence (right column, f-j) of short wavelength acoustic actuation***.

actuation on vapor formation over the plain heater (cf., Figure 5.5), the actuation breaks up the large vapor bubbles that form above the heater's surface into smaller vapor bubbles. As noted above, the apparent reduction in vapor mass may be associated with enhanced condensation in the liquid pool as a result of the breakup and the increased vapor-liquid interfaces rather than alteration of the boiling process. It is remarkable that at low power levels the actuation results in a visibly clear section of the upper surface area of the microchannels (e.g., compare Figures 5.19a and f). The differences between the vapor structure in the absence and presence of actuation are the plain and textured surfaces are apparent even up to 300 W/cm$^2$ (Figure 5.19e and j).

Due to the large parameter space in application of boiling (ambient pressure, working fluid, surface material, etc.), comparison of the performance between different experiments is difficult. Nevertheless, Figure 5.20 shows a comparison between the present measurements using surface microchannels in the absence and presence of acoustic actuation and prior work in which boiling heat transfer was enhanced under

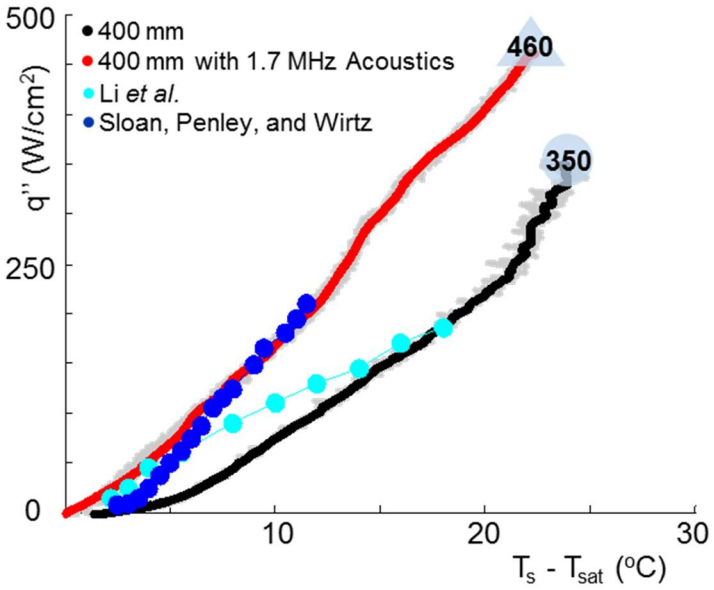


**Figure 5.20.** Boiling curves with 400 μm channels in the ***absence*** and ***presence*** of actuation. Data from Li *et al.* (2007) and Sloan, Penley, and Wirtz (2009) are shown for comparison.

similar experimental conditions (namely, using water under atmospheric pressure and similar heater surface material). Specifically, the present data are compared with the measurements that utilized textured surfaces with smaller-scale features such as copper nano-rods (Li et al., 2007), and laminated mesh screens (Sloan et al., 2009). It is clear that even in the absence of acoustic actuation, the relatively simple microchannels of the present investigations yield significant increases in CHF compared to the other surfaces, although the surface superheat is not as low. In the presence of acoustic actuation, the surface superheat is lowered and is comparable to the performance of laminated screens (Sloan et al., 2009), but with significantly higher CHF.

Based on the electric power dissipated by the actuator (12.7 W), the extension of the critical heat flux from 350 W/cm$^2$ to 460 W/cm$^2$ on a 2 cm$^2$ boiling surface with open microchannels represents a coefficient of performance ($\Delta q$ / $P_{act}$) of 17.3.

# CHAPTER VI

# CONDENSATION ENHANCEMENT
# USING LONG-WAVELENGTH ACOUSTIC ACTUATION

The use of long wavelength acoustic actuation to enhance condensation was investigated primarily by injecting vapor from a reservoir through an orifice in a pool of subcooled liquid at atmospheric pressure. The effects of the actuation was investigated at several variants of the nominal conditions (225 W vapor power dissipation, 5.3 mm diameter injection orifice, and 25$^{o}$ subcooled liquid) and are described in §6.1. Of particular interest are the effects of the actuation on the thermal boundary layer at the vapor-liquid interface which were investigated using Schlieren imaging and are described in §6.2. In addition to atmospheric ambient pressure, the condensation in the subcooled bath was also investigated at reduced pressure (15 kPa, §6.3). Finally, the effects of the actuation on condensation above a boiling surface submerged in the subcooled liquid pool was investigated using the submerged heater (cf. §3.1) and is described in §6.4.

## 6.1 Condensation Enhancement of Vapor at Atmospheric Pressure

The injection of vapor through an orifice into a subcooled liquid pool is more complex than corresponding injection of air because condensation at the liquid/vapor interface affects the flow through the orifice. In fact, the vapor flow into a subcooled liquid pool was categorized by de With *et al.* (2007) into separate regimes described as chugging, bubbling, jet, and supersonic jet that are characterized by the mass flow rate, nozzle diameter, and the degree of liquid subcooling. In the present setup, the vapor mass flow rate is selected to be in the bubbling regime by proper selection of the heater power, the (interchangeable) orifice diameter, and the temperature setting of the subcooled liquid

(cf. Section 3.2). In this regime, the vapor flow forms discrete bubbles that become detached time-periodically (10-30 Hz) and advected by buoyancy. The actuation schemes, as used in Chapters 6-8, did not change the flow regime from bubbling flow.

Although the vapor mass flow rate could not be measured directly, it was estimated from the average size of the bubbles and their frequency. For reference, at a heater power of 360 W and orifice diameter $d_o$ = 5.3 mm the vapor mass flow rate was estimated to be $4.03 \cdot 10^{-5}$ kg/s based on the mean bubble size found using image processing techniques (see §3.2) and ejection frequency, which corresponded to a visualized heat flow rate (based on enthalpy of vaporization) of 90 W. It should be noted however, that the actual vapor mass flow rate was significantly higher, due to condensation during bubble formation and growth at the orifice. The data of Cho and Lee (1991) for vapor bubble formation at an orifice indicate total condensation rate of 60% during the bubble growth at $T_{subcool}$ = 25 $^{o}$C; i.e., a visualized mass flow rate based on average bubble size at liftoff of only 40% of the total mass flow rate. Applied to the current visualized mass flow rate, this yields an estimated heat dissipation of 225 W through the orifice into the top tank, demonstrating the importance of condensation during vapor bubble growth. The losses to the ambient may be significant (135 W) due to the experimental design which allowed for ease of visualization at the expense of thermal losses.

High-speed video images of vapor bubbles exiting at a nozzle $d_o$ = 5.3 mm into subcooled water at $T_{subcool}$ = 25 $^{o}$C are shown in Figures 6.1a-e and f-j in the absence and presence of acoustic actuation, respectively. The imaged area is chosen such that bubbles completely condense within the field of view. The long wavelength [O(1 kHz)] actuation is applied at peak-to-peak amplitude of 5 kPa. In the absence of actuation, bubbles form with a regular frequency as smooth, spherical bubbles (Figure 6.1a-b) and are ejected from the nozzle, with the pinch-off process leading to a liquid spear (Figure 6.1c) which drives the rapid condensation of the vapor mass after separation (Figure 6.1d-e). This

process repeats with a typical frequency of 20 Hz. Note that sometimes the pinch-off process can also drive the lower vapor interface towards the vapor reservoir (Figure 6.1d-e, lower bubble), although it typically recovers prior to entering the orifice. The presence of actuation (Figures 6.1f-j) leads to a drastic reduction in the size of the formed bubbles. As the bubble grows, the surface Faraday waves are clearly visible in Figure 6.1f-g. The collapse of the bubble after separation from the nozzle is so sudden it is not captured on this sequence, hence the lack of bubble visible in Figure 6.1h. Note that the frequency of bubble ejection is roughly maintained at 20 Hz, and the overall area of vapor visible has been significantly reduced; quantifying this reduction will be accomplished in the following figures. These images show that the actuation led to the

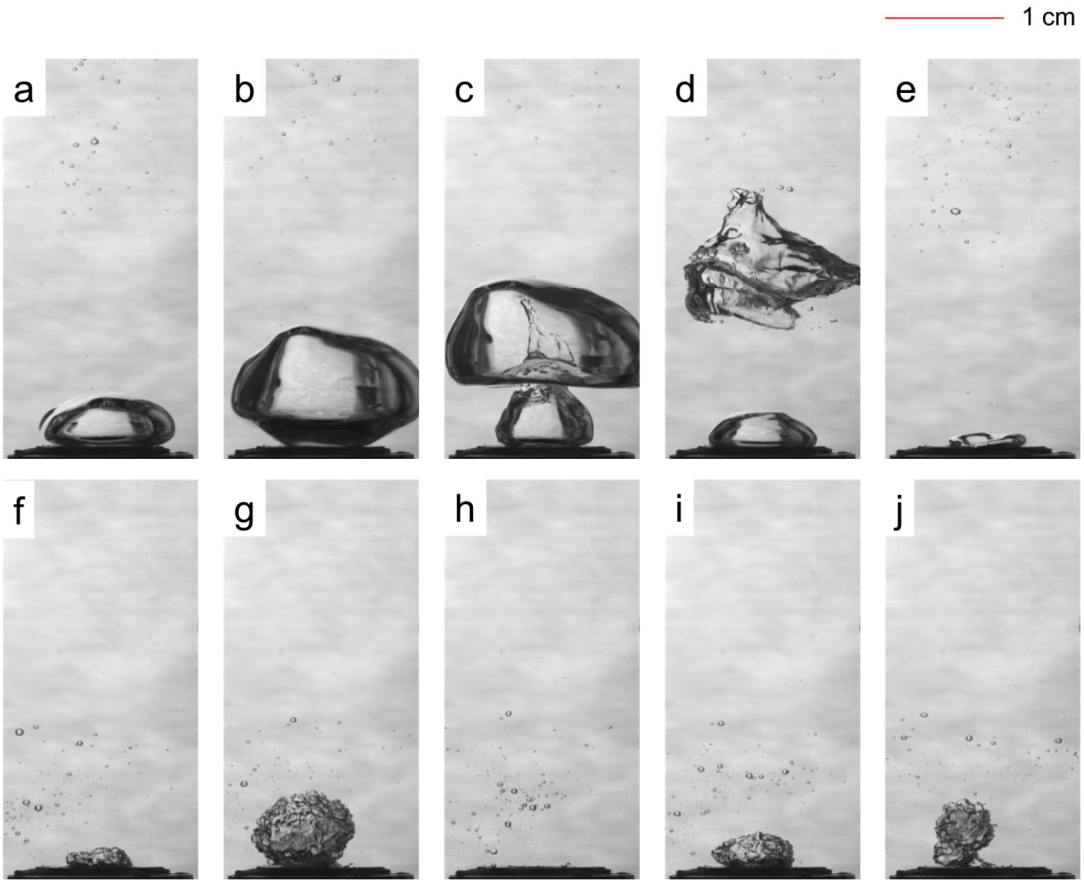


**Figure 6.1.** Vapor bubble rising in absence (a-e) and presence (f-j) of acoustic actuation. Long wavelength actuation is applied at peak-to-peak amplitude of 5 kPa.

formation of Faraday waves (characteristic scale of 1.15 mm) as discussed in Section 4.1. It is noteworthy that such waves also form on the liquid-gas interface of air bubbles (cf. Figure 4.4) but in the absence of condensation there was no change in the bubble size. The actuation-induced reduction in vapor volume is apparently caused by enhanced condensation as the Faraday waves disrupt the thermal boundary layer at the vapor-liquid interface (cf. §6.2), and enhance the thermal mixing with the subcooled surrounding liquid through the motion of the interface; these surface disturbances simultaneously increase the interface and therefore heat transfer area, further augmenting total heat transfer rates. These effects increase the rate of heat transfer from the bubble and thereby the vapor condensation rate leading to the substantial decrease in bubble size.

Individual detached bubbles are tracked, and their volumes are estimated using MATLAB image analysis in the absence and presence of acoustic actuation (the procedure is described in §3.2; note that to ensure the conditions for each bubble were as identical as possible, the image sequences for unactuated and actuated bubbles were taken from the same high speed video). Time traces of the bubble volume $V(t)$ in the absence and presence of actuation are shown in Figures 6.2a and b in which $V(t)$ is

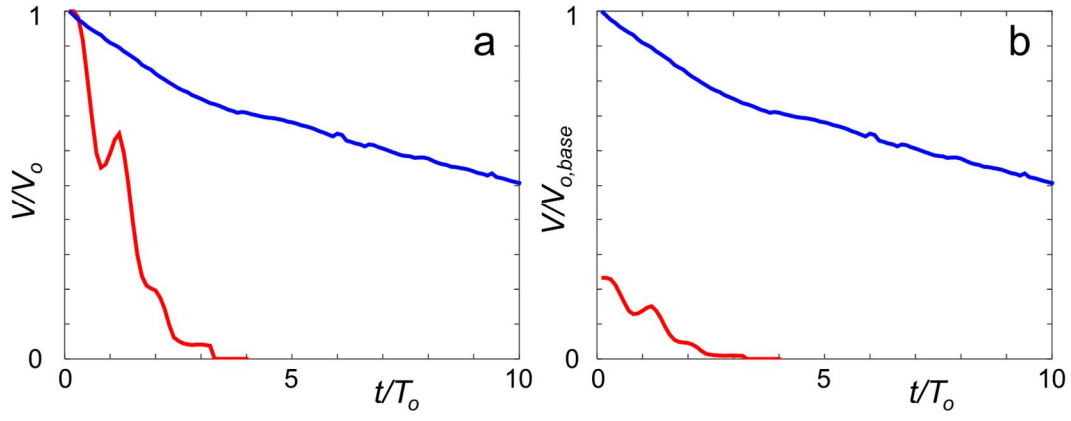


**Figure 6.2.** Time traces of vapor bubble volume as the bubble is advected away from the orifice in ***absence*** and ***presence*** of 5 kPa acoustic field. In (a) *V(t)* is normalized by $V_o$, each bubbles individual initial volume and in (b) *V(t)* is normalized by $V_{o,base}$, the initial volume of the unactuated vapor bubble.

normalized by either each bubbles' individual initial volumes $V_o$ or $V_{o,base}$, respectively, and $t$ is normalized by the actuation period $T_o$ = 1 msec. The naturally condensing bubble (blue) undergoes a relatively steady rate of condensation after separation from the orifice. In the presence of acoustic actuation (red), it is clear that the bubble's volume decreases quite rapidly, completely condensing by four actuation cycles after separation from the orifice**,** although it should be noted that capillary waves are present on the liquid vapor interface during the bubble growth and by the time the bubble has detached from the orifice it is already smaller than the corresponding bubble in the absence of actuation at the time of its departure from the nozzle, reducing the total heat transfer required to complete condensation. It is noteworthy that the time trace of $V/V_o$ in the presence of actuation exhibits significant oscillations of the bubble's volume at the actuation period (1 msec). The local maxima and minima of this trace correspond to the low and high time-periodic pressure peaks of the actuation waveform as it changes the static pressure around the bubble, compressing the vapor, although as the actuation frequency is well above the characteristic resonance frequency of these bubbles (~330 Hz), the bubble acts as an undamped oscillator and its volume lags the actuation (Leighton, 1994). In Figure 6.2b, normalizing both bubbles' volumes by the initial volume of the baseline bubble (as opposed to normalizing by each individual initial volume as in 6.2a) demonstrates the significantly reduced scale of the acoustically actuated bubble at its time of departure, as it is nearly 70% smaller at $t/T_o = 0$, indicating that a significant portion of the heat has already been transferred to the surrounding fluid. The actuated bubble still completes its collapse within 4 actuation cycles, although the rate of change appears less drastic than in Figure 6.2a due to the different normalization scheme.

Time traces of the total projected vapor area, i.e., over the life cycles of several bubble above the orifice within the field of view of the video images $A(t)$ are computed following the procedure described in §3.2. The projected areas in the absence and

presence of actuation are normalized by the (base) time-averaged vapor area in the absence of actuation $A^* = A(t)/A_{mean,base}$ and are shown in Figure 6.3. These data show that the peak vapor area in the absence of actuation is 2.7 times higher than the corresponding peak in the presence of actuation, and the time-averaged projected vapor area in the absence of actuation is 5.25 times higher.

The image processing procedure discussed in §3.2 does not measure area changes that result from small-scale, short-wavelength spatial perturbations that affect the bubble's *texture*, only changes in the bubble's *shape*, and therefore the contribution to the total heat transfer coefficient by texture area changes is not determined. However, images at the vapor-liquid interface suggest that the characteristic amplitude of the surface waves is smaller than one half of the length of the surface capillary disturbance $\lambda_a$ (1.15 mm) and therefore, considering the surface area of a sinusoidal surface

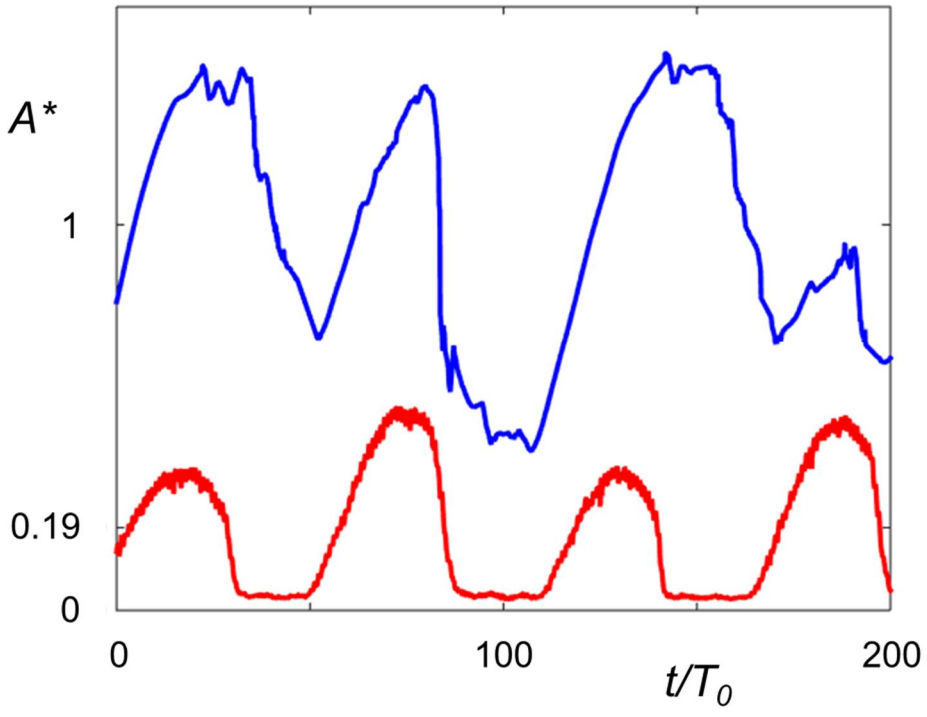


**Figure 6.3.** Time traces of total projected vapor area fraction above the orifice in the absence (***blue***) and presence (***red***) of acoustic field.

(where $z = 0.5\lambda_a \sin(x \cdot 2\pi/\lambda_a) \cdot 0.5\lambda_a \sin(y \cdot 2\pi/\lambda_a)$ over the rectangular domain from $x,y=(0,0)$ to $x,y=(\lambda_a,\lambda_a)$), the increase in liquid-vapor interfacial area induced by the surface waves is estimated to be no more than 48% of the large-scale surface area that is textured by the waves (i.e., projected and computed spherical areas). Correcting the results of the projected vapor area changes for the increase in vapor interface area due to surface texture with the above estimate, the time-averaged vapor area in the absence of actuation is 3.55 times higher than in the presence of actuation, which indicates that area enhancement from surface texture changes alone cannot explain the observed changes in projected vapor area.

The (global) enhancement of the time-averaged heat transfer coefficient by acoustic actuation is estimated relative to the base condensation (in the absence of actuation) using a simple 1-D analysis. Since the time-averaged total dissipated power $\dot{q}$ and the temperature difference $\Delta T$ between the vapor saturation temperature and the subcooled liquid are the same for both the actuated and unactuated processes, the ratio of the time-averaged overall heat transfer coefficients $U$ [W/(m$^2$·K)] between the saturated vapor phase and the subcooled liquid are estimated using a total thermal resistance $R_{tot} = (UA)^{-1}$ such that $\dot{q} = R_{tot}^{-1} \cdot \Delta T$ and therefore $\dot{q} = U \cdot A \cdot \Delta T$, where $A$ is the time-averaged liquid-vapor interface area and $\Delta T$ is the temperature difference between the saturated vapor and the subcooled liquid; this takes into all forms of thermal resistance between the saturated vapor and the subcooled liquid. Assuming spherical bubbles, the time-averaged total vapor interface area is taken to be $4A(t)$ where $A(t)$ is the time-averaged projected vapor area determined from the high-speed image processing outlined above (cf. §3.2). It is noted that the data in the absence and presence of actuation are acquired sequentially to avoid low-frequency temperature fluctuations in the bulk fluid. Therefore since the power dissipation does not change:

$$\dot{q}_{base} = U_{base} A_{base} (T_{sat} - T_{bulk}) = U_{act} A_{act} (T_{sat} - T_{bulk}) = \dot{q}_{act} \qquad 6.1$$

and since the driving temperature difference does not change, the ratio of the global time-averaged heat transfer coefficients is:

$$\frac{U_{act}}{U_{base}} = \frac{A_{base}}{A_{act}} = 3.55 \qquad 6.2$$

(an increase of 255%). The Schlieren investigations in §6.2 indicate that the presence of the surface waves results in profound changes in the thermal boundary layer over the surface of the vapor bubble and therefore the increase in the global heat transfer coefficient and the concomitant reduction in vapor volume can be primarily attributed to this surface instability.

Because practical condenser designs would preferably use the largest diameter orifices possible that avoid backflow to the vapor supply, the effects of the acoustic actuation were investigated using three orifice diameters (vapor power 225 W, $T_{subcool}$ = 25°C). Figure 6.4 compares time-averaged vapor area fraction $<\tilde{A}_{vap}>$ (i.e., the time-averaged vapor area normalized by the area of the field of view) in the absence and presence of actuation. Note that while the heater power dissipation was held invariant, the

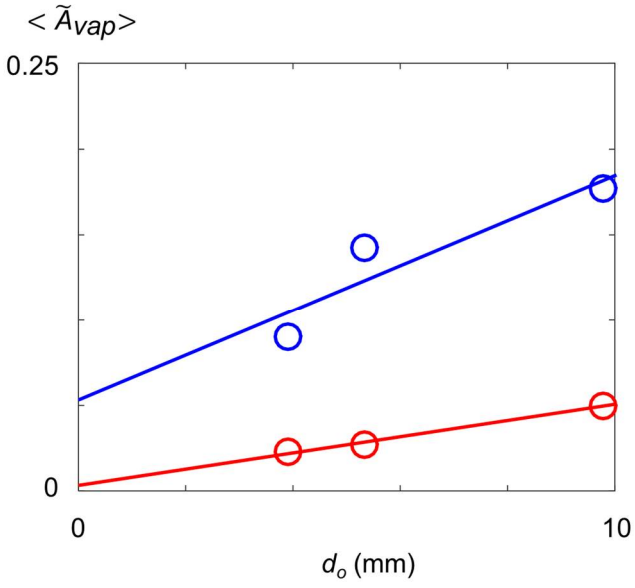


**Figure 6.4.** Variation of the time-averaged vapor area fraction with orifice diameter in the absence (***blue***) and presence (***red***) of acoustic actuation.

combination of the vapor mass flow rate changing slightly due to changes in pressure drop (which increases with decreasing orifice diameter) and the ejection speed decreasing as orifice diameter increased (therefore the corresponding base flow heat transfer coefficient decreased, as it depends on the relative speed across the vapor-liquid interface) led to an increase in the vapor area fraction in the absence of actuation as orifice diameter increased. Despite the slight changes in the unactuated vapor area fraction, the data in Figure 6.4 show that the reduction in vapor area is roughly uniform (72, 81, and 74% with increasing diameter) across these orifice diameters.

## 6.2 Schlieren Imaging

The Schlieren imaging system described in §3.3 was used to visualize the condensation in the subcooled liquid pool, with specific attention to imaging of the thermal boundary layer and mixing at the liquid-vapor interface of the vapor bubbles as they become detached from the orifice, and are advected by buoyancy until they ultimately collapse. Figure 6.5 compares sequences of high-speed Schlieren images (10 msec apart) in the absence (a-f) and presence (g-l) of a long wavelength acoustic field at 225 W vapor thermal power, 5.3 mm diameter injection orifice, and 25$^{o}$ subcooled liquid. In the absence of actuation, the bubble is growing at the orifice in Figures 6.5a-b and then become detached and is advected in the subcooled liquid (Figures 6.5c-f) as a new bubble begins to form at the orifice (Figures 6.5df). The bubble forms and is advected in the wake of an earlier detached bubble in which the remnants of thermal mixing are still apparent, and the thermal fluctuations are apparent in the liquid flow over the new bubble (Figures 6.5a-c). Other than these thermal fluctuations, the surface of the new bubble is initially virtually free of thermal disturbances. Only after the bubble becomes detached (frame c onward) is there evidence of condensed hot fluid, initially in the near wake of the detached bubble in Figures 6.5c and d (apparently as a result of the detachment of the liquid vapor interface from the orifice), that is followed by massive thermal disturbance as the bubble develops strong deformation of the interface and begins to collapse in Figures 6.5d-f. The collapse of the bubble is associated with the appearance of a nearly vertical liquid spear within the vapor volume that forms at the wake interface of the bubble and reaches its front interface in Figure 6.5d (cf. Figure 6.1c). The appearance of this liquid spear reshapes the bubble into a torus and apparently hastens its rapid collapse while the hot condensed fluid is advected away from the nozzle, forming the wake that begins to wrap over the new bubble (Figures 6.5d-f). The condensation process is apparently far more intense in the presence of the acoustic actuation (Figure 6.5g-l) as is evidenced by the mass of condensed fluid that is advected vertically in Figures 6.5g-l

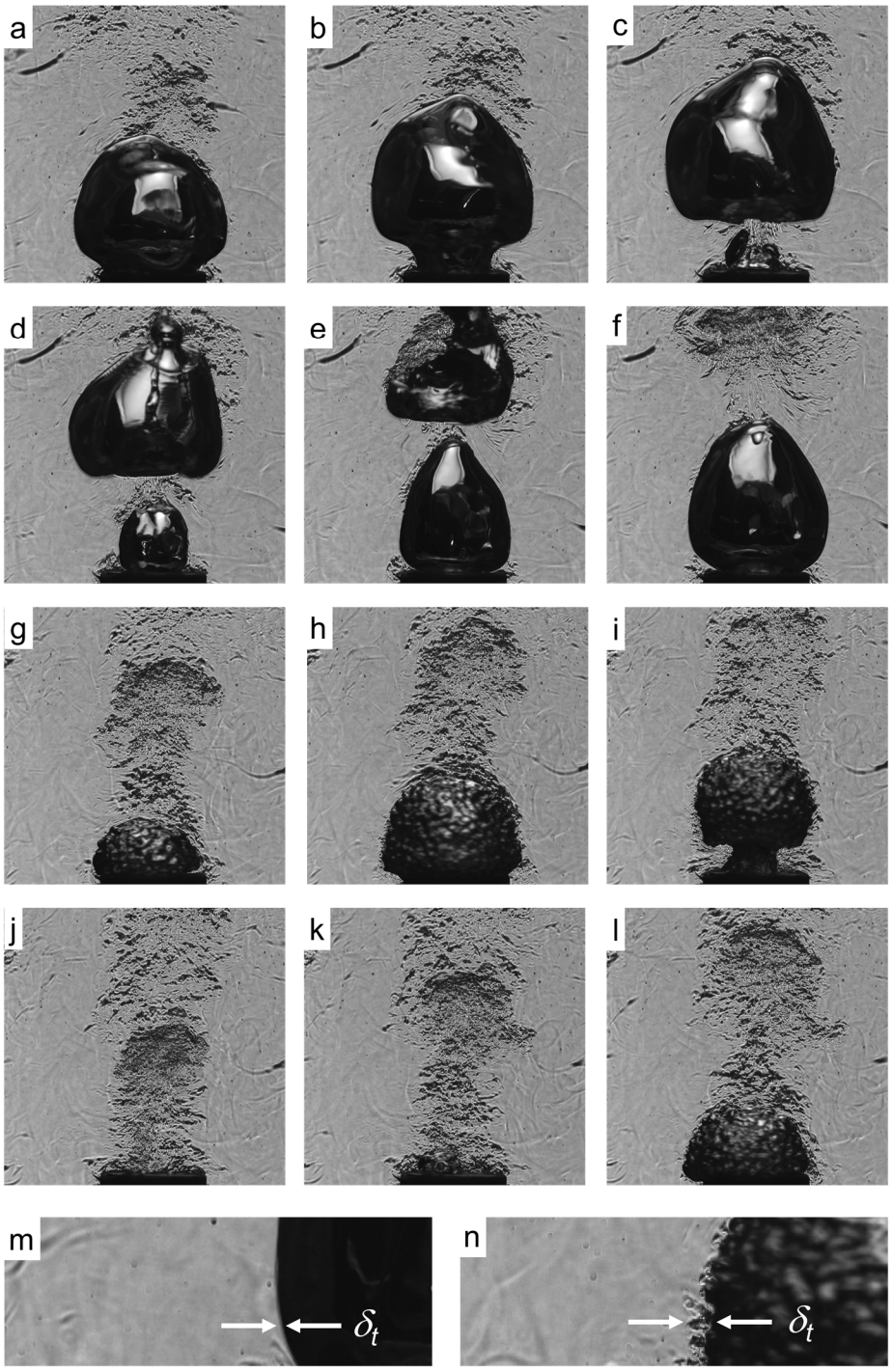


**Figure 6.5.** High-speed Schlieren images (10 msec apart) of a condensing vapor bubble in the absence (a-f) and presence (g-l) of long-wavelength acoustic actuation. The corresponding thermal boundary layer at the liquid-vapor interface of a bubble that is still attached to the orifice are shown in (m) and (n).

resembling the signature of a turbulent vortex ring (Glezer and Coles, 1990). As noted in connection with Figure 6.1, the actuation leads to the formation of Faraday waves on the liquid-vapor interface that are accompanied by strong thermal fluctuations (Figure 6.5g-i), especially along the side interfaces of the bubble. These thermal boundary layers are apparently driven by the motion of the interface and are associated with enhanced heat transfer while the bubble is still attached, followed by rapid collapse within 10 msec (significantly faster than in the absence of actuation) once the bubble is separated from the orifice (Figures 6.5j-l). As noted in connection with Figures 6.5g and h, the volume of the collapsed bubble in Figures 6.5j-l apparently forms a vortex-ring like structure by the toroidal collapse of the vapor volume. The difference between the formation of the thermal boundary layer over the surface of the bubble in the absence and presence of actuation is demonstrated in Figures 6.5m and n, respectively. While the thermal boundary layer in the absence of actuation is primarily affected by the radial motion of the interface and by diffusion, significant thermal fluctuations are visible in the presence of actuation. It is conjectured that the interfacial motion associated with the local capillary wave crests lead to the penetration of local fingers of either subcooled liquid into the vapor volume or of vapor into the subcooled liquid that result in significant enhancement of the heat transfer and condensation.

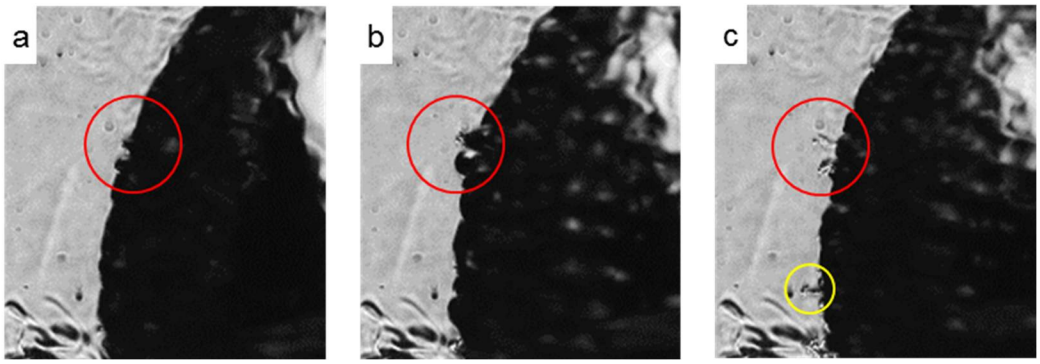


**Figure 6.6.** Schlieren images (0.6 msec apart) showing the ejection of vapor by the action of the capillary surface waves marked by red circles in (a-c) and by a yellow circle in (c).

The sequence of images in Figure 6.6 shows a magnified view of the interface in the presence of actuation that are acquired 0.6 msec apart. Note that the reflection at the center of the bubble interface from the secondary light source that allows visual inspection of the surface texture in addition to the Schlieren disturbances is visible. Figure 6.6a is 5 msec following the onset of the acoustic actuation, while the amplitude of the surface waves is increasing. These images show small vapor volumes (marked by red circles) that are displaced outward relative to the interface (Figures 6.6a and b) by the capillary wave action and are ultimately retracted back (in Figure 6.6c) leaving some condensed fluid behind them. Figure 6.6c also shows evidence of another ejection of vapor at a wave crest (marked by a yellow circle). It is apparent that the motion of the interface leads to the overall growth in the surface thermal boundary layer that is intensified with the amplitude of the waves as is evident in Figures 6.6a-c.

The temporal changes in the thermal boundary layer of an attached bubble are investigated using Schlieren image sequences. While the intensity of the thermal fluctuations at a given azimuthal position on the bubble cannot be determined because of the integrating effect of the Schlieren imaging, the thickness of the boundary layer at the meridional plane (i.e., maximum curvature) can be assessed. The boundary layer thickness is computed from a time sequence of 100 images (0.1 msec apart) using the horizontal variation of the image light intensity $I(x; y, t)$ along a pixel row that crosses the liquid vapor interface. $I(x; y, t)$ is computed for ten adjacent pixel rows within an image segment that is 200 μm high and is approximately centered vertically about the maximum curvature of the bubble. The respective intensity traces along a single row in the absence and presence of actuation are shown for reference in Figures 6.7a and d. The characteristic thickness of the thermal boundary layer at this elevation is approximated by considering the corresponding distributions of the square of the local intensity derivative $[I'(x; y, t)]^2$ that are shown in Figures 6.7b and e along with a zoomed-in view near the

interface in Figures 6.7c and f. The width of the local maximum of $[I'(x; y, t)]^2$ is determined in the presence and absence of actuation as shown in Figures 6.7c and f and is averaged over the ten rows within each image and then over the 100 images in the sequence. These data show that the respective average and standard deviation of the

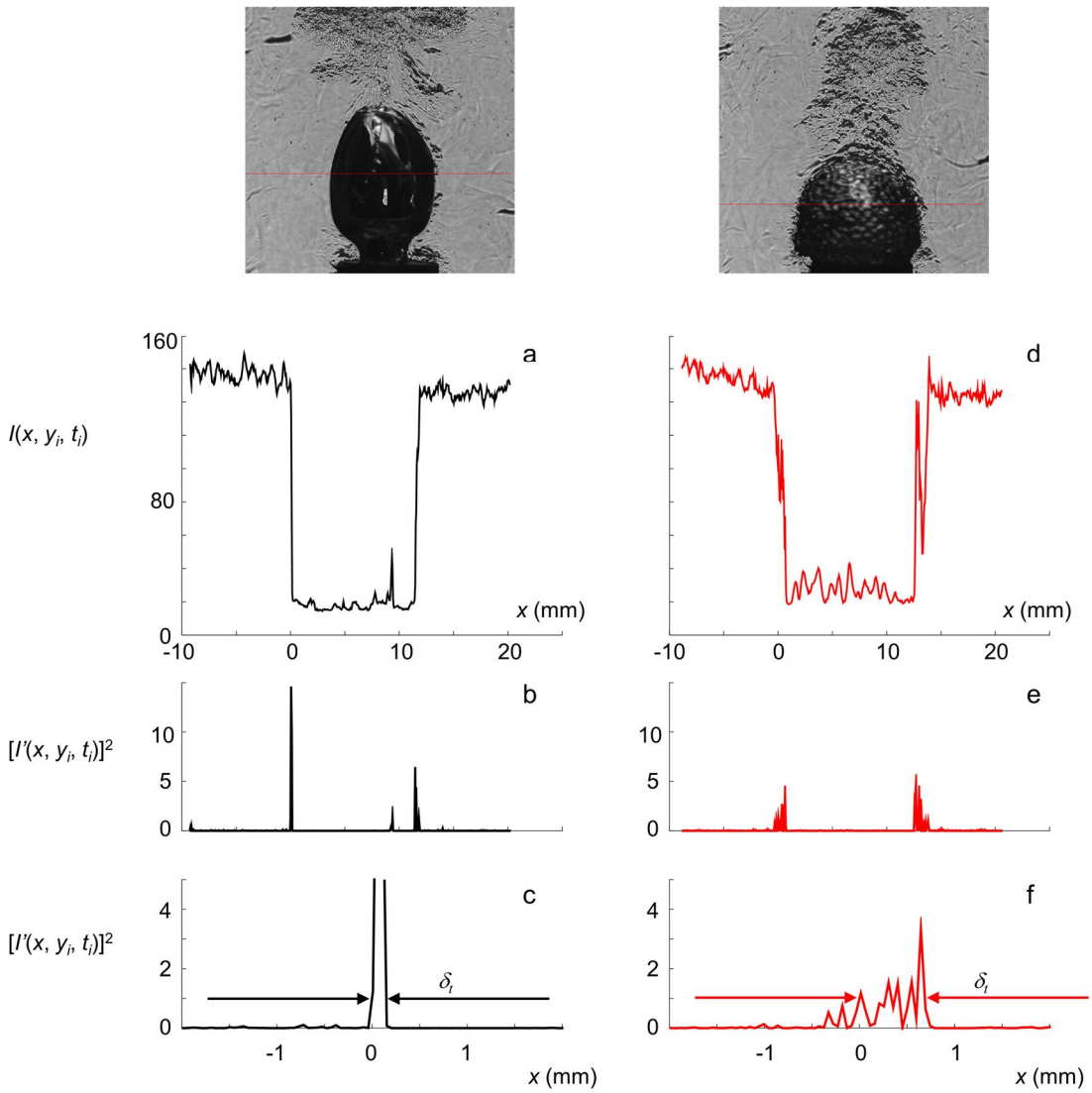


**Figure 6.7.** Respective traces of intensity $I(x; y_i, t_i)$ and of $[I'(x; y_i, t_i)]^2$ across a Schlieren image in the ***absence*** (a, b), and ***presence*** (d, e) of acoustic actuation at example elevation $y_i$ and time $t_i$. Magnified segments of $[I'(x; y_i, t_i)]^2$ used to determine the width of the thermal boundary $\delta_t$ at this elevation and time (c, and f). Example images with marked interrogation line shown above for comparison.

thickness of the thermal boundary layer in the presence and absence of actuation are $\overline{\delta_t}$ = 0.62 and 0.09 mm, and $\overline{\delta_t}$-*std* = 0.21 and 0.003 mm.

The variation with time (corresponding to ten actuation cycles) of spatially-averaged $\delta_t$ ($t$) over the attached vapor bubble in the absence and presence of actuation is shown in Figure 6.8, (a linear least squares fit for each set is included for reference). These distributions show that while the bubble is attached to the orifice its thermal boundary layer thickness is nearly time-invariant in the absence of actuation. In fact, even though a growth of about 0.007 mm/msec would be expected due to diffusion (assuming a quiescent flow and semi-infinite medium at a constant surface temperature), there is a slight *decrease* in the computed $\delta_t$ ($t$) ostensibly as a result of the expansion of the interface. However, in the presence of actuation $\delta_t$ ($t$) increases (nearly linearly) with time at a rate of about 0.067 mm/msec. Based on the least squared fit to $\delta_t$, at $t/T_o$=0 in the presence of actuation $\delta_t$ is 2.9 times larger than the unactuated $\delta_t$ as the actuation is already present as the vapor is ejected from the orifice prior to the start of the measurements, and the bubble grows in the wake of the previous bubble (the thermal wake in the absence of actuation is considerably weaker). The data in the presence of actuation indicate that $\delta_t$ does not vary significantly with the induced time-periodic pressure (i.e. actuation phase), and therefore it may be concluded that the thermal boundary layer thickness's growth, when spatially averaged, is not strongly locked to the phase of the local surface waves that cumulatively contribute to its growth nor to the expansion and contraction of the bubble. This is interesting given that, as noted in the discussion of Figure 6.6, the growth of individual disturbances appears to be locked to the phase of the local interfacial surface wave. The exact cause for the discrepancy in the spatially-averaged data is unknown.

Although the Schlieren images clearly demonstrate the growth of the thermal boundary layer, diagnostic techniques such as PIV of the shed disturbances would

enhance the understanding of the boundary layer growth process. Hopfinger and Das (2009) theorized that interfacial area increases were responsible for the enhanced mass transfer at a planar interface undergoing capillary wave motion, but noted that this effect did not exist for forcing amplitudes between the critical amplitude for capillary wave formation and a second critical value (4.5 times the wave formation critical amplitude). If the mechanism is dependent on the motions observed in the Schlieren images after the onset of actuation in Figure 6.6 (which did not form at low wave amplitudes), it would explain the findings of Hopfinger and Das; resolution of the induced motions in the fluid would be useful to separate the effects of interfacial motion from that of area enhancement. The current PIV setup (§3.4) was unable to reliably resolve these motions;

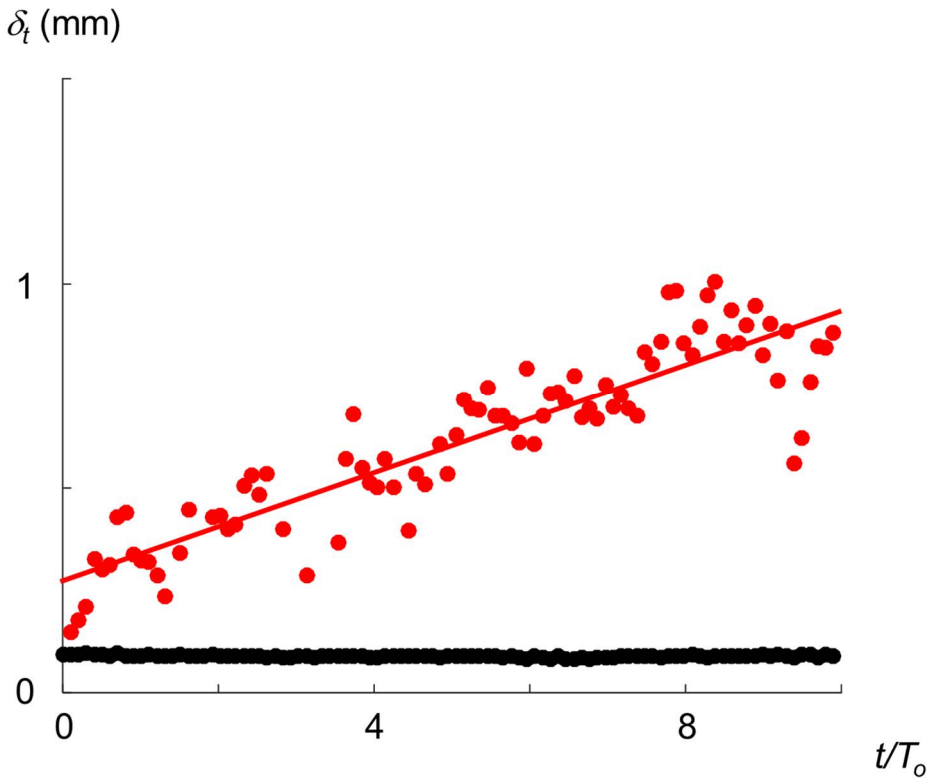


**Figure 6.8.** Variation with time of the thickness of the thermal boundary layer over the attached bubble during 10 actuation periods in the ***presence*** and ***absence*** of acoustic actuation. While $\delta_t$ is nearly invariant in the absence of actuation, it increases (on average) at 0.067 mm/msec in the presence of actuation.

although particle motion due to the interfacial surface waves was sometimes observable in the images, vector generation after the masking process could not resolve these small-scale motions, perhaps due to significant out-of-plane motion.

### 6.3 Condensation Enhancement at Reduced Ambient Pressure

The condensation enhancement of vapor was further investigated at reduced pressure which is relevant in a number of applications (e.g., dry-cooled power plant condensers). As noted in §3.2, the ambient pressure in the test tank was set using a vacuum pump (15 kPa, corresponding to $T_{sat}$ = 54°C). For direct comparison with the measurements at atmospheric pressure, the actuators' placement relative to the orifice was unchanged and the actuators were run at 5 kPa peak-to-peak. Because of the low pressure, it was not practical to maintain the same vapor mass flow rate due to prohibitively high volume flow rates as a result of the change in specific volume of vapor and consequently, the heater power in the vapor cell was set at 125 W, with the losses from the saturated lower tank leading to a vapor power dissipation of 65 W (note that the reduction in losses is due to the lower saturation temperature in the lower tank). This allowed the vapor to condense in a reasonable volume between the actuators and primarily within the field of view of the high-speed camera. Furthermore, to ensure bubbling flow through the orifice

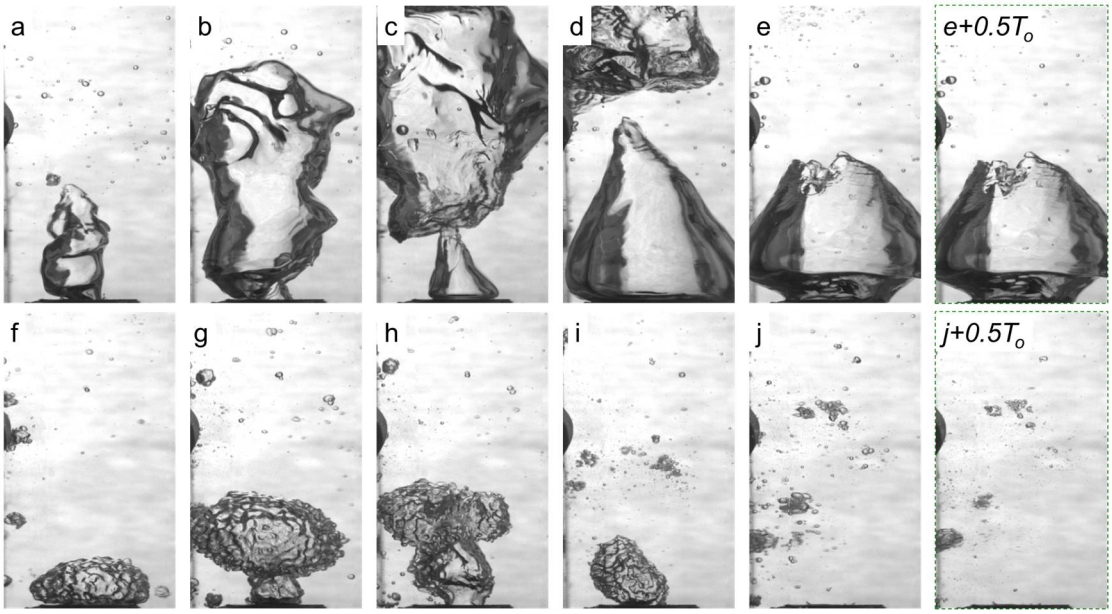


**Figure 6.9.** Vapor bubbles rising in absence (a-e) and presence (f-j) of acoustic actuation at reduced ambient pressure of 15 kPa. For reference, the image 0.5 actuation periods relative to frame e and j are included to demonstrate the volumetric oscillation of small noncondensable bubbles under acoustic actuation.

(and avoid chugging flow) the subcooling in the upper tank was reduced to 8 $^{o}$C. It should be noted that even though the water was heated to its saturation temperature prior to data acquisition, incomplete deaeration was evident during the condensation by the presence of bubbles of noncondensable gas.

The effect of the reduced pressure (15 kPa) on the evolution of the vapor bubbles in the absence (top) and presence (bottom) of acoustic actuation is shown in a sequence of high-speed video images (80 msec total elapsed time) in Figures 6.9a-e and f-j, respectively ($d_o$ = 5.3 mm, and $T_{sat}$ - $T_{bulk}$ = 8 $^{o}$C). As noted above, due to the increase in specific volume of the vapor, the characteristic scale of the vapor bubbles in the absence of actuation (Figures 6.9a-e) is significantly larger compared to the bubbles formed at atmospheric pressure (cf. Figure 6.1a-e). It was also observed that despite the reduction in subcooling of the bulk fluid, the collapse of the vapor bubbles occurred much faster than

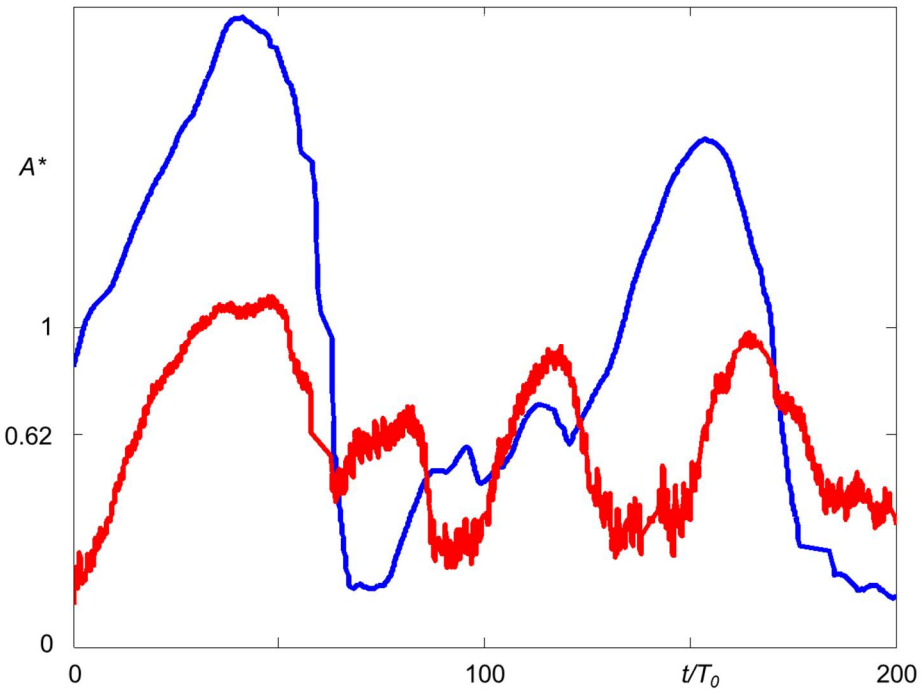


**Figure 6.10.**. Time traces of total projected vapor area fraction above the orifice in the absence (***blue***) and presence (***red***) of acoustic field in low ambient pressure.

the atmospheric bubbles, as the large-volume bubbles had comparatively little mass requiring phase change. Bubbling flow did appear to be maintained through the nozzle at these conditions (note the pinch-off process between Figure 6.9b-c-d did not lead to significant backflow into the orifice). These images (Figure 6.9a-e) also show smaller bubbles around the large rising vapor mass, ostensibly a mixture of vapor and air which came out of solution and are primarily remnants from past vapor collapses. The effect of the actuation (Figure 6.9f-j) is quite remarkable; as with the acoustically actuated atmospheric configuration of Figure 6.1, surface capillary waves are visible on the vapor bubbles (Figure 6.9f-i), leading to quicker collapse of the vapor bubbles. The scale of the capillary waves does not appear to depend on ambient pressure, in accordance with Equation 4.5. Note that the collapse of the vapor pocket which occurs after Figure 6.9h leads to the clump of noncondensable bubbles visible in the center of Figure 6.9i, similar to the bubbles in other frames both with and without acoustic actuation. These small noncondensable bubbles in the presence of acoustic actuation (Figure 6.9i- j; especially Figure 6.9i, center of frame) are quite significant as they are driven below their resonance frequency (despite the reduction in ambient pressure, their natural resonance frequency is 1.2-2.5 kHz for observed diameter of 1-2 mm) and tend to travel towards antinodes (i.e. the actuator surface; see §4.1), affecting the propagation of the acoustic field by dissipating energy (through thermal and viscous mechanisms) through their own expansion and contraction as well as scattering the acoustic wave (Leighton 1994). As their volume fluctuations can be significant (noting that the 5 kPa pressure field is over 30% of the ambient pressure of 15 kPa, small bubble volumes nearly doubling between high/low pressure states were observed: compare Figure 6.9j and Figure 6.9j+0.5$T_o$), the dissipation is also significant and clearly over time affected the ability of the acoustic actuation to create surface capillary waves on the large vapor bubble surface, especially when the vapor mass was still connected to the vapor reservoir through the orifice

(compare the sharper peaks on the interface of Figure 6.1g at atmospheric pressure to that of Figure 6.9f). Note that the presence of similar small air bubbles at atmospheric pressure had much smaller volume fluctuations (cf Figure 6.1f-j) and did not appear to have the same deleterious effect on the creation of surface disturbances.

Similar to the analysis discussed in connection with Figures 6.3, Figure 6.10 compares the normalized vapor area $A^* = A/A_{mean,base}$ in the absence and presence of actuation at the reduced pressure. These data show that the unactuated process is not as neatly time periodic as at atmospheric pressures, evident by the multiple local maxima in the second ejection process in the unactuated blue curve ($75 < t/T_o < 150$) and the peak vapor area is higher (twice the mean vapor area, versus a peak of 1.5 times the mean vapor area for the atmospheric pressure data in Figure 6.3). The red curve of Figure 6.10 shows that the presence of long-wavelength actuation has increased the frequency of bubble collapse, as well as reducing the peak vapor area to that of the mean vapor area without actuation. The reduction of large-amplitude changes in vapor area (and, by extension, vapor volume) leads to a steadier process with less powerful vapor collapses. This positive effect is more influential at low ambient pressures, where powerful vapor collapses can be problematic to system components as well as leading to chugging flow in the orifice. The data in Figure 6.10 also shows that in the presence of actuation, the time-averaged projected vapor area fraction is reduced by 38% compared to 81% at atmospheric pressure; correcting for the area increases from surface texture, the vapor area fraction is reduced by 8.3% and based on Equations Eqs. 6.1-2 the heat transfer coefficient is increased by 9 percent. However, as noted above, incomplete deaeration at low pressures can lead to some reduction in effectiveness and should be avoided.

## 6.4 Condensation Enhancement Above a Boiling Surface

Enhanced condensation by the interaction of long wavelength acoustic actuation with vapor bubbles that are formed on and detach from a boiling surface submerged in subcooled liquid are investigated. Unlike the effects of the actuation on condensation during vapor injection, when the vapor forms on a submerged heated surface the actuation affects the vapor mass while it forms and grows on the surface, and following detachment. The interaction of the actuation with the boiling process is discussed in §5.2, and so in this section, attention is restricted to the effects of the actuation on the detached vapor bubbles that are no longer connected by vapor stems. As with vapor bubbles that are directly injected (cf. §6.1-3) the actuation induces surface Faraday waves at the liquid vapor interface and dramatically increase the heat transfer to the subcooled liquid and the condensation rate by affecting the thermal boundary layer on the surfaces of the bubbles.

High-speed images of vapor above the boiling surface were analyzed to compare the condensation rates of individual bubbles in the absence and presence of actuation. The evaporation was adjusted to produce large vapor slugs that are advected above the heater surface at high heat flux (100 W/cm$^2$) with a nominal period of 0.1 seconds and $T_{bulk}$ = 85$^o$C. To improve bubble repeatability and to ensure the conditions for each bubble were as identical as possible, the image sequences were taken from the same 1-second high speed video (where actuation turns on halfway into the video period, and representative bubbles are chosen from the first half and the second half of the video for the baseline and actuated case, respectively). Figures 6.12a-d and e-g shows high-speed images of the boiling surface and the advecting bubbles in absence and presence of actuation, respectively and demonstrate the accelerated condensation of the detached bubbles in the presence of actuation. Time traces of the volume of detached bubbles (not shown) demonstrate that in the presence of actuation, the bubble is almost fully condensed within 14 actuation periods, whereas in the absence of actuation the bubble's

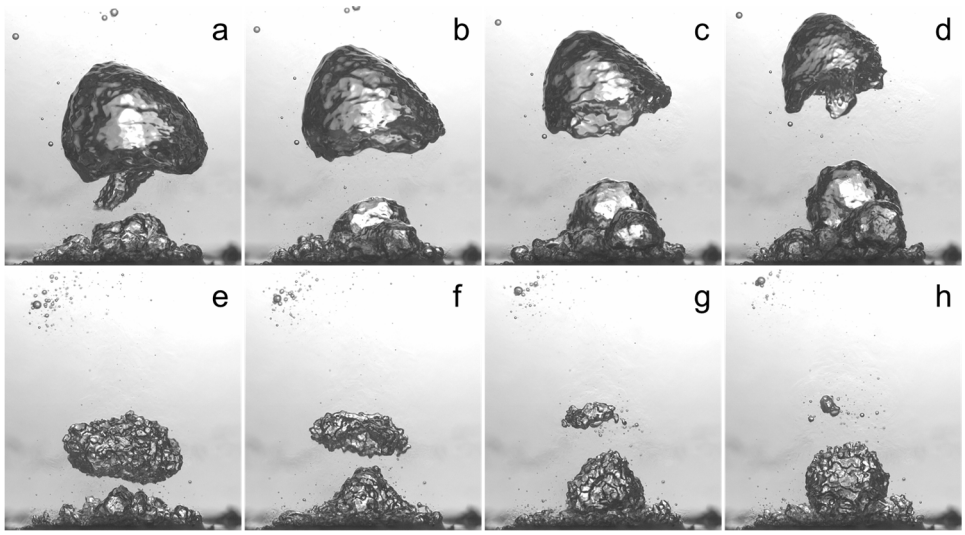


**Figure 6.11.** Images of rising vapor slugs (15 msec apart) in the absence (a-d) and presence (e-h) of long wavelength acoustic actuation.

volume at that point is about 40% of its initial volume. The time-averaged vapor fraction in the presence of actuation is 46% that of the bubble in the absence of actuation.

The primary objective of this segment of the investigations was to determine the characteristic wavelengths of the surface Faraday waves using spatial 2-D Fourier transform of zoomed-in images of the surfaces of isolated rising vapor bubbles in the absence and presence of actuation (a typical image is shown for reference in Figure 6.13). Applying a Hanning window to the image, taking the Fourier transform and averaging over 40 successive frames helped reduce low-frequency noise and fluctuations. Pairs of 2D spatial spectra (in the absence and presence of actuation) were subtracted from each other to remove inherent image disturbances (e.g., due to bubble illumination), leaving distinct peaks where the spatial frequency of intensity fluctuations was most different between the two vapor bubbles (Figure 6.12a). Note that the contour map of Figure 6.12a shows that there is significantly more difference in the power of intensity fluctuations in the vertical direction; manual inspection of the images (e.g. Figure 6.13) shows this is due to uneven lighting of the bulk bubble, which is due to the presence of the relatively dark surface of the bottom of the tank near the lower half of the bubble. In an ideal case,

the spatial wavelength (and therefore computed pixel frequency) would be independent of directionality, which would make a contour map of fluctuation intensities contain a maximum region the shape of a ring at constant pixel frequency.

The maximum computed value from Figure 6.12a was then transformed from a pixel frequency to a length scale. Figure 6.12b shows a 1-dimensional model of an interface

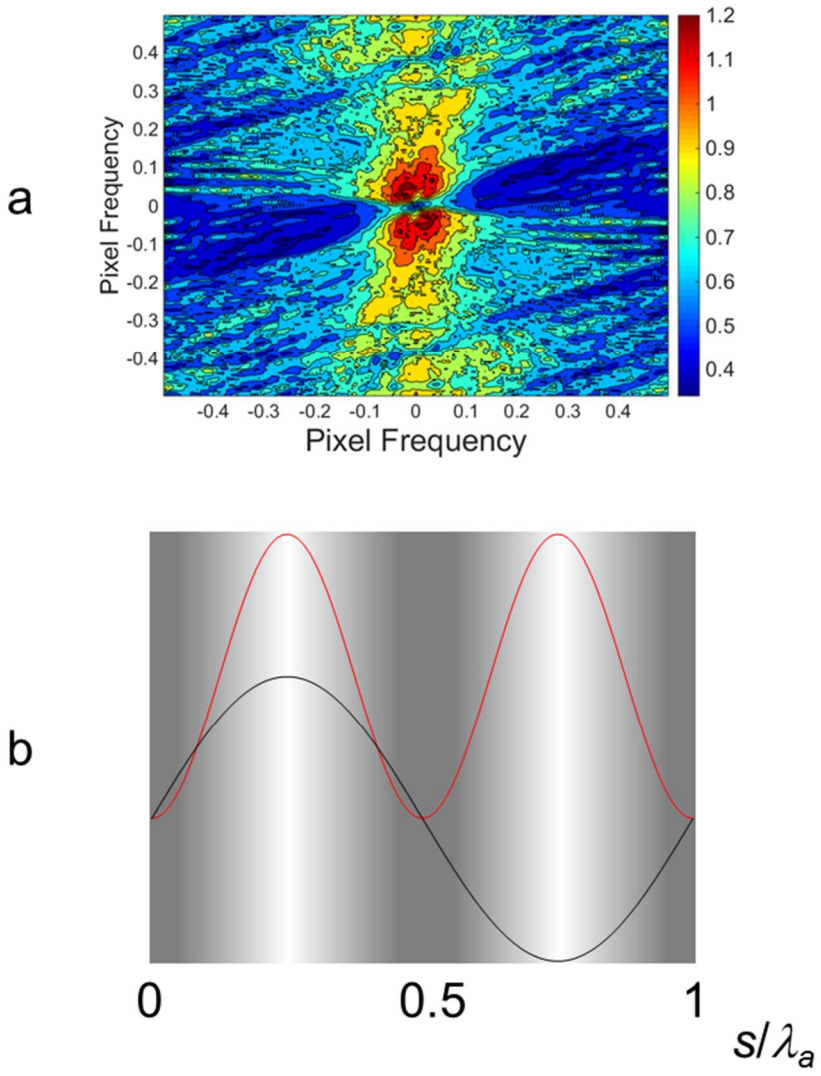


**Figure 6.12.** Difference between 2D spatial Fourier transforms of baseline and acoustically-enhanced bubble surface used to compute capillary wavelength (a). Schematic relating the wavelength of a 1-D surface disturbance (side view: ***black*** line) with the imaged surface (shading) and the intensity fluctuations across the surface disturbance (***red*** line).

wave (black line – side view of the interface) with the shading behind the figure indicating what would be observed in an image looking through the interface from above when the interface is backlit. The interface locations where the interface is closer to parallel to the rays from the backlighting source to the observer ($s/\lambda_a$ = 0, 0.5, 1) appear as dark areas, and areas where the interface is normal to the light rays from the backlighting to the observer ($s/\lambda_a$ = 0.25, 0.75) appear as light areas. The observed intensity over this range is then approximated by the red curve in Figure 6.12b, which demonstrates that the calculated wavelength based on observed intensity fluctuations is half that of the wavelength of the interface disturbance. Therefore, the computed wavelength from the 2-D Fourier transform in Figure 6.12a is half the *actual* surface wavelength. Correcting for this fact, the result is a measurement of 0.89 mm for the wavelength of the surface waves. This wavelength is overlayed on an image of the interface in Figure 6.13, which shows the method resolves a wavelength close to what

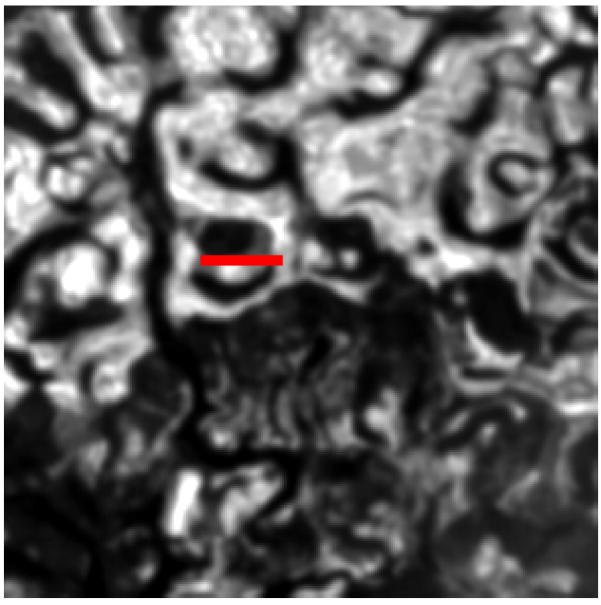

**Figure 6.13.** Image of liquid-vapor interface in the presence of long wavelength actuation. The red line segment shows the spatial wavelength computed from 2-D Fourier transform.

would be expected, despite the low coherence of the surface disturbances. A similar routine was run using acoustic actuation at 830 Hz, which resulted in a surface wavelength of 1.07 mm. It is remarkable that these results are in reasonable agreement with the simple dispersion relationship $\lambda^3 = (8\pi\sigma) / (\rho f^2)$ for Faraday waves that was developed by Rayleigh (1883), although the calculated values are shorter by about 25% than the predicted values. The uneven lighting may be contributing to the offset percentage error of computed $\lambda_a$ for the two acoustic frequencies.

# CHAPTER VII

# ENHANCEMENT OF CONDENSATION USING SHORT-WAVELENGTH ACOUSTIC ACTUATION

Investigations of the utility of acoustic actuation for enhancement of condensation was continued by utilizing short wavelength (MHz) actuation. Similar to the investigations at long wavelength (kHz), the investigations utilized vapor injection from a reservoir through an orifice into a pool of subcooled liquid at atmospheric pressure. The effects of pulsed-modulated actuation were investigated at the nominal conditions (225 W vapor thermal power, 5.3 mm diameter injection orifice, and 25$^{o}$C subcooled liquid) and are described in §7.1. The utility of pulse-modulated actuation was explored at reduced vapor mass flow rates including the time-dependent characteristics of vapor collapse and is discussed in §7.2. The effects of an alternative actuation orientation were investigated at the nominal conditions and are described in §7.3.

## 7.1 Pulsed Short-Wavelength Condensation

Short wavelength ultrasonic (1.7 MHz) acoustic actuation also significantly enhances vapor condensation. The actuation is typically applied by an acoustic beam that is emitted by an ultrasonic transducer (the intensity of the acoustic field decreases like the inverse of the distance $r$ from the transducer, and also roughly Gaussian radially from the centerline of the transducer), and is pointed at the liquid-vapor interface. However, as discussed in §4.1, unlike the coupling of long wavelength actuation (cf. Chapter 6), vapor bubbles having O(1 cm) characteristic length scales that are of interest in the context of vapor condensation in subcooled liquid have a resonance frequency O(1 kHz) and are not

receptive to acoustic actuation at a wavelength of O(1 mm) (Leighton 1994). Furthermore, the corresponding wavelength of capillary waves induced at the liquid vapor interface at this actuation frequency is about 8 μm (Rayleigh 1883), and these waves are too small to generate significant mixing by their motion although at high acoustic intensities the tips of the capillary waves can pinch off to form droplets.

Short wavelength acoustic actuation at the vapor-liquid interface is effected by exploiting the mismatch in acoustic impedance between the vapor and liquid phases. Therefore, as discussed in §4.2, the radiation pressure due to the reflection of a reasonably collimated incident acoustic beam that is incident on the liquid-vapor interface results in a local force on the interface (Cheeke 2002). If the scale of the interface is smaller than the diameter of the acoustic beam, in the form of bubbles, the acoustic force can repel the bubbles away from the transducer. On larger scale interface the acoustic interaction can lead to a local deformation or depression of the interface into the vapor phase. As the interface deforms, the acoustic reflections within the depression can lead to local focusing that further increases the acoustic intensity at the interface and can result in local droplet ejection into the vapor phase either by the formation of capillary waves which can pinch off micron-scale droplets or the formation and collapse of cavitation bubbles that eject O(100 μm) droplets (Bunkin *et al.*, 1986, Barreras *et al.*, 2002, Tomita, 2014). The interaction of an acoustic beam of sufficiently high intensity with nominally similar scale bubbles leads to large-scale deformation of the liquid-vapor interface which continues to extend into the vapor phase and can form a spear-like protrusion that reaches the bubble surface at the opposite end and alter the vapor volume from a spheroid to a torus. The combined effects of surface deformation and droplet ejection significantly increase the surface area and heat transfer coefficient of the vapor-liquid interfaces and thereby accelerate the collapse of the vapor volume. In addition, the

impingement of the ejected droplets on the vapor interface can lead to additional disturbances that enhance the thermal boundary layer at the interface.

The effects of short wavelength acoustic actuation on condensation of a train of vapor injected into the subcooled pool from a lower vapor reservoir (cf. §3.2) are first investigated when the centerline of the acoustic beam and the ultrasonic transducer are collinear with and directed towards the centerline of the vapor orifice (cf. Figure 3.3c). In contrast to the global long wavelength acoustic actuation, the interaction of the acoustic beam with the vapor-liquid interface as the vapor is injected into the liquid pool can lead to partial blockage (or resistance) at the orifice, and therefore constrain the vapor flow and result in an increase the saturation pressure in the vapor reservoir. This could also possibly change the flow regime from the desired bubbling flow to chugging flow. Therefore, in the present investigations, the short wavelength acoustic actuation is temporally-modulated in synchronization with the formation of vapor bubbles at the orifice, so that the actuation is only present momentarily once there is sufficient vapor flow through the orifice. In addition to regulation of the vapor flow and the formation of the vapor bubbles, this approach to the actuation also avoids significant changes in the saturation pressure of the vapor reservoir, and minimizes the actuation power. As noted in §3.2, the acoustic actuation is triggered by the bubble formation using a low power laser and phototransistor (cf. Figures 3.6-8) across the vapor orifice. The timing of the actuation is readily adjusted by the vertical position of the laser beam ($h_{trigger}$ above the orifice exit plane) and a delay circuit that determines the duration of the actuation.

Accelerated condensation of a train of vapor bubbles is captured in a sequence of high-speed video images (7.5 msec apart) in Figures 7.1a-e and 7.1f-j in the absence and presence of actuation, respectively (where $d_o$ = 5.3 mm, $h_{trigger} = 0.94d_o$, $T_{pulse}$ = 20 msec, $Q_{vapor}$ = 225 W, and the nominal bubble formation period $T_b$ is 50 msec). As shown in Figures 7.1a-e, the generation conditions in the absence of actuation lead to a reasonably-

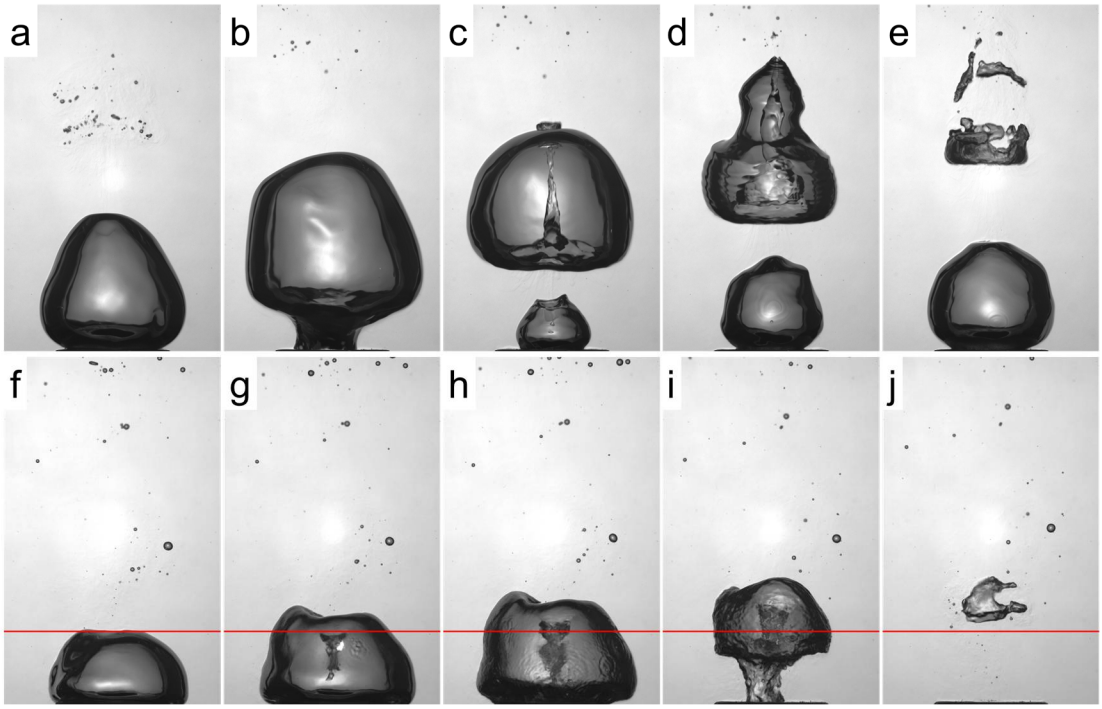


**Figure 7.1.** High speed video images (7.5 msec apart) of vapor bubble formation in the absence (a-e) and presence (f-j) of pulsed acoustic actuation (20 msec) normal to the orifice. The elevation of the trigger laser ($0.94d_o$) is marked in f-j.

regular train of isolated bubbles that do not directly interact with each other (by contact of their vapor-liquid interfaces). Clearly, the formation conditions can be adjusted to deliberately effect interactions between successive bubbles that can affect the dynamics of the natural (unforced) condensation as discussed in §7.2 and Chapter 8. In Figures 7.1a-e the natural condensation is dominated by surface-tension-induced pinch-off during the detachment of the spherical bubble in Figure 7.1a-b that leads to the formation of a spear-like column of subcooled liquid that is injected into the vapor volume from below (Figure 7.1c). The liquid spear ultimately propagates through the entire volume and interacts with its front surface to form a vapor torus (Figure 7.1d). The ensuing topological changes usher the condensation in Figure 7.1e.

The momentary pressure impulse effected by pulsed acoustic actuation from above induces the formation of a liquid spear on the top surface of the bubble as shown in Figure 7.1g. The acoustically-induced spear is similar in appearance to the natural spear

that forms by the bubble detachment in Figure 7.1c, however, it can be triggered on-demand at an earlier time in the bubble lifecycle to precede the pinch-off, while the bubble is still attached as shown in Figure 7.1f. Once the acoustic pulse commences, the bubble begins to form a torus (Figure 7.1g) while it is still attached to the orifice and the duration of the actuation can be adjusted to enable full formation of the torus and effectively induce detachment and rapid condensation (Figures 7.1i and j). Figures 7.1g and h also shows the impact of droplets ejected from the spear onto the front (in this view) surface of the bubble, and the formation of surface waves. Although the actuation is terminated in Figure 7.1i, the central liquid spear is still clearly visible. In contrast to the formation of the bubbles in the absence of actuation which can easily interact and perhaps slow the condensation process, the pulsed ultrasound actuation can be used to regulate bubble injection and enforce rapid condensation of single bubbles next to the orifice. The separation between successive bubbles is investigated using particle image velocimetry in Chapter 8.

The thermal changes associated with the vapor bubble condensation in Figure 7.1 are visualized using Schlieren imaging as shown in Figures 7.2a-e and f-j in the presence and absence of actuation, respectively. Although the vapor formation conditions are nearly identical, the images in Figure 7.2a-e show interactions of successive bubbles in Figures 7.2d and e owing to slight variations in the timing of the detachment of the leading bubble. Figures 7.2a and b show that as the bubble forms at the orifice, there are remnants of warm fluid owing to the collapse and condensation of the previous bubbles. Similar to Figure 7.1c, Figure 7.2c shows the detached bubble and the formation of the subsequent bubble at the orifice. However, the pinch-off is apparently not axisymmetric and the liquid spear interacts off center with the bubble's surface. Furthermore, the subsequent bubble appears to be stretched towards the earlier (detached) bubble (Figure 7.2d), ostensibly owing to the induced flow during the pinch-off, but the interaction is

abated owing to the condensation of the earlier bubble (Figure 7.2e). The concentration of warm condensed liquid is clearly visible in Figure 7.2e. In the presence of pulsed actuation, the warm, condensed fluid remains in closer proximity to the orifice (Figure 7.2f), due to the nearby collapse of the previous bubble. This indicates that the residence time in the presence of actuation is such that bubble ejection and the buoyancy force are nearly opposed by the downwards forces associated with the acoustic actuation (both radiation pressure and the enhanced condensation-induced deformation at the upper interface lead to downwards flow as noted in connection with the discussion of Figure

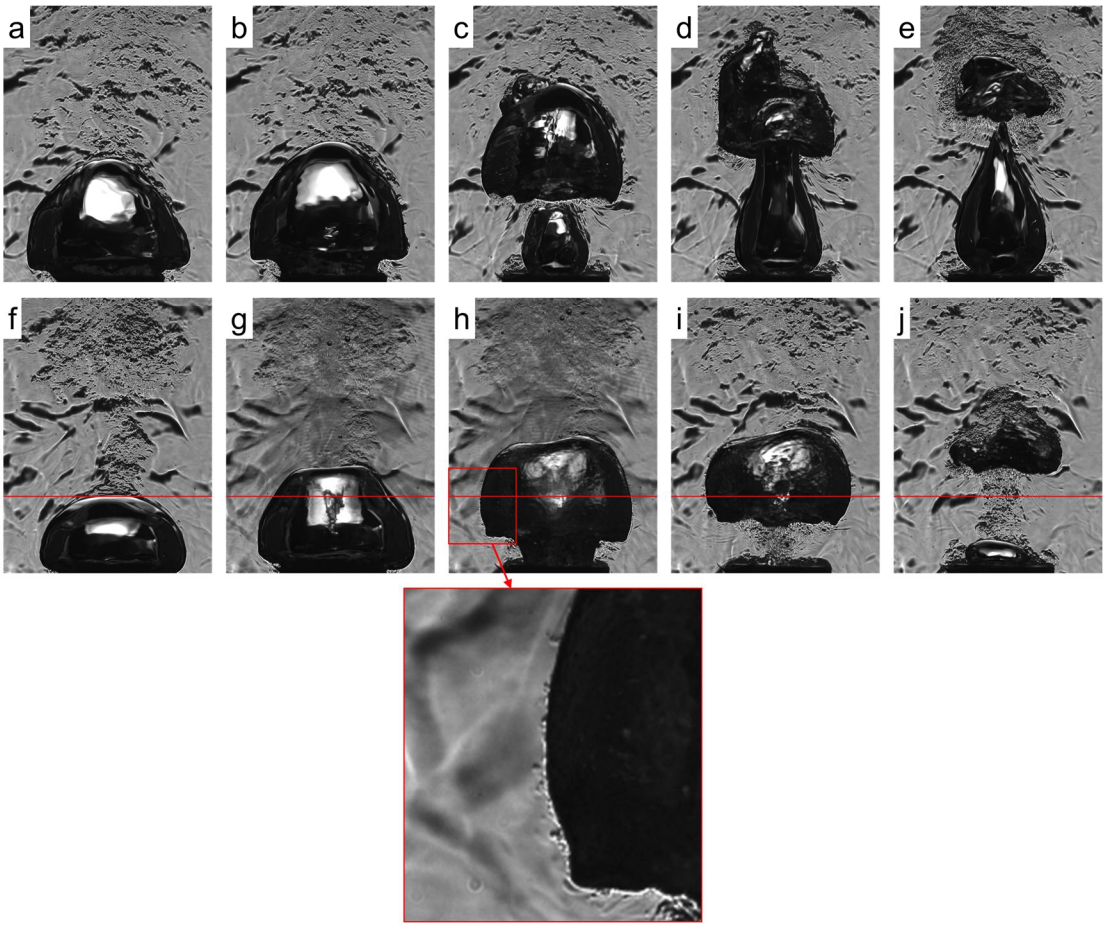


**Figure 7.2.** High-speed Schlieren images (7.5 msec apart) of condensing vapor bubbles in the absence (a-f) and presence (g-l) of pulsed short-wavelength acoustic actuation (the centerline of the acoustic transducer is aligned with the centerline of the orifice). The inset shows impact of droplets on outer interface. The elevation of the trigger laser ($0.94d_o$) is marked in f-j.

7.14f-j in §7.3). Figures 7.2g and h show the changes in index of refraction that are associated with acoustic wave fronts which cannot be resolved in the presence the long wavelength acoustic actuation. In Figure 7.2, the acoustic pulse is triggered between Figure 7.2.f and Figure 7.2.g, and is present only in Figure 7.2.g-h. The subsequent collapse of the vapor bubble (Figure 7.2.i-j) occurs following the formation of a toroidal vapor volume (Figure 7.2j also shows the onset of the formation of a new vapor bubble). A close inspection of a magnified segment of the outer liquid-vapor interface in Figure 7.2h (shown as an inset) exhibits the thermal signature of the interactions of liquid droplets that are ejected from the liquid spear by the focusing of the incident acoustic beam. These droplets of the subcooled liquid can clearly act as condensation sites while they travel through the vapor volume within the bubble, heat up, and, with sufficient momentum can cross the outer bubble interface into the subcooled liquid where they are visible in the Schlieren image (though some of the droplets can also evaporate as they travel through the vapor volume).

Similar to the thermal analysis in §6.1, the effect of the pulsed actuation on the global heat transfer coefficient can be assessed by considering the changes in the surface area of the vapor bubbles. As noted in Chapter 6, the high-speed video sequences from which the changes in the vapor volume or area are estimated include segments of vapor injection in the absence and presence of the acoustic actuation so that the corresponding dissipated heater power and the bulk fluid and saturation temperatures are nearly the same. While the procedure and notation used in Chapter 6 are unchanged, the normalization of the temporal variation of the vapor area is modified. While in Chapter 6 the characteristic time scale was taken to be the actuation period $T_0$, the period of the short wavelength actuation is not a relevant time scale here, and instead, the time series of the vapor area are normalized by the characteristic period of bubble ejection in the absence of actuation $T_b$ (50 msec in Figure 7.3-6).

Figure 7.3 shows time traces of normalized projected vapor area ($A^* = A/A_{mean,base}$) in the absence and presence of pulsed short wavelength acoustic actuation where the triggering laser is placed 1 cm ($1.9d_o$) above the orifice and the duration of the actuation pulses is 20 msec. Using equations 6.1-2, and the time-averaged vapor areas (as noted in Figure 7.3, the vapor area in the presence of actuation is reduced by 59%), the global heat transfer coefficient in the presence of actuation increases by 144%. It is noted that the ejection frequency does not change appreciably in the presence of actuation indicating that the saturation pressure and temperature of the steam reservoir do not change appreciably, and therefore the time-averaged dissipated heater power and the vapor mass flow rate are nominally invariant. Furthermore, the time trace in the absence of actuation exhibits an occasional double-peak (e.g., at $t/T_b = 0.4$ or 1.4) corresponding to the ejection of a subsequent vapor bubble prior to complete condensation of the earlier bubble. This does not occur in the presence of pulsed acoustic actuation because the condensation starts earlier and is complete prior to the ejection of the next bubble. Time

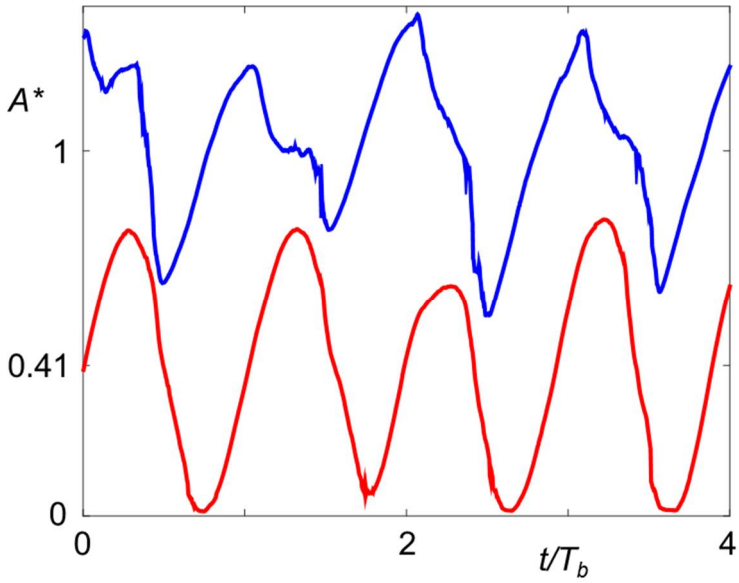


**Figure 7.3.** Time traces of total projected vapor area fraction above the orifice in the ***absence*** and ***presence*** of acoustic actuation. The time averaged values are noted by tick marks.

traces of the vapor volume of individual bubbles after their separation from the orifice in the absence and presence of actuation each normalized by its initial volumes along with the time trace of the vapor volume of the actuated bubble normalized by the initial volume of the bubble in the absence of actuation are shown in Figure 7.4. Although there is significant enhancement to the overall heat transfer (as demonstrated by Figure 7.3), the rate of the condensation in the presence of the pulsed short wavelength actuation is slower compared to the corresponding long wavelength actuation in Figure 6.2. This disparity in rates results from the pulsed modulation of the short wavelength actuation that is applied briefly during the bubble's growth and lasts only 20 msec ($0.4T_b$), ending close to the bubble detachment while the long wavelength actuation which is continuous can also enhance condensation after bubble detachment.

By moving the triggering laser to lower elevation ($h$ = 5 mm; $0.94d_o$), such that the actuation is triggered earlier during the formation of the vapor bubble, it is possible to reduce the vapor area further by reducing the scale of the detached bubbles in the

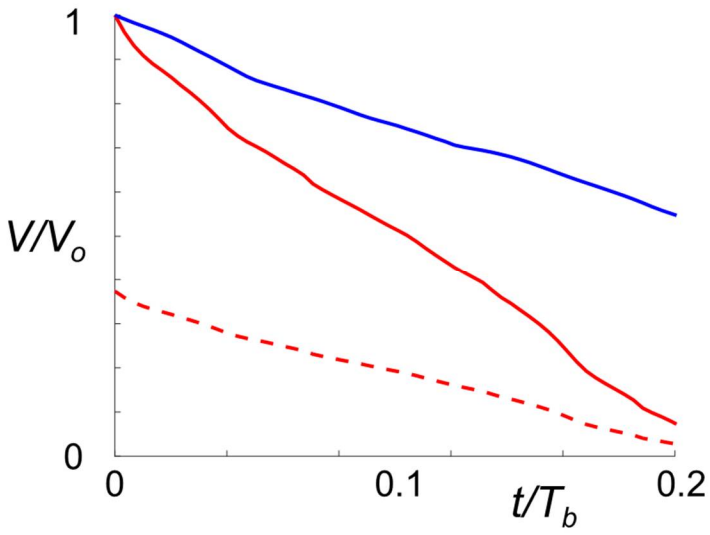


**Figure 7.4.** Time traces of vapor bubble volume as the bubble is advected away from the orifice in ***absence*** and ***presence*** of pulsed acoustic actuation. The dashed line is the time trace of the actuated bubble normalized by the volume in the absence of actuation.

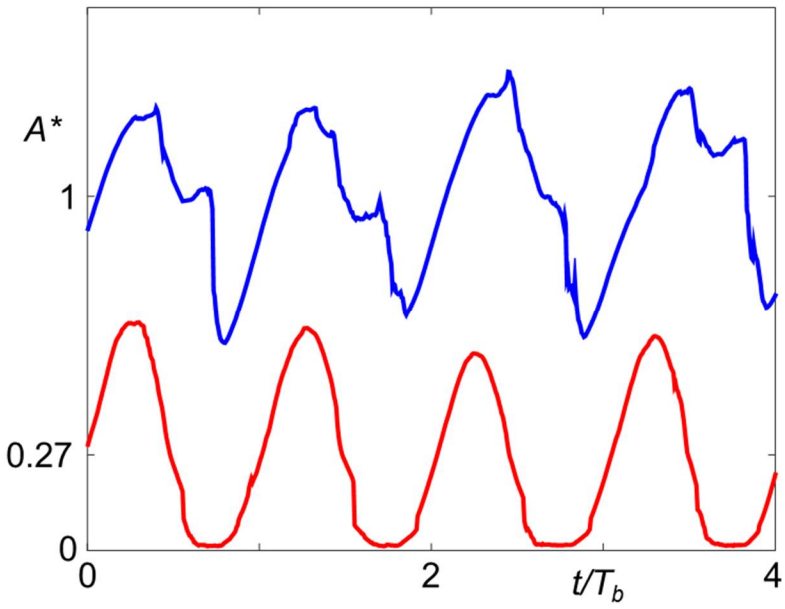


**Figure 7.5.** As in Figure 7.3 when the pulsed acoustic actuation (pulse duration is 20 msec) is triggered earlier during the formation of the attached bubble.

presence of actuation. In Figure 7.5, the triggering laser is placed 5 mm ($0.94d_o$) above the orifice (compared to 1 cm in Figure 7.3) while the duration of the actuation pulse is unchanged (20 msec), and the average vapor area is reduced by 73% (compared to 59% in Figure 7.3), which corresponds to an increase of 270% increase in the global heat transfer coefficient (144% in Figure 7.3). As noted in connection with Figure 7.3, the pulsed acoustic actuation eliminate the double-peak in the time traces of total projected vapor area fraction above the orifice in the absence of actuation. The time variation of the corresponding normalized volumes of the condensing vapor bubbles in the absence and presence of actuation after their separation from the orifice (Figure 7.6) shows that the initial volume of the actuated vapor bubble is significantly reduced when the pulsed actuation is applied earlier while the forming vapor bubble is attached to the orifice. Compared to the data in Figures 7.4 (trigger elevation $1.9d_o$), initial volume decreases from 37 to 15% of the initial bubble volume in the absence of actuation. As shown by the solid red line in Figure 7.6, the reduction in the initial volume in Figure 7.6 results in

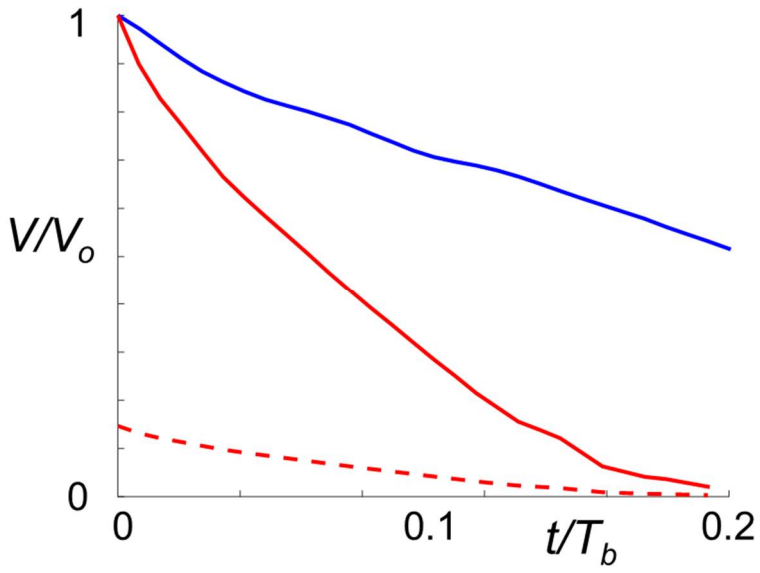


**Figure 7.6.** As in Figure 7.4 when the pulsed acoustic actuation (pulse duration is 20 msec) is triggered earlier during the formation of the attached bubble.

faster collapse and condensation since, compared to the larger initial actuated vapor bubble size (Figure 7.4, solid red line), the smaller bubble has a higher surface-to-volume ratio.

## 7.2 Pulsed Short-Wavelength Condensation at Reduced Vapor Mass Flow Rate

The role of pulsed short-wavelength actuation in enhancement of vapor condensation is investigated in detail using more sophisticated image processing including spatial and temporal tracking of the volumes of individual bubbles (and their area) in the absence and presence of pulsed acoustic actuation. Improved white-light and Schlieren imaging and analysis were achieved with nominally steady formation and detachment of a train of vapor with limited interaction between successive bubbles (compared to the configuration of §7.1) utilizing lower vapor mass flow rate through a smaller 2.3 mm diameter orifice at vapor power of 20 W, and subcooled temperature of 8±1 $^{o}$C ($T_b \approx 80$ msec). Pulsed modulated actuation was used at $T_{pulse} = 20$ msec, or 25% duty cycle.

The ensuing flow characteristics of trains of vapor bubbles in the absence and presence of actuation are depicted in Figure 7.7a-l and m-x. These images demonstrate the lack of interaction between subsequent bubbles for both naturally condensing and acoustically actuated bubbles (in contrast to Figures 7.1-2). In the absence of actuation, the vapor bubble grows at the orifice until pinch-off occurs around $t/T_b = 0.25$ (Figure 7.7e-f). The bottom interface, driven by surface tension, creates a liquid spear that propagates through the bubble (Figure 7.7g-h) before forming a torus (Figure 7.7i). This torus then breaks down (Figure 7.7j), and the bubble completely condenses. In the presence of actuation, when a triggering laser detects the bubble, a 20 msec acoustic pulse begins to deform the upper interface (Figure 7.7o). The combination of the liquid spear as well as droplet ejection increases the condensation rate such that the bubble's growth at the orifice is slowed (note the similar size between Figure 7.7o-r). After separation from the orifice (Figure 7.7r), which is also after the actuation pulse has ended, the bubble finishes naturally condensing.

Figure 7.8 shows Schlieren images of similar bubbles at a few key moments and allows visualization of the heat transfer process. The most important observations are the lack of thermal gradients surrounding the baseline bubble prior to the formation of the

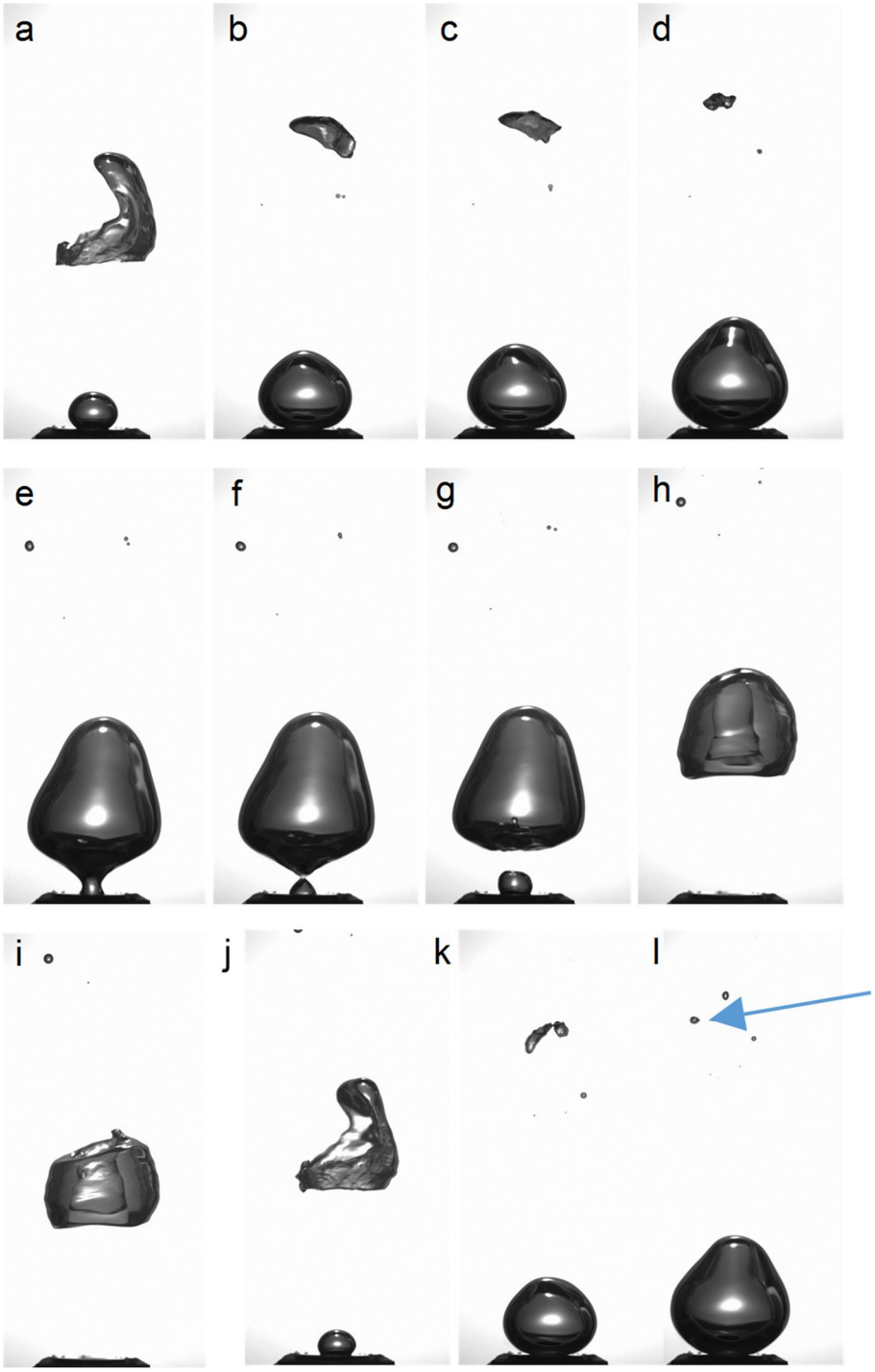


**Figure 7.7.** Images corresponding to moments of interest for Figures 7.12-7.15: $t/T_b$ = -0.125, 0.0, 0.019, 0.088, 0.250, 0.266, 0.294, 0.506, 0.559, 0.672, 0.834, 0.938. Arrow denotes position of tracked bubble in frame l.

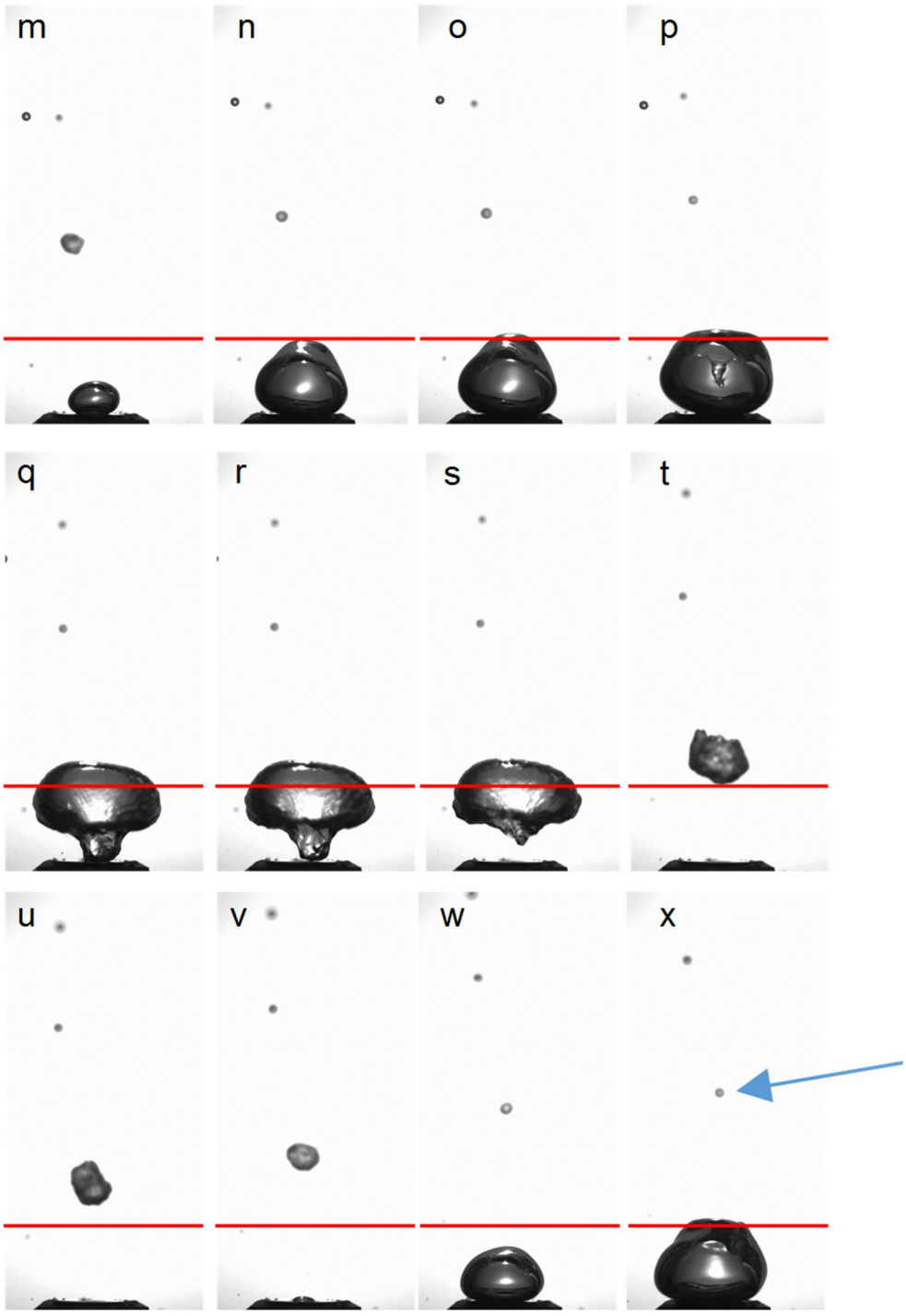


**Figure 7.7 continued.** Images corresponding to moments of interest for Figures 7.12-7.15: $t/T_b$ = -0.125, 0.0, 0.019, 0.088, 0.250, 0.266, 0.294, 0.506, 0.559, 0.672, 0.834, 0.938. Arrow denotes position of tracked bubble in frame x. The elevation of the centerline of the acoustic beam ($2.2d_o$) is marked in m-x.

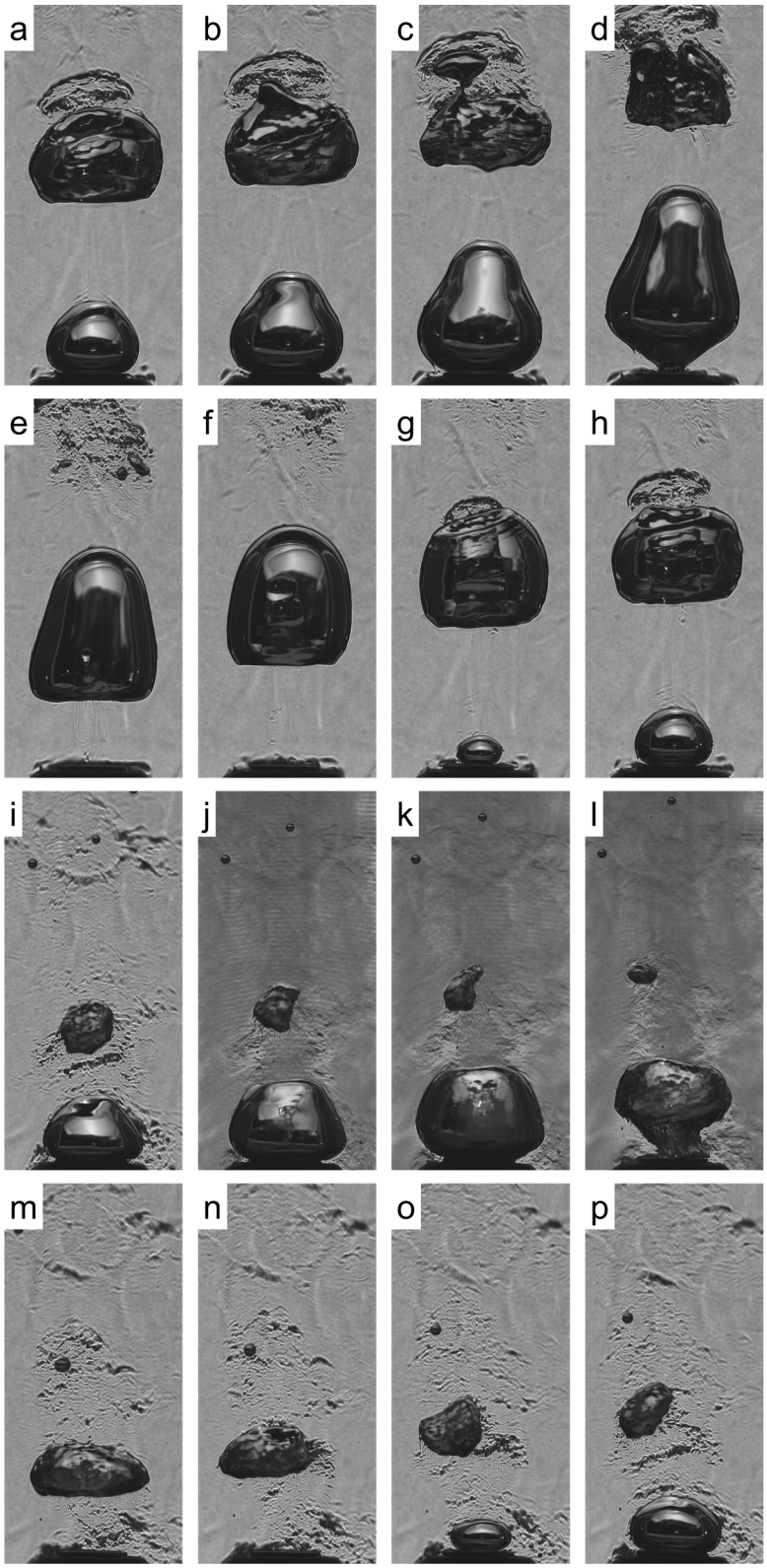


**Figure 7.8.** Schlieren images corresponding to flow fields of interest: $t/T_b$ = 0.0, 0.063, 0.125, 0.250, 0.375, 0.500, 0.625, 0.750.

torus (Figure 7.8f), and the enduring thermal gradients near the orifice in the case with acoustics actuation, due to the induced condensation while the bubble is near the orifice as well as the lower overall upwards trajectory of the bubble (Figure 7.8o). Clearly, when the bubble is naturally condensing, the majority of heat transfer is occurring at the inner surface and after the formation and collapse of the torus. The Schlieren images show the formation of a vortex ring consisting of hot fluid created by the torus formation process (Figure 7.8g-h); Chapter 8 will allow quantification of the velocities and vortices induced by this motion. Similarly, the torus which is formed via acoustic actuation also leads to a mass of hot fluid, albeit ejected through the bottom of the bubble near the nozzle (Figure 7.8m, under the bubble).

Using similar image area analysis as in Figures 7.3 and 7.5, the acoustic actuation in this configuration results in an average reduction of 53% (not plotted) in the vapor area corresponding to 112% increase in the global heat transfer coefficient, compared to 73% and 270% in §7.1, although the enhancement per degree of subcooling is slightly higher (14% vs. 11% per degree subcooling, respectively).

Data sets of time traces of the volumes of successive bubbles captured within the field of view ($7d_o$ x $21d_o$ above the vapor orifice) in the absence and presence of actuation are shown in Figure 7.9a. In addition to 30 individual traces for both the absence and presence of actuation (captured using 6 high-speed video sequences), the phase-averaged data ($<V(t)>$) and the boundaries of ±0.5 standard deviation (*std*) are also included for each set. The vapor volume within the field of view is normalized by the maximum phase-averaged vapor volume in the absence of actuation $\Psi$. In Figure 7.9a, $t/T_b = 0$ is selected to coincide with the onset of the pulsed actuation. All the individual traces are aligned in time so that at $t/T_b = -0.125$ (or -10 ms) the volume of the forming vapor bubble at the exit orifice is within $\pm 2.5 \cdot 10^{-3} \Psi$. This start point captured of the growth prior to actuation onset ($t/T_b = 0$) for the actuated bubbles, and essentially covered the

entire growth and collapse of the bubbles. Note that because the actuation is triggered when the bubble interface crosses the laser beam, there is a slight spread in the onset of actuation which is smaller than $\pm 0.01 T_b$ (or ±0.8 msec). The traces in Figure 7.9a show two distinct domains during the ejection cycle of successive bubbles that are characterized by rapid growth while the bubble is attached to the orifice and are followed by decay that is associated with the bubble detachment, advection and condensation. These data show that the magnitude of the characteristic growth rate is higher than the decay rate. As shown in Figures 7.7a-l, in the absence of actuation, the bubble reaches its maximum volume while it is still attached to the orifice, and begins to condense with a commensurate decrease in volume after it is detached from the orifice. However, as a result of the pulsed actuation (Figure 7.7m-x), the maximum volume is reached and then begins to decrease while the bubble is still attached to the orifice. The two data sets emphasize the difference between the evolution of the bubbles in the absence and presence of actuation. While in the absence of actuation there is relatively little scatter in the temporal occurrence of the maximum volume ($t_{max}std$ = 7.75x10$^{-3}T_b$, or 0.62 msec) where $\Psi$ = 0.822 cc and $\Psi std$ = 0.084 cc, in the presence of actuation the scatter in $t_{max}std$ is significantly higher (2.25x10$^{-2}$ $T_b$, 1.8 msec), $\Psi_{act}$ is 44% lower (0.361 cc) and with a significant increase in variance ($\Psi_{act}$-$std$ = 0.079 cc). The average size of the unactuated bubbles at ejection (0.822 cc) and the ejection rate (12.5 Hz) corresponded to a visualized heat rate of 13.9 W; corrected for the condensation which occurs during vapor bubble growth at this subcooling (69%), the vapor power dissipation is 20 W (Cho and Lee 1991). The losses from the experimental setup (140 W) are essentially the same as in §6.1 and 7.1 as the conditions in the lower tank (saturated liquid-vapor mixture) are unchanged.

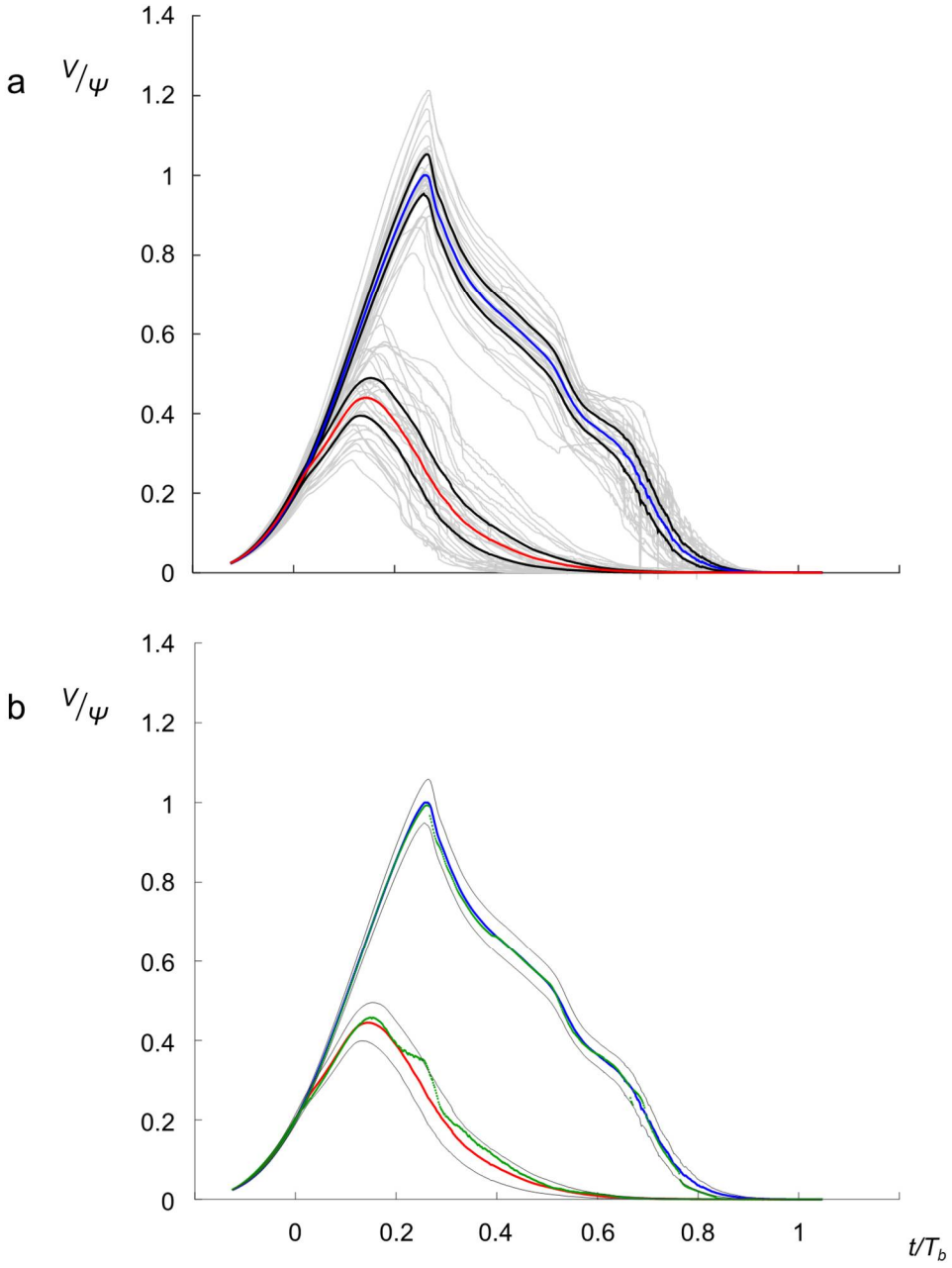


**Figure 7.9.** (a): Time traces of the volumes of successive bubbles captured within the field of view of Figure 7.7 in the absence and presence of actuation. In addition to **30 individual traces**, the phase-averaged volume (<V(t)>) (in the ***absence*** and ***presence*** of actuation) and the boundaries of ±0.5 standard deviation (std) are also included for each set (in **black**). The vapor volume within the field of view is normalized by the maximum phase-averaged vapor volume in the absence of actuation Ψ. (b): Comparison of vapor bubble volume, base flow and acoustically actuated, single instance (**green**). Average (***absence***, ***presence***) and 1-STD wide range (***black***) for baseline and actuation cases shown for reference.

In addition to considering the phase-averaged evolution of the vapor bubbles, it is also desirable to investigate details of the bubble dynamics by selecting a *single* representative realization within a given sequence that is reasonably close to the phase-averaged data in order to assess some the salient features that may be masked by the phase-averaged analysis. To this end, bubble realizations are selected so that the variation of their volumes are close to the phase averaged volumes in the absence and presence of actuation. These selections are shown in Figure 7.9b along with the phase-averaged and its standard deviation traces from Figure 7.9a. Note that the selected realizations are depicted in the images of Figure 7.7. In the absence of actuation, the volume of the individual realization is remarkably close to the phase-averaged trace during the entire ejection cycle. In the presence of acoustic actuation, the volume of the single realization is also close to the phase-averaged trace but exhibits a deviation in the range $0.2 < t/T_b < 0.3$ (including a change in slope at $t/T_b = 0.25$) as a result of the bubble detachment. In what follows, these individual realizations are analyzed along with the phase-averaged data.

The temporal variations in the volume of the attached and advected bubbles are assessed from time derivative of the average volume traces in Figure 7.12 $(T_b/\Psi)(dV/dt)$ in the absence and presence of actuation that are computed using a 5-point sliding average and plotted in Figure 7.10 ((a): average bubbles; (b): representative bubbles). These data show that prior to the onset of actuation (i.e., $t/T_b < 0$), the growth rate of the bubbles are identical. However, following the onset of actuation at $t/T_b = 0$, the volume growth is slower until the maximum volume is reached at $t/T_b = 0.142$ (about halfway through the actuation pulse), and thereafter the volume of the bubble decreases during the second half of the actuation pulse before the bubble becomes detached (cf. Figure 7.7q-r). These data show that the detachment occurs at about the same time ($t/T_b \sim= 0.25$) during the vapor ejection cycle in the absence and presence of actuation where the rate of the

decrease in volume is largest for the actuated bubble, and the bubble volume in the absence of actuation is largest. Following the termination of the pulsed actuation, the mean actuated bubble growth rate decays monotonically while in the absence of actuation the volume undergoes three distinct temporal changes (local peaks of $dV/dt$). Immediately following detachment ($t/T_b$ ~= 0.25) the volume is rapidly reduced by the deformation of the lower interface into the interior of the bubble (Figure 7.7f-g), the second peak at $t/T_b$ = 0.53 marks the formation of the torus (Figure 7.7h-i), and the third peak around $t/T_b$ = 0.7 is associated with the break-up of the torus (Figure 7.7j).

Figure 10b shows $(T_b/\Psi)(dV/dt)$ for the representative bubbles. For the naturally condensing bubble (blue), the curve is essentially unchanged (excepting additional noise). For the acoustically actuated bubble, there are two local minima in $(T_b/\Psi)(dV/dt)$, corresponding first to the shrinking of the bubble after its maximum volume is reached partway through acoustic actuation (t/Tb = 0.18), with a second corresponding to immediately after the pinch-off and separation from the nozzle (t/Tb = 0.26). Averaging over multiple acoustically actuated bubble realizations (Figure 10.a) obscures the presence of two distinct minima. Otherwise, there is agreement between the representative case and the mean over 30 bubbles.

Time traces of the positions of extrema on the front (upper) and back (lower) surfaces in the absence and presence of actuation are shown in Figure 7.11 for 5 bubbles within a continuous video sequence. In the absence of actuation, the top surface moves with nearly constant speed (0.38 m/sec) while the bubble is forming, and slows down (to 0.19 m/sec) following its detachment ($t/T_b \approx 0.25$) with a temporary pause at torus formation ($t/T_b \approx 0.5$), and then increases again (to 0.40 m/sec) following the formation of the torus ($t/T_b \approx 0.56$). The bottom surface moves at nearly constant speed (0.29 m/sec) following detachment (faster than the top surface) which increases further (to 0.78 m/sec) at $t/T_b >$ 0.7. In contrast, as result of the actuation, the top surface moves at a slower but nearly

constant speed (~0.13 m/sec) following actuation onset while the speed of the lower surface is nearly the same as in the absence of actuation from $t/T_b \approx 0.4$ through $t/T_b \approx 0.7$. Note the spread in interface location increases over time, marking the importance of examining not only the mean characteristics of bubbles but also representative examples whose details are not obscured by averaging. In three of the curves, for example, a

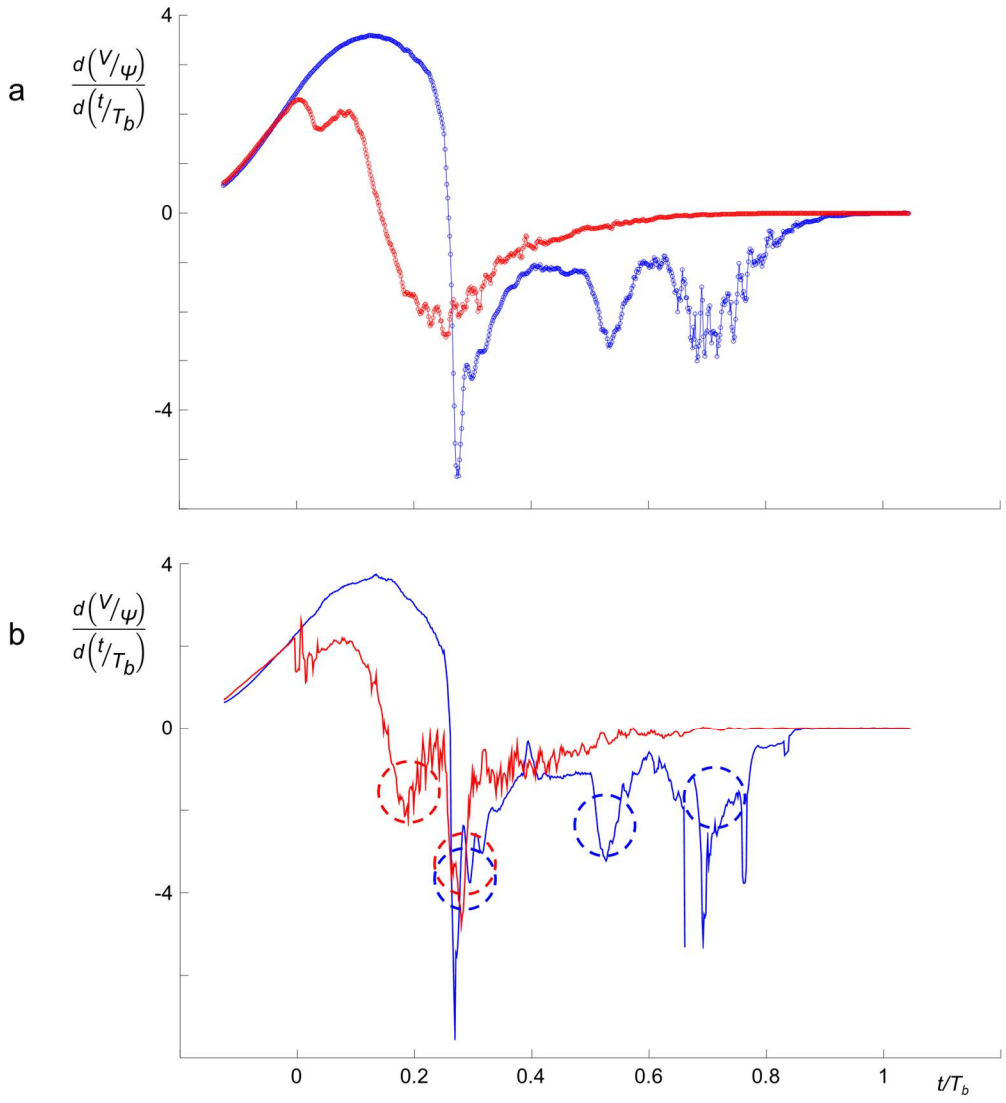


**Figure 7.10.** (a): Time derivative of the phase-averaged volume traces in Figure 7.7 in the ***absence*** and ***presence*** of pulsed actuation show that the curves begin to diverge following the onset of actuation at $t/T_b = 0$. (b): As in (a), but for the individual bubble realizations (cf. Figure 7.9b, green traces). Circles denote periods of high condensation.

temporary increase in upper interface location can be observed at $t/T_b = 0.42$; this corresponds to a droplet ejected from the liquid spear as it first forms after pinch-off which only occasionally exists. The sudden drop in upper interface location for one of the naturally condensing bubbles at $t/T_b = 0.7$ corresponds to a toroidal breakup which has caused multiple daughter bubbles, with the image processing routine following the larger, lower vapor mass after the break; such a bubble would make a poor choice for a representative case.

The temporal variation of the vapor volume is used in conjunction with a simple control volume analysis to assess the temporal heat transfer coefficient $U$ of the vapor bubbles and their total heat rate $\dot{q}$ as they are formed and advected (cf. Appendix A). The mass and energy balance of a deformable control volume whose boundary matches the

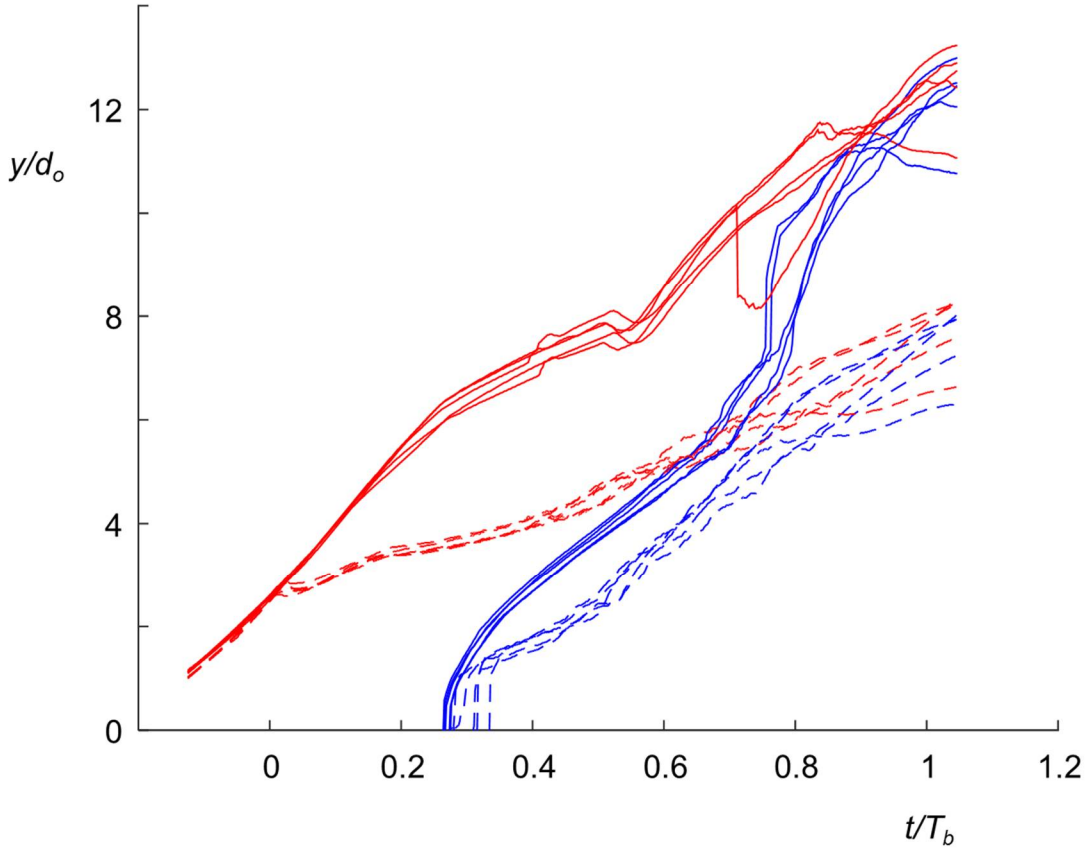


**Figure 7.11.** Time traces of the positions of extrema on the ***front (upper)*** and ***back (lower)*** surfaces of vapor bubbles in the absence (solid lines) and presence (dashed lines) of actuation for 5 bubbles within a continuous video sequence.

bubble interface are used in two time domains namely, before ($t/T_b < 0.25$) and after ($t/T_b > 0.25$) the bubbles are detached from the orifice. In the absence of actuation ($-0.125 < t/T_b < 0.25$) it is assumed that due to condensation at the bubble's surface there is a constant heat transfer coefficient such that the ratio between the total mass flow rate through the orifice and the integral of the bubble's growth rate satisfies the observed ratio (68% observed mass/actual mass), with the condensed mass (i.e. difference in total mass flow rate and observed growth) directly related to the constant heat transfer coefficient, the bubble area, driving temperature difference $\Delta T$ and the enthalpy of vaporization $h_{fg}$ (cf. Appendix A). In addition, in the presence of pulsed actuation ($0 < t/T_b < 0.25$) it is assumed that neither the actuation nor the enhanced condensation rate affect the mass flow rate through the orifice, leaving the overall heat transfer coefficient a function of the previously calculated overall heat transfer coefficient times the area ratio between the actuated and unactuated bubble, plus an *enhancement* of the heat transfer coefficient related to the difference in the volume growth rate between the unactuated and the actuated bubbles.

As shown in Appendix A, when the bubble is attached to the orifice ($-0.125 < t/T_b < 0.25$) the overall heat transfer coefficient is determined by:

$$U_{base} = \frac{\Gamma\left(\frac{h_{fg}}{v_g}\right)\int\frac{dV}{dt}dt}{\int 4\pi\left(\frac{3V}{4\pi}\right)^{2/3}\Delta T dt} \qquad 7.1$$

(where $\Gamma$ is the ratio between condensed mass flow and observed mass flow, $h_{fg}$ is the enthalpy of vaporization, $\Delta T$ is the temperature difference between the saturated vapor and the subcooled liquid and $v_g$ is the specific volume of the vapor phase), and is calculated to be $1.05 \cdot 10^4$ [W/(m$^2$K]. When the bubble is attached in the presence of

pulsed actuation ($0 < t/T_b < 0.25$), the overall heat transfer coefficient is:

$$U_{act} = \frac{\frac{h_{fg}}{v_g}\left(\frac{dV_{base}}{dt} - \frac{dV_{act}}{dt}\right) + U_{base} 4\pi \left(\frac{3V_{base}}{4\pi}\right)^{2/3} \Delta T}{4\pi \left(\frac{3V_{act}}{4\pi}\right)^{2/3} \Delta T} \quad 7.2$$

Following detachment, the overall heat transfer coefficient is simply:

$$U = \frac{-\left(\frac{h_{fg}}{v_g}\right)\frac{dV}{dt}}{4\pi \left(\frac{3V}{4\pi}\right)^{2/3} \Delta T} \quad 7.3$$

The instantaneous heat rate $\dot{q}(t)$ is determined by multiplying the heat transfer coefficient by the bubble's area and the $\Delta T$ between the saturated vapor and the subcooled liquid, and the time series of the computed heat transfer coefficient and heat rate had outliers removed using a Hampel filter (half-window size 2 msec). The computed $U$ [W/(m$^2$K)] and heat $\dot{q}$ [W] are left dimensional to enable simple comparison with results from the literature. The data near the common boundary of the time domains ($t/T_b = 0.25$) showed good agreement in magnitude (within ±7% of the local average value).

Figure 7.12a shows the time trace of the computed overall heat transfer coefficient based on the vapor volumes of the phase-averaged distributions and the representative realizations. In the absence of actuation, the overall heat transfer coefficient when the bubble is attached and growing was computed to be, on average, $1.05 \cdot 10^4$ W/(m$^2$K), which is of the same order of other measurements (e.g., Terasaka *et al.*, 1999). Following detachment, the heat transfer coefficient exhibits three peaks: during the pinch-off process, and during the formation and breakup of the toroidal volume. The highest overall heat transfer coefficients are observed during toroidal breakup, with a nominal magnitude of $3 \cdot 10^4$ W/(m$^2$K) and peaks up to $5 \cdot 10^4$ W/(m$^2$K). The heat transfer coefficient during growth, after detachment but prior to toroidal formation, and between toroidal formation and toroidal breakup is within $0.81 \pm 0.2 \cdot 10^4$ W/(m$^2$K). In the presence of acoustic actuation, the heat transfer coefficients of the representative realization and of

the phase averaged distributions are close with a few exceptions. Both distributions exhibit a sharp increase following the onset of the actuation [to $2.25 \cdot 10^4$ W/(m$^2$K)] followed by a gradual increase to a local maximum of approximately $5.5 \cdot 10^4$ W/(m$^2$K) at $t/T_b = 0.2$ and diminution near the termination of the actuation pulse actuation prior to bubble detachment. Diminution for the representative bubble is more rapid initially, although there is another, weaker peak at $t/T_b = 0.28$ for the representative bubble that is associated with the separation and pinch-off process, making the average value over this region nearly equal for the mean and representative cases. Following the detachment, both traces exhibit a slow reduction through the end of the ejection cycle. It is clear that the heat transfer coefficient traces in the absence and presence of actuation exhibit strong disparities during the formation of the attached bubble and during the breakup of the toroidal vapor volume in the absence of actuation. It is believed that the former difference is due to the influence of the acoustic actuation significantly increasing the heat transfer coefficient for the actuated bubble, and that the latter is due to the disparity of size and general velocity during toroidal breakup changing its relative influence (both are much greater for the relatively larger unactuated bubble).

The corresponding time traces of the heat rates from the vapor bubbles are plotted in Figure 7.12b. In the absence of actuation a pronounced peak in the heat rate (65-100 W) occurs at $t/T_b = 0.26$ following the detachment from the orifice while the bubble volume has just passed its largest point and is rapidly shrinking (cf. Figure 7.10). The time traces also include two additional peaks at $t/T_b = 0.53$ (38 W) and 0.7 (40 W) that correspond to torus formation and toroidal breakup. These peaks are remarkable because by this time, the volume of the vapor is significantly lower (cf. Figure 7.9) and the heat transfer area is reduced. The similarity of the heat rate magnitudes between $-0.125 < t/T_b < 0.25$ (when the bubble is attached), $0.38 < t/T_b < 0.5$ (after detachment and prior to the formation of the torus), and $0.58 < t/T_b < 0.63$ (after torus formation prior to its collapse) implies that,

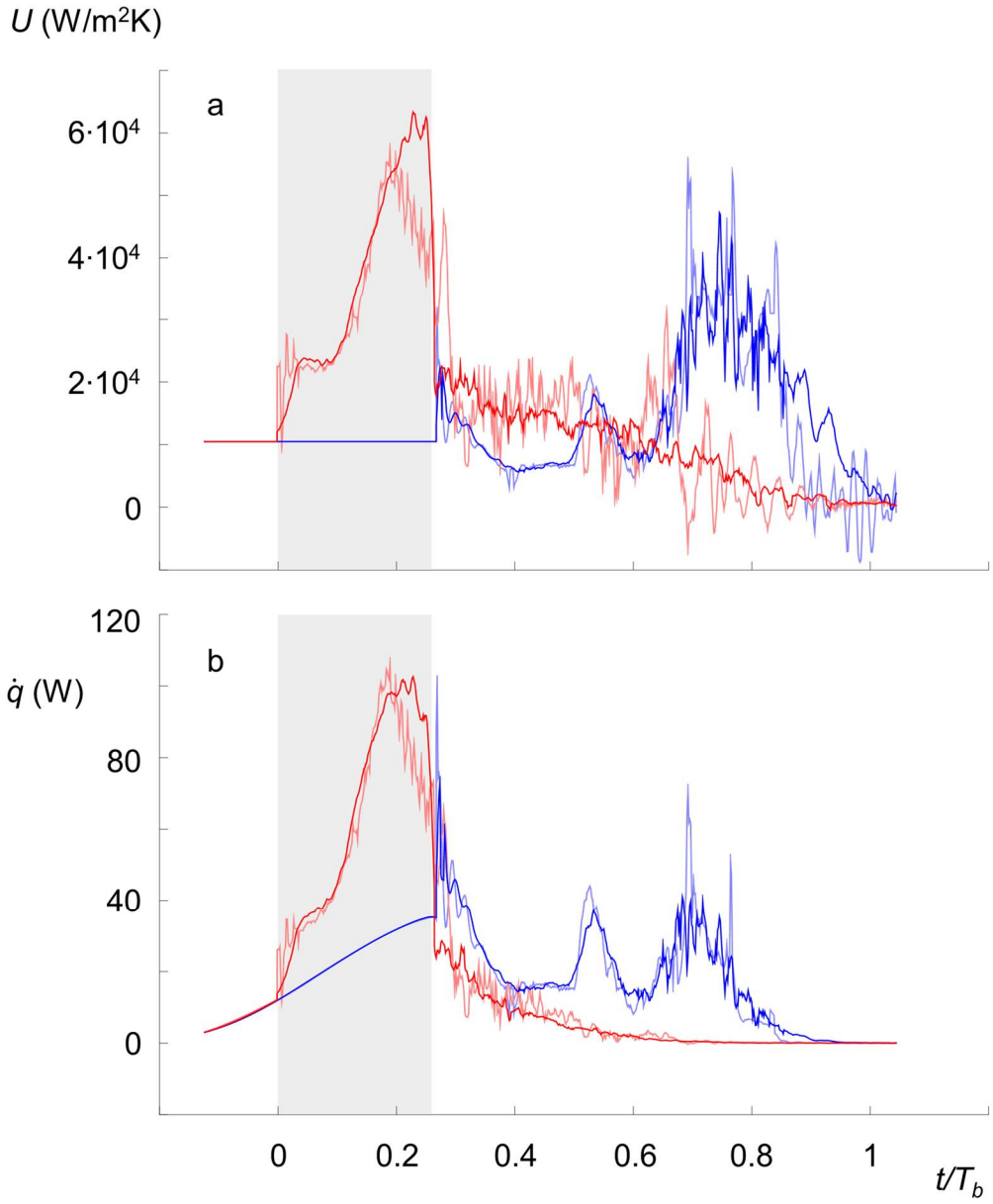


**Figure 7.12.** Time traces of the overall heat transfer coefficient (a) and heat rate (b) for the phase averaged and the representative realization in the absence (***phase averaged***, and ***representative realization***) and presence (***phase averaged***, and ***representative realization***) of pulsed actuation (20 msec). Shaded region denotes time when acoustic actuation pulse is active, if applicable.

absent any topological changes of the bubble surface, the heat rate is on average 16 W. Similar to the temporal changes in $U(t)$ (Figure 7.12a), following the onset of actuation, there is an immediate jump in heat rate to about 32 W that is followed by growth to a peak of ~100 W at $t/T_b = 0.2$, well before the acoustic actuation is terminated. As shown in Figure 7.16b, the time trace of the representative realization shows another narrow local peak in heat rate (65 W at $t/T_b = 0.28$) that is associated with the detachment. Following the detachment, the heat rate decreases monotonically through the end of the condensation process (without the large increase associated with toroidal breakup which was observed in the naturally condensing bubble at $t/T_b = 07$).

### 7.3 Sideward Short-Wavelength Actuation

The effect of the pulsed short wavelength actuation when the acoustic beam is oriented normal to the centerline of the orifice aimed across the orifice (cf. Figure 3.3d) and operated in a continuous mode is shown using a sequence of high-speed images (7.5 msec apart) in Figures 7.13 (white light) and 7.14 (Schlieren) at the same operating thermal conditions as in Figures 7.1 and 7.2. Images of bubble formation and condensation in the absence of actuation (Figures 7.13a-e, similar to the corresponding images in Figure 7.1) are included for reference and show the liquid-vapor interface pinch-off during detachment, the formation of the liquid spear, and the bubble collapse

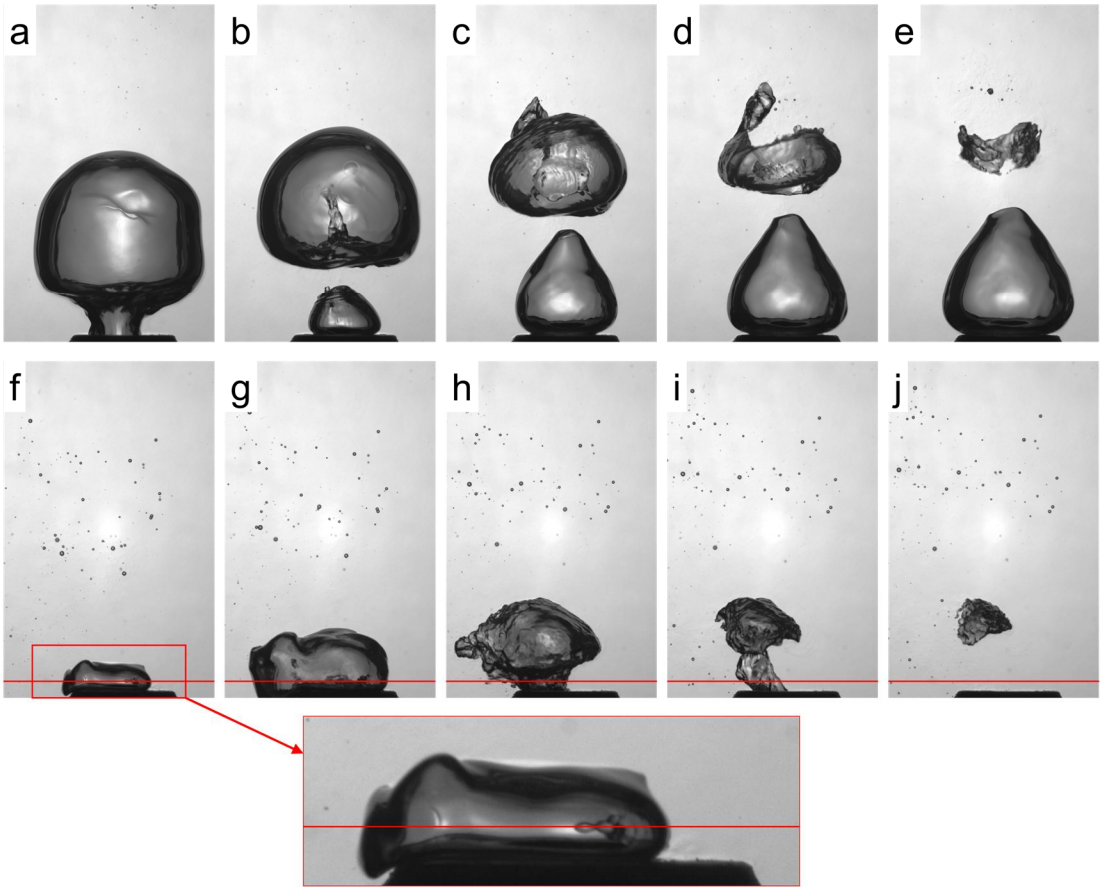


**Figure 7.13.** High speed video images (7.5 msec apart) of vapor bubble formation in the absence (a-e) and presence (f-j) of continuous acoustic actuation (20 msec) normal to the centerline of the orifice. The formation of the liquid spear is shown in the enlarged inset. The elevation of the centerline of the acoustic beam ($0.25d_o$) is marked in f-j.

following its detachment. In Figure 7.13f-j the centerline of the continuous acoustic beam is normal and intersects the centerline of the vapor orifice (from right to left) at $0.25d_o$ above the exit plane (the nominal beam diameter is between $-0.7 < y/d_o < 1.2$). These images show significant differences between the evolution of the vapor bubbles when the actuation is applied normal to the centerline of the exit orifice of the vapor (e.g., Figures 7.1f-j and 7.13f-j). This difference is associated with the *direction* of the surface force that is effected by the actuation and the ensuing condensation. When the actuation is applied normal to the centerline of the vapor orifice, the vapor mass is deflected horizontally during its formation (to the right in by about $1.5d_o$ in Figures 7.13f and g) as a result of the surface force effected by the actuation on the liquid-vapor interface. The images in Figures 7.13-14 and the data in Figure 7.15 indicate that the forming vapor bubble is forced to detach from the orifice when it reaches a given size (that is determined by the amplitude of the actuation and the cross sectional scale of the acoustic beam), and therefore, the formation process is sped up and the detached bubbles are smaller than in Figure 7.2.

In common with Figure 7.1, the images in Figure 7.13 show the formation of an induced liquid spear, however, here the spear is penetrating the bubble volume horizontally from the right towards its left side. The onset of the formation of the spear is visible in a magnification of Figure 7.13f that is shown as an inset. The formation of the spear results in internal ejection of liquid droplets that are evident on the surface in Figures 7.13g and h as the entire bubble is deflected farther to the left and rapidly collapses and condenses in the bulk liquid (Figures 7.13i and j). The corresponding Schlieren images to Figure 7.13 in the absence and presence of actuation are shown in Figure 7.14a-e, and f-j, respectively. Perhaps the most salient feature in the presence of actuation is the left tilt (nearly $35^o$ relative to the centerline of the orifice) of the thermal plume that marks trajectory of the detached vapor bubbles as they condense. This

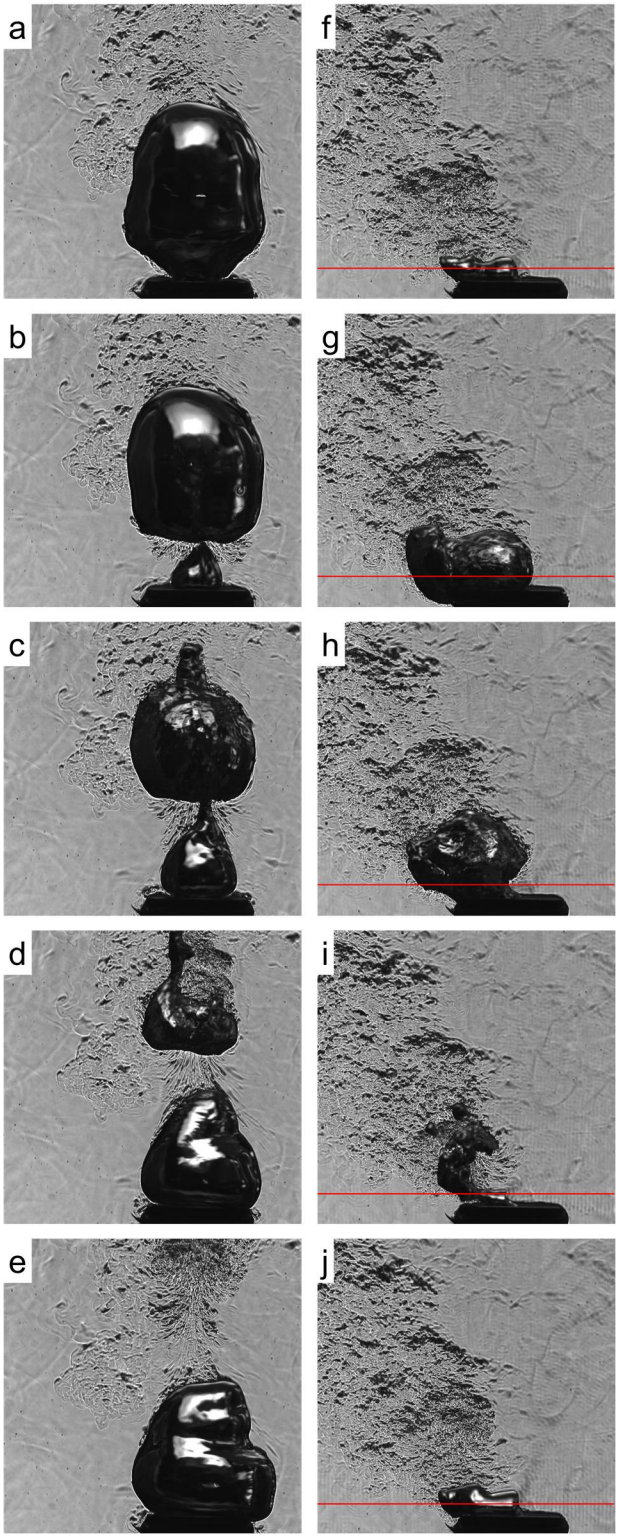


**Figure 7.14.** High-speed Schlieren images as in Figure 7.2 when the continuous actuation is normal to the orifice centerline. The elevation of the centerline of the acoustic beam ($0.25d_o$) is marked in f-j.

trajectory marks the balance between the buoyancy force and acoustic surface force plus asymmetric bubble collapse that results in the deflection of the bubbles and marks the enhanced rate of condensation. It is noteworthy that the deflection diminishes towards the upper left side of the images ($y/d_o > 3.5$) as the acoustic force diminishes as the vapor volume leaves the beam. While in the absence of actuation the collapse of the bubble appears to lead to the formation of a vortex ring (Figures 7.14a-c, and Figure 7.2 above) of condensed fluid that continue to move vertically as a result of the impulse of the vortex (cf. Chapter 8), the interaction with the acoustic beam apparently prevents the formation of an organized vortex.

Time traces of total projected vapor area fraction above the orifice in the absence and presence of side acoustic actuation corresponding to the high-speed video sequence of Figure 7.13 are shown in Figure 7.15. These data indicate that side actuation leads to a larger decrease in vapor area compared to normal actuation (along the orifice centerline, cf. Figures 7.3 and 7.5) of up to 77% compared to 73%, respectively. The corresponding increase in the global heat transfer coefficient by side actuation relative to the flow in the

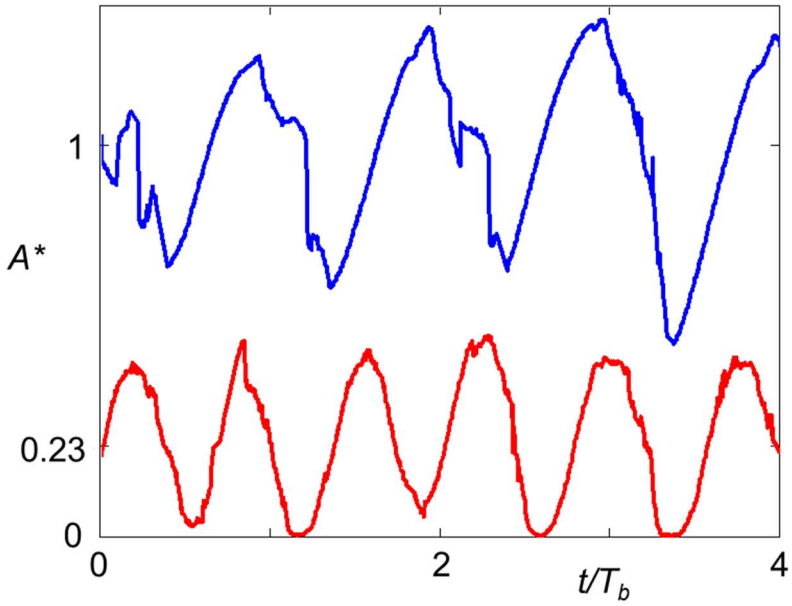


**Figure 7.15.** As in Figure 7.3 during continuous acoustic actuation normal to the centerline of the vapor orifice ($0.25d_o$).

absence of actuation is 330% (compared to 270% for normal actuation). Clearly, these increases are partially associated with the increased duty cycle of the side actuation (100% compared to 40% for normal actuation), indicating that the efficiency of pulsed actuation is actually higher. Another feature of the time trace in the presence of side actuation is the increased frequency of vapor bubble formation and detachment compared to the detachment frequency in the absence of actuation (~30 and ~20 Hz, respectively). As noted above, this is the result of the forced detachment of smaller bubbles by the acoustic side force when they reach a critical volume that is determined by the acoustic intensity, the diameter of the acoustic beam, and the bubble residence time.

# CHAPTER IIX

## PARTICLE IMAGE VELOCIMETRY OF PULSED ULTRASONIC CONDENSATION

As discussed in Chapter 7 in connection with the Schlieren visualization (cf. Figure 7.2), condensation enhancement by pulsed, short-wavelength acoustic actuation is effected by two potential mechanisms. First, the deformation of the liquid-vapor interface that scales with the characteristic length of the bubble of as a result of the acoustic radiation pressure, and second, the formation of small-scale droplets that are ejected from the liquid spear that protrudes into the vapor volume as a result of local focusing of the acoustic beam. The role of droplet formation in the condensation was assessed by estimating the liquid mass that is atomized at the liquid vapor interface by pulsed acoustic actuation. An upper bound was estimated by placing the ultrasonic transducer below the free surface in a water tank such that the acoustic beam is directed normal to the surface. The tank was placed on a scale, and an air stream flowing along the free surface was used to sweep the formed droplet away and prevent them from falling back into the water. When the actuator was operated for 500 pulses of 20 msec each, the mass loss of water from the tank was 10.35 grams or 0.0207 gram/pulse. Using a simple energy balance, the minimum water mass (assuming a temperature rise from the subcooled liquid temperature to the saturation temperature) required to absorb the heat of complete phase change of a nominal (single) vapor bubble in Chapter 7 is $m_{droplets} = E/(c_p \cdot \Delta T) = [(V_o/v_g) \cdot h_{fg}]/(c_p \cdot \Delta T) = 0.033$ grams. Therefore, the mass of the ejected droplets in a single actuation pulse represents, at most, 63% of the mass required to completely condense a bubble, with incomplete temperature rise likely due to the

droplets short residence time. Therefore, it is assessed that condensation enhancement is partially due to the large-scale deformations of the liquid vapor interface.

The present chapter focuses on PIV measurements (cf. §3.4) of the velocity field associated with the interface deformations in the absence and presence of actuation with the objective of elucidating some aspects of the role of surface deformations in the heat transfer from the bubbles and the ensuing condensation. Two sets of measurements are conducted in the warm liquid surrounding condensing non-interacting (nearly isolated, §7.2) and interacting (cf. §7.1) vapor bubbles and are described in §8.1 and §8.2. The dynamics of isolated vapor bubbles are compared with the flow around air bubbles of similar volume that are rising in an isothermal liquid bath.

Because of the dispersion in the path followed by successive bubbles that are rising freely under buoyancy in the liquid bath, phase-averaged data can mask some important features of the instantaneous flow field in a single realization. Therefore, the present measurements rely on the similarity of individual realizations to the phase-averaged measurements (as discussed in connection with Figure 7.9). The present PIV measurements are acquired at high frame rates (10 kHz) and are temporally averaged over a subset of 5 consecutive frames (0.5 ms) during which the bubble position is nearly invariant (within 0.2 mm) and flow field does not change appreciably. This approach overcomes potential deficiencies (e.g., missing velocity data) in individual images and velocity vectors that are greater than one standard deviation from the corresponding subset mean are removed. In the present data the domain on the far side of the bubble (relative to the direction of the laser sheet) is masked to remove the optically distorted region of the laser sheet caused by passing through the vapor volume.

The liquid-vapor interface of a given vapor bubble was determined from the instantaneous PIV measurements by finding the extent of the blanked vectors along the centerline of the orifice. The positions of the extents of the blanked vectors corresponded

to the region masked by the image processing routines prior to PIV processing which were specifically employed to remove the bubble from the PIV vector field (§3.4). If necessary, the extents of a particular blanked region could be recorded between frames to track a specific bubble (if multiple bubbles existed along the centerline at a time). Figure 8.1 shows a vector field overlayed on a representative bubble; the locations along the

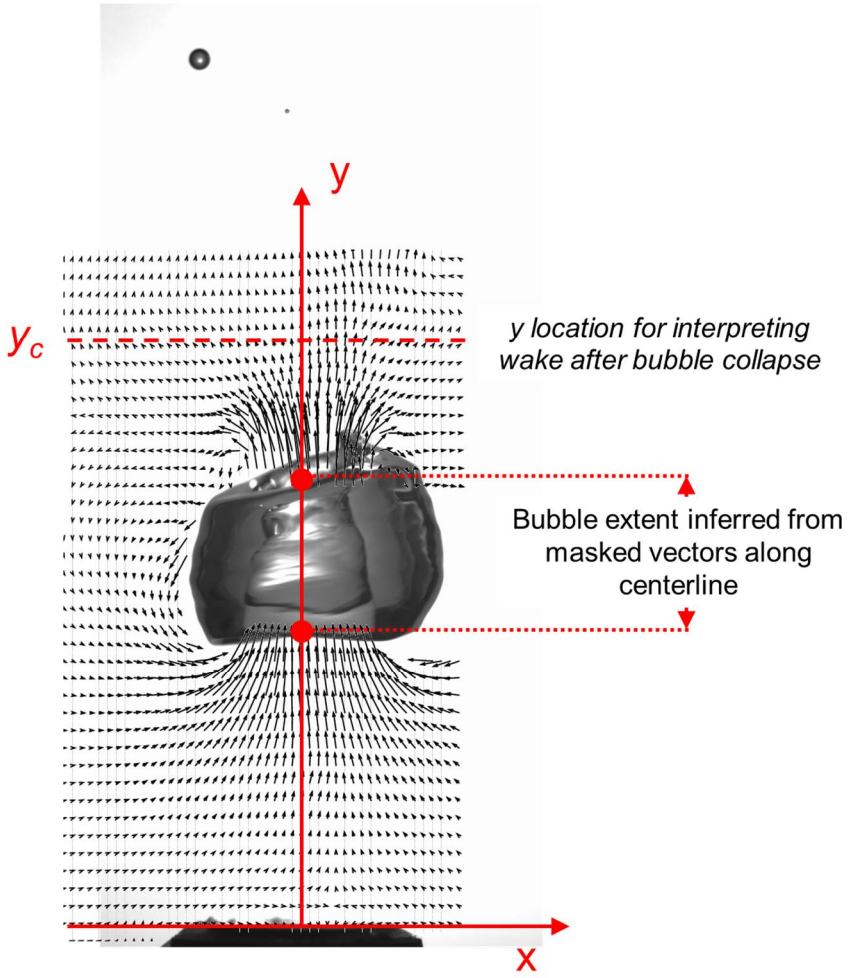


**Figure 8.1.** Comparison of an image of a vapor bubble (cf. Figure 7.7) with a distribution of velocity vectors in a PIV image of a corresponding vapor bubble that is formed under the same thermal conditions. The vertical elevation of the bubble may be inferred from the overlaid PIV data, and the streamwise height of the vapor volume may be assessed from its intersection with the $y$ (vertical) axis. The dashed line $y = y_c$ is the height at which the bubble exhibits complete condensation. The PIV and the image fields of view are not the same.

centerline in the PIV data used to infer the extents are noted. Also denoted in Figure 8.1 is a cross-stream line at height $y = y_c$, the height at which complete condensation occurred. Data at elevation $y_c$ will be used to interrogate the wake of the collapsed bubble.

### 8.1 The Flow Field of Non-Interacting Vapor Bubbles

In order to select a PIV data sequence of the most representative realization, a fourth-order polynomial fit to the inferred position of the bubbles' liquid-vapor interfaces in several PIV sequences captured in the absence and presence of actuation were compared with the corresponding interfaces of the representative realizations in §7.2 (cf. Figures 7.7 and 7.11), and the closest visual interfacial match was selected. The fitted trajectories of the top and bottom interfaces of the bubbles in the selected PIV sequences (in the absence and presence of actuation), are plotted in Figure 8.2 along with the corresponding trajectories of the interfaces based on the image sequences of the representative realization (Figure 7.7). Note that the PIV data only captures the slice of the bubble in the laser sheet, and the interface was determined solely by the extent of the blanked vectors along the centerline. When tracking bubbles in §7.2, the full extents of the bubble interfaces were used (i.e. the high and low points could be both off-center and at a different depth from the PIV plane). For this reason, the fit is significantly better when the bubble is more axi-symmetric; that is, prior to the torus formation, with the fit suffering greatly at toroidal collapse (cf. Figure 8.1, where the rear interface of the torus is clearly higher than the front interface; PIV data would not perceive this). Note that in Figure 8.2, the torus forms at $t/T_b \approx 0.5$; by $t/T_b \approx 0.6$, the interface curves computed by the PIV (especially the top interfaces of the naturally condensing bubbles) diverge from the white-light interface curves as the PIV routine can no longer track interfaces collapsing outside of its interrogation region. The actuated bubbles do not suffer from the same problem, possibly due to the reduced size of the vapor bubble at toroidal collapse reducing the propensity for the remaining vapor to move significantly off-center.

The trajectories of the vapor bubbles (denoted by the blanked area without vectors) can also be assessed from *y-t* diagrams of color raster plots of the vertical velocity along the centerline of the bubble $v(y, t; x = 0)$ in the absence (Figure 8.3a) and presence (Figure 8.3b) of pulsed actuation. In this formulation, Figures 8.3a and b show the time history of the streamwise velocity at some fixed elevation $y$ = const above the orifice and the velocity along the centerline at some given time $t$ = const during the ejection cycle. The position of the bubble on the centerline is visualized by a blanked line segment that is occupied by vapor. Relative to the onset of the PIV data acquisition in these measurements, the pulsed actuation was triggered $0.063T_b$ (5 msec) later, and the detachment of the bubbles in the absence and presence of actuation occurred about $0.32T_b$ (25 msec) and $0.37T_b$ (29 msec) after PIV acquisition onset, respectively; the data time series was shifted such that actuation starts at $t/T_b = 0$. The PIV data were normalized

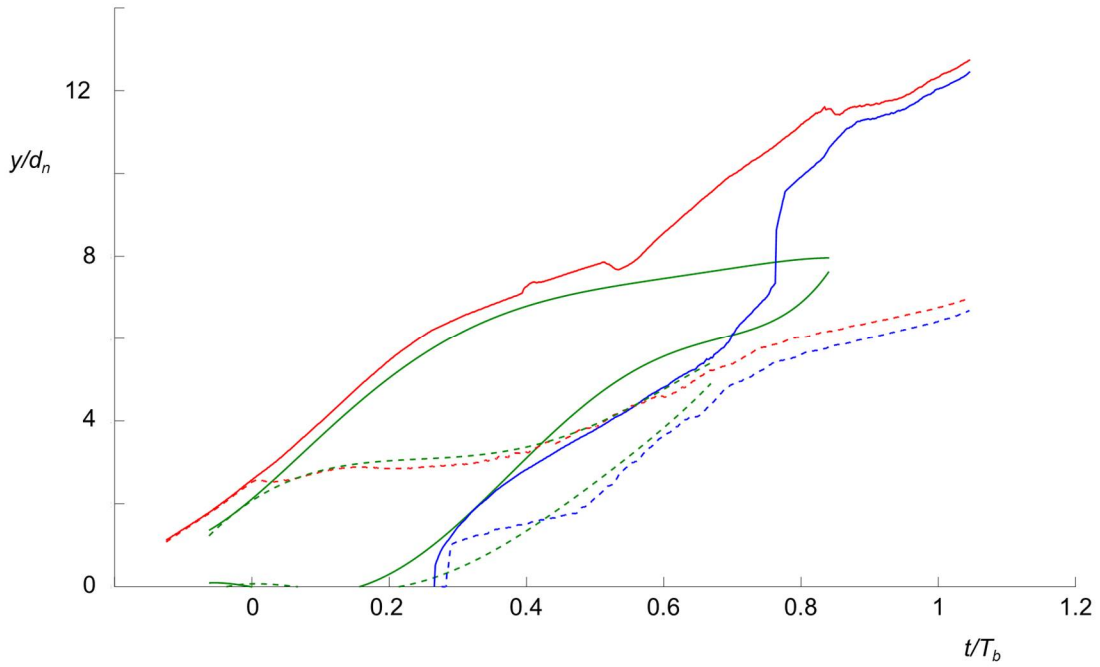


**Figure 8.2.** Time traces of the positions of extrema on the front (***upper***) and back (***lower***) surfaces of vapor bubbles in the ***absence*** (solid lines) and ***presence*** (dashed lines) of actuation from images of the preferred realization, and centerline extrema of the ***PIV data*** (using 4th order polynomial fit).

using the same characteristic scales as in §7.2: $d_o$ = 2.3 mm, $T_b$ = 80 msec, and terminal velocity $V_t$= 0.55 m/sec.

In the absence of actuation (Figure 8.3a), the motions of the top and bottom interfaces are similar to the data in Figures 7.10 and 7.12. While the bubble is attached (cf. Figures 7.7a-e), the top interface and the fluid displaced by the interface moves at nearly constant speed ($v/V_t \approx 0.75$). Following detachment ($t/T_b$ = 0.32, cf. Figures 7.7f-l) the top interface begins to slow down (nominal speed $0.45V_t$) while the bottom interface accelerates as the pinch off due to surface tension drives the lower interface of the bubble upwards to form a torus ($0 < y/d_o < 2.5$, $0.27 < t/T_b < 0.38$, with nominal and peak vertical velocity $v/V_t$ = 1.49 and 1.78, respectively). The vapor connected to the reservoir moves downwards after the vapor bubble separates, inducing a downward motion in the adjacent liquid ($0 < y/d_o < 0.3$ and $0.3 < t/T_b < 0.6$). As noted in connection with the images in Figure 7.8g-h, the formation of the torus is accompanied by vertical (streamwise) ejection of liquid as is evident by the streak of higher streamwise velocity within the domain $7 < y/d_o < 11$, $0.5 < t/T_b < 0.8$ with speeds in the range $1.27 < v/V_t < 1.46$ while the top interface slows down relative to the bottom interfaces, and the bubble scale diminishes. The collapse of the torus (cf. Figure 7.8d-e) induces another jet-like ejection in the domain $7.5 < y/d_o < 10$, $0.78 < t/T_b < 0.93$ with a somewhat slower speed $1.09 < v/V_t < 1.27$. These observations corroborate the conjecture made by Eames (2010) that the advection of the vortex that forms following the collapse of the bubble (as depicted by the slope of the high axial velocity streak $7 < y/d_o < 10$, $0.55 < t/T_b < 0.8$) is commensurate with the speed of the bubble's initial motion, although the data in Figure 8.3 indicates a better agreement with the speed of the top interface of the *attached* bubble rather than the *unattached* bubble (as can be inferred from the slope of the blanked domain).

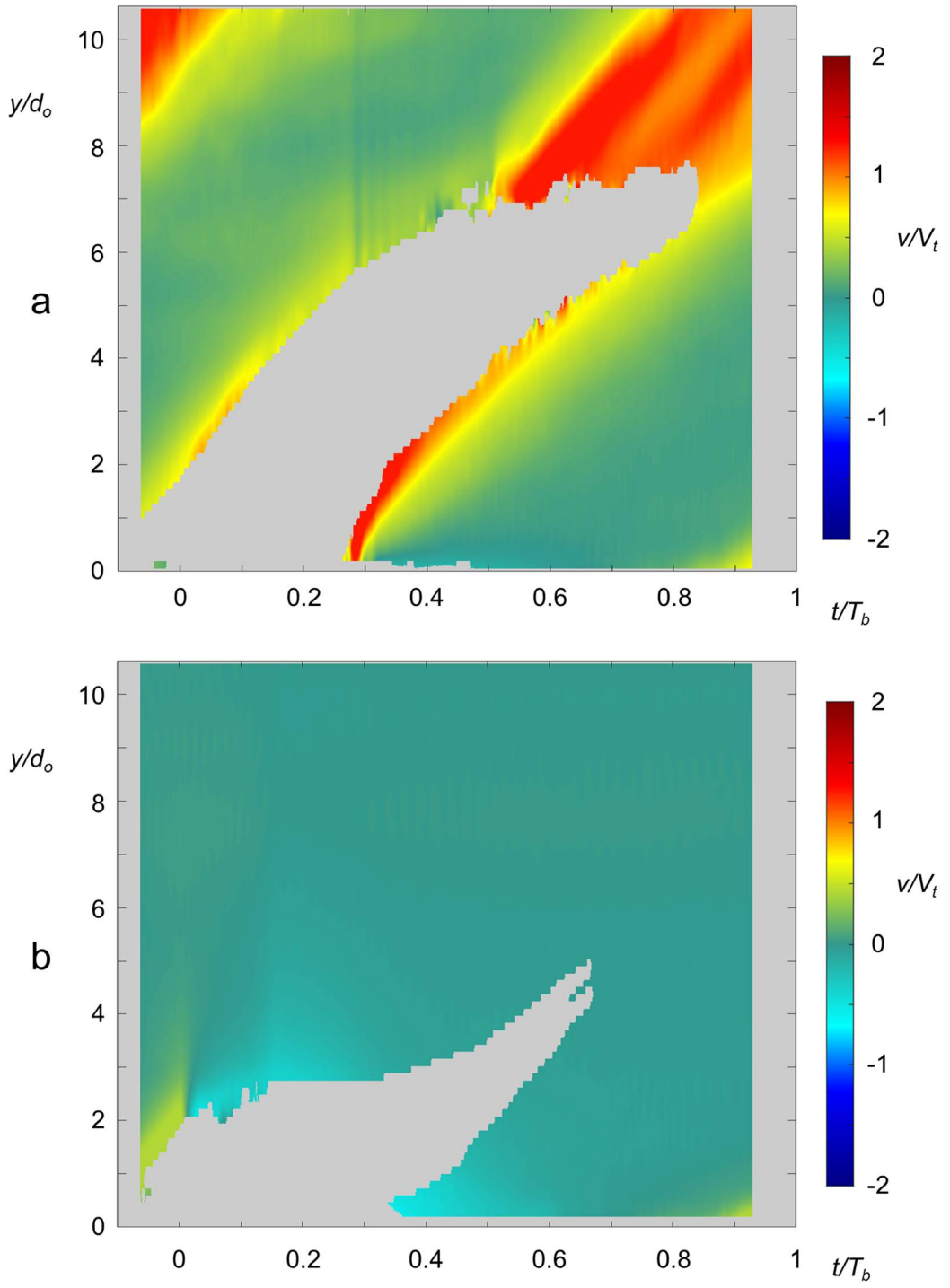


**Figure 8.3.** Color raster plots of *y*-*t* distributions of the vertical velocity along the centerline of the bubble $v(y, t; x = 0)$ in the absence (a) and presence (b) of pulsed actuation. This presentation yields the time history of the streamwise velocity at some fixed elevation $y$ = const above the orifice and the velocity along the centerline at a given time $t$ = const during the ejection cycle.

In the presence of actuation (Figure 8.3b) there is a profound change in the spatial and temporal shape of the vapor bubble as a result of the enhanced condensation, and in the corresponding characteristics of the motion along the centerline, as manifested in the motions of the top and bottom interfaces. While before the onset of the actuation ($t/T_b < 0$) the interface motion is similar to Figure 8.3a, during the actuation ($0 < t/T_b < 0.25$) the top interface slows down and appears to stop at $y \approx 2.75d_o$ while the bubble is still attached as the downward spear is formed by the actuation (cf. Figures 7.7o-q). These changes are accompanied by liquid flow along the centerline towards the bubble ($2 < y/d_o < 3$, $0 < t/T_b < 0.3$) although the nearly immediate onset and absence of significant downward flow at $y/d_o > 5$ demonstrates the insignificance of acoustic streaming. The motion of the bottom interface which commences after detachment (and the termination of the actuation, cf. Figures 7.7r; 7.8 m-n) is also considerably slower than in Figure 8.3a, and the axial velocity behind the upward motion of the interface is reversed ($0 < y/d_o < 0.5$, $0.32 < t/T_b < 0.6$). Similar to Figure 8.3a, when the bubble forms a torus at $t/T_b \approx 0.5$, the axial velocity at the exit (for the actuated bubble, the bottom interface; for the naturally condensing bubble, the top interface) interface is faster than the entrained flow at the intake interface ($-0.68V_t$ compared to $-0.21V_t$, where the respective speeds in the absence of actuation are $1.36V_t$ and $0.91V_t$). The higher speed at the bottom interface in the presence of actuation may be attributed to the combined effects of the actuation and the condensation process. However, in the absence of actuation, the initial deformation induced by surface tension restricts motion once the curvature of the lower interface changes rather than continuing to accelerate the interface and therefore the increased flow rate (out of the torus) is entirely due to condensation. This will be corroborated by comparison to the dynamics of flow around a detaching air bubble of similar volume in the absence of condensation shortly. Near the end of the ejection cycle, the vertical flow recovers in the domain $y/d_o < 1$ and $t/T_b > 0.8$,

corresponding to the upwards flow which precedes the ejection of a subsequent bubble from the orifice that is similar to the flow in the absence of actuation in Figure 8.3a indicating that the conditions at the orifice (and the steam reservoir) are not significantly altered by the pulsed actuation.

The effects of condensation on the bubble dynamics depicted in Figures 8.3a and b are assessed by comparing its evolution and flow field to the flow around an air bubble that is ejected from the same orifice into an isothermal tank and has nearly the same volume when it detaches from the orifice before forming a torus. In order to avoid interactions between successive air bubbles the mass flow rate of the air bubbles was reduced and their detachment frequency was significantly lower ($T_b$ = 500 msec compared to 80 msec for the vapor). Figure 8.4 shows side by side high-speed images of vapor and air bubbles of similar volumes prior to detachment (Figure 8.4a). However, after separation from the orifice, the condensation process aids the formation of the torus and therefore the torus of the vapor bubble forms after a shorter time period and at a lower elevation than the air bubble and the characteristic scale of the vapor bubble rapidly diminishes due to condensation (Figures 8.4b-f).

Because of the disparity in the temporal and spatial evolution of the air bubbles, the PIV field of view that was needed to capture their evolution had to be extended and to capture bubble detachment, advection, and the formation of the toroidal volume, the PIV field of view was "stitched" from two smaller fields at different elevations (these vapor and air bubbles have the same terminal velocity $V_t$ = 0.55 m/sec). Similar to Figure 8.3, Figure 8.5 shows color raster plots of *y*-*t* distributions of the vertical velocity along the centerline of the air bubble $v(y, t; x = 0)$. Note that the discontinuity around $y/d_o = 10$ is due to lower light intensity at the edges of the laser sheet. Of primary interest is the evolution and speed of the upper and lower interfaces of the air bubble during its initial advection and following the formation of the toroidal volume compared to the

condensing vapor bubble. Although the data in Figure 8.5 show that the air bubble rises slightly faster than the vapor bubble in the absence of acoustic actuation (e.g., $7.2d_o$ vs. $7d_o$ at $t$ = 36 msec) and the torus forms later and at a higher location, they share several similar features: following separation from the orifice, the upper interface slows from $0.72V_t$ to $0.37V_t$ ( the change in slope at $y/d_o = 6$, $t/T_b = 0.05$ corresponds to Figure 8.4b), the highest speeds (up to $1.09V_t$) are associated with the pinch-off, and prior to torus

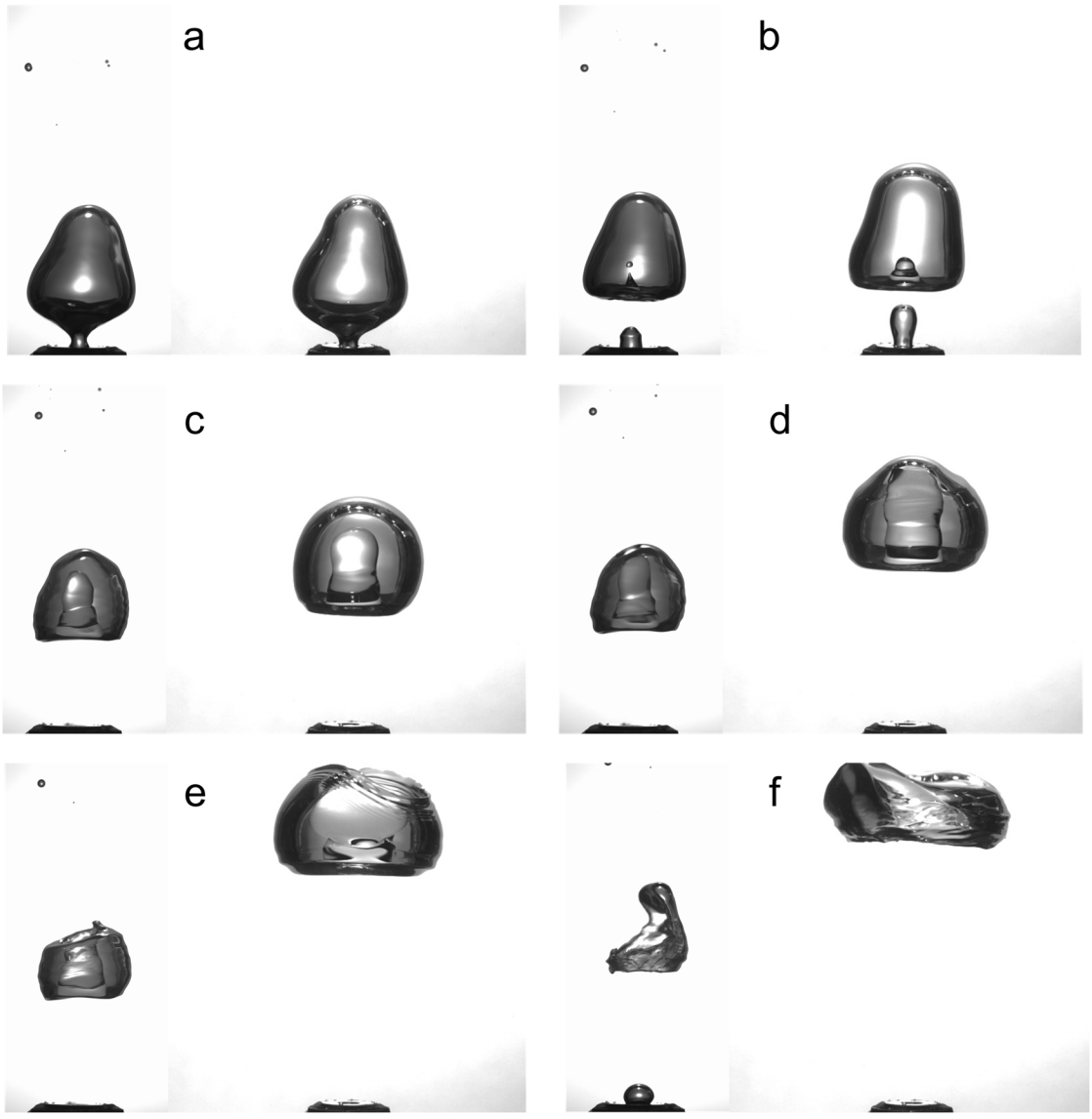


**Figure 8.4.** High-speed images pairs of vapor (left) and air bubbles during: a) prior to detachment from the orifice, b) after pinch-off, c) during large-scale deformation, d) prior to toroidal formation, e) after toroidal formation, and f) during toroidal collapse.

formation the entrained flow at the bottom surface of the bubble occurs at a higher speed ($0.72V_t$) than at the top interface ($0.37V_t$) (cf. Figure 8.4c-d). Also, similar to the vapor bubble, when the torus forms ($y/d_o = 14.5$, $t/T_b \approx 0.2$), the position of the top surface remains nearly invariant relative to the tank after the highest central point is punctured by the liquid stem, as the highest point on the bubble moves radially outward at roughly constant elevation (relative to the bubble, the highest point is moving downwards due to the curvature of the top interface) while the lower interface continues to rise with the bubble (c.f. Figure 8.4e-f). However, following the formation of the torus, there are some significant differences compared to the evolution of the vapor bubble. At $t/T_b = 0.29$ (cf. Figure 8.4f), the torus is formed and the flow is both entrained at the bottom interface and exiting at the top interface at $0.64V_t$ (~$0.28V_t$ relative to the bubble's motion). After the bottom interface of the bubble changed from convex to concave, the force of the surface

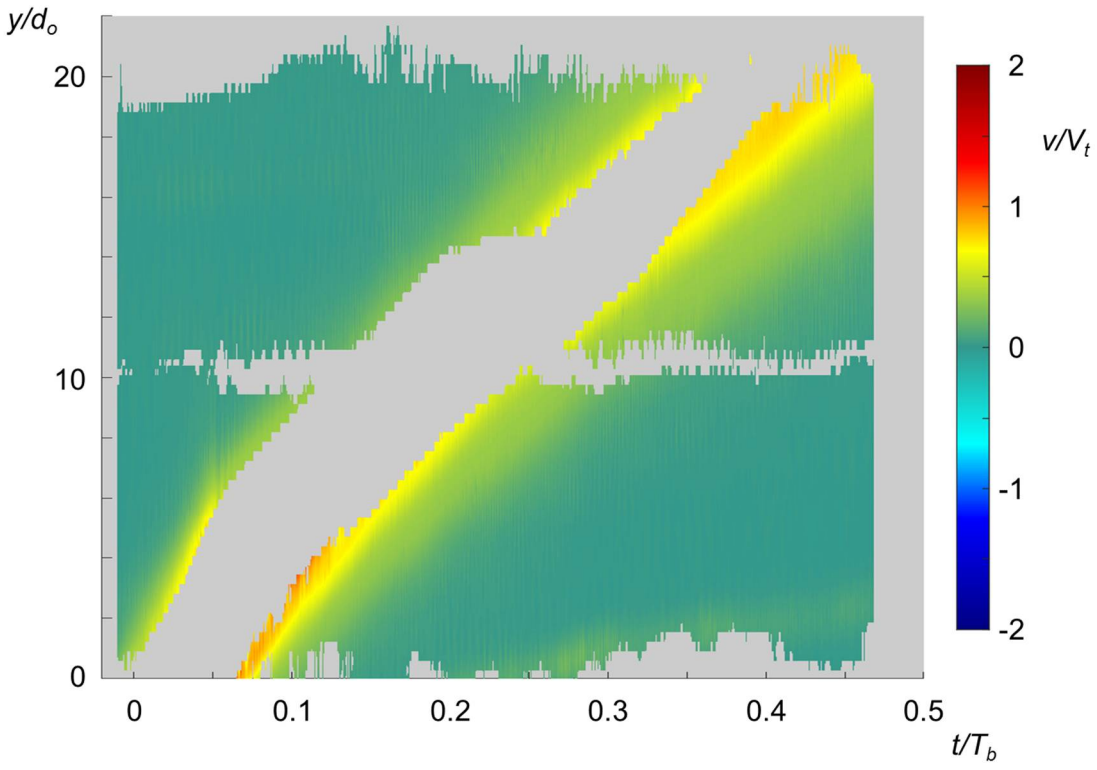


**Figure 8.5.** As in Figure 8.2 for an air bubble (cf. Figure 8.7a-f) where the images of the air bubble in roughly correspond to $t/T_b = 0.05, 0.075, 0.125, 0.175, 0.2, 0.25$.

tension was opposite to the direction of motion and therefore the speed of the interface and the flow through the central liquid stem was slower than the initial speed of the entrained flow. This effect is different than in the vapor bubble, where the speed of the fluid exiting from the top interface of the torus is significantly faster ($1.36V_t$) than the entrained flow at the bottom interface ($0.91V_t$). *Clearly, the differences between the inlet and outlet flow into the torus of the vapor bubble are associated with the condensation, which also accounts for the higher flow speeds even during the pinch-off process where surface tension is less influential at the higher bulk temperatures* (the surface tension decreases from 72 mN/m at 20 ºC to about 60 mN/m at 92 ºC).

Detailed measurements of the velocity fields of non-interacting vapor bubbles in the absence and presence of actuation are shown in Figures 8.6 and 8.7 using color raster plots of azimuthal vorticity concentrations superposed with velocity vectors during several instances in the ejection cycle of the bubble. For clarity, the velocity vectors are plotted on every other row of the 50 x 84 data grid and only vectors having magnitudes greater than $0.55V_t$ are included. Figure 8.6a ($t/T_b = 0$) is representative of the bubble growth as it is attached to the orifice, as the subcooled liquid is displaced by the growing vapor volume, and it also shows the wake of the earlier bubble as it is advected through the top end of the field of view. The pinch-off process is beginning in Figure 8.6b ($t/T_b = 0.25$), as the subcooled liquid is drawn towards the orifice. The motion behind the detached bubble (Figure 8.6c, $t/T_b = 0.30$) shows the presence of liquid through the wake of the bubble and the onset of the nearly-symmetric motion towards the bubble's volume by the receding liquid-vapor interface. Also noticeable is the reduction in the speed of the liquid (relative to the plotted threshold speed) near the top interface as indicated near the flow centerline in Figure 8.3a ($5.7 < y/d_o < 7$, $0.3 < t/T_b < 0.49$). The induced velocity in the near wake of the bubble that is associated with the rapid recession of the liquid vapor interface as a prelude to the formation of the vapor torus is evident in Figure 8.6d

($t/T_b$ = 0.35), and Figure 8.6e ($t/T_b$ = 0.563) shows the flow following torus formation. The data in Figure 8.6e clearly exhibits nearly-uniform flow through the bottom surface of the torus, and a starting jet ejection of liquid from its top interface that is accompanied by the formation of a vortex ring adjacent to the exit plane of the torus flow. The formation of this vortex ring in the absence of a solid surface is remarkable, and it is indicative of the induced flow within the vapor volume as a result of the shear at the liquid-vapor interface. It is also noted that counter clockwise vorticity concentration also appears in the inlet flow into the bottom surface of the torus in Figures 8.6c-e indicating the presence of a shear boundary layer at its inner surface. This shows that the mass of warm liquid that is observed in the Schlieren images in Figures 7.8a-d;g-h is comprised of liquid that is entrained through the toroidal vapor volume and includes liquid that is condensed at the inner torus interface (the thermal boundary layer at the visible segment of the bottom visible liquid-vapor interface is not resolved in the Schlieren images). The torus-induced jet flow is also present in Figure 8.6f ($t/T_b$ = 0.70) that captures the advection of the initial vortex ring of the starting jet (which has advected a distance of 1.8$d_o$) and the formation of the next vortex near the exit plane on the bubble's top surface. As noted in connection with Figure 8.3a, the advection speed of the initial vortex ring is similar to the initial vertical velocity of the growing bubble. As the torus continues to collapse in Figures 8.5g and h ($t/T_b$ = 0.80 and 0.85), the jet through the torus intensifies and spreads radially. The collapse of the torus leads to merging of the front and rear (same sense) vortices that accompany the motion of the volume of the condensed and entrained subcooled liquid mixture. By Figure 8.5i ($t/T_b$ = 0.90), the vapor is no longer detected in the PIV plane, and the vortices continue to merge and seem to weaken. This process is associated with the rate of volume change of the vapor bubble in Figure 7.10, where the third condensation spurt associated with the bubble collapse is wider spaced spatially and temporally.

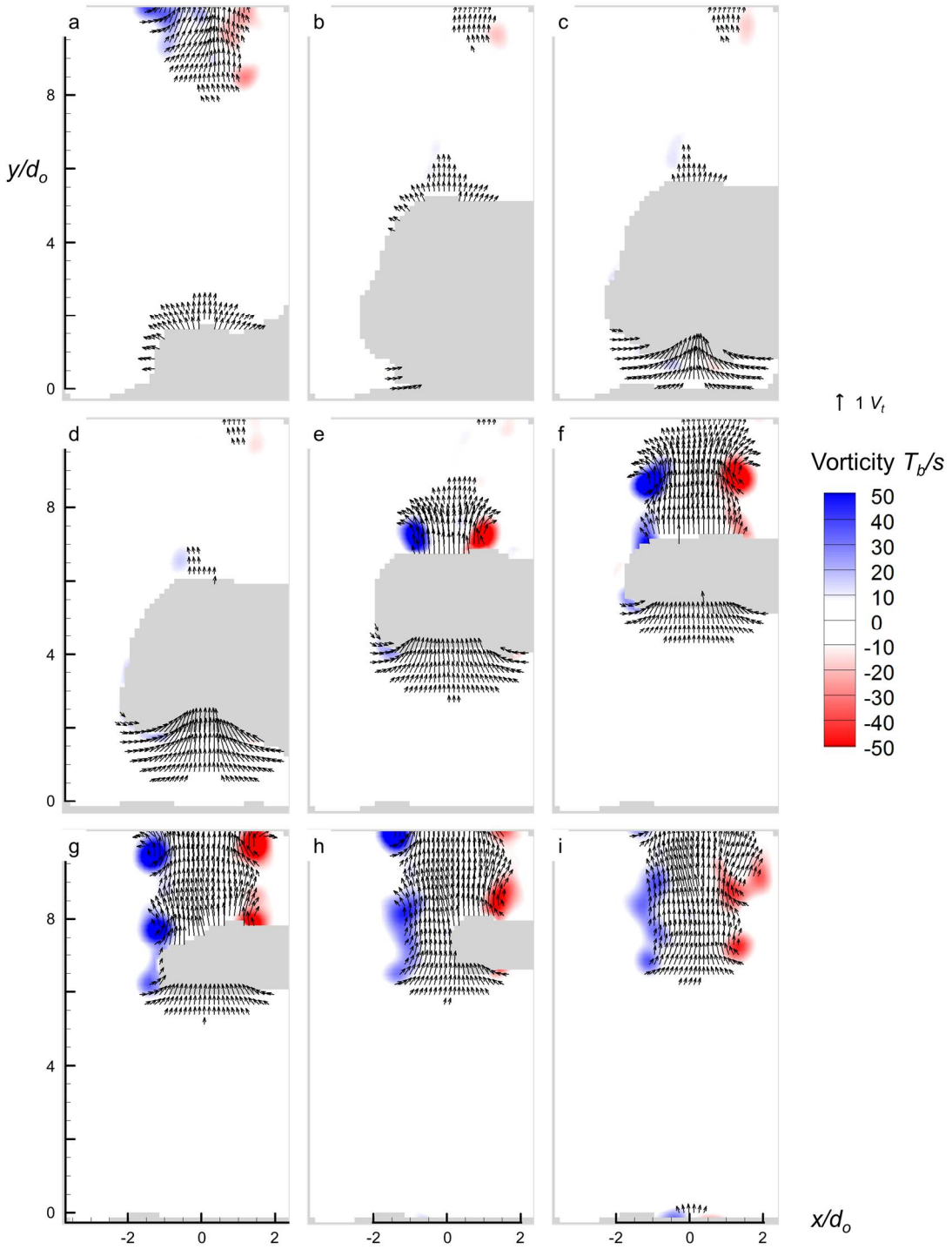


**Figure 8.6.** Color raster plots of azimuthal vorticity concentrations superposed with velocity vectors during several instances in the ejection cycle of the vapor bubble in Figure 8.3a at $t/T_b$ = 0 (a), 0.25 (b), 0.30 (c), 0.35 (d), 0.563 (e), 0.70 (f), 0.80 (g), 0.85 (h), and 0.90 (i).

The corresponding sequence of raster plots of vorticity and velocity vectors in the presence of pulsed actuation are shown in Figure 8.7 (the velocity threshold for vector plotting is $0.2V_t$). The growth phase of the attached bubble (Figure 8.7a, $t/T_b = 0$) is similar to Figure 8.6a. However, following the onset of the pulsed actuation (Figure 8.7b and c, $t/T_b = 0.05$ and 0.15) the formation of the liquid spear by the actuation results in inward fluid motion into the top surface while the sides of the bubble (the left side is visible) continue to spread into the subcooled liquid. Figure 8.7d and e ($t/T_b = 0.25$ and 0.30) follow the termination of the acoustic actuation and the majority of the bubble's interface exhibits inward motion that is indicative of enhanced condensation and reduction in the vapor volume (cf. Figure 7.10). Following the detachment of the bubble (Figure 8.7f, $t/T_b = 0.40$) the flow exiting the torus below the vapor volume is visible as the bubble is advected upward. These data show that the volume of liquid that exits at the bottom interface of the torus is higher than the influx at the top surface as a result of enhanced condensation within the torus (cf. Figure 7.8) and that the induced jet flow is forced to turn upward (on the right) and forms a CW vortex. The next frame in the sequence (Figure 8.7g, $t/T_b = 0.45$) shows that as the bubble is advected, the jet of condensed liquid has intensified and forms a vortex ring (similar to the jet that emanates from the top surface of the torus in Figure 8.6e), and the jet flow leads to entrainment of ambient liquid ($x/d_o = -1.5$, $y/d_o = 1$) that may help enhance the condensation rate near the bottom surface of the torus (cf. the Schlieren images in Figure 7.8l-m). Following the termination of the actuation, the jet motion through the torus subsides and the vortex ring is advected towards the surface of the orifice and spreads radially as it interacts with its image (Figures 8.7h and i, $t/T_b = 0.50$ and 0.60) as the remainder of the vapor volume condenses by about $5d_o$ above the orifice, lower than the height ($7d_o$) reached by the vapor volume in the absence of condensation, and induces significantly less flow perturbations at its final elevation.

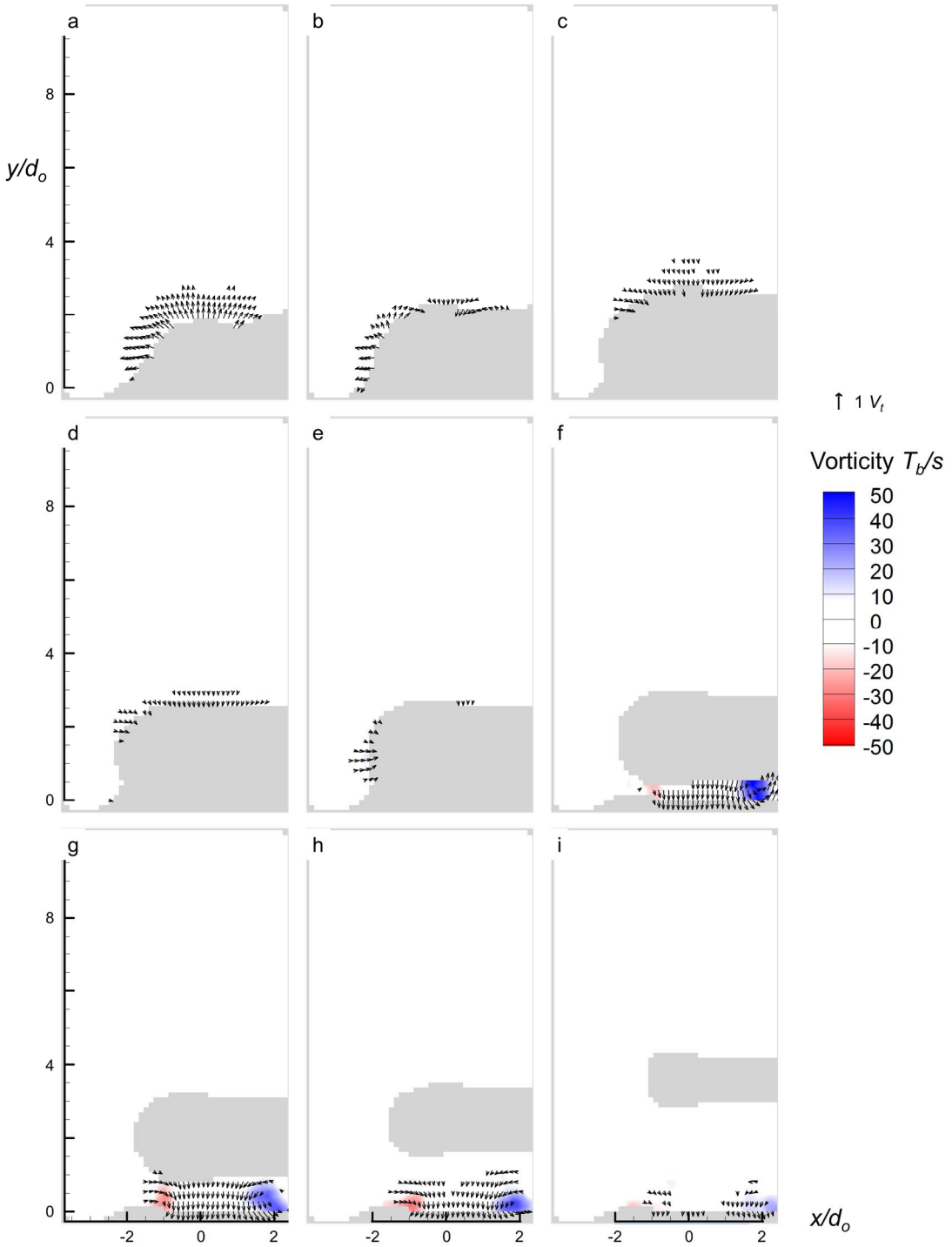


**Figure 8.7.** As in Figure 8.6 (corresponding to Figure 8.3b) at $t/T_b$ = 0 (a), 0.05 (b), 0.15 (c), 0.25 (d), 0.30 (e), 0.40 (f), 0.45 (g), 0.50 (h), and 0.60 (i).

The flow in the bulk fluid following the complete collapse and condensation of the vapor bubble in the absence of actuation is investigated using *x*-*t* distributions of color raster plots of the vertical velocity $v(x, t; y = 5.9d_o)$ as shown in Figure 8.8. At the onset of the data acquisition, the remnants of the flow induced by the preceding vapor bubble is evident in the domain $-1.3 < x/d_o < 1.3$, $t/T_b < 0.1$, followed by a nearly-quiescent period through $t/T_b \approx 0.5$ before the induced flow of the next bubble is sensed. The flow induced by the momentary jet that results from the formation and collapse of the torus is marked by two local spanwise maxima of the vertical velocity that are centered about the axial *y* axis at $t/T_b = 0.65$ (~$1.4V_t$) and 0.82 (~$1.2V_t$). As shown in Figure 8.2, the jet flow appears to quickly intensify following the formation of the torus, subsides somewhat (a local minimum at $t/T_b = 0.75$, $1.06V_t$), and then intensifies again with the final collapse of

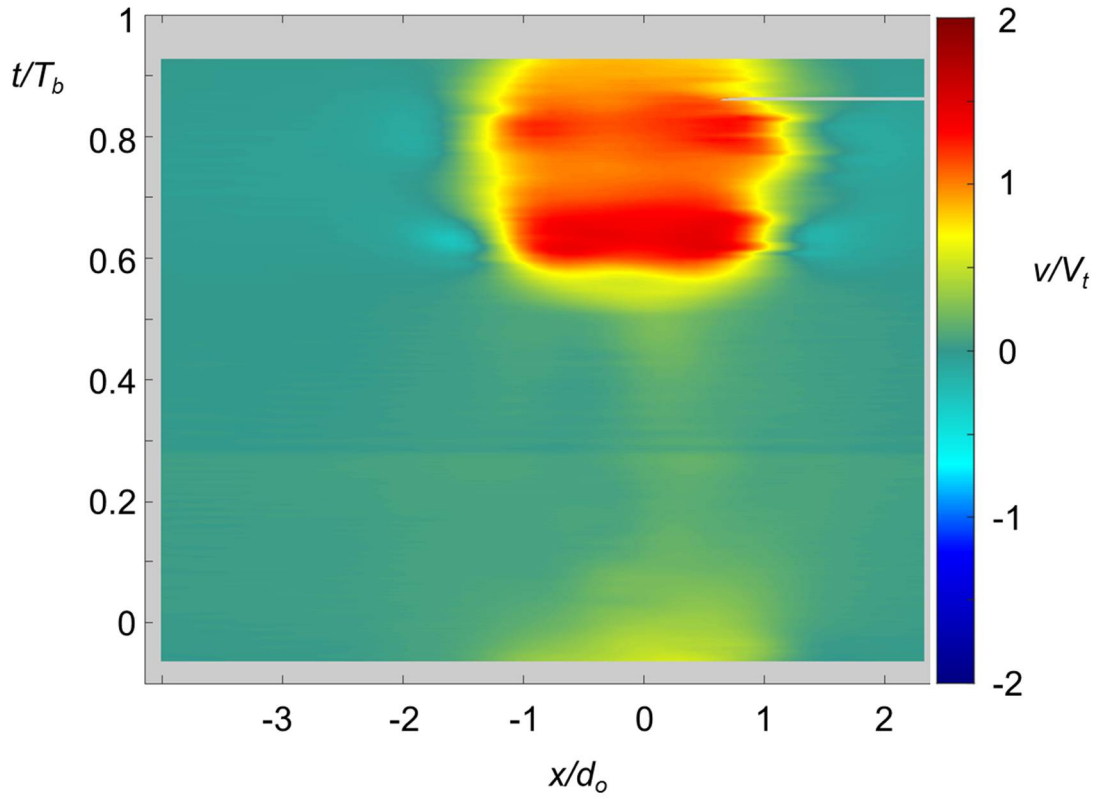


**Figure 8.8.** Color raster plots of x-t distributions of the vertical velocity at a given elevation $v(x, t; y = 5.9d_o)$ in the absence of actuation during the formation and collapse of the vapor torus.

the vapor volume. The corresponding *x*-*t* color raster plots of the vorticity concentrations are shown in Figure 8.9 (at $y = 5.9d_o$). These data show the advection of the vortex rings that are formed by the impulse associated with the starting jet following the formation of the torus and during its collapse (centered at $t/T_b = 0.63$ and 0.81). These data also show that the momentary jet previously examined forms internal vortices of opposite sense that may be associated with the internal ejection of condensed fluid from the inner surface of the torus; the maximum vorticity advects through this vertical location slightly prior to the maximum velocity. Note that in the presence of actuation the formation of the torus and the collapse of the vapor volume result in a momentary jet that is directed towards the orifice plane (cf. Figure 8.7f-h), and, as a result the induced flow that is associated with the collapse and the condensation is directed towards that exit plane and rapidly subsides, leaving nearly quiescent flow at elevation $y/d_o = 5.9$.

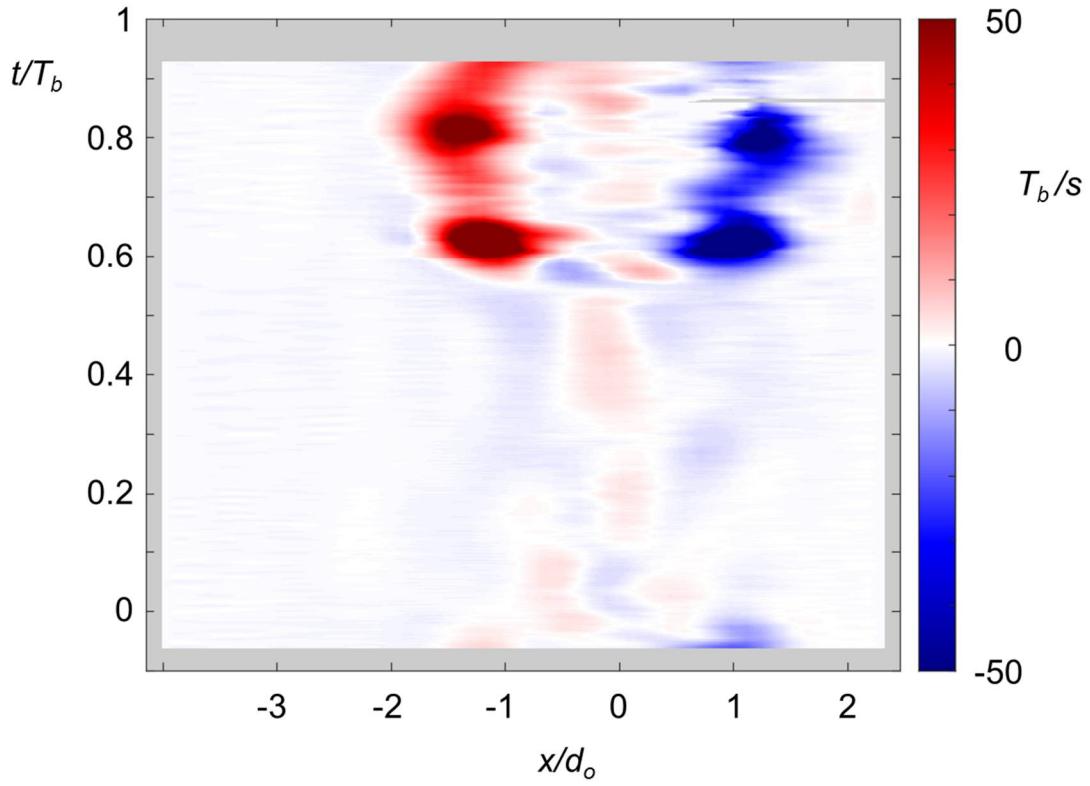


**Figure 8.9.** As in Figure 8.8 showing color raster plot of azimuthal vorticity $\omega_{xy}(x, t; y = 5.9d_o)$.

**8.2 Comparison to PIV of Canonical Bubbles**

The flow field associated with interacting vapor bubbles in the absence and presence of actuation as discussed in §7.1 (vapor dissipation of 225 W, $d_o$ = 5.3 mm, 25ºC subcooling, $T_b$ = 50 ms, and $V_t$ = 0.70 m/sec) is investigated using PIV. As shown in Figure 7.1 under these conditions successive bubbles are nominally separated by $0.56d_o$, or about $0.1T_b$. Similar to Figure 8.3, Figures 8.10a and b show the trajectories of successive bubbles in *y-t* diagrams of color raster plots of the vertical velocity along the centerline of the bubbles, i.e., $v(y, t; x = 0)$ in the absence (Figure 8.10a) and presence (Figure 8.10b) of pulsed actuation. As shown in Figure 10a, owing to higher subcooling and larger mass flow rates the vapor bubbles can induce faster vertical speed (up to $2.6V_t$), and collapse more rapidly compared to vapor bubbles that form at the thermal conditions of Figure 8.3a. While pinch-off is not as visible as in Figure 8.3a, the data near $t/T_b$ = -0.2 and $y/d_o$ = 0.3 indicates the induced flow speed is $2.43V_t$. The ejected jet following the formation ($t/T_b > 0.30$, $y/d_o > 4.1$) and collapse ($t/T_b > 0.42$, $y/d_o > 3.7$) of the toroidal vapor volume reaches its maximum speed about $2.17V_t$ during the collapse (unlike the data in Figure 8.3a), and the duration of the collapse process after torus formation is within $0.13T_b$ (6.5 msec) (cf. Figure 7.1) compared to $0.35T_b$ (28 msec) (cf. Figure 7.7). Similar to the formation of the torus at reduced mass flow rate, the liquid flow speed *increases* as it passes through the vapor torus as a result of the condensation. For example, at $t/T_b$ = 1.35 the fluid speed increases from $1.15V_t$ to $2.00V_t$ at the inlet and exit planes, respectively, compared to $0.90V_t$ and $1.36V_t$ at $t/T_b$ = 0.55 in Figure 8.3a. The larger fractional increase in liquid flux associated with the higher vapor mass flux and higher subcooling is associated with the stronger effect of condensation.

In the presence of acoustic actuation (Figure 8.10b), successive vapor bubbles are more spaced spatially and temporally because the (triggered) actuation enhances the condensation rate and reduces the bubble residence time. Similar to the motion at reduced vapor mass flow rate and lower subcooling (Figure 8.3b), the motion of the top

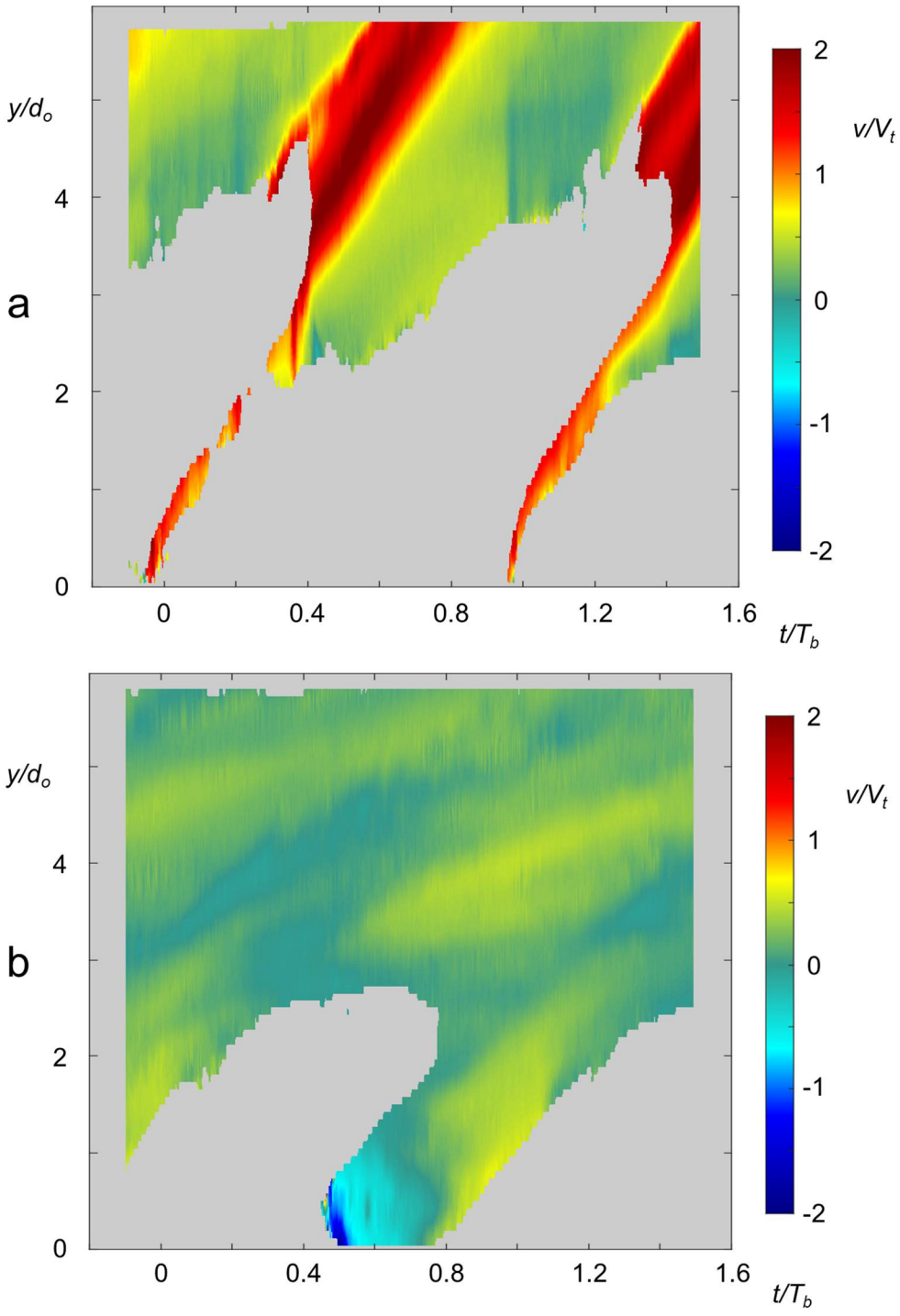


**Figure 8.10.** As in Figures 8.3a and b for increased vapor volume flow rate and subcooling.

interface of the attached bubble prior to the onset of actuation is reasonably smooth. Following the onset of actuation, the growth of the top interface is slowed, and there is a slight downward flow as the actuation is terminated ($0.30 < t/T_b < 0.40$, $2.50 < y/d_o < 2.65$, c.f. Figures 7.1g-h). The flow near the bottom interface of the bubble immediately following detachment ($0.45 < t/T_b < 0.75$, $0 < y/d_o < 1.2$) exhibits significant downwards flow with a highest speed of $-1.86V_t$ that persists until the ejection of the subsequent bubble about $0.25T_b$ later. Unlike the vapor bubbles that form at reduced mass flow rate and lower subcooling (Figure 8.3b), the collapse of the remaining vapor volume following the termination of the (pulse) actuation ($0.40 < t/T_b < 0.78$, $0.5 < y/d_o < 2.65$) along with the increased subcooling induces upwards flow at speeds up to $0.50V_t$, considerably slower than in the absence of actuation (Figure 8.10a). *These data indicate that the increased liquid flow rate through the vapor torus is the result of the accelerated condensation that for a given actuation power is clearly intensified with increased vapor mass flow rate and subcooling.* For example, at $t/T_b = 0.49$ the fluid speed relative to the vapor volume increases from $-0.04V_t$ to $-1.03V_t$ between at the inlet (top) and exit (bottom) planes, respectively (compared to the corresponding speeds induced by the effects of the actuation at the lower vapor mass and subcooling in Figure 8.3b, namely, $-0.14V_t$ and $-0.64V_t$ at $t/T_b = 0.31$).

Similar to Figures 8.6 and 8.7, Figures 8.11 and 8.12 show color raster plots of azimuthal vorticity concentrations superposed with velocity vectors during several instances in the ejection cycle of the vapor bubbles in Figures 8.10a and b. As with the PIV data acquisition at reduced vapor mass flow rate and subcooling, the acquisition is triggered via laser to the evolution of the attached bubble. However, as shown in the sequence of Figure 8.11 (using a vector plotting threshold of $1V_t$), in the absence of actuation the acquisition commenced a bit later, when the height of the upper surface of the vapor exceeded the triggering elevation. Because this data set captured the collapse

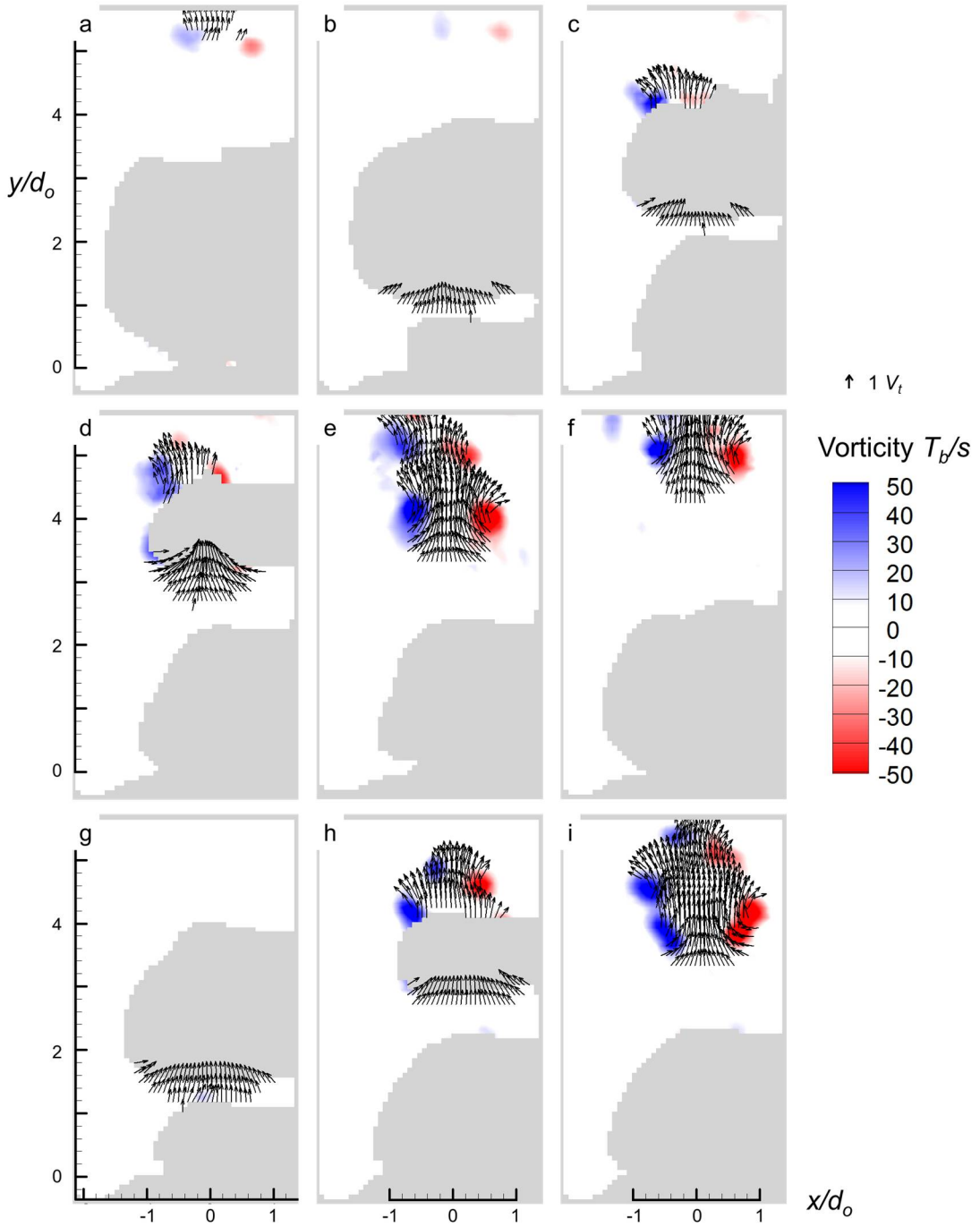


**Figure 8.11.** Color raster plots of azimuthal vorticity concentrations superposed with velocity vectors during several instances in the ejection cycle of vapor bubbles in Figure 8.10a at $t/T_b$ = -0.08 (a), 0.08 (b), 0.32 (c), 0.40 (d), 0.48 (e), 0.64 (f), 1.12 (g), 1.36 (h), and 1.44 (i).

of two successive bubbles, the delayed triggering does not pose a problem. The successive bubbles are separated in Figure 11b ($t/T_b$ = 0.08), but the vapor injection rate causes the second bubble to remain in close proximity. The onset of the liquid ejection caused by the formation of the vapor torus is shown in Figure 8.11c ($t/T_b$ = 0.32) with a slight asymmetry that is caused by the wake of the earlier bubble. The rapid collapse continues in Figures 8.11d and e ($t/T_b$ = 0.40, and 0.48), as the speed of the liquid at the bottom and top surfaces of the torus increase as is evident by the formation of a stronger second vortex ring. The collapse of the torus propels the condensed liquid and it is exiting the field of view along with the induced vortices in Figure 8.11f ($t/T_b$ = 0.64) while the subsequent vapor bubble is still attached to the orifice and comes in contact with cooler liquid as shown in the corresponding Schlieren images in Figure 7.2. The detachment and collapse of the subsequent vapor bubble are shown in Figures 8.11g-i. ($t/T_b$ = 1.12, 1.36, and 1.44, respectively). Similar to Figure 8.6g-i, Figure 8.11i shows the presence of *three* interacting vortex rings (the first, formed by the torus in Figure 8.11h, at $y/d_o$ = 5.2, and the two additional vortices are formed at $y/d_o$ = 4.4 and 3.8 during the collapse of the torus).

The corresponding data in the presence of pulsed actuation are shown in Figure 8.12 (using a lower vector plotting threshold of 0.45$V_t$). The laser triggering works better in the presence of acoustic actuation since the actuation increases the temporal and spatial separation between successive bubbles, and due to the increased vapor mass flow rate the upward flow of liquid is slowed but not reversed by the onset of actuation. Figure 8.12a-c show the attached vapor bubble and the remnants of the flow induced by the previous bubble above it (note the flow towards the bubble in Figure 8.12c, $t/T_b$ = 0.32). The actuation is terminated between at $t/T_b$ = 0.40 (between Figures 8.12c and d) and the bubble becomes fully detached in Figure 8.12e and the flow in its near wake shows the liquid jet that is induced by the actuation from above. Unlike the flow around the vapor

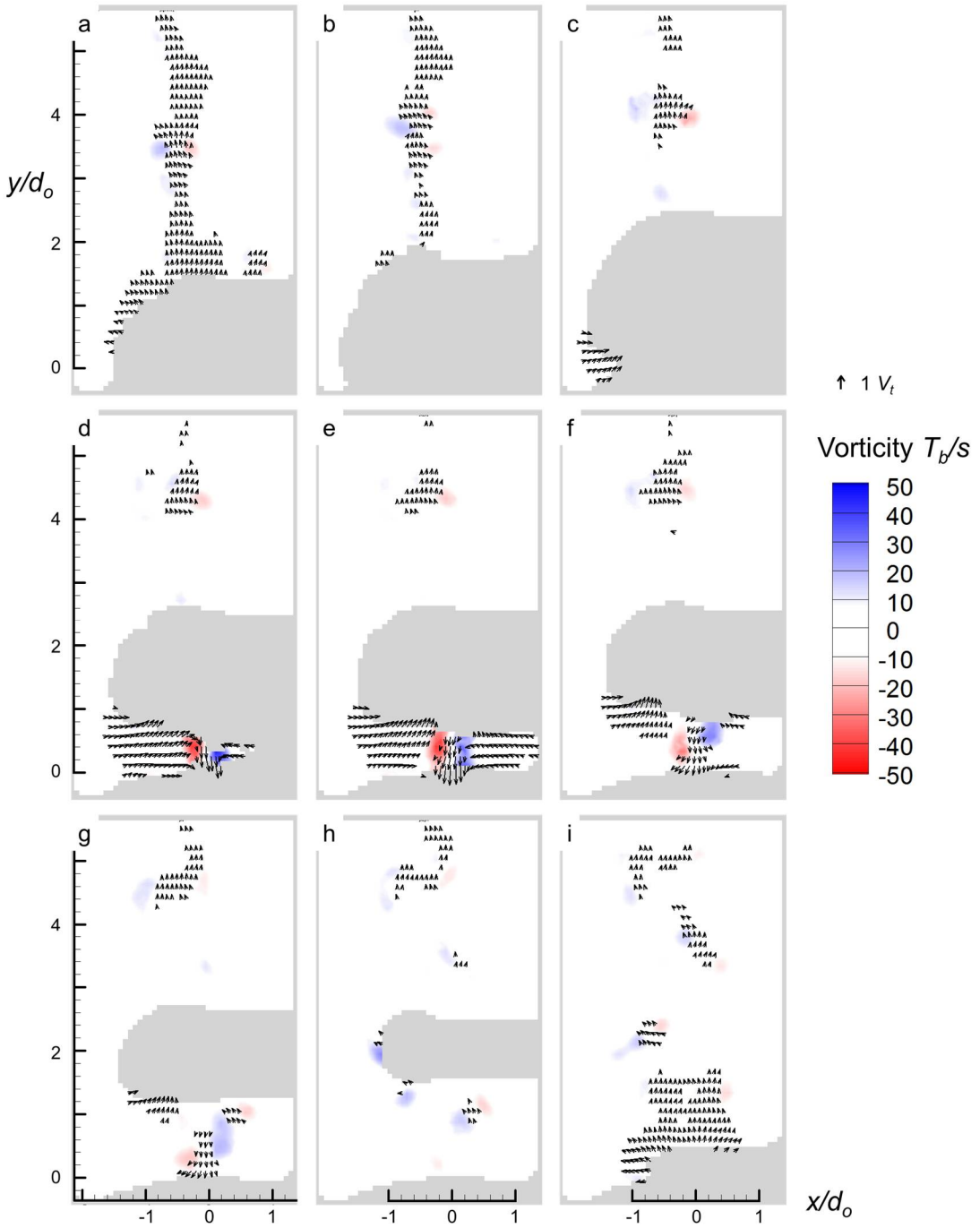


**Figure 8.12** As in Figure 8.11 (corresponding to Figure 8.10b) at $t/T_b$ = 0 (a), 0.16 (b), 0.32 (c), 0.48 (d), 0.50 (e), 0.56 (f), 0.62 (g), 0.72 (h), and 0.88 (i).

bubble at reduced vapor mass flow rate and subcooling, the entrained flow is partially directed towards the exit plane of the torus flow indicating lower pressure due to intensified bubble collapse. However, the induced vortex ring appears to be weaker in the presence of actuation compared to the vortices that form near the top surface of the vapor volume in the absence of actuation. This difference is probably caused by the proximity of the exit plane of the orifice and may be affected by the presence of the subsequent vapor interface. In Figure 8.12e ($t/T_b = 0.50$) the downwards flow interacts with the subsequent vapor volume and this interaction leads to an intensification of the induced flow near the orifice perhaps as a result of acoustic interaction causing pinch-off from the subsequent vapor volume closer to the orifice, causing collapse of the vapor still attached to the reservoir (cf. Figure 8.11b,g). The induced flow underneath the advecting vapor bubble weakens by Figure 8.12f and g ($t/T_b = 0.56$ and 0.62). The data in Figure 8.12 indicates that the performance of the actuation can be further optimized by varying the timing and duration of the pulse. As noted in §5.3 the acoustic radiation pressure induced by the actuation beam is about 5.1 kPa and can lead to increased flow resistance at the orifice (compared to, nominally, 101 kPa saturation pressure in the steam reservoir). The duration of this induced pressure can be adjusted by the pulse timing to minimize its effect or could, if necessary, be used to regulate the steam flow out of the reservoir. By comparison, the increase in pressure by the flow of condensed liquid towards the orifice plane in the presence of actuation can be estimated from PIV measurements. The present data show that the maximum induced flow towards the orifice is 1.3 m/sec (for approximately 1 msec), while the average induced flow towards the orifice is about 0.35 m/sec (for approximately 15 msec). The stagnation pressures associated with these flows are 0.85 kPa and 0.061 kPa or less than 1.3% of the average acoustic radiation pressure. Hence the effect of the acoustic pressure would be clearly dominant, and its effect on the orifice in the absence of a vapor bubble should be

minimized through the use of triggered pulses. It is also noteworthy that compared to condensation in the absence of actuation, the data in Figure 8.12 indicate that the actuation leads to a significant reduction in the distribution and magnitude of the residual flow between condensing bubbles and thereby regulates their trajectories and enables easier targeting by the acoustic beam.

Finally, Figures 8.13a and b show color raster plots of $x$-$t$ distributions of the vertical velocity at an elevation of complete condensation $v(x, t; y = 4.7d_o)$ in the absence and presence of actuation during the formation and collapse of the vapor torus. In the absence of actuation, there are two separate bubble collapses within the duration of the data ($1.6T_b$) each of which forms a distinct mass of condensed liquid with significant vertical speeds. Similar to the formation and collapse of the torus at lower vapor mass flow rate and subcooling, the ejection of each liquid jet is characterized by two local velocity maxima namely, during the formation ($t/T_b = 0.4$) and subsequent collapse ($t/T_b = 0.6$) of the vapor torus. As was noted in connection with Figure 8.10a the induced speed of the ejected liquid during the torus collapse higher than during its formation. Figure 8.13b, shows the equivalent data in the presence of acoustics which demonstrates that the remnants of induced vertical velocity perturbations are considerably smaller.

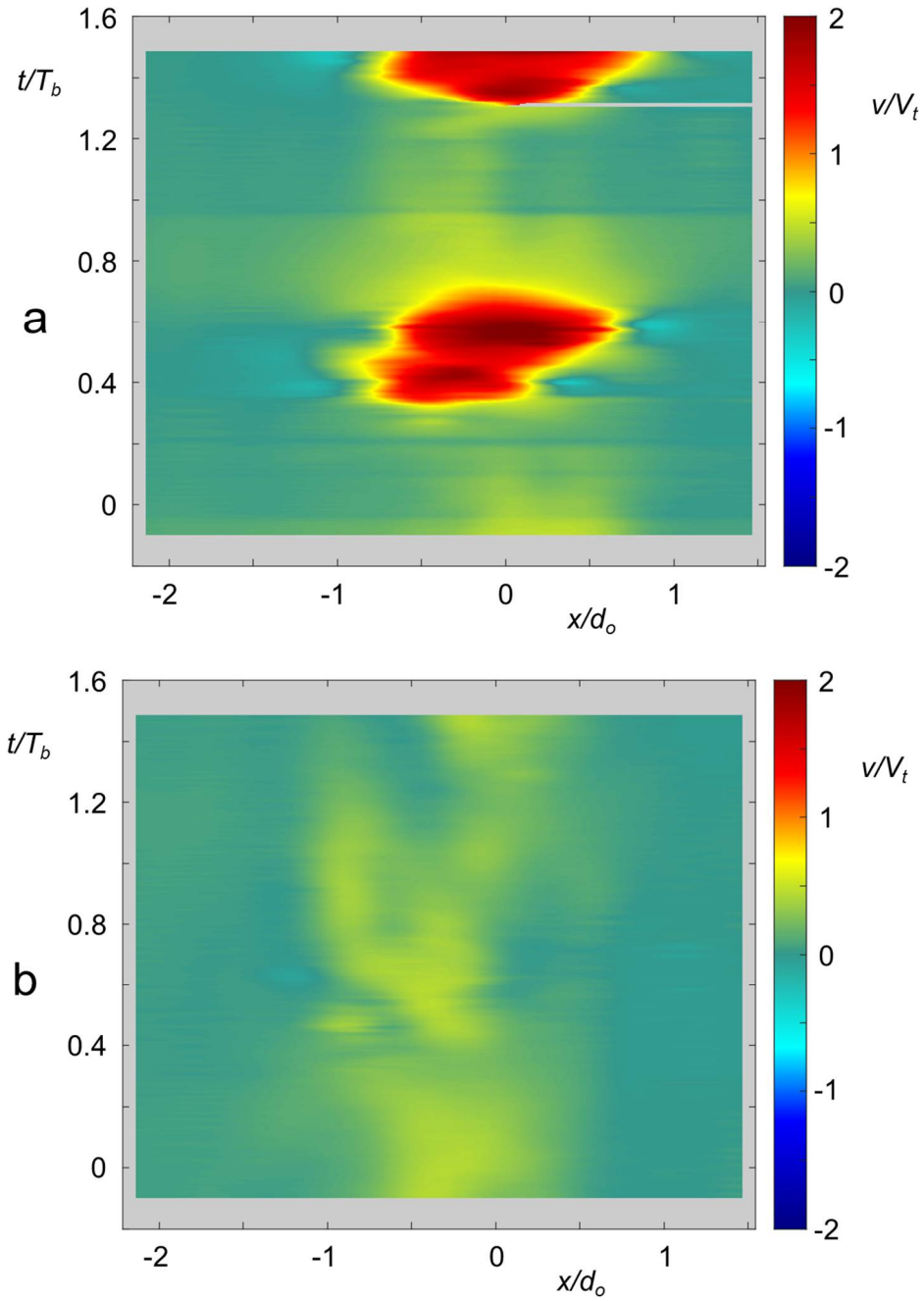


**Figure 8.13.** Color raster plots of x-t distributions of the vertical velocity at a given elevation $v(x, t; y = 4.7d_o)$ in the absence (a) and presence (b) of actuation during the formation and collapse of the vapor torus.

# CHAPTER IX

# CONCLUSIONS

The present investigations have demonstrated that two-phase heat transfer in a liquid pool can be significantly enhanced by independently (or simultaneously) augmenting the boiling and condensation processes to enable high heat fluxes by using acoustic actuation that is transmitted through the working liquid. The nonintrusive low-power actuation is applied at the flow boundary and exploits the acoustic properties mismatch at the liquid vapor interface of the vapor bubbles. The investigations focus on the fundamental mechanisms of the interfacial acoustic interactions during boiling, leading to control and regulation of the vapor bubbles that form on the heated surface (and raising the critical heat flux limit), and during direct contact condensation of vapor bubbles that are formed and advected in subcooled liquid. For each process, the interfacial interactions are elucidated in two limits of long and short actuation wavelength. Wavelengths that are much larger than the characteristic scale of the vapor bubbles [O(1 kHz, 1 m)] lead to the formation and amplification of capillary surface waves on liquid vapor interfaces. When the actuation is used on a boiling surface, a modest decrease of surface superheat and increase in CHF is achievable. When this actuation is used to enhance condensation, the capillary waves significantly increase the heat transfer coefficient to the surrounding fluid by mixing the interfacial thermal boundary layer, even accounting for the increase in interface area. Short actuation wavelengths [O(1 MHz), O(1 mm)] effect surface forces on vapor bubbles of all scales. When the actuation is used on a boiling surface, the nucleation process and ensuing vapor advection is affected by these forces such that the CHF is significantly increased and the heat transfer coefficient at low heat fluxes decreases or increases in the absence and presence of surface texture, respectively. When

it is used to enhance condensation, the short-wavelength actuation's forces can that lead to local interfacial deformations and injection of a subcooled liquid jet and atomized droplets into the vapor volume, significantly increasing the condensation rate.

*Enhanced Boiling using Acoustic Actuation*

Boiling heat transfer from a submerged surface in a subcooled liquid bath was investigated using plain (smooth) and textured (arrays of intersecting open surface microchannels machined onto the surface) heated surfaces. The channel intersections provide distinct, separated vapor nucleation sites and enable the transport of make-up liquid to the boiling sites thereby affecting the evolution and advection of the vapor bubbles. The microchannels control the location, growth, and detachment of the vapor bubbles and lead to a reduction in the mean surface superheat and to a significant increase in the critical heat flux compared to a plain smooth heater surface (with CHF limits of 350 and 110 W/cm$^2$, respectively).

The boiling heat transfer on both the plain and textured surfaces is strongly affected by short wavelength ultrasonic acoustic forcing (1.7 MHz, or a characteristic wavelength of 900 μm) that controls the formation and evolution of the vapor bubbles and inhibits the transition to film boiling at the critical heat flux. The acoustic actuation induces interfacial forces that affect the bubbles' contact line with the surface leading to their detachment, and further, induces break-up of the vapor-liquid interface that leads to enhanced condensation in the bulk fluid. The effects of the acoustic actuation were first investigated on the planar (baseline) surface and then in the presence of surface microchannels. It is shown that on the smooth surface the actuation increases the surface superheat (up to 7 $^o$C) relative to the baseline, and the CHF from 110 to 183 W/cm$^2$ (65%). The increase in surface superheat is caused by the suppression of boiling at most nucleation sites and the removal of small [O(10 μm)] vapor bubbles from preferred, active nucleation sites before they can grow significantly, and is equivalent to a reduction

in heat transfer coefficient from the boiling surface. However, this suppression is diminished at surface protrusions, such as edge discontinuities that form nucleation sites and reduce the increase in surface superheat. Such deliberate nucleation sites were formed by the integration of surface-embedded temperature sensors. At these preferred nucleation sites within the ultrasonic beam, transitory nucleation events lead to large vapor formations, temporarily reducing surface superheat near the vapor production sites, where the effectiveness depends on relative location of the nucleation site to the incidence of the centerline of the acoustic beam. At the same time, the fast removal of small-scale vapor bubbles from the surface by the actuation-induced body forces contributes to a reduction in the vapor mass and accelerated condensation over the surface, and ultimately to an increase in the CHF limit, despite the reduction in boiling efficiency at lower heat fluxes. In the presence of surface texturing such as embedded microchannels acoustic actuation *reduces* the surface superheat (compared to an increase in superheat over the featureless surface) indicating a significant increase in bubble formation and detachment rates that is accompanied by entrainment of sub-cooled fluid through the channels. It is clear the vapor suppression effects on the smooth surface do not significantly affect the grid of nucleation sites within the texturing features, therefore making the combined use of texturing (e.g., microchannels) and acoustic actuation an attractive approach for practical applications. In the presence of 400 μm-wide surface microchannels, the actuation leads to a 30% improvement in the critical heat flux (from 350 W/cm$^2$ to 460 W/cm$^2$, in stagnant bulk fluid) while reducing the surface superheat (or equivalently, increasing the heat transfer coefficient) over the entire boiling curve (by an average of 7 $^o$C).

The present investigations demonstrated that while long-wavelength acoustic actuation had profound effects on the condensation process, its effects on vapor formation during

boiling were somewhat limited and yields a modest increase in critical heat flux on the plain surface (from 110 to 128 W/cm$^2$).

The interaction between the short-wavelength acoustic actuation and the nucleating vapor bubbles, and the *diverging* behavior of surface superheat in the presence of acoustic actuation on a smooth or textured surface, as well as the *similarity* of behavior of the CHF on both types of surfaces, is an important contribution to insight into the boiling process in the presence of acoustic actuation. It is anticipated that the discovery of the increased boiling efficiency and extension of the critical heat flux limit by regulation and enhancement of vaporization at nucleation sites on textured surfaces in the presence of short-wavelength acoustic actuation will help pave the way towards its adoption for active enhancement of the boiling process in a broad range of practical applications.

*Enhanced Condensation using Long-Wavelength Acoustic Actuation*

The effects of long wavelength acoustic actuation [O(1 kHz, 1 m)] on the rate of direct contact condensation of and enhanced heat transfer from vapor bubbles injected into a subcooled liquid bath were investigated. Long wavelength acoustic actuation leads to the formation of capillary (Faraday) waves on the liquid vapor interface of the bubbles while they are attached to the injection orifice and during advection following their detachment.

It is shown that the motions of the liquid vapor interface caused by the capillary waves disrupt the interface's thermal boundary layer and thereby increases the rate of heat transfer from the bubble to the surrounding subcooled liquid leading to enhanced condensation and a significant reduction in vapor volume. In the presence of actuation, the nominal volume of the bubbles that are detached and advected from the vapor orifice is decreased to about a third of the bubbles volume in the absence of actuation, and the condensation is nearly completed in less than 5 actuation cycles (about 5 msec at an injection rate of 20 Hz) following advection.

Digital image analysis of high-speed video sequences shows that in the presence of actuation the time-averaged total vapor interface area is decreased by a factor of 3.55, corresponding to an increase in overall heat transfer coefficient of 255%. Corresponding high-speed Schlieren imaging reveals that in the absence of acoustic actuation heat transfer from the thermal boundary layer on the liquid-vapor interface to the subcooled liquid is primarily affected by diffusion when the bubble is attached prior to advection, and its thermal boundary layer thickness is nearly time-invariant, measuring about ~1% of the bubble diameter. However, in the presence of actuation, significant thermal fluctuations that are associated with the local capillary wave crests lead to the penetration of local fingers of either subcooled liquid into the vapor volume or of vapor into the subcooled liquid. Individual, small vapor volumes are displaced outward relative to the interface by the capillary wave action ultimately retracting back leaving some condensed fluid behind them. In the presence of actuation, the thermal boundary layer thickness of the attached bubble increases nearly linearly at a rate of 0.067 mm/msec. The motion of the interface leads to an overall growth in the thickness of the surface thermal boundary layer resulting in significant enhancement of heat transfer and condensation that is intensified with the amplitude of the induced surface waves. The data in the presence of actuation indicate that the thermal boundary layer thickness does not vary significantly at the actuation or surface wave frequencies, and therefore it may be concluded that its growth, on average, is not strongly locked to the local surface waves that cumulatively contribute to its growth nor to the expansion and contraction of the bubble.

The wavelength of these surface disturbances on the vapor-liquid interface are confirmed to scale in accordance with the existing theory, i.e., the surface wavelength increased with decreasing frequency, pointing to the possibility of higher amplitude waves at lower frequencies due to a corresponding reduction in the stability threshold and

therefore corresponding increases in thermal boundary layer growth and actuation effectiveness.

The present measurements also demonstrated that acoustically-induced surface capillary waves are also effected at reduced ambient pressure (0.15 atm) with little or no effect on their spatial wavelength and lead to accelerated condensation rate and collapse of the vapor volume. The condensation, which is effective even with incomplete deaeration of the subcooled liquid, leads to increases in overall heat transfer coefficient of up to 9%.

The role of the motion of the surface capillary waves leading to the growth of thermal disturbances in the liquid surrounding a vapor bubble is essential information related to the mechanism by which the heat transfer is enhanced, and indicates that the increased-area effect is not solely responsible and therefore the choice of acoustic frequency (and therefore surface wavelength) may significantly affect the total achievable heat transfer enhancement.

*Enhanced Condensation using Short-Wavelength Acoustic Actuation*

Direct contact condensation heat transfer in a subcooled liquid bath was also investigated in the presence of short-wavelength acoustic actuation [O(1 MHz), O(1 mm)]. It is shown that the interaction of a short-wavelength acoustic beam of sufficiently high intensity with vapor volumes having a characteristic scale that is nominally at least twice the beam width leads to large-scale deformation of the liquid-vapor interface forming a spear-like protrusion that reaches the bubble surface at the opposite end and alters the vapor volume from a spheroid to a torus. Furthermore, the focusing of the acoustic waves within the spear leads to liquid atomization at the spear-vapor interface. The combined effects of surface deformation and droplet ejection significantly increases the surface area and heat transfer coefficient of the vapor-liquid interface and thereby accelerates the collapse of the vapor volume (although it is shown that the limited mass

of the atomized droplets likely contribute only up to 63% of the observed condensation, depending on the liquid subcooling and vapor bubble size). The present investigations also showed that this process is qualitatively similar to the natural deformations of a condensing vapor bubble, which, following surface-tension driven pinch-off from the vapor reservoir, deforms through the lower interface into a torus. However, while the acoustically-induced spear is similar in appearance to the natural spear that forms after the bubble detachment, it can be triggered on-demand using pulse-modulated acoustic actuation earlier in the bubble lifecycle to precede the pinch-off, while the bubble is still attached to the vapor reservoir. Once the acoustic pulse commences, the vapor bubble begins to form a torus and the duration of the actuation can be adjusted to enable full formation of the torus and effectively induce detachment and rapid condensation.

High-speed Schlieren imaging of the condensing vapor bubbles revealed that the condensation of the vapor bubbles is strongly associated with the formation and collapse of a toroidal vapor volume (especially the interior surface of the torus) that is produced either by interfacial surface tension pinch-off process or induced by acoustic actuation. Investigations of the deformation-driven flow field of the condensing vapor bubbles using particle image velocimetry (PIV) revealed that the formation of the toroidal vapor volumes is accompanied by an induced central jet of subcooled liquid through the inner liquid volume bound by the toroid. It is found that the vertical flow speed through the toroid is significantly increased by the condensation process. While in the absence of actuation the momentary liquid jet that is induced by the formation of the toroidal vapor volume points in the direction of bubble advection, in the presence of actuation the jet is directed towards the exit plane of the vapor orifice, and if the timing of the pulsed actuation is such that the vapor bubble is still attached (or just about to detach), the jet spreads laterally across the orifice exit. The present measurements also showed that the impulse that is associated with the formation of the jet is accompanied by formation of

multiple vortex rings that continue to be advected even after the condensation is complete. Processing of the high-speed video image sequences shows that the presence of actuation leads to significant reductions in the time-averaged vapor area and concomitant increase in the overall heat transfer coefficient increases of up to 270% compared to condensation in the absence of actuation. Temporal estimates of overall heat transfer coefficient using control volume analysis at a reduced vapor mass flow rate (lower power dissipation and subcooling, using a smaller vapor orifice) shows that in the absence of actuation the peak heat transfer coefficients occur during toroidal breakup while the vapor bubbles are advected away from the orifice. However, pulsed actuation can lead to the formation of the toroidal vapor volume significantly earlier during the nominally time-periodic vapor ejection cycle and the peak heat transfer coefficient is achieved while the bubble is still attached to the orifice prior to separation. These findings clearly point to the ability of the actuation to regulate and accelerate vapor condensation.

In an alternate configuration of the actuation in which a continuous acoustic beam was directed normal to the centerline of the vapor orifice, it was demonstrated that the flow of vapor can be deliberately regulated by forced detachment of vapor bubbles when they reach a given volume. This regulation of the bubble formation leads to higher ejection frequencies of smaller vapor bubbles which rapidly condense in the bulk fluid (as the thermal plume is deflected by the actuation) and to an increase of 330% in overall heat transfer coefficient.

To the best of the author's knowledge, the use of short-wavelength acoustic actuation to accelerate condensation by exploiting the acoustic impedance mismatch at the liquid vapor interface to effect bulk deformation and droplet ejection is a new contribution. The work of this thesis presents a foundation of knowledge on short wavelength acoustic actuation for condensation enhancement. Considering its temporal and spatial

controllability and the robustness of the acoustic actuators it holds even more promise for implementation in practical systems than long wavelength actuation.

*Recommendations for Future Work*

The present investigations have pointed out to several aspects that merit further consideration.

1. Based on the present findings of the coupling of short wavelength acoustic actuation with boiling on textured surfaces that are designed for high-density nucleation sites, it appears that actuation in the presence of even smaller-scale features (such as deposited particle features or hierarchical features) should be investigated to further increase the enhancement. Investigations of boiling surfaces with higher-density nucleation sites but a nominally smooth (on a mm-scale) surface can help clarify the mechanisms of the interactions between acoustic radiation and vapor nucleation.
2. Longer wavelength acoustic actuation should be pursued for increased condensation enhancement. As noted, if the scale of the surface capillary waves is increased, it may also lead to larger amplitudes surface disturbances (as the stability threshold decreases) and therefore faster growth of the thermal boundary layer and further increases in condensation rates. For this reason, it seems unlikely that acoustic actuation in the 10-100 kHz range would be optimal (although the receptivity threshold should be considered), with 300-1000 Hz a more likely range for ideal operating frequencies. It appears that the enhanced heat transfer prior to the breakup of the capillary waves (i.e. bubble ejection/droplet ejection), is due not only to increases in interface area but also by induced motion in the liquid. Beyond the capillary wave amplitude limit where wave break-up occurs, further increases in heat transfer are expected to depend on area increases only, as the

amplitude of the induced motion in the liquid is likely to saturate along with amplitude of the capillary waves.

3. Condensation enhancement of vapor ejection from multiple adjacent orifices using short wavelength acoustic actuation should be investigated with emphasis on spatial coverage of the actuation, and potential cross interaction between the adjacent vapor columns in the presence of phased pulsed actuation. The ability of acoustic actuation to modify the vapor flow regime of both a single orifice and an array of orifices should also be investigated.

## APPENDIX A

## BUBBLE GROWTH AND COLLAPSE MODELS FOR GENERATING HEAT TRANSFER CHARACTERISTICS FROM VOLUMETRIC DATA

The purpose of this control volume analysis is to provide a mechanism for estimating the heat transfer of a naturally condensing bubble as well as an acoustically actuated bubble both during the growth phase (while attached to a vapor reservoir) as well as during the collapse phase (after separation, when no further vapor mass is entering the

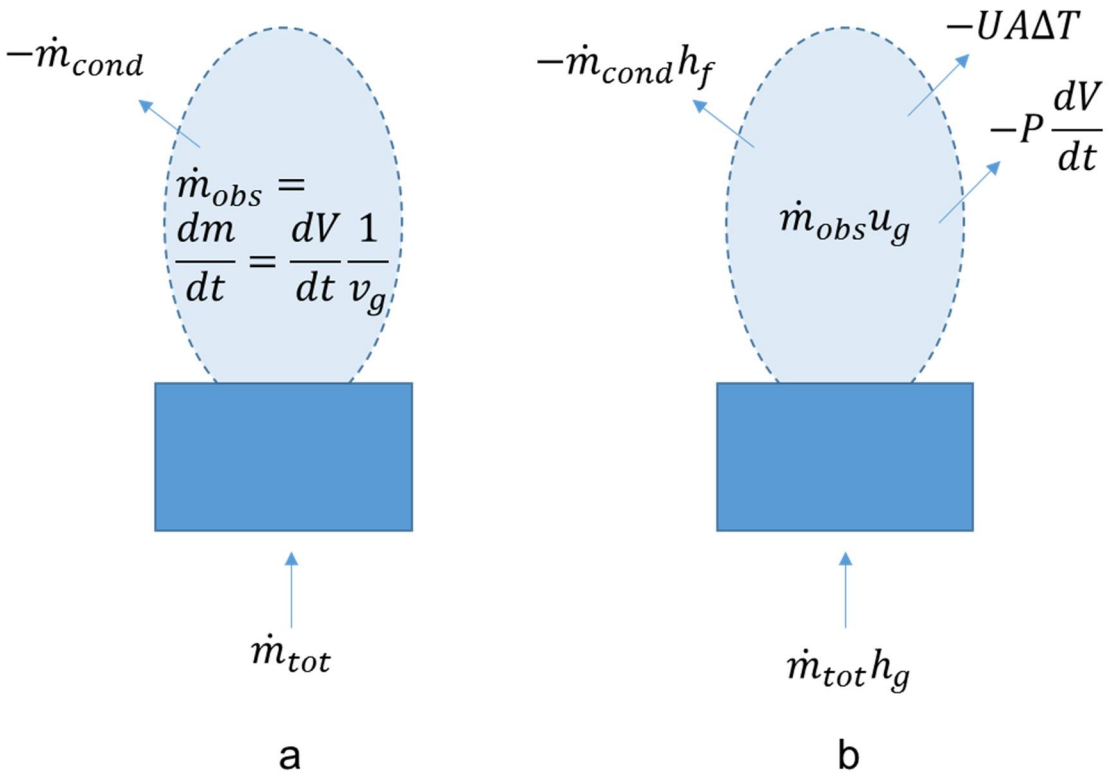


**Figure A.1.** The control bubble and conservation of mass relationships (a) and conservation of energy relationships (b) while attached to the orifice during the growth phase.

bubble). A diagram of the "control bubble," which is a region defined as vapor (which is allowed to both change mass and change volume), is shown in Figure A.1a (conservation of mass) and b (conservation of energy). It has been developed using a simple thermodynamic control volume; for calculations, it was assumed that the gaseous phase properties were the saturated properties at 1 atm and 100 $^{o}$C, with the liquid phase properties always at 1 atm and 92 $^{o}$C. The temperature difference between the bubble and its surroundings for the purposes of defining overall heat transfer coefficient was assumed to be constant 8 $^{o}$C. The bubble was, whether attached to an orifice or not, assumed to be a spherical shape; i.e. having a defined relationship between surface area (used for the heat rate term) and volume such that $V = (4/3)\pi r^3$ and $A = 4\pi r^2$. The pressure within the bubble was assumed to be saturation pressure (i.e., surface tension and curvature were not included to model the overpressure due to surface tension, nor was the effect of static pressure).

The mass conservation of the attached bubbles is defined by:

$$\dot{m}_{tot} - \dot{m}_{cond} = \dot{m}_{obs} \qquad \text{A.1}$$

While the baseline bubble was attached to the orifice, it was assumed that the overall heat transfer coefficient $U_{base}$ was constant, and that a relationship $\gamma$ between the total mass flow rate through the orifice and the observed mass flow rate (based on the changing volume of the bubble) was required, such that over the time during attachment the following held:

$$\gamma \int \dot{m}_{tot} dt = \int \dot{m}_{obs} dt \qquad \text{A.2}$$

$$\int \dot{m}_{cond} dt = \left(\frac{1}{\gamma} - 1\right) \int \dot{m}_{obs} dt = \Gamma \int \dot{m}_{obs} dt \qquad \text{A.3}$$

Based on the observed average bubble volume and measured heater dissipation for the configuration of §7.2, $\gamma = 0.69$, $\Gamma = 0.45$.

The observed mass flow rate could be calculated by the image processed data through the following:

$$\dot{m}_{obs} = \frac{dV}{dt}\frac{1}{v_g} \quad \text{A.4}$$

The energy of the attached, condensing vapor bubble is given by:

$$\dot{Q}_{net} - \dot{W}_{net,out} + \sum \dot{m}h = \frac{dE}{dt} \quad \text{A.5}$$

$$-U_{base}A\Delta T - P\frac{dV}{dt} + \dot{m}_{tot}h_g - \dot{m}_{cond}h_f = \dot{m}_{obs}u_g \quad \text{A.6}$$

The total heat transfer is directly related to the mass flow of condensate leaving the system by:

$$UA\Delta T = \dot{m}_{cond}h_{fg} \quad \text{A.7}$$

With the relationship between the spherical volume and area known, this yields:

$$U_{base}4\pi\left(\frac{3V}{4\pi}\right)^{2/3}\Delta T = \dot{m}_{cond}h_{fg} \quad \text{A.8}$$

Replacing the condensation term by combining Eq. A.8 with Eq. A.3 yields:

$$U_{base}\int 4\pi\left(\frac{3V}{4\pi}\right)^{2/3}\Delta T dt = \Gamma\int \dot{m}_{obs}h_{fg}dt \quad \text{A.9}$$

Finally, combining Eq. A.9 with Eq. A.4 and rearranging terms yields the expression for overall heat transfer coefficient of a bubble attached to an orifice under base flow conditions (including prior to acoustic actuation):

$$U_{base} = \frac{\Gamma\left(\frac{h_{fg}}{v_g}\right)\int\frac{dV}{dt}dt}{\int 4\pi\left(\frac{3V}{4\pi}\right)^{2/3}\Delta T dt} \quad \text{A.10}$$

This relationship holds for the baseline bubble under separation from the orifice, and the acoustically actuated bubble prior to actuation onset. From the available data, $U_{base}$ was computed to be $1.05\cdot10^4$ [W/(m$^2$K)]. After actuation onset, the overall heat transfer coefficient is no longer known, nor can it be assumed to be constant. To accommodate for this fact, a simplifying assumption must be made: while the acoustically actuated

bubble remains attached to the orifice, the mass flow rate through the orifice is assumed to be equal to that of a mean base flow bubble at the same moment in its life cycle; i.e.:

$$\dot{m}_{tot,base} = \dot{m}_{tot,act} \tag{A.11}$$

From A.1, A.4, and A.7

$$\dot{m}_{tot} = \frac{dV_{base}}{dt}\frac{1}{v_g} + \frac{U_{base}A_{base}\Delta T}{h_{fg}} \tag{A.12}$$

Then Eq A.6 and Eq. A.11 may be used to generate the following:

$$-U_{act}A_{act}\Delta T - P\frac{dV_{at}}{dt} + \dot{m}_{tot}h_g - \dot{m}_{cond,act}h_f = \dot{m}_{obs,act}u_g \tag{A.13}$$

Noting that A.7 holds for all bubbles, it may be used with A.13 and A.12 and combining thermodynamic properties ($h_{fg} + h_f = h_g$ ; $u_g + Pv_g = h_g$)

$$-U_{act}A_{act}\Delta T\left(\frac{h_g}{h_{fg}}\right) + \dot{m}_{tot}h_g = \frac{dV_{act}}{dt}\frac{1}{v_g}h_g \tag{A.14}$$

Then combining A.14 with A.12 and rearranging yields

$$U_{act}A_{act}\Delta T = \frac{h_{fg}}{v_g}\left(\frac{dV_{base}}{dt} - \frac{dV_{act}}{dt}\right) + U_{base}A_{base}\Delta T \tag{A.15}$$

Finally, by using the relationship between volume and area and recognizing that $U_{base}$ was previously determined to be $1.7\cdot10^4$ [W/(m$^2$K)], a final relationship for $U_{act}$ while the bubble is attached to the nozzle is found as a function of volume data:

$$U_{act} = \frac{\frac{h_{fg}}{v_g}\left(\frac{dV_{base}}{dt} - \frac{dV_{act}}{dt}\right) + U_{base}4\pi\left(\frac{3V_{base}}{4\pi}\right)^{2/3}\Delta T}{4\pi\left(\frac{3V_{act}}{4\pi}\right)^{2/3}\Delta T} \tag{A.16}$$

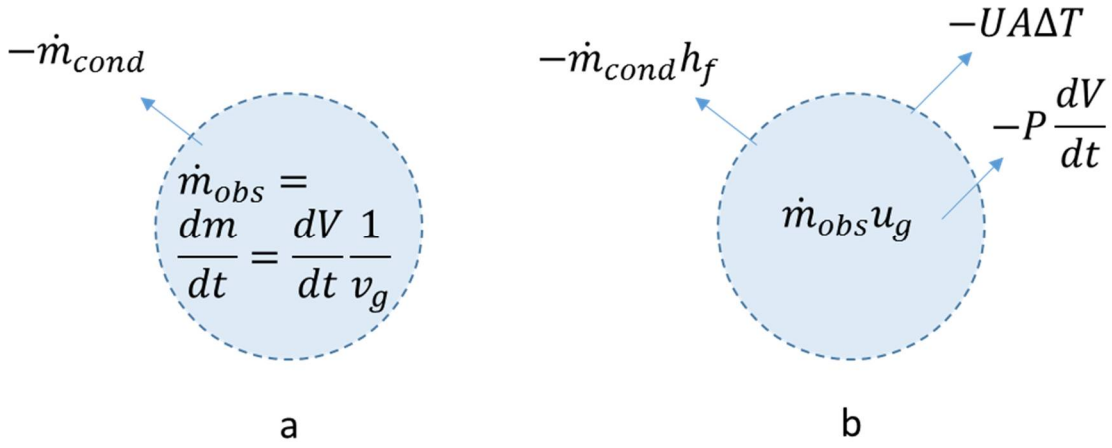


**Figure A.3.** The control bubble and conservation of mass relationships (a) and conservation of energy relationships (b) after separation from the orifice.

The model is significantly simplified after the bubble separates from the orifice, as there is no longer a mass flow rate into the bubbles that must be accounted for. Figure A.2a shows the conservation of mass for the bubble after advection from the orifice, and Figure A.2b shows conservation of energy.

Equation A.1 and A.6 now simplify to:

$$-\dot{m}_{cond} = \dot{m}_{obs} \tag{A.17}$$

$$-UA\Delta T - P\frac{dV}{dt} - \dot{m}_{cond}h_f = \dot{m}_{obs}u_g \tag{A.18}$$

Which may be combined and rearranged to yield the overall heat transfer coefficient for a bubble as a function of observed volume:

$$U = \frac{-\frac{dV}{dt}\left(\frac{u_g - h_f}{v_g} + P\right)}{4\pi\left(\frac{3V}{4\pi}\right)^{2/3}\Delta T} = \frac{-\frac{dV}{dt}\left(\frac{h_{fg}}{v_g}\right)}{4\pi\left(\frac{3V}{4\pi}\right)^{2/3}\Delta T} \tag{A.19}$$

Where the second equality is generated through the use of thermodynamic property relationships.

To generate the instantaneous heat rate $\dot{q}$, Eqs. A.10 (i.e., the resulting constant), A.16, and A.19 may be multiplied by the instantaneous area of the bubble and the constant $\Delta T$. The base flow bubble was assumed to be governed by constant $U_{base}$ until separation at $t/T_b = 0.25$, when it switched to being governed by Eq. A.19, while the acoustically actuated bubble had three domains: for $t/T_b < 0$, $U_{base}$ was used; for $0 < t/T_b < 0.25$, Eq. A.16 was used; for $t/T_b > 0.25$ Eq. A.19 was used.

Caution should be used regarding the heat transfer coefficients and heat rates generated through this analysis. Data, especially for a single bubble realization, tend to be noisy. The analysis used to transform bubble volume into heat transfer coefficient built in several assumptions, such as the relationship between observed bubble volume and mass flow rate through the orifice during the attached phase as well as a constant heat transfer coefficient during this time period for the unactuated bubble, and the unchanging orifice mass flow rate between the baseline and acoustically actuated bubble while attached to the orifice. The analysis did not consider the role noncondensable gas slowing the condensation, the role of the thermal boundary layer decreasing apparent $\Delta T$ over time, or other effects which would have required adding terms not directly derived from the experimental data. As noted previously, the raw data is not volume but approximated volume based on frontal area and a spherical assumption, making it likely that the local peaks in heat rate are due to “catch-up” effects where bubble deformation reveals the extent of prior condensation not previously visualized. This analysis is not to be used for engineering calculations (nor should the data generated through its use be used for engineering calculations).

## REFERENCES


Abe Y Kawaji M Watanabe T 2002 “Study on the bubble motion control by ultrasonic wave,” Experimental Thermal and Fluid Science 26 817–826

Agostini B Fabbri M Park J E Wojtan L Thome J R, and Michel B 2007 “State of the art of high heat flux cooling technologies,” Heat Transfer Eng. 28 258–8

Al Issa, S., P. Weisensee, and R. Macian-Juan. 2014. “Experimental Investigation of Steam Bubble Condensation in Vertical Large Diameter Geometry under Atmospheric Pressure and Different Flow Conditions.” International Journal of Heat and Mass Transfer 70. 918–29.

Bar-Cohen A 1993 “Thermal management of electronic components with dielectric liquids,” JSME B 36 1–25

Barreras F Amaveda H and Lozano S 2002 “Transient high-frequency ultrasonic water atomization,” Experiments in Fluids 33 405-413

Berenson P J 1962 “Experiments on Pool-Boiling Heat Transfer,” International Journal of Heat and Mass Transfer 5 985-999

Bergles A E 1997 "Enhancement of pool boiling," Int J. Refrig. 20 545-551

Bjerknes V 1906 Fields of Force, Columbia University Press, New York

Bunkin F V Kravtsov Y A Lyakhov G A 1986 “Acoustic analogues of nonlinear-optics phenomena,” Soviet Physics Uspekhi 29 607-619

Celata G P Cumo M Farello G E and Focardi G 1986 “Direct Contact Condensation of Steam on Slowly Moving Water,” Nuclear Engineernig and Design, 96(1) 21-31

Cheeke J D N 2002 Fundamentals and applications of ultrasonic waves, CRC Press, Boca Raton, FL

Chien L-H and Webb R L 1998 “Visualization of pool boiling on enhanced surfaces,” Experimental Thermal and Fluid Science 16 332-341

Cho S C and Lee W K 1991 “Steam bubble formation at a submerged orifice in quiescent water,” Chemical Engineering Science 46(3) 789-795

Cooke D and Kandlikar S G 2011 “Pool Boiling Heat Transfer and Bubble Dynamics Over Plain and Enhanced Microchannels,” Journal of Heat Transfer 133

Cooper M G and Lloyd A J P 1969 “The Microlayer in Nucleate Pool Boiling,” International Journal of Heat and Mass Transfer 12 895-913

Crum L A 1975 “Bjerknes forces on bubbles in a stationary sound field,” Journal of the Acoustical Society of America 57 1363-1370

Dahikar S K Sathe M J and Joshi J B 2010 “Investigation of flow and temperature patterns in direct contact condensation using PIV, PLIF, and CFD,” Chemical Engineering Science 65 4606-4620

de With A P Calay R K and de With G 2007 “Three-dimensional condensation regime diagram for direct contact condensation of steam injected into water,” International Journal of Heat and Mass Transfer 50(9) 1762-1770

Dhir V K 1998 “Boiling Heat Transfer,” Annual Review of Fluid Mechanics 30 365-401

Douglas Z Boziuk T R Smith M K and Glezer A 2012 “Acoustically enhanced boiling heat transfer,” Physics of Fluids 24(5)

Douglas, Z 2007 *Acoustically Enhanced Boiling Heat Transfer* Master’s Thesis, Georgia Institute of Technology

Eames I 2010 “Momentum Conservation and Condensing Vapor Bubbles,” Journal of Heat Transfer 132

Eller A 1968 “Force on a Bubble in a Standing Acoustic Wave,” Journal of the Acoustical Society of America 43 170-171

Eller A I Crum L A 1970 “Instability of the Motion of a Pulsating Bubble in a Sound Field,” Journal of the Acoustical Society of America, 47(3 part 2), 762-767

Fair J R “Direct Contact Gas-Liquid Heat Exchange for Energy Recovery,” Journal of Heat Transfer 112 212-222

Faraday M 1831 “On the forms and states assumed by fluids in contact with vibrating elastic surfaces,” Philosophical Transactions of the Royal Society of London 121 299-340

Florschuetz L W and Chao B T 1965 “On the Mechanics of Vapor Bubble Collapse,” Journal of Heat Transfer 87 209-220

Glezer A and Coles D 1990 “An experimental study of a turbulent vortex ring,” Journal of Fluid Mechanics 211 243-283

Hao Y Oguz H N and Prosperetti A 2001 “The action of pressure-radiation forces on pulsating vapor bubbles,” Phys. of Fluids 13 1167-77

Heffington S Tillery S Smith M and Glezer A 2003 “Enhanced boiling heat transfer by submerged, vibration induced jets,” Therminic: 9th International, Aix-en-Provence, France

Hetsroni G Moldavsky L Fichman M Pogrebnyak E Mosyak A 2014 “Ultrasonic enhancement of subcooled pool boiling of freely oscillated wires,” Int. J. of Multiphase Flow. 67 13-21

Hopfinger E.J., and Das, S. P. 2009. “Mass Transfer Enhancement by Capillary Waves at a Liquid – Vapour Interface,” Experiments in Fluids, 46:4 597–605.

Iida Y and Tsutsui K 1992 “Effects of Ultrasonic Waves on Natural Convection, Nucleate Boiling, and Film Boiling Heat Transfer from a Wire to a Saturated Liquid,” Experimental Thermal and Fluid Science 5 108-115

Isakoff S E 1956 “Effect of an ultrasonic field on boiling heat transfer – Exploratory investigation,” Stanford University Press, Stanford, CA, 15–28

Jacobs H R 1988 “Direct-Contact Heat Transfer for Process Technologies,” Journal of Heat Transfer 110

Kalman H and Mori Y H 2002 “Experimental analysis of a single vapor bubble condensing in subcooled liquid,” Chemical Engineering Journal 85 197-206

Kamei S and Hirata M 1976 “High Speed Photographic Study on the Condensation of Vapor Bubbles in the Subcooled Liquid,” SPIE High Speed Photography 97

Kamei S and Hirata M 1990 “Condensing Phenomena of a Single Vapor Bubble into Subcooled Water,” Experimental Heat Transfer 3 173-182

Kar, S, X D Chen, and M I Nelson. 2007. “Direct-Contact Heat Transfer Coefficient for Condensing Vapour Bubble in Stagnant Liquid Pool.” Chemical Engineering Research and Design 85 (3): 320–28.

Kelvin L (W Thompson) 1871 “Hydrokinetic solutions and observations,” Philosophical Magazine 4 42 362-377

Kim H-Y Kim Y G and Kang B H 2004 “Enhancement of natural convection and pool boiling heat transfer via ultrasonic vibration,” Int. J. Heat Mass Trans 47 2831–40

Kim, Seong Jin, and Goon Cherl Park. 2011. “Interfacial Heat Transfer of Condensing Bubble in Subcooled Boiling Flow at Low Pressure.” International Journal of Heat and Mass Transfer 54 (13–14). 2962–74.

Kinsler L E Frey A R Coppens A B and Sanders J V 2000 Fundamentals of Acoustics, 4th Ed. John Wiley and Sons, Inc., New York, NY

Kocamustafaogullari G and Ishii M 1983 “Interfacial Area and Nucleation Site Density in Boiling Systems,” International Journal of Heat and Mass Transfer 26 (9) 1377-1387

Kumar K and Tuckerman L S 1994 “Parametric Instability of the interface between two fluids,” Journal of Fluid Mechanics 279 49-68

Lang R J 1962 “Ultrasonic Atomization of Liquids,” Journal of the Acoustical Society of America, 34(1) 6-8

Launay S Fedorov A Joshi Y Cao A and Ajayan P 2006 “Hybrid micro-nano structured thermal interfaces for pool boiling heat transfer enhancement,” Microelectronics Journal 37 1158-1164

Lee C P and Wang T G 1993 “Acoustic radiation force on a bubble,” Journal of the Acoustical Society of America 93 1637-1640

Leighton T G 1994 The Acoustic Bubble, Academic, San Diego CA

Li B Han X Wan Z Wang X Tang Y 2016 “Influence of ultrasound on heat transfer of copper tubes with different surface characteristics in sub-cooled boiling,” Applied Therm. Eng. 92 93-103

Li C and Peterson G P 2007 “Parametric Study of Pool Boiling on Horizontal Highly Conductive Microporous coated surfaces,” Journal of Heat Transfer 129 1465-1475

Li C Wang Z Wang P-I Peles Y Koratkar N and Peterson G P 2008 “Nanostructured copper interfaces for enhanced boiling,” Small 4 1084-1088

Maksimov A O and Leighton T G 2012 “Pattern formation on the surface of a bubble driven by an acoustic field,” Proceedings of the Royal Society A 468 57-75

Maksimov A O Leighton T G 2012 “Pattern formation on the surface of a bubble driven by an acoustic field,” Proceedings of the Royal Society A: Mathematical, Physical and Engineering Science, 468(2137), 57-75

Maksimov A O Leighton T G and Birkin P R 2008 “Self focusing of acoustically excited Faraday ripples on a bubble wall,” Physics Letters A 372 3210-3216

McGillis W R and Carey V P 1991 “Pool boiling enhancement techniques for water at low pressure,” 7th IEEE Semiconductor Thermal Measurement and Management Symposium, 64

Mudawar I 2001 “Assessment of high-heat-flux thermal management schemes,” IEEE Transactions on Components and Packaging Technology 24 122–41

Nogueira J Lecuona A and Rodriguez PA 1997 “Data validation, false vectors correction and derived magnitudes calculations on PIV data,” Measurement Science and Technology 8 (12) 1493-1501

Nukiyama, S 1934 “The maximum and minimum values of heat Q transmitted from metal to boiling water under atmospheric pressure,” J. Japan Soc. Mech. Engrs 37 367-374

Nukiyama, S 1984 “The maximum and minimum values of heat Q transmitted from metal to boiling water under atmospheric pressure,” International Journal of Heat and Mass Transfer 27(7) 959-970

O'Hanley H Coyle C, Buongiorno J McKrell T Hu L-W Rubner M, and Cohen R 2013 "Separate effects of surface roughness, wettability, and porosity on the boiling critical heat flux," Applied Physics Letters 103(2)

Panton R L 2005 Incompressible Flow, John Wiley & Sons, Inc, Hoboken NJ

Park K A and Bergles A E 1988 “Ultrasonic enhancement of saturated and subcooled pool boiling,” Int. J. Heat Mass Trans. 31 664–7

Pascual CC Jeter S M and Abdel-Khalik S I 2002 “Visualization of boiling bubble dynamics using a flat uniformly heated transparent surface,” International Journal of Heat and Mass Transfer 45 691-696

Propseretti A 1984 “Bubble phenomena in sound fields: part one,” Ultrasonics 22(2) 69-77

Prosperetti, Andrea. 2017. “Vapor Bubbles.” Annual Review of Fluid Mechanics 49 (1)

Qu, Xiao Hang, Mao Cheng Tian, Guan Min Zhang, and Xue Li Leng. 2015. “Experimental and Numerical Investigations on the Air-Steam Mixture Bubble

Condensation Characteristics in Stagnant Cool Water." Nuclear Engineering and Design 285. 188–96.

Rayleigh L1883 "On the crispations of fluid resting upon a vibrating surface," Philosophical Magazine 5 16 50-58

Schmidt H 1977 "Bubble Formation and Heat Transfer during Dispersion of Superheated Steam in Saturated Water I," International Journal of Heat and Mass Transfer 20 635-646

Settles G S 2001 Schlieren and Shadowgraph Techniques, Springer-Verlag Berlin, Germany

Sideman S and Moalem-Maron D 1982 "Direct contact condensation," Advances in Heat Transfer 15 227-281

Simon J C Sapozhnikov O A Khokhlova V A Crum L A and Bailey M R 2015 "Ultrasonic atomization of liquids in drop-chain acoustic fountains," Journal of Fluid Mechanics 766 129-146

Sitter J S Snyder T J Chung J N and Marston P L 1998 "Terrestrial and microgravity pool boiling heat transfer from a wire in an acoustic field," Int. J. Heat Mass Trans. 41 2143-55

Sloan A Penley S and Wirtz R A 2009 "Sub-Atmospheric Pressure Pool Boiling of Water on a Screen-Laminate Enhanced Surface," 25th IEEE SEMI-THERM Symposium 246-253

Sun K-H and Lienhard J H 1970 "The Peak Pool Boiling Heat Flux on Horizontal Cylinders," International Journal of Heat and Mass Transfer 13 1425-1439

Tang J Yan C and Sun L 2009 "Enhanced vapor bubble condensation and collapse with ultrasonic vibration," Experimental Thermal and Fluid Science 70 115-124

Tang, Jiguo, Changqi Yan, and Licheng Sun. 2015. "Effects of Noncondensable Gas and Ultrasonic Vibration on Vapor Bubble Condensing and Collapsing." Experimental Thermal and Fluid Science 61 210–20.

Tang, Jiguo, Changqi Yan, and Licheng Sun. 2016. "Enhanced Vapor Bubble Condensation and Collapse with Ultrasonic Vibration." Experimental Thermal and Fluid Science 70. 115–24.

Terasaka K Sun W-Y Prakoso T and Tsuge H 1999 "Measurement of Heat Transfer Coefficient for Direct-Contact Condensation during Bubble Growth in Liquid," Journal of Chemical Engineering of Japan 32(5) 594-599

Tian, W X, R H Chen, J L Zuo, S Z Qiu, G H Su, Y Ishiwatari, and Y Oka. 2014. "Numerical Simulation on Collapse of Vapor Bubble Using Particle Method." Heat Transfer Engineering 35 (6–8): 753–63.

Tillery S W Heffington S N Smith M K and Glezer A 2006 "Boiling heat transfer enhancement using a submerged, vibration-induced jet," J. Electron. Packag. 128 145–49

Tomita Y 2014 “Jet atomization and cavitation induced by interactions between focused ultrasound and a water surface,” Physics of Fluids 26

Torr, G. R. "The acoustic radiation force." American Journal of Physics 52, no. 5 (1984): 402-408.

Trinh E H Thiessen D B and Holt R G 1998 “Driven and freely decaying nonlinear shape oscillations of drops and bubbles immersed in a liquid: experimental result,” Journal of Fluid Mechanics, 364, 253-272

Ueno I Hattori Y and Hosoya R “Condensation and Collapse of Vapor Bubbles Injected in Subcooled Pool,” Microgravity Sci. Technol. 23 73-77

Vukasinovic B Smith M K and Glezer A 2007 “Dynamics of a sessile drop in forced vibration,” Journal of Fluid Mechanics, *587*, 395-423

Westerweel J and Scarano F 2005 “Universal outlier detection for PIV data,”
Experiments in Fluids 39 (6) 1096-1100

Wong S W and Chon W Y 1967 “Effects of ultrasonic vibrations on burnout heat flux and critical temperature difference,” Can. J. Chem. Eng. 45 384–5

Zerby M and Kuszewski M 2002 “Final report on next generation thermal management (NGTM) for power electronics,” NSWCCD Technical Report TR-82-2002012

Zuber, N 1959 *Hydrodynamic Aspects of Boiling Heat Transfer* Doctoral Thesis, University of California Los Angeles

Krasil’nikov, V A 1963 Sound and Ultrasound Waves, 3rd Ed., Israel Program for Scientific Translations Ltd., Jerusalem, Israel.

# VITA

Thomas Robert Boziuk was somewhat precariously born to his parents Victoria and Joseph at their home in Sudbury, Massachusetts on November 11th 1986 in advance of the planned transportation to Framingham. He grew up at that house for 18 years along with his older brother William, both educated by the Sudbury public school system, before attending Tufts University, where he received his B.S. in Mechanical Engineering in the spring of 2009. He drove to Atlanta two weeks later to begin his work at Georgia Institute of Technology, where he earned his M.S. in Mechanical Engineering in the spring of 2013. He will be lecturing at Georgia Tech Lorraine in the fall of 2017 prior to pursuing further research. He lives in Atlanta, Georgia with his wife Kelly-Ann and their dog Isabel, and when he is not in the lab, he enjoys photography, woodworking, and dreaming of building a sailboat.